DOT/FAA/AR-08/52

Air Traffic Organization
Operations Planning
Office of Aviation Research
and Development
Washington, DC 20591

Characterization and Structural Behavior of Braided Composites

January 2009

Final Report

U.S. Department of Transportation
Federal Aviation Administration

NOTICE

Technical Report Documentation Page

1. Report No.	2. Government Accession No.	3. Recipient's Catalog No.
DOT/FAA/AR-08/52		

4. Title and Subtitle	5. Report Date
CHARACTERIZATION AND STRUCTURAL BEHAVIOR OF BRAIDED COMPOSITES	January 2009
	6. Performing Organization Code

7. Author(s)	8. Performing Organization Report No.
Ajit D. Kelkar* and John D. Whitcomb**	

9. Performing Organization Name and Address	10. Work Unit No. (TRAIS)
*Department of Mechanical Engineering North Carolina A&T State University 626 McNair Hall, 1601 E. Market Street Greensboro, NC 27411 **Department of Aerospace Engineering Texas A&M University 3141 TAMU College Station, TX 77843	
	11. Contract or Grant No. DTFA03-01-C00033

12. Sponsoring Agency Name and Address	13. Type of Report and Period Covered
U.S. Department of Transportation Federal Aviation Administration Air Traffic Organization Operations Planning Office of Aviation Research and Development Washington, DC 20591	Final Report
	14. Sponsoring Agency Code AIR-100

15. Supplementary Notes

The Federal Aviation Administration Technical Monitor was Curtis Davies.

16. Abstract

The growing interest in small business jets in the general aviation industry is the motivation of this present research. The major objective in the small business jet industry is to reduce costs while keeping takeoff weights below 12,500 lb (5670 kg), which is a requirement of the Federal Aviation Administration. The overall objective of this research is the performance evaluation and modeling of biaxial braided composites manufactured using vacuum-assisted resin transfer molding.

Biaxial braided composites with different braid angles were manufactured using carbon braids and two different resin systems (vinyl ester and epoxy). Static tension and tension-tension fatigue tests were performed. It was concluded that the Sigmoidal function accurately represents the stress-fatigue life curve of braided composites. It was observed that the braid angle has great influence on mechanical properties but has less effect on endurance limits. The variation in ultimate tensile strength between the specimens caused large scatter in the fatigue data. A new approach based on statistical analysis techniques for conducting fatigue tests is recommended. A new approach was developed to model stiffness degradation curves. This model was proven to be very efficient in all the three major stages of stiffness degradation.

A computational micromechanics strategy was developed to model 2x2 braids. Since the tow cross-section along the towpath is not uniform, direct finite element mesh generation for the model is difficult. A mapping technique was developed to generate the finite element mesh for various 2x2 biaxial braids from the previously developed mesh for the twill weave. This resulted in substantial time savings. By exploiting symmetry operations such as mirroring, rotation, or a combination of the two, the analysis region was greatly reduced.

The analyses for different braids have shown that the peak stresses in the tow mainly occur at the undulating region and along the edges of the tow. Stress distribution in braids was also compared with those in equivalent laminates. A considerable volume of the tow (10%-45% for the range of parameters studied) had stresses larger than an equivalent lamina. The severity of stresses in a braid as compared to those in an equivalent lamina depends upon braid geometric parameters. Braid angle changes the stress distribution in the tow considerably. The severity of peak stresses seems to be increasing linearly with an increase in waviness ratio.

17. Key Words	18. Distribution Statement
Composites, Braiding, VARTM, Fatigue, Analytical modeling	This document is available to the U.S. public through the National Technical Information Service (NTIS) Springfield, Virginia 22161.

19. Security Classif. (of this report)	20. Security Classif. (of this page)	21. No. of Pages	22. Price
Unclassified	Unclassified	181	

ACKNOWLEDGEMENTS

The authors want to thank the Federal Aviation Administration for funding this work, especially to Mr. Curtis Davies, who coordinated all the activities. The authors acknowledge the efforts of our students Xiaodong Tang, Jitendra Tate, and Deepak Goyal who helped to make this project a success.

TABLE OF CONTENTS

LIST OF FIGURES

LIST OF TABLES

LIST OF ACRONYMS AND SYMBOLS

2D	Two-dimensional
3D	Three-dimensional
BA	Braided angle
cp	Centipoise
CV	Sample coefficient of variation, in percent
DGEBA	Diglycidyl ether of biphenol A
DM	Derakane momentum
EVA	Ethylene vinyl acetate
FAA	Federal Aviation Administration
kg	Kilogram
PC	Personal computer
RTM	Resin transfer molding
S-N	Stress-fatigue life
SEM	Scanning electron microscope
T_g	Glass transition temperature
TGMDA	Tetraglycidyl methylene dianiline
UD	Unidirectional
UTS	Ultimate tensile strength
VARTM	Vacuum-assisted resin transfer molding
VOC	Volatile organic content
WR	Waviness ratio

EXECUTIVE SUMMARY

The growing interest in small business jets in the general aviation industry is the motivation of this present research. The major objective in the small business jet industry is to reduce costs while keeping takeoff weights below 12,500 lb (5670 kg), which is a requirement of the Federal Aviation Administration. The overall objective of this research is the performance evaluation and modeling of biaxial braided composites manufactured using vacuum-assisted resin transfer molding (VARTM).

The natural conformability of biaxial braids makes them more cost competitive than woven fabric. The VARTM process has proven to be low in cost compared to resin transfer molding. Thus, the combination of biaxial braids and the VARTM process is likely to considerably reduce overall costs. Before the braids can be used confidently in the primary structures, it is necessary to understand the performance of biaxial braided composites under various loading conditions and especially under fatigue.

Biaxial braided composites with different braid angles were manufactured using carbon braids and two different resin systems (vinyl ester and epoxy). Static tension and tension-tension fatigue tests were performed. It was concluded that the Sigmoidal function accurately represents the stress-fatigue life curve of braided composites. It was observed that the braid angle has great influence on mechanical properties but has less effect on endurance limits.

It was observed that the variation in ultimate tensile strength between the specimens caused large scatter in the fatigue data. A new approach based on statistical analysis techniques for conducting fatigue tests is recommended.

The different mechanisms of fatigue failure of composites are reflected in the stiffness degradation, which can be measured nondestructively. A new approach was developed to model stiffness degradation curves. This model was proven to be very efficient in all the three major stages of stiffness degradation.

A computational micromechanics strategy was developed to model 2x2 braids. Since the tow cross-section along the towpath is not uniform, direct finite element mesh generation for the model is difficult. A mapping technique was developed to generate the finite element mesh for various 2x2 biaxial braids from the previously developed mesh for the twill weave. This resulted in substantial time savings. By exploiting symmetry operations such as mirroring, rotation, or a combination of the two, the analysis region was greatly reduced.

This work presents an investigation of the effect of various parameters such as braid angle, waviness ratio (WR), material properties, and cross-section shape on the effective engineering properties of the 2x2 braids. Extensive parametric studies were conducted for two material systems: (1) glass fiber/epoxy matrix (S2/SC-15) and (2) carbon fiber/epoxy matrix (AS4/411-350). Equivalent laminated materials with angle plies and a resin layer were also analyzed to compare the difference in predictions from full three-dimensional finite element analyses of the 2x2 braided composites. The predictions are also compared with experimental results for a carbon/epoxy material system.

The effect of variation in braid parameters on the progressive failure behavior of a 2x2 braided composite laminate was studied. A bottom-up multiscale finite element modeling approach was employed that sequentially considered the fiber/matrix scale, the tow architecture scale, and the laminate scale.

The analyses for different braids have shown that the peak stresses in the tow mainly occur at the undulating region and along the edges of the tow. Stress distribution in braids was also compared with those in equivalent laminates. A considerable volume of the tow (10%-45% for the range of parameters studied) had stresses larger than an equivalent lamina. The severity of stresses in a braid as compared to those in an equivalent lamina depends upon braid geometric parameters. Braid angle changes the stress distribution in the tow considerably. The severity of peak stresses seems to be increasing linearly with an increase in WR.

1. INTRODUCTION.

1.1 MOTIVATION.

The motivation for the present research was to meet the challenges of small business jet applications for which the Federal Aviation Administration (FAA) (Title 14 Code of Federal Regulations Part 23, Appendix C, Single Pilot Certification) requires a takeoff weight of 12,500 lb (5670 kilogram (kg)) or less. Typically, small business jets have a seven-passenger capacity, maximum cruise speed of 530 mph (465 knots or 853 kilometers per hour (km/h)) and a maximum range of 1875 miles (3000 km). Their cost ranges from 3.5 to 4.5 million U.S. dollars. The major objectives in the small business jet industry are to reduce costs while keeping weight below 12,500 lb (5670 kgf). Reduced weight is possible only if the primary and secondary structures are made of lightweight composite materials. Thus, competitive costs depend on the selection of fabric, resin, and manufacturing methods. The main design feature of small business jets today is a composite fuselage built with automated fiber placement techniques (Aerospace Technology Magazine aerospace-technology.com/projects/raytheon .premier1/, September 6, 2008)

Biaxial braided fabric, with its natural conformability, can fit over any complex shape. Thus, there is no need for cutting, stitching, and fiber placement as required for woven fabric. This ability reduces part count and makes biaxial braided fabric useful for primary structures like the fuselage. Braided composites have been proven to be cost-competitive. It was recently proven that carbon braids are extremely efficient for single-part airfoil sections like wing flaps (Swain, 2000). Vacuum-assisted resin transfer molding (VARTM) is a low-cost manufacturing process with the capability of manufacturing complex parts with higher fiber volume fractions than those from hand lay-up.

Braided composite manufactured using the VARTM process is one of the major candidates for small business jet applications. Although braided composites have an enormous number of applications, the interest of the present research is in small business jet applications. The primary focus is on the manufacturing of braided composites using VARTM, performance evaluation, and analytical modeling.

1.2 BRAIDED FABRIC.

The commonly used composites are tape laminates and textile composites. Tape laminates have good in-plane properties. Textile composites, which include woven, braided, and knitted fabrics, are also important when considering out-of-plane properties. Textile composites generally have better dimensional stability, out-of-plane properties, and impact and delamination resistance. Figure 1-1 shows the different orthogonal weave patterns of textile fabric (Whitcomb and Tang, 1999).

Braiding is an ancient textile process that is simple and highly productive. Braided fabric is used for many secondary structures such as stiffeners, wing spars, floor beams, fuselage frames, ducting, and housings in aerospace applications. There is a growing interest in using this technique to manufacture composite preforms for primary structures like wing flaps, horizontal stabilizers, and fuselage especially for small business jet applications (Swain, 2000).

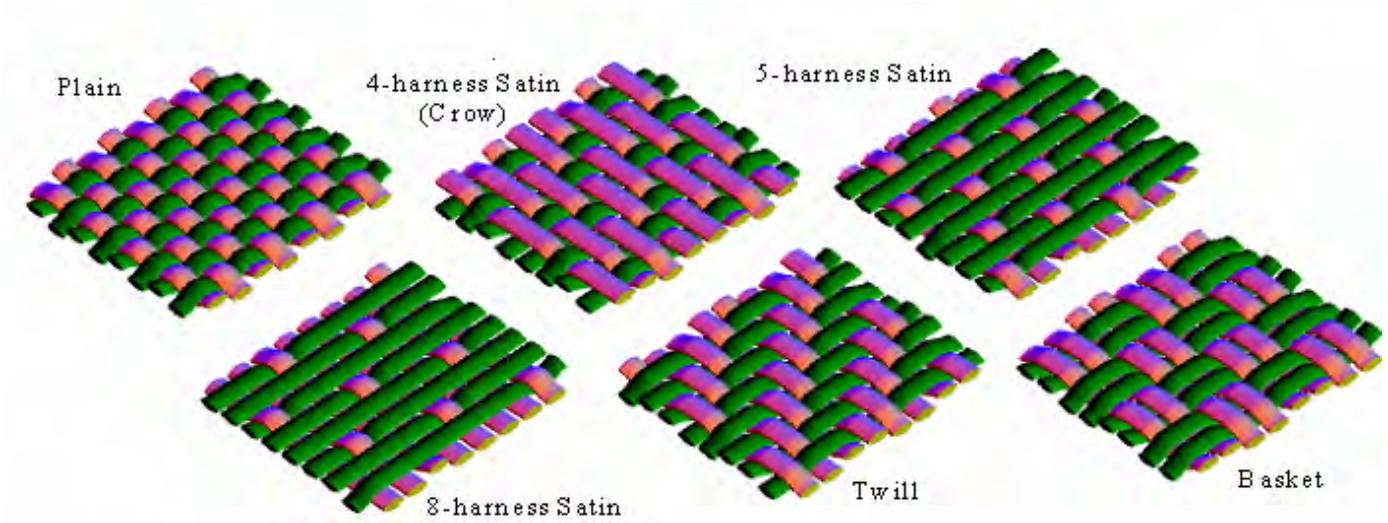

Figure 1-1. Different Weave Patterns of Textile Fabric (Plain, Twill, Satin, and Basket) (Whitcomb and Tang, 1999)

Figure 1-2(a) shows the manufacturing of planar braids consisting of a braider head and a traversing mechanism. Yarns are intertwined and laid on the mandrel. In biaxial braiding, two sets of yarn carriers move along intersecting undulating circular paths in opposite directions to form tubular interlaced fabric. Introducing axial yarns in the lengthwise direction forms a triaxial braid (Kumar and Wang, 1997). Figure 1-2(b) displays the carriers on the working model of a braider (Courtesy of A&P Technology, Inc.). Figure 1-3 shows the biaxial and triaxial braids. Braid architecture resembles a combination of filament winding and weaving. Fibers in braided tubes have continuity between the ends of the part and are mechanically interlocked.

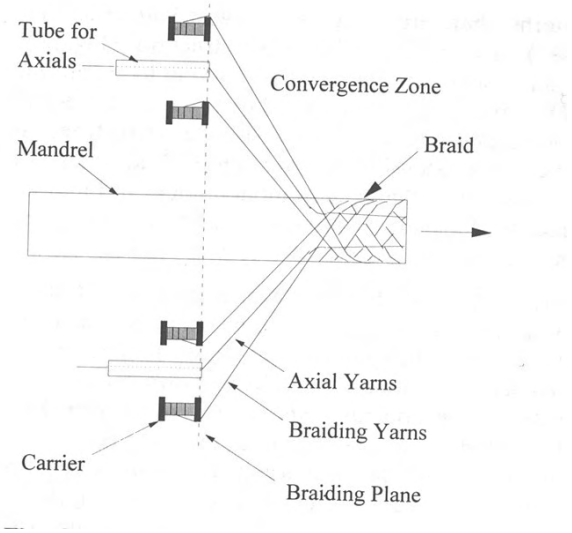

(a)

(b)

Figure 1-2. (a) Schematic of Braiding Process (Kumar and Wang, 1997) and (b) Working Model of Braider (Courtesy of A&P Technology, Inc.)

Figure 1-3. (a) Biaxial Braid and (b) Triaxial Braid (Byun, 2000)

Biaxial braided tubes have natural conformability, also referred to as Chinese finger trap, which refers to the diameter reduction when the tubes are pulled along lengthwise. The braid tube fits over the complex components easily. Therefore, cutting, stitching, and fiber placement are not required as in woven fabric. The tube form of braid is supplied on reels, as shown in figure 1-4. The introduction of axial yarn in triaxial braid locks the diameter and stops the braid's natural conformability. Braided tubes are cut along the braid axis and the edges are fused or stitched to create slit sleeves (http://www.braider.com). As the slit sleeves are fused at the edges, they maintain a constant braid angle during processing. The braided composites' mechanical properties are sensitive to the braid angle. Therefore, slit sleeves were used in the latter part of this research.

Figure 1-4. Biaxial Braided Tubes on Reel

Full coverage of the braid is desirable to obtain high-fiber volume fraction in the final composites. A relationship exists between the circumferences, braid angle, yarn width, and the number of yarns in the braid for full fabric cover (Seobroto and Ko, 1989). The number of carriers on the machine limits the number of yarns.

Biaxial braids are classified as diamond braid (1/1), regular braid (2/2), and Hercules braid (3/3) depending on the interlacement as shown in figure 1-5 (Kumar and Wang, 1997). The braided tubes are specified at ±45° orientation. Fiber orientation is the angle measured from the axis of the braid to the axis of the bias yarns. This angle is also called the braid angle, the fiber angle, or the bias angle and is usually denoted by θ (figure 1-3). Fiber orientation typically ranges from 15° to 75°. When a biaxial braid tube is used for a component of varying cross-sections, the braid angle, thickness, and areal weight (yield) vary from point to point.

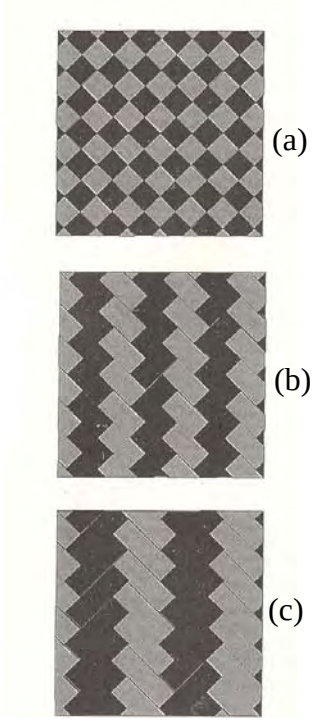

Figure 1-5. Braiding Pattern Types (a) Diamond Braid (1/1), (b) Regular Braid (2/2), and (c) Hercules Braid (3/3) (Kumar and Wang, 1997)

Advantages of braided composites can be summarized as:

- Braided structures are impact resistant. Since all the fibers in the structure are involved in the load distribution, the braid absorbs a large amount of energy as it fails. These braids are used in fan blade containment in commercial aircraft and energy-absorbing crash structures in Formula One racing cars (A&P Technology, Inc., http://www .braider.com/index_hi.html).

- Since braids are woven on the bias, they provide very efficient reinforcement for parts that are subjected to torsional loads such as drive shafts (A&P Technology, Inc., http://www.braider.com/index_hi.html).

- Braided composites greatly improve interlaminar shear properties. There is virtually no delamination observed when braided composites are subjected to fatigue loadings (Tate and Kelkar, 2003a,b).

- Braided composites have better fatigue life. They have outperformed unidirectional laminates for jet engine stator vanes in fatigue strength (A&P Technology, Inc., http://www.braider.com/index_hi.html).

- It has been proven that braiding can be used to improve performance and reduce the manufacturing cost of composite structures. Braiding has been compared with other manufacturing methods such as filament winding, manual and automated tape lay-up, roll wrapping (tape winding) and pultrusion in terms of versatility, component reproducibility, composite quality/structural integrity, design flexibility, damage tolerance, repairability, microcracking resistance, joints/attachments, resistance to thermally induced twist, and lower manufacturing costs (Munjal and Maloney, 1990).

- Braided composites exhibited better fatigue strength in comparison to compression-molded unidirectional prepreg laminates for jet engine stator vanes. Vanes molded with the use of braided composites also reduced costs (A&P Technology, Inc., http://www.braider.com/index_hi.html).

Braided composites have a wide range of applications in the aerospace, industrial, medical, and recreational industries. Figure 1-6 shows the aircraft applications of braided composites (wing flap and jet engine stator vane).

(a)

(b)

Figure 1-6. Aircraft Applications of Braided Composites
(a) Jet Engine Stator Vane (Courtesy of A&P Technology) and
(b) Wing Flap (Courtesy of Raytheon Aircraft Company)

1.3 REVIEW OF EARLIER WORK.

A systematic literature review of earlier research in the areas of manufacturing, performance evaluation, and modeling is presented in the following sections.

1.3.1 Resin Transfer Molding and VARTM Manufacturing Processes.

There are many processes available for composite manufacturing: hand lay-up, wet lay-up, autoclave, resin transfer molding (RTM), and VARTM. Autoclave and RTM are the most popular processes in the aircraft industry.

Autoclave processing is used extensively for manufacturing high-performance aerospace parts. It consists of a pressure vessel that is capable of applying heat and pressure (up to 7 bar ~ 100 psig) simultaneously. The major difficulty in the autoclave process is the high capitalization cost, which arises from stringent pressure code regulations.

RTM is a widely accepted process in the aerospace industry due to its cost-effectiveness and the quality of the parts it produces. During the RTM process, a mold is loaded with the fabric material and then closed. The resin is then injected into the mold. The mold with the fabric is often placed under vacuum pressure so that all the entrapped air is removed (Strong, 1989). A considerable amount of research has been performed to study various aspects of RTM. Hess (1990) explained how this method can be used effectively for manufacturing braided composite structures for naval structures and helicopter components. High-quality graphite/epoxy braided composite tubes for space structures are successfully produced by RTM (Munjal, et al., 1990). Automated tow placement and stitching of dry textile composite preform followed by RTM has been investigated as a cost-effective manufacturing process for obtaining damage tolerant fuselage and wing structures for transport aircraft (Deaton, et al., 1992). Kobayashi, et al. (1992) fabricated T-shaped braided graphite/epoxy composite truss joints. Beck (1993) explained the finer points of an RTM process for fabricating structures. Lee, et al. (1997) suggested different ways to make this process more reliable. Many researchers have used this process to manufacture high-quality braided composites. Swain (2000) explained how structurally sound aircraft components can be fabricated by using carbon fiber braided sleeves with epoxy resin.

Principally, VARTM and RTM are similar. However, there is no external pressure applied to the mold in VARTM. As the name suggests, VARTM is a resin transfer molding with the use of a vacuum. The dry preform is placed in the mold and vacuum bagged. A low-viscosity resin is then drawn into the mold through the aid of the vacuum. The pressure differential between resin at atmospheric pressure and vacuum is a driving force for resin impregnation. The VARTM process is explained in detail in section 2. This process is becoming very popular because of the following advantages:

- Simple low-cost tooling
- Practicality of very large and complex components
- Higher-fiber volume fractions than those composites produced from hand lay-up
- Reduced environmental concerns than those composites produced from hand lay-up

VARTM is a comparatively new process and many researchers are investigating its various aspects. Nguyen, et al. (1997) evaluated this process with little modifications for large-scale composite ship structures. Pike, et al. (1996) used this process for producing structural laminates with integrated armor for ground combat vehicle hulls. Advances in VARTM were studied by Beckwith and Hyland (1998) and the relationship between various forms of the RTM have been reported. Kelkar, et al. (1999) compared the performance of composites manufactured using the RTM and the VARTM processes for composite integral armor vehicle applications. It was determined that the moduli, ultimate tensile strength, and fatigue life of RTM and VARTM panels are comparable if the fiber volume fractions remain the same. Heider, et al. (2000) studied this process for complete automation, and sensing and control for manufacturing large-scale composite parts. Rigas, et al. (2001) have explained the cost-effectiveness of this process in manufacturing ballistic, multifunctional, composite material systems, and structures.

1.3.2 Braided Composites Under Static Loading.

Naik, et al. (1995) studied the effects of braiding parameters, such as yarn size, braid angle, and the percentage of axial yarns, in two-dimensional (2D) triaxial braided composites. The researchers concluded that stiffness properties are not a function of yarn size but are strongly influenced by braid angle and the percentage of axial yarns. Increasing braid angle reduces the longitudinal modulus while increasing the transverse modulus. Shear modulus and the in-plane Poisson's ratio increase with an increase in braid angle. Shear modulus peaks at 45° and then declines, whereas in-plane Poisson's ratio peaks at 30° before it declines. Figures 1-7 through 1-9 show the effect of braid angle on in-plane moduli (E_x, E_y, and E_z), shear moduli (G_{xy}, G_{xz}, and G_{yz}), and Poisson's ratio (ν_{xy}, ν_{xz}, and ν_{yz}). In these figures, the subscripts L and T are used to indicate x and y directions, respectively.

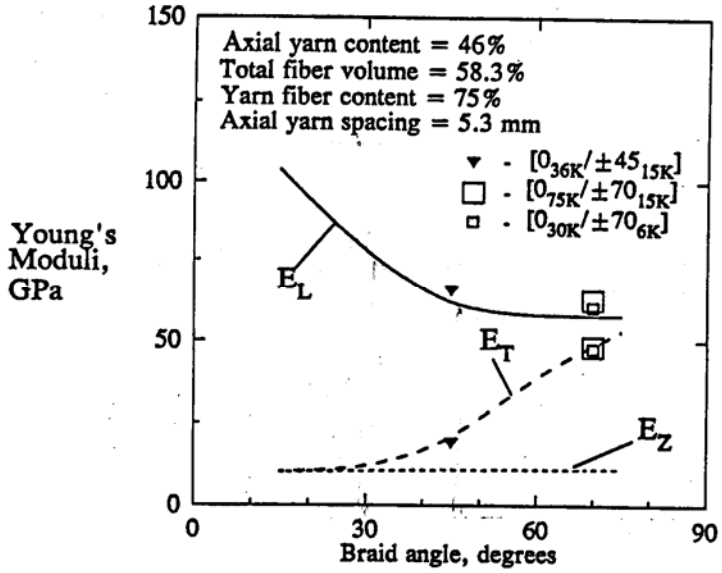

Figure 1-7. Effect of Braid Angle on In-Plane Moduli (Naik, et al., 1995)

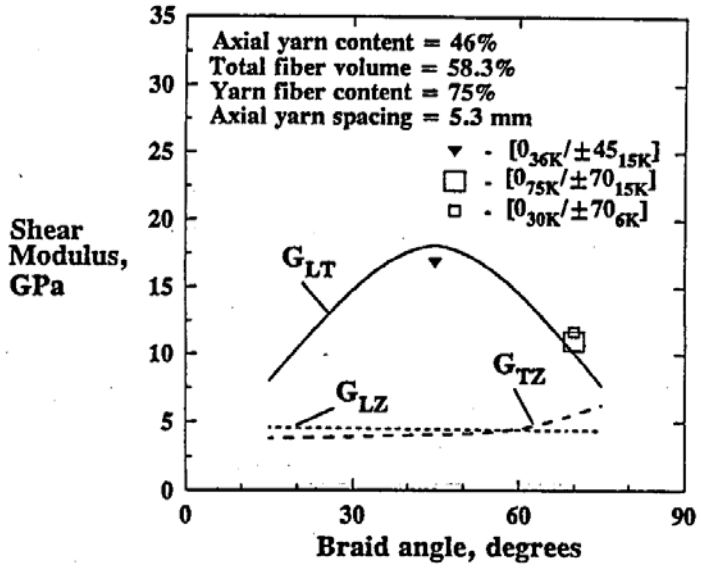

Figure 1-8. Effect of Braid Angle on Shear Moduli (Naik, et al., 1995)

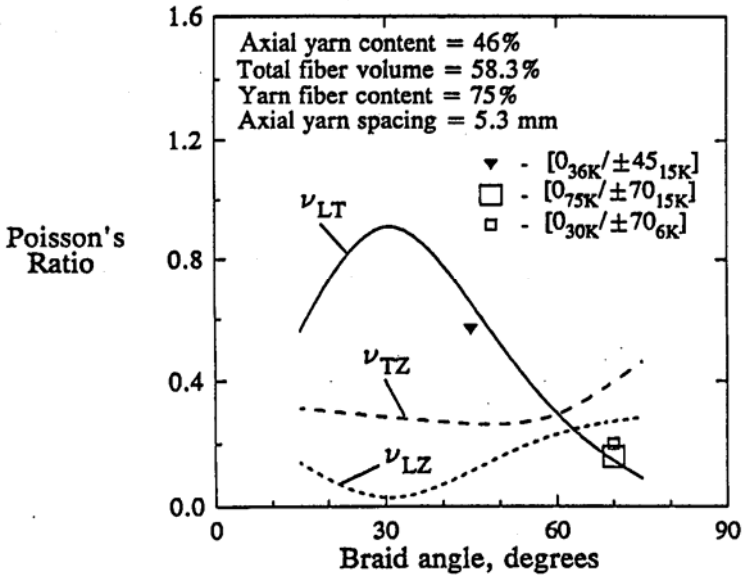

Figure 1-9. Effect of Braid Angle on Poisson's Ratio (Naik, et al., 1993)

Minguet (1995) compared the mechanical properties of graphite/epoxy tape laminates and 2D triaxial braided composite in tension in both longitudinal and transverse directions. The longitudinal modulus of both material forms was found to be quite similar, but the transverse modulus of the braids was lower. The longitudinal strength of the braids was lower than that of the laminates, while the transverse strength was significantly lower. The crimp in the tows of the braid may have been the main cause of the reduced properties.

Smith and Swanson (1996) conducted a series of biaxial tests to measure the strength of 2D triaxial braided carbon specimens and compared the measured strength with that of laminates fabricated with similar materials and fiber orientations. Failures controlled by the axial fibers were found to have reasonably similar values of ultimate strength for braids and laminates, with the braid specimens having somewhat lower values because of irregularities in the axial fibers related to the various braid designs. However, when failures were controlled by the fibers in the braid direction, the strength of the braid specimens was much less than that of the laminates.

Falzon and Herszberg (1998) conducted tension, compression, and shear tests to evaluate the mechanical performance of 2D triaxial braided carbon/epoxy composites. The performance of braided composite was compared with unidirectional (UD) tape laminates. It was found that braided composites have a comparable tension and compression stiffness to the laminate. However, there was considerably reduced tension and compression strength attributed to the fiber damage and fiber tow waviness. Tension tests on the fiber tows revealed a 20% reduction in tension strength resulting from fiber damage during the braiding process.

Chen, et al. (1998) demonstrated the sensitivity of strength to a small degree of misalignment (±1° to ±5°) in braid angle in 2D triaxial braided composites. Clemente, et al. (1998) showed that 2D triaxial braided composite structures exhibit very effective energy absorption compared to traditional materials.

The literature review indicates that most of the work was done on 2D triaxial braided composites, and very little work was done in the area of performance evaluation and modeling of biaxial braided composites.

1.3.3 Fatigue.

1.3.3.1 Fatigue of Multidirectional and Woven Composites.

The fatigue mechanism in composites is much more complex than that of metals. The damage may be in one or more forms, such as a failure in a fiber-matrix interface, a matrix cracking, delaminations, and final fiber breakage. Both matrix cracking and delamination reduce stored energy and stiffness. Detectable damage can be found very early in the fatigue life. The damage causes a reduction of elastic properties such as stiffness. There is always a correlation between damage and stiffness reduction. Since the reduction of stiffness (or damage) occurs long before the composite is in danger, the definition of fatigue failure in composite materials may change from one application to another.

Fatigue in multidirectional tape laminates is a well-understood phenomenon. The damage takes place in three stages, as shown in figure 1-10. The three main stages in the fatigue life are cross-ply cracks with large initial stiffness reduction, initiation and propagation of delamination of plies with slow stiffness reduction, and complete delamination and fiber failure (Reifsnider, 1990).

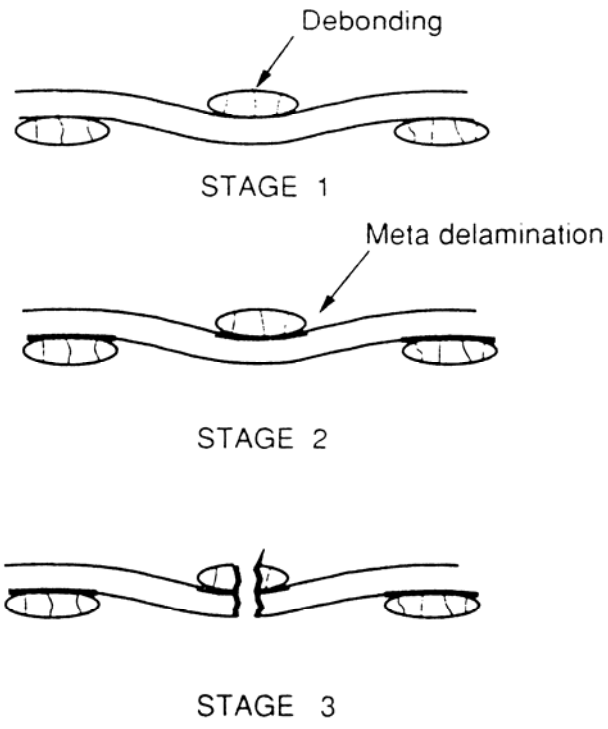

Figure 1-10. Fatigue Damage Mechanisms in Composite Laminate

Fujii and Amijima (1993) proposed the three-stage failure mechanism model for woven composites as measured by modulus decay, as shown in figure 1-11.

- Stage I: Debonds (between fiber and the matrix) in the weft occur near the crossover points. The number of matrix cracks also increases rapidly. At a cycle ratio (n/N) of 0.1, debonds in the weft do not progress very much and the matrix crack density does not increase significantly. This stage is termed the meta-characteristic damage state. The modulus decreases rapidly.

- Stage II: In this stage, debonds occur in the warp direction. The debonds in warp and meta-delamination mainly cause gradual modulus decay in an almost linear fashion. This stage constitutes more than 75% of the total fatigue life.

- Stage III: Final failure occurs with the breakage of fibers. However, the final stage is sometimes hardly distinguishable. The stiffness decreases rapidly again during the last few cycles before the specimen fails.

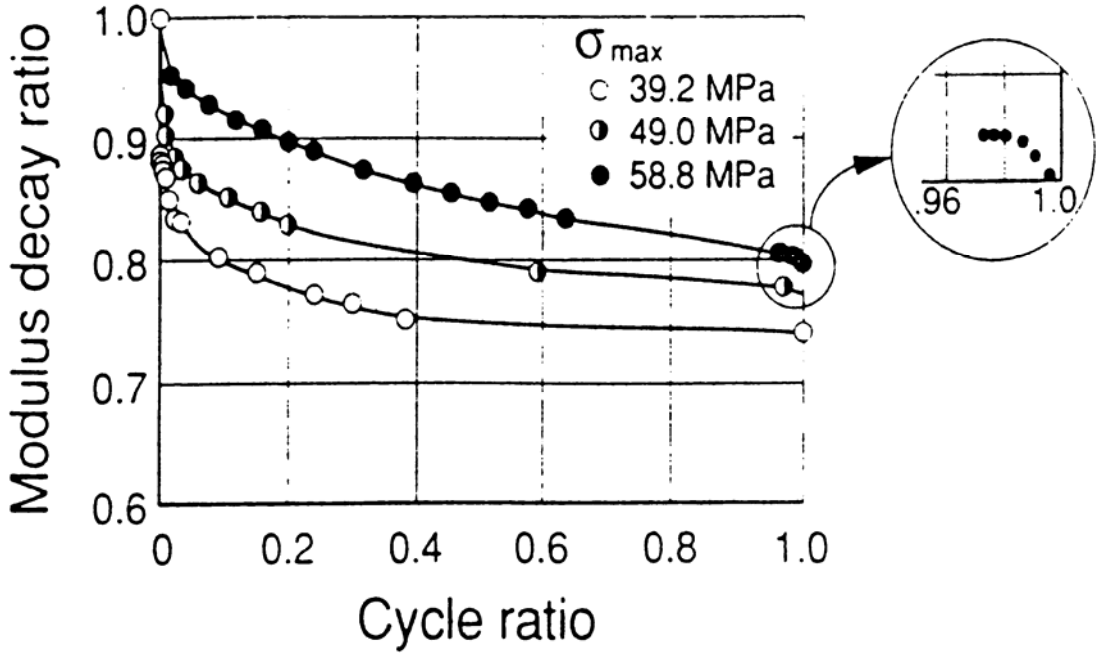

Figure 1-11. Modulus Decay Under Fatigue Loading in Woven Composites

1.3.3.2 Fatigue of Braided Composites.

Although braided fabric resembles woven fabric, it is inappropriate to apply the damage mechanism concepts of woven composites to braided composites. This is because the woven fabrics have orthogonal weaving, that is, warp and fill tows run 0º and 90º, but braided fabrics tows run at θ/-θ angles. In the case of braided composites, very little work is performed on fatigue damage, the relationship between internal damage, and macroscopic properties, such as stiffness, interlaminar stresses, and the delamination of the braided composites. Some additional work performed is discussed in the following paragraphs.

Two discontinuous blade-stiffened specimens of three-dimensional (3D) braided composites (0º/±17º) and 3D orthogonal woven composites (0º/90º/90º) were evaluated under tension-tension fatigue (S/S_u = 0.6, 5-10 Hz, and R = 0.1). It was found that both specimens survived one million cycles, but the woven panel lost its stiffener. The residual strength of braided and woven composite specimens was 88.6% and 90.9% of their static strength (Shivkumar, et al., 1999).

Carlos (1994) studied fatigue behavior of 3D triaxially (0°/±30º) braided carbon/epoxy composites in tension-tension fatigue at 10-Hz frequencies with an R ratio of 0.1. He reported ±5º variations in braid angle when the specimens were manufactured using braided tubes and compression molding. The specimens survived one million cycles at the applied stress level of 50% of the ultimate tensile strength. There was a large scatter in fatigue data, which may have resulted from the variation in braid angle.

Portanova and Deaton (1995) evaluated fatigue (5 Hz and R = 0.1) resistance of multiaxial braided, 3D graphite/epoxy composites in both unnotched and postimpacted conditions. Damage

initiation and growth were documented using radiography and ultrasonic through-transmission (C-scans). Stiffness and strength degradation were measured as a function of applied cycles.

The effect of elevated (107ºC) and lower (-40ºC) temperatures on the fatigue behavior of RTM manufactured triaxially braided (30º/0º/30º) glass/vinyl ester was determined. Results showed a significant decrease in tensile and fatigue strength at 107°C and a modest increase at -40ºC (Houston and Chernenkoff, 1992).

Burr, et al. (1995) conducted tension-tension fatigue tests on 2D triaxial braided composites. The first types of damage that occurred were splits in the braider bundles and cracks in the resin rich areas. Once a sufficient density of this type of damage occurred, the axial bundles began to disbond from the surrounding constituents and continued to do so until ultimate failure.

The literature review clearly indicates that there is a need to understand the behavior of biaxial braided composite under tension-tension fatigue loading.

1.3.3.3 Fatigue Modeling of Composite Materials.

Fatigue damage modeling is difficult because there are many damage mechanisms (matrix cracking, fiber/matrix debonding, delamination, and fiber breakage) and because the test specimens are not heterogeneous. It is impossible to produce specimens with identical microstructural features. Therefore, a material damage model including all the damage states is difficult to establish.

Degrieck and Paepegem (2001) provided an excellent review of major fatigue models. These models can be classified in three major categories: fatigue life models using stress-fatigue lift (S-N) curves, phenomenological models for residual stiffness/strength, and progressive damage models using variables related to damage (transverse matrix cracks, delamination size).

1.3.3.3.1 Fatigue-Life Model.

Fawaz and Ellyin (1994) proposed a semilog linear relationship between applied cyclic stress, *S*, and the number of cycles to failure, *N*, for laminated composites.

$$S = S_u\,(m \log N + b)$$

where S_u is the mean static strength, and *m* and *b* are constants. Low values of *m* and high values of *b* indicated higher fatigue strength. This is the most popular linear model used in conventional laminated composites. The values of constants *m* and *b* for different material systems are presented in table 1-1 (Maurice, 2000).

Table 1-1. Fatigue Performances of Laminated Composites

Material System	*R*	*m*	*b*
E-glass/ductile epoxy–UD	0.1	-0.1573	1.3743
T300 carbon/ductile epoxy–UD	0.1	-0.0542	1.0420
E-glass/brittle epoxy–UD	0.1	-0.1110	1.0935
T300 carbon/brittle epoxy–UD	0.1	-0.0873	1.2103
E-glass/epoxy $[0/90]_s$	0.05	-0.0815	0.9340

1.3.3.3.2 Phenomenological (Stiffness Degradation) Model.

The fatigue damage in composites can be evaluated by measuring the residual stiffness or strength. Measurement of the residual strength is a destructive test and, thus, cannot be used to predict or track the fatigue damage. On the other hand, stiffness can be measured nondestructively. Therefore, the stiffness degradation model is much more applicable to the practical design of composite structures (Lee, et al., 1996). There is an enormous number of models developed by researchers. Only the major stiffness degradation models relevant to braided composites are discussed in detail in the following paragraphs.

Hwang and Han (1986a, 1986b) introduced the concept of the fatigue modulus defined as the ratio of applied stress and resultant strain at a specific cycle. The fatigue modulus degradation rate was assumed to follow a power function of the number of fatigue cycles.

$$\frac{dF}{dn} = -Acn^{C-1}$$

where *A* and *c* were material constants. Further they assumed that applied cyclic stress σ_a varied linearly with resultant strain in any arbitrary loading cycle, so that

$$\sigma_a = F(n_i) \times \varepsilon(n_i)$$

where $F(n_i)$ and $\varepsilon(n_i)$ were the fatigue modulus and strain at loading cycle n_i, respectively. After integration and introduction of the strain failure criteria, the fatigue life *N* was calculated as:

$$N = [B(1-r)]^{1/c}$$

where $r = \frac{\sigma_a}{\sigma_u}$ was the ratio of the applied cyclic stress to the ultimate static strength, and *B* and *c* were material constants.

The variable *D* has been used in residual stiffness models to describe stiffness loss, as $D = \left(1 - \frac{E}{E_o}\right)$, where E_o is the initial tangent modulus.

1.3.3.3.3 Progressive Damage Models.

Hwang and Han (1986a) proposed three cumulative damage models based on the fatigue modulus $F(n)$ and the resultant strain. Model III demonstrated better agreement with experimental data than the first two models (I and II). In the third model, residual stiffness D was defined as:

$$D = \frac{r}{1-r} \cdot \left[\frac{F_0}{F(n)} - 1 \right].$$

Fatigue modulus $F(n)$ was the ratio of applied stress to corresponding strain at n^{th} cycle. F_0 was the modulus defined for static strength to corresponding strain.

Failure occurred when

$$D = \sum_{i=1}^{m} \Delta D_i = 1$$

where ΔD_i was the amount of damage accumulation during fatigue at stress level r_i and m was the number of load sequences until final failure.

Whitworth (1987) proposed a residual stiffness model for graphite/epoxy composites:

$$\left(\frac{E(N^*)}{E(0)} \right)^a = 1 - H \cdot \left(1 - \frac{S}{R(0)} \right)^a N^*$$

where $N^* = n/N$ was the ratio of applied cycles to the fatigue life N, S was the applied stress level, $R(0)$ was the static strength, $E(0)$ was the initial modulus, and a and H were parameters independent of the applied stress level.

This residual stiffness model was used by Whitworth (1990) to propose a cumulative damage model, where the damage function was defined as:

$$D = \left[\frac{H \times (1 - \bar{S})^a}{1 - \bar{S}^a} \right] \times \frac{n}{N}$$

where $\bar{S} = \frac{S}{R(0)}$ was the normalized applied stress range and a and H were parameters.

When $D = 0$, no cycles were applied and $E = E(0)$. When $D = 1$, the residual modulus equaled the failure stiffness E_f.

Recently, Whitworth (1998) proposed a new residual stiffness model, which followed the degradation law:

$$\frac{dE^*(n)}{dn} = \frac{-a}{(n+1)\left[E^*(n)\right]^{m-1}}$$

where $E^*(n) = E(n)/E(N)$ was the ratio of the residual stiffness to the failure stiffness $E(N)$, n was the number of loading cycles, and a and m were parameters that depended on the applied stress, loading frequency, and so forth. The residual stiffness $E(n)$ could be expressed in terms of the static tensile strength S_u with the introduction of the strain failure criterion. A statistical distribution of the residual stiffness could then be obtained, if the static ultimate strength could be represented by a two-parameter Weibull distribution.

Yang, et al. (1990) developed a residual stiffness model for fiber-dominated composite laminates:

$$\frac{dE(n)}{dn} = -E(0)Q\nu n^{\nu-1}$$

where Q and ν were two parameters correlated by a linear equation. Experimental data revealed that ν could be written as a linear function of the applied stress level. The researchers also derived a statistical distribution of the residual stiffness. They observed that this model was not immediately applicable to matrix-dominated composite laminates because the stress-strain curve was no longer linear. Yang, et al. (1992) extended the model for matrix-dominated composites by replacing the modulus $E(n)$ by the fatigue modulus $F(n)$. The latter was defined as the applied stress level S divided by the corresponding strain at the n^{th} cycle. They derived an expression relating the fatigue modulus $F(0)$ with the initial stiffness $E(0)$ through the modeling of the nonlinear stress-strain response. They proved that this new damage law was a particular case of fiber-dominated composites. The model for matrix-dominated behavior was applied to the fatigue behavior of $[\pm 45°]_{2S}$ graphite/epoxy laminates.

The stiffness degradation diagram of woven composites (figure 1-11) shows three distinct stages. There is a rapid stiffness decline in the first stage; the second stage shows gradual stiffness decay in an almost linear fashion; and the stiffness decreases rapidly again during the third stage. Almost all of the models discussed above do not predict all three stages.

The linear fatigue-life model on a semilog scale and the stiffness degradation models discussed above may not represent the exact behavior of biaxial braided composites. A different approach is developed for braided composites and discussed in sections 3 and 4.

1.3.4 Finite Element Modeling.

A thorough understanding of the behavior of the 2x2 braids is required to exploit the advantages these materials offer. To achieve this, computational micromechanics analyses were performed to predict the effective engineering properties and the 3D stress state.

First, the finite element meshes for braids were generated. For conducting parametric studies, meshes were required to be generated. Earlier (Tang, 2001), a strategy was described for generating the finite element meshes for a wide variety of weaves using a general-purpose preprocessor Meshweaver. Since the 2x2 braid architecture is similar to that of the twill weave, a mapping technique was used to generate the braid meshes from the meshes of the twill weave. Solid models of the braids were generated for thorough understanding of its architecture and its effect on the effective properties and the stress distribution. In any finite element analysis, it is useful to minimize the analysis region to save computational time and computer memory. The boundary conditions were imposed in such a way that periodicity and symmetries (Tang and Whitcomb, 2003) that exist in the microstructure of the braids could be exploited to minimize the analysis region. Boundary conditions that include a number of multipoint constraints were derived using a technique given in Tang and Whitcomb, 2003.

Obtaining effective engineering properties is the first order of concern for any structural analysis. Parametric studies were conducted to obtain effective properties. The effect of various parameters like braid angle, waviness ratio (WR), material system, and stacking sequence was analyzed. Thus, the dominant characteristics that determine the behavior of the 2x2 braids were identified. The effective property results produced by this 3D finite element analysis were compared with an equivalent laminate analysis, because laminate theory codes are widely available and understood. It was investigated whether the effective properties of the braids can be predicted using the laminate theory and how much error there is in doing so. Also, such comparisons revealed relative performance.

Practical textile composites do not have perfectly uniform and periodic microstructures, and thus, their behavior cannot be completely characterized by conducting periodic analysis on single unit cells. Numerous cases were run (in addition to the 450 cases run for parametric studies for effective properties) to characterize progressive failure analysis of 2x2 braids with microstructural variation, including the variation of braid angle, WR, and fiber volume fraction in the fiber tow.

The stress distribution in braided composites is complex even for simple uniaxial loading. Interlacing the tows creates a complex load path that results in full 3D stress distributions. The location and magnitude of peak stresses depend on the particular stress component and vary with various braid architecture parameters such as braid angle and degree of waviness. Finite element analyses for different braids were performed to find peak magnitudes and locations. The stress distribution in braids was compared with those in equivalent laminates.

1.4 RESEARCH OBJECTIVE.

In summary, the objective of the present research was to manufacture braided composites using a low-cost VARTM process and to study their performance in fatigue loading. The research also developed an analytical model for stiffness degradation model to predict residual stiffness. The detailed 3D finite element model that considered undulations and fiber continuity was developed. The mesh generation strategy, finite element models, results of effective properties, progressive failure analysis, and stress distribution is presented. The research focused on the following.

- The design and modification of VARTM process parameters to manufacture braided composites using two different resin systems (i.e., vinyl ester and epoxy).

- The studies of the effects of braid angles on mechanical properties.

- The study of fatigue behavior of a biaxial braided composite in tension-tension fatigue loading and the effects of braid angles on fatigue performance.

- The development of a stress-fatigue life diagram (S/S_u-N) and stiffness degradation diagram related to fatigue performance.

- The comparison of the fatigue performance of two resin systems (i.e., vinyl ester and epoxy).

- The development of a stiffness degradation model for braided composites.

- The definition of the idealized tow architecture to analyze the microstructure of the 2x2 braids and generation of meshes for 3D finite element analysis.

- Parameters such as braid angle, WR, tow cross-section, stacking sequence, and material properties were studied as to their influence on the effective engineering properties of the 2x2 braids.

- The comparison of experimental results with 3D finite element model.

- The comparison of the difference in predictions of the 3D finite element analysis and the simple 3D laminate analysis.

- The prediction of the 3D stress state in the tow and determination of the effect of the braid angle and WR on location and magnitude of the peak stresses.

- The characterization of the progressive failure behavior of 2x2 braids with microstructural heterogeneity.

1.5 RELATED DOCUMENTATION.

1.5.1 Journal Articles.

1. Jitendra S. Tate and A.D. Kelkar, "Effect of Braid Angle on Fatigue Performance of Biaxial Braided Composites," *Composites Part A: Applied Science and Engineering*, 2005.

2. Ajit D. Kelkar and Jitendra S. Tate, "Low Cost Manufacturing of Textile Composite Using VARTM Process," *Journal of Manufacturing Technology and Research*, Vol. 1, July 2004.

3. Jitendra S. Tate and Ajit D. Kelkar, "Stiffness Degradation Modeling of Biaxial Braided Composites," *Composites Part B: Engineering*, 2005.

4. Jitendra S. Tate and Ajit D. Kelkar, "VARTM Manufacturing of Carbon Biaxial Braided Composites using EPON 9504 Epoxy Resin System," *Journal of Advanced Materials* (SAMPE), 2005.

5. Tang, X., Whitcomb, J., Kelkar, A.D., and Tate, J., "Progressive Failure Analysis of 2x2 Braided Composites Exhibiting Multiscale Heterogeneity," *Journal of Composites Science & Technology*, 2005.

6. Goyal, D., Tang, X., and Whitcomb, J.D., "Effect of Various Parameters on Effective Engineering Properties of 2x2 Braided Composites," *Journal for Mechanics of Advanced Materials and Structures*, 2004.

7. D. Goyal and J.D. Whitcomb, "Analysis of Stress Concentrations in 2x2 Braided Composites," *Journal of Composite Materials*, 2004.

1.5.2 Conference Proceedings.

1. Jitendra S. Tate, Ajit D. Kelkar, and Ronnie Bolick, "Performance Evaluation of Notched Biaxial Braided Composites," *ASME 2004 International Mechanical Engineering Congress and Exposition*, Anaheim, California, IMECE2004-59883, November 13-19, 2004.

2. Jitendra S. Tate and Ajit D. Kelkar, "Effect of Braid Angle on Fatigue Performance of Biaxial Braided Composites," *The 3rd Conference on Fatigue of Composites*, Kyoto, Japan, September 13-15, 2004.

3. Jitendra S. Tate, Ajit D. Kelkar, and Ronnie Bolick, "Tension and Fatigue Behavior of Slit Sleeve Braided Composites," *11th International Conference on Composites/Nano Engineering (ICCE11)*, South Carolina, August 11-14, 2004.

4. Jitendra S. Tate, Ajit D. Kelkar, and Vinaya A. Kelkar, "Failure Analysis of Biaxial Braided Composites Under Fatigue Loading," *The 15th European Conference of Fracture*, Stockholm, Sweden, August 11-13, 2004.

5. Ajit D. Kelkar, Jitendra S. Tate, and John D. Whitcomb, "Durability of VARTM Manufactured Textile Composites," *International Conference on Advances in Structural Integrity*, Bangalore, India, July 14-17, 2004.

6. Jitendra S. Tate, Ajit D. Kelkar, and John Rice, "Feasibility Study of VARTM Manufacturing of Carbon Biaxial Braided Composites Using EPON 9504 Epoxy Resin System," *JISSE-8, 8th International SAMPE Symposium & Exhibition*, Vol. 1, ISBN 4-9900028-8-1, Tokyo, 12-21 November 2003, pp. 1145-1148.

7. Ajit D. Kelkar and Jitendra S. Tate, "Fatigue Behavior of VARTM Manufactured Biaxial Braided Composites," *ASME 2003 International Mechanical Engineering Congress and RD & D Exposition*, Washington, DC, USA, November 15-21, 2003, n 43850.

8. Ajit D. Kelkar, Jitendra S. Tate, and Ron Bolick, "Introduction to Low Cost Manufacturing of Composite Laminates," *ASEE 2003 Annual Conference & Exposition*, Nashville, Tennessee, USA, June 22-25, 2003, Session 2003-2526.

9. Ajit D. Kelkar and Jitendra S. Tate, "Effect of Fatigue Loading on the Stiffness Degradation of VARTM Manufactured Biaxial Braided Composites," *9th International Conference on the Mechanical Behavior of Materials (ICM9)*, PALEXPO Congress Center, Geneva, Switzerland, May 25-29, 2003, pp. 46.

10. Ajit. D. Kelkar and Jitendra S. Tate, "Low Cost Manufacturing of Textile Composites Using Vacuum Assisted Resin Transfer Molding," *Proceedings of the 20th All India Manufacturing Technology*, Design and Research Conference, Ranchi, India, December 2002, pp. 712-716.

11. Kelkar, Ajit D. and Jitendra S. Tate, "Low Cost Manufacturing of Biaxial Braided Composite Laminate," *Ninth Annual International Conference on Composite Engineering*, San Diego, California, USA, July 2002, pp. 373-374.

12. X. Tang, J. Whitcomb, D. Goyal, and A.D. Kelkar, "Effect of Braid Angle and Waviness Ratio on Effective Moduli of 2x2 Biaxial Braided Composites," *44th AIAA/ASME/ASCE/AHS/ASC Structures, Structural Dynamics, and Materials Conference*, Norfolk, Virginia, AIAA Paper 2003-1475.

13. Xiaodong Tang, John D. Whitcomb, Ajit D. Kelkar, and Jitendra S. Tate, "Progressive Failure Analysis of 2x2 Braided Composites Exhibiting Multiscale Heterogeneity," *18th American Society for Composites Technical Conference*, Gainesville, Florida, USA, 18-22 October 2003.

14. Xiaodong Tang, John D. Whitcomb, and Deepak Goyal, "Micromechanics Modeling of 2x2 Braided Composites," *ASME 2002 Conference*.

15. D. Goyal and J.D. Whitcomb, "Analysis of Stress Concentrations in 2x2 Braided Composites," *International Conference on Computational and Experimental Engineering and Sciences*, 2004.

16. J.D. Whitcomb and D. Goyal, "Effect of Braid Design on Stress Concentration Magnitude and Location," *ASME Symposium on Textiles*, 2004.

1.5.3 Theses.

1. Jitendra S. Tate, May 2004, "Performance Evaluation and Modeling of Braided Composites," Ph.D. dissertation, Department of Mechanical Engineering. North Carolina A&T State University, Greensboro, North Carolina.

2. D. Goyal, "Analysis of 2x2 Braided Composites," MS thesis, Department of Aerospace Engineering, Texas A&M University, College Station, Texas, August 2003.

2. LOW-COST MANUFACTURING OF BRAIDED COMPOSITES.

2.1 INTRODUCTION.

There are various methods that can be used to manufacture composite laminates. These methods include wet lay-up, autoclave processing, filament winding, pultrusion, RTM, and VARTM. VARTM is a comparatively new process and is proven to be cost-effective compared to RTM. The braided composite laminates in the present research are manufactured using the VARTM process.

During VARTM, dry fabric is placed into a tool and vacuum bagged in conjunction with the resin distribution line, the vacuum distribution line, and the distribution media. A low-viscosity resin is drawn into the fabric through a vacuum. Resin distribution media ensures resin infiltration in the through-the-thickness direction. The key to successful resin infiltration of the fabric is the design and placement of the resin distribution media, which allows complete wet-out of the fabric and eliminates voids and dry spots. Properly designed and properly placed resin distribution media eliminate race tracking and resin leakage around the fabric (Seeman, 1990 and 1994). The schematic for the fabrication is shown in figure 2-1.

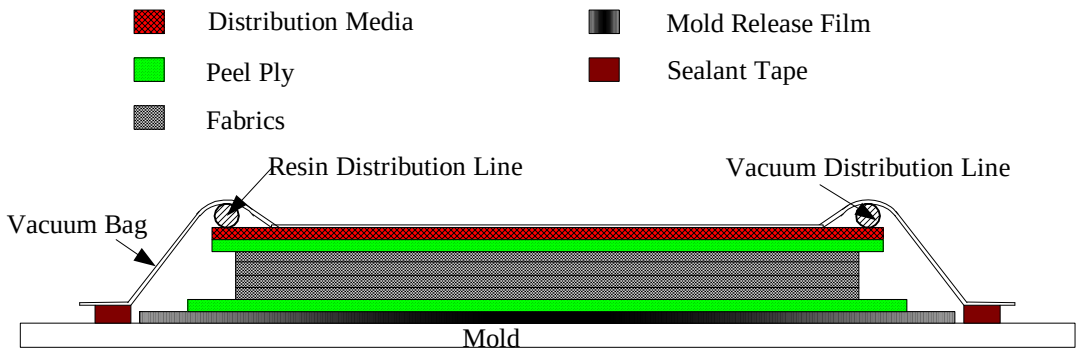

Figure 2-1. Schematic for VARTM

The parameters of the VARTM process are currently designed by a trial and error method. Therefore, a series of experiments are required to design a suitable distribution media and to determine the proper location of the resin line and the vacuum line. Attempts have been made to develop simulation tools for this process (Loos, et al., 2001, ccm.udel.edu, University of Delaware). Accurate predictions by simulation are possible only if all the resin and fabric properties are known, which is usually not the case. Although the experimental approach is time-consuming and expensive, there are currently no alternative methods to optimize the VARTM process parameters.

2.1.1 Selection of Fibers and Fabrics.

Carbon fibers are used in aircraft applications because of their high specific strength (strength-to-density ratio) and high specific modulus (modulus-to-density ratio) compared to glass fibers. Moreover, carbon fibers have better moisture resistance and a very low coefficient of linear expansion. However, carbon fibers do have some shortcomings. They are expensive, brittle, and

have a low-impact resistance and a low elongation. The very low coefficient of linear expansion complicates the processing. Carbon fibers are surface treated to improve the fiber/matrix interfacial bonding and, in turn, the interlaminar shear strength. Organic coatings known as size are also added to carbon fibers to improve fiber/matrix bonds and to protect fibers during handling and processing. The major manufacturers of carbon fibers are Hexcel, Inc., Amoco Performance Products, Inc., Grafil, Inc., and Union Carbide, Inc.

The fabrics used in the present research were 2x2 biaxial carbon braided tubes and slit sleeves manufactured by A&P Technology, Inc. The fibers used for both braided tubes and slit sleeves were AS4 manufactured by Hexcel, Inc. The properties of AS4 fiber as supplied by the manufacturer are listed in table 2-1 (Abdallah, 2002).

Table 2-1. Properties of AS4 Carbon Fiber (Hexcel, Inc.)

E_{f11}, Msi (GPa)	$E_{f22} = E_{f33}$, Msi (GPa)	$G_{f12} = G_{f13}$, Msi (GPa)	G_{f23}, Msi (GPa)	$\nu_{f12} = \nu_{f13}$	ν_{f23}	ρ_f, g/cm^3 (lb/in^3)	S_u, ksi (MPa)	ε_u, (%)
33 (227.53)	2.4 (16.55)	3.6 (24.82)	0.99 (6.89)	0.2	0.25	1.79 (0.0645)	602 (4150)	1.82

Note: Diameter of fibers = 7 μm

The selected braided tubes are suitable for high-load applications and are the preferred choice of small aircraft manufacturers. When the diameter of braided tubes is 2 in. (50.8 mm) and the braid angle is 45°, the areal weight is 19.9 oz/yd^2 (675 g/m^2). Areal weight of braided fabrics is a function of braid angle. Slit sleeve is a special braid manufactured with a constant braid angle throughout the fabric. Slit sleeves look like woven fabrics, but their tows are at [θ/-θ] angles. Braided tubes are manufactured at required braid angles and are then slit to create slit sleeves. The edges are fused with a small amount of ethylene vinyl acetate (EVA) adhesive. The adhesive maintains a constant braid angle even during handling. Slit sleeves with braid angles of 30° and 45° were used in the present research. The numbers of fibers in a tow in the present research were 12,000 (generally specified as 12k tow size).

2.1.2 Selection of Resin.

Resin plays a very important role in polymer matrix composites. Although the loads are mainly carried by fibers, modulus, failure strain, and resin/matrix adhesion play a dominant role in the performance of composites. Resin also determines the type of fabrication process, the service temperature, and the flammability and corrosion resistance of the composite. Since the focus of the present research was a material system for small business jet applications, different resins systems were considered. Aircraft applications require resins with high-glass transition temperature (T_g), high-damage tolerance, high-impact resistance, and high-fatigue life. Physically, glass transition is a reversible change in amorphous polymers from (or to) a viscous to (or from) a hard and brittle phase. For most applications, it is a practical measure of the upper use (service) temperature of composites. The value of T_g depends on the test method. Usually, resin manufacturers provide the value of heat distortion temperature found by ASTM D 648. Sometimes T_g is also determined as the temperature at which the Young's modulus begins to

decline. T_g defined this way has been found equivalent to the heat distortion temperature (Juska and Puckett, 1997).

From a VARTM processing point of view, the viscosity of the resin should be 100 to 1000 centipoises (cp) (Smith, 2001). Low-viscosity resin is not able to impregnate fabric thoroughly and leaves dry fabrics and voids. Low-viscosity resins also have high concentrations of reactive diluents, which tend to vaporize under vacuum and create voids. On the other hand, high-viscosity resin is not able to flow through the fabric and gels in the fabric. Most of the resins available in the market for VARTM processing have a viscosity of 350 to 500 cp at 77ºF (25ºC). Gel time is also an important parameter in processing. Gel time is the period of time from the initial mixing of the resin to the point when gelation occurs, as defined by the specific test method. Many resin manufacturers specify gel time as the time required for mixed resin to double its viscosity. However, from the processing point of view, the time when resin is unable to flow through fabrics is important.

The most commonly used thermoset resins for aerospace applications are vinyl esters and epoxies. Thermoset resins have excellent adhesion, high thermal stability, high chemical resistance, and less creep than thermoplastics. Their low viscosity prior to cure aids in the complete wet-out of the fabric. Vinyl esters have a higher failure strain than polyesters, which improve mechanical properties, impact resistance, and fatigue life. The formulation of vinyl esters is complicated and consists of a catalyst, a promoter, and a gel-time retardant. A catalyst is a substance that promotes or controls the curing of resin without being consumed in the reaction. A promoter is a chemical additive that accelerates the curing process. The curing of thermoset resin is an exothermic reaction. It dissipates heat to the surroundings. Gel-time retardant is a chemical additive that absorbs free radicals once the exothermic reaction has begun. It retards the curing process so that molding is complete before the resin gels. Many vinyl esters are available on the market that have similar mechanical properties to those of epoxies. Most of the vinyl esters also cure at room temperature but still have a high heat distortion temperature of 194ºF (90ºC) without postcure (Juska and Puckett, 1997).

Epoxy resins dominate the aerospace composite market. Their high curing temperature of approximately 350ºF (177ºC) boosts their T_g to 302ºF (150ºC). Epoxies also have high fracture toughness, which makes them superior in fatigue. Epoxies have a low cure shrinkage compared to vinyl esters, so there is less possibility of a component cracking during cure. Epoxies have a simple formulation (two-part systems) consisting of an epoxy and a curing agent. The epoxy determines the mechanical properties, and the curing agent decides the cure temperature. T_g is governed by both the epoxy and the curing agent. Common epoxy chemistries are tetraglycidyl methylene dianiline (TGMDA), diglycidyl ether of biphenol A (DGEBA), and phenol-formaldehyde novolac epoxy. TGMDA epoxies have higher mechanical properties and a higher T_g, and DGEBA epoxies have higher failure strain and lower water absorption (Juska and Puckett, 1997).

Two resin systems were selected that meet the requirements of VARTM processing and have comparatively high T_g. They were Derakane Momentum 411-350 vinyl ester, (DM 411-350), manufactured by Dow Chemical Company, Inc. and EPON 9504 epoxy, manufactured by Resolution Performance Products, Inc., The DM 411-350 resin system is extensively used in

adverse chemical environments. Applications include chemical processing, pulp and paper, and the food and beverage industry. DM 411-350 vinyl ester resin systems have also been investigated for sandwich structures used in aerospace applications (Smith, 2001). EPON 9504 epoxy resin systems have high tensile strength and elongation, which impart superior composite properties. The flexural fatigue performance of fiberglass laminates made from the EPON 9504 resin system manufactured by VARTM is much higher than that of laminates made with vinyl ester, modified vinyl ester, or isophthalic polyester resins. Therefore, the use of the EPON 9504 resin system in the fabrication of fatigue-resistant structures is significantly more economical than the use of vinyl ester or polyester resins (Resolution Performance Products, Inc.). Smith (2001) investigated DM 411-350 for VARTM processing and provided properties of the resin. The experimental properties of EPON 9504 were evaluated from static tensile tests on neat resin coupons. Table 2-2 lists the properties of both resins.

Table 2-2. Properties of DM 411-350 and EPON 9504

Property	DM 411-350		EPON 9504	
	Mfr. Value	Exp. Value	Mfr. Value	Exp. Value
Tensile Strength, ksi (MPa)	11.45 (79.0)	---	11.10 (76.5)	9.42 (64.94)
Tensile Modulus, Msi (GPa)	0.45 (3.1)	0.49(3.4)	0.465 (3.2)	0.43 (2.96)
Tensile Elongation, %	6.5	---	7.8	2.83 Elongation at UTS
Poisson's Ratio	---	0.35	---	0.38
Glass Transition Temperature ºF (ºC)	---	(220) 104	230-276 (110-135) DMA	---
Heat Distortion Temperature ºF (ºC) ASTM D648	215 (102)	---	199 (93)	---
Viscosity of mix at 77ºF (25ºC), cp	350	---	350	350
Flexural Strength, ksi (MPa)	17 (117)	---	18.4 (126.8)	---
Flexural Modulus, Msi (GPa)	0.45 (3.1)	---	0.47 (3.24)	---
Density of cured resin, g/cm^3 (lb/in^3)	1.13 (0.041)	1.12 (0.040)	1.13 (0.041)	1.16 (0.042)
Gel time at 77ºF (25ºC), minutes	40 to 60	90 Time when resin gelled preventing flow	60 Time to double the viscosity	100 Time when resin gelled preventing flow

Table 2-2. Properties of DM 411-350 and EPON 9504 (Continued)

Property	DM 411-350		EPON 9504	
	Mfr. Value	Exp. Value	Mfr. Value	Exp. Value
Formulation (Recommended by manufacturer)	Resin (100) + Promoter (0.02 - 0.13%) + Retardant (0.015-0.0175%) + Catalyst (1-1.5%) by weight		Resin (100) + curing agent (26%) by weight	
Chemical Description	Resin—bisphenol-A epoxy resin Promoter—CoNap 6% Retardant—2,4 Pentanedione Catalyst—MEKP		Resin—bisphenol-A epoxy resin (modified) Curing Agent—Non-MDA (methylene dianiline) proprietary polyamine	
Manufacturer	Dow Chemical Company		Resolution Performance Products	

UTS = Ultimate tensile strength
MEKP = Methylethyl ketone peroxide
MDA = Methylene dianiline
DMA = Dynamic mechanical analysis

Both resins have a viscosity of 350 cp at a temperature of 77ºF (25ºC), which makes them suitable for processing at this lower temperature. Other mechanical properties of the resins are almost identical. However, EPON 9504 has a higher T_g of 230º-275ºF (110º-135ºC) and a higher elongation (7.8%) than that of DM 411-350. The price of EPON 9504 is also much lower than the price of DM 411-350.

VARTM was successfully implemented in the beginning for biaxial carbon braided tubes using DM 411-350 at a room temperature of 77ºF (25ºC). EPON 9504 experienced difficulties processing at room temperature. Typical steps in the VARTM processing are discussed in the next section, and details pertaining to the VARTM processing of DM 411-350 and EPON 9504 are discussed in the following sections.

2.2 STEPS IN VARTM PROCESSING.

Typically, the VARTM process involves the following steps (Kelkar and Tate, 2002 and 2003c):

1. Mold Preparation and Vacuum Bagging
2. Formulation and Degassing of Resin
3. Resin Impregnation and Curing

2.2.1 Mold Preparation and Vacuum Bagging.

In VARTM there is a typical sequence of vacuum bagging. The sequence of lay-up from bottom to top is mold, mold surface protection film, bottom release fabric (also called bottom peel ply), fabrics, top release fabric (also called top peel ply), resin distribution media, vacuum and resin

distribution lines, and vacuum bag. The vacuum bag is sealed using sealant tape. This procedure is depicted in figure 2-2.

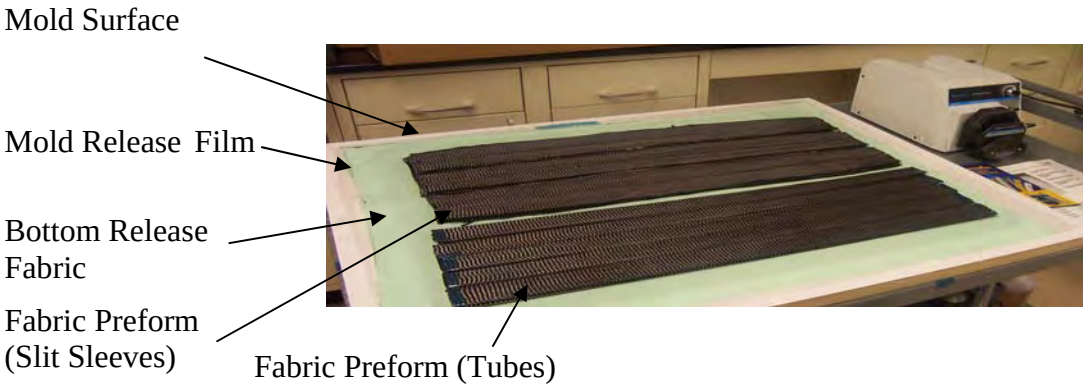

(a)

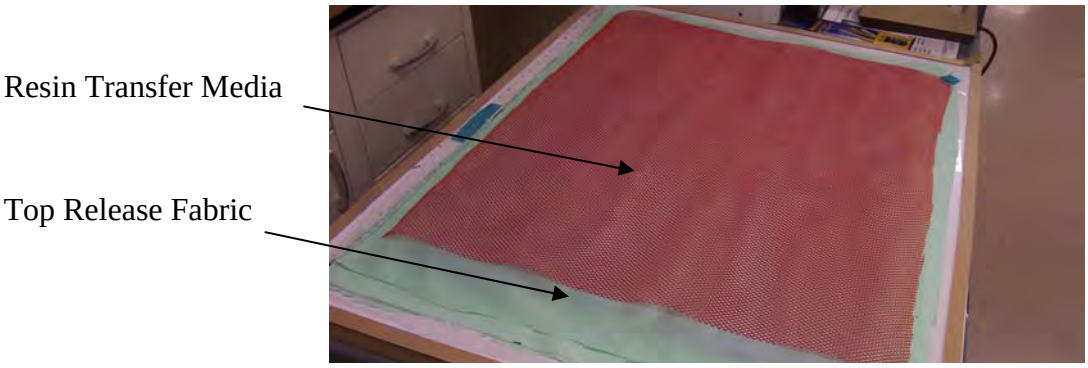

(b)

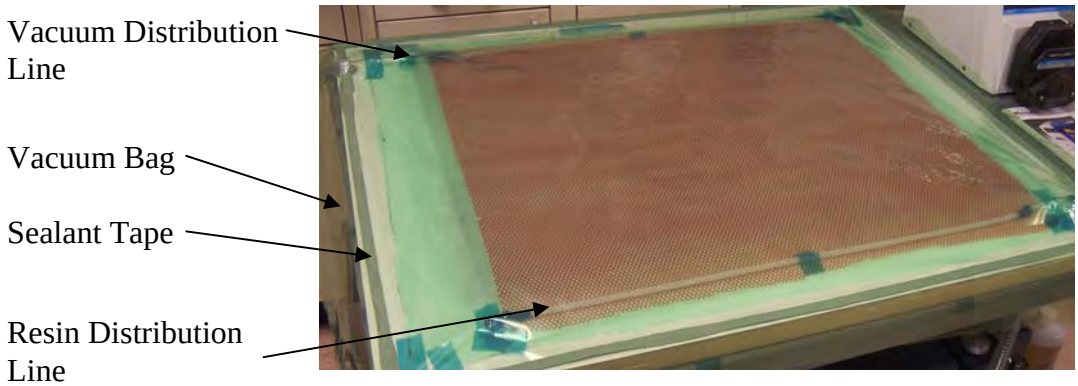

(c)

Figure 2-2. Steps in Fabric Lay-Up

The purpose of each of these items is as follows.

- In figure 2-2(a):

  Mold Surface: The mold used for the fabrication is a plywood plate lined with Formica™ at the top surface. A heated metal plate (usually aluminum) is also popular.

  Mold Release Film (Surface Protection): Two layers of sand paste wax are applied to the surface. A 25-μm polyester film is then used to protect the mold surface. The wax and polyester film facilitates easy removal of the panel from the mold surface after the fabrication process is completed.

  Bottom Release Fabric (Peel Ply): This is a porous nylon fabric, which leaves an impression on the part suitable for secondary adhesive bonding (like tabbing) without further surface preparation. Its use is optional.

  Fabric Preforms: The fabrics used in this research were 2x2 biaxial braided tubes and slit sleeves. Braided tubes were flattened to a width of 1.75 in. (44.5 mm). A braided tube with a width of 1.75 in. (44.5 mm) provided a braid angle of ~25º. Two tubes were stacked above each other, creating four layers. Precaution was taken so that the braid angle (25º) was undisturbed and the width of 1.75 was (44.5 mm) maintained. This method is referred to as a collapse method. Four slit sleeves were also stacked above each other to obtain four layers.

- In figure 2-2(b):

  Top Release Fabric (Peel Ply): This is the same material as the bottom release fabric. It is laid on top of the braided fabrics to facilitate the flow of resin through it. It also leaves an impression on the part suitable for secondary bonding without further surface preparation.

  Resin Transfer (Distribution) Media: The distribution media is a polyethylene mesh laid on top of the top release fabric. This helps maintain an even distribution of resin and facilitates the flow of resin through the thickness of the panel.

  The use of distribution media is a patented technology termed as Seemann Composite Resin Infusion Manufacturing Process that was invented by W. H. Seemann. Seemann also patented different patterns of distribution media and the placement technique for these patterns (Seemann, 1990 and 1994). Distribution media control the flow of resin through the thickness. Resin flows quickly through the media and then remains in the mesh pockets. It then travels through the thickness.

- In figure 2-2(c):

  Resin and Vacuum Distribution Lines: Spirally cut, high-density polyethylene tubes are used for this purpose. These lines are laid above the distribution media at two sides of the fabric lay-up and can run along the length or along the width. One end of the resin

line is closed and the other end is connected to the resin supply through the flow control device (if used). The vacuum line is closed at one end and connected to the vacuum pump through the vacuum gage.

A breather material acts as a distributor medium for the air and escaping volatiles and gases. It is placed over the resin distribution media and the resin and vacuum lines. It also acts as a buffer between the vacuum bag wrinkles and the part surface. It is a highly porous material composed mostly of fiberglass, polyester felt, and cotton. The use of a breather is optional. It was not used in this research.

Vacuum Bag and Sealant Tape: The vacuum bag is made from 25-μm nylon film. The film is placed completely over the mold area and sealed firmly using a special sealant tape. The sealant seals the vacuum bag and helps maintain a uniform vacuum throughout the molding process.

The other equipment used in the processing included a vacuum pump, flow control devices (optional), a vacuum gage, a degassing chamber, a temperature and humidity gage, and a stop watch. Flow control devices like valves, clamps, and peristaltic pumps are used with certain material systems. These devices deliver a controlled amount of resin according to the unit time in the mold. Thus, the resin has a chance to flow through the thickness and complete wet-out of the fabrics is ensured. A peristaltic pump delivers a fixed amount of resin in the mold per unit of time. The quantity of resin (e.g., cm^3/min) is dependent on the pump speed. The pump speed is selected according to the fabric-resin system and the thickness of the panel.

Once the fabrics and other relevant materials are laid down in the required sequence, the entire mold is sealed with sealant and a vacuum bag. The vacuum pump is then used to maintain the lowest possible vacuum pressure throughout the process. Bag leaks are the most common problems that occur in VARTM. One of the reasons for leaks is a damaged vacuum bag. A vacuum bag is typically made of nylon film. The moisture level in the surrounding environment affects the nylon film. Dry and brittle film can cause cracking when handled frequently. Another common reason for bag leak is foreign material entrapped between the vacuum bag and the sealant tape. Once the leaks have been removed and the vacuum bag is completely sealed, the vacuum pump remains running for at least 1 to 2 hours to achieve a good vacuum in the bag. The typical vacuum achieved is in the order of 0.5 torr. The vacuum pump is then shut off, and the vacuum line is clamped. If the bag remains tight and holds almost the same vacuum after 1 to 2 hours, the mold is ready for resin impregnation.

The vacuum plays a vital role in the VARTM process. The pressure differential between the atmosphere and the vacuum provides the driving force for infusing the resin into the mold. The vacuum also removes all of the air from the mold before and during the introduction of resin (TPI Composites, Inc., http://www.tpicomp.com/technology).

2.2.2 Formulation and Degassing of Resin.

DM 411-350 was mixed with a catalyst, a promoter, and a gel-time retardant, and EPON 9504 was mixed with a curing agent (EPI-CURE 9554) in the proportions suggested by the resin manufacturer. The resin had to be free from entrapped air and gases that could cause voids

before being added to the mold. After the mixing of all the ingredients, the resin container was kept in the degassing chamber to maintain a vacuum of approximately 5-10 torr, as shown in figure 2-3. The vacuum in the chamber removed all the entrapped air and gases out of the resin. This was a crucial step in the VARTM process and had to be performed very carefully to ensure high-quality composite panels. Degassing resin for too short a period of time could not ensure complete removal of the entrapped air and gases. If the resin was degassed for too long a period of time, some of the ingredients (mainly styrene) in the resin could evaporate during processing. This would change the final formulation of resin and also create voids. Five to ten minutes was sufficient to remove all the entrapped air and gases.

Figure 2-3. Degassing Chamber

2.2.3 Resin Impregnation and Curing.

The resin impregnation process was different for DM 411-350 and EPON 9504. The resin was injected into the mold at a very slow rate for DM 411-350. The flow of resin was controlled with the help of a peristaltic pump along with an ON-OFF timer. The resin was injected in the mold until the whole panel was soaked. Figure 2-4 displays the resin impregnation setup. Panels remained in the mold for 18 to 24 hours at room temperature for curing, which is termed the green cure.

A peristaltic pump was not used for EPON 9504. The mold and resin were heated to 120ºF (49ºC) for 20 hours in the oven, and impregnation was completed in the oven at 120ºF (49ºC). Figure 2-5 displays the resin impregnation setup for EPON 9504. After the impregnation, the oven temperature remained at 120ºF (49ºC) for 2 hours before it was turned off. Panels were kept in the mold for 16 hours for the green cure.

Postcure is the final and most important step in VARTM processing. Although the degree of cure increases with time at room temperature, postcuring at elevated temperatures accelerates the process and achieves an ultimate heat distortion temperature and optimal mechanical properties. The manufacturer of the resin recommends the postcure cycle according to the type of curing agent in the resin system.

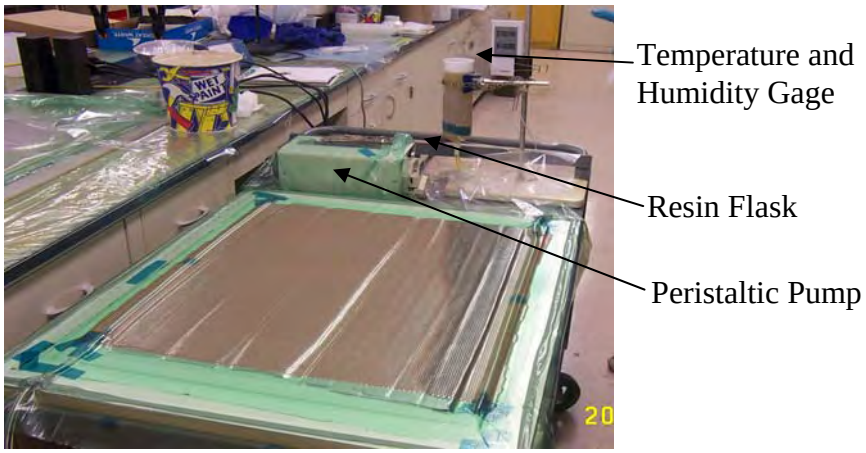

Figure 2-4. Resin Impregnation of DM 411-350 Resin System

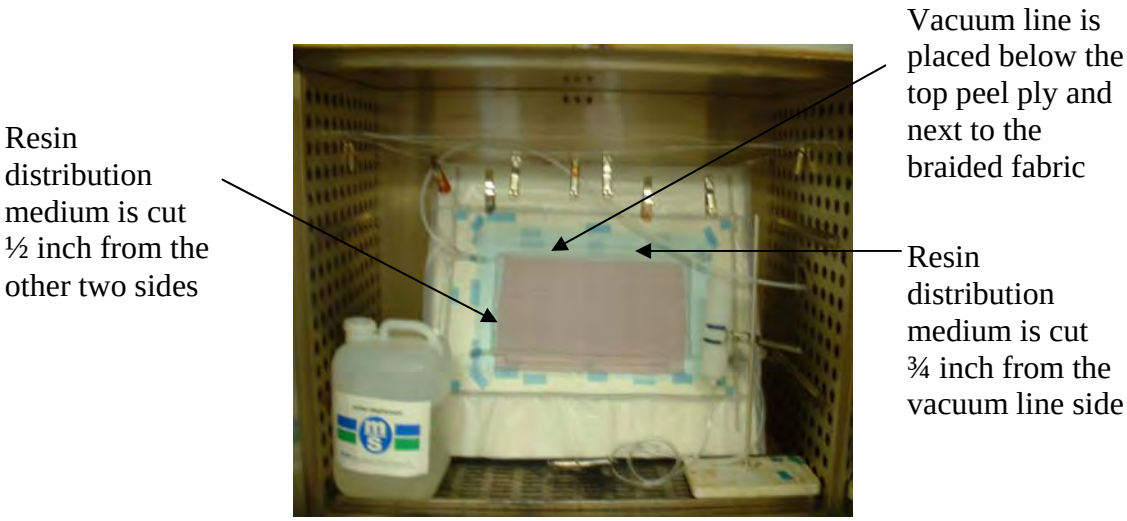

Figure 2-5. Resin Impregnation of EPON 9504 Resin System

Postcure was performed at the temperatures and time recommended by the resin manufacturer. The braided composites of DM 411-350 were kept in the oven at 187ºF (86ºC) for 8 hours and then cooled in the oven to room temperature. The braided composites made of EPON 9504 were kept in the oven at 201ºF (94ºC) for 1 hour and then cooled in the oven to room temperature.

2.3 VACUUM-ASSISTED RESIN TRANSFER MOLDING PROCESSING USING DM 411-350 AND EPON 9504.

The typical steps in VARTM processing for both resins were the same, but with a few different parameters. This section explains the details pertaining to both resin systems. Table 2-3 summarizes the differences. Extensive study on EPON 9504 was required to reach a particular combination of process parameters such as time, temperature, and the design of resin distribution media.

Table 2-3. Vacuum-Assisted Resin Transfer Molding Process Parameters for DM 411-350 and EPON 9504 Resins

	DM 411-350	EPON 9504
Processing temperature, ºF (ºC)	77 (25)	120 (49)
Mold heating, ºF (ºC)	No	120 (49)
Resin temperature during mixing, ºF (ºC)	77 (25)	120 (49)
Peristaltic pump with ON-OFF timer	Yes	No
Distribution media	Cut short in length from edges of fabrics	Cut 0.5 in. (12.7 mm) short in length from edges of fabrics and 0.75 in. (19 mm) short near vacuum line
Vacuum distribution line placement	Above distribution media	Below distribution media and below top peel ply, and adjacent to braided fabrics
Processing time for panel of size 22 in. x 9.5 in. (56 cm x 24 cm)	30 minutes	10 minutes

2.3.1 Vacuum-Assisted Resin Transfer Molding Using DM 411-350 Vinyl Ester Resin.

2.3.1.1 Resin Distribution Media and Flow Control Devices.

The placement and design of resin distribution media play dominant roles in the complete wet-out of the fabric. Its permeability and placement determine the boundary conditions for the flow. Distribution media for DM 411-350 was placed so that the entire fabric was covered in the width direction and cut 0.5 in. (12.7 mm) short in the length direction, as shown in figure 2-6. Both the resin distribution line and the vacuum distribution lines were placed on top of the distribution media. Resin flowed across the width through the distribution media in the in-plane direction and seeped through the vacuum line. This prevented complete wet-out of the fabrics. Thus, the design required a flow control device such as a peristaltic pump that could deliver a controlled amount of resin in the mold. There was a fixed amount of resin entering the mold so that resin would remain in the mesh pockets of the distribution media and then flow through the thickness. The flow of resin was further controlled by use of an ON-OFF timer. A cycle of 30 seconds on and 30 seconds off was used based on previous experience with the resin. The use of the peristaltic pump and the ON-OFF timer significantly increased the impregnation time. It took almost 40 minutes to impregnate a panel 22 in. long by 9.5 in. wide (56 by 24 cm).

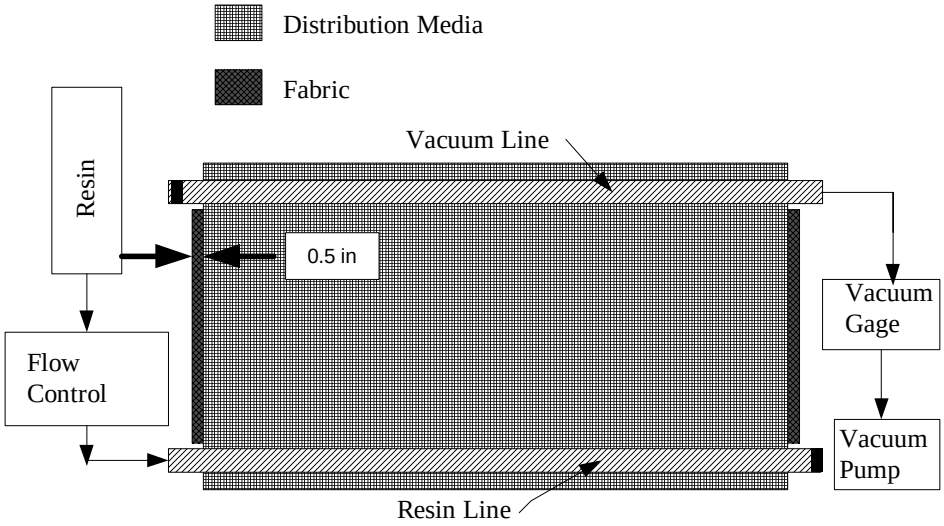

Figure 2-6. Vacuum-Assisted Resin Transfer Molding Using DM 411-350 Resin System

2.3.1.2 Processing Temperature and Gel Time.

The viscosity of the resin is a function of its initial temperature. When resin is mixed with a catalyst or curing agents, the viscosity initially declines and then increases along with the temperature. When the viscosity reaches a certain value, the resin is unable to flow and gels in the mold. According to the manufacturer, the gel time for DM 411-350 at 77ºF (25ºC) is 40 to 60 minutes. Gel time can be increased by experimenting with the formulation of the resin. Use of the formulation in table 2-2 increased gel time to 90 minutes (Smith, 2001). It is very important to design a VARTM process in such a way that the total time required for degassing and resin impregnation is less than the gel time. Processing for DM 411-350 was performed at a room temperature of 70ºF (21ºC) with the aid of a flow control device. Degassing and impregnation took 40 minutes, which was less than the gel time.

The VARTM process was appropriate for the DM 411-350 resin with the above-mentioned design of resin distribution media and the use of a flow control device. The quality of composite panels was good and a fiber volume fraction as high as 57% was achieved. The major drawback of this design was the higher processing time and the complications involved with the peristaltic pump and the ON-OFF timer. This design would be expensive for a mass production environment or the production of large components. Large components typically require the laying of multiple resin and vacuum lines to ensure complete wet-out of the fabrics.

2.3.2 Vacuum-Assisted Resin Transfer Molding Using EPON 9504 Epoxy Resin.

2.3.2.1 Resin Distribution Media.

The use of the peristaltic pump with the ON-OFF timer increased impregnation time considerably. Therefore, experiments with EPON 9504 used a proper design of the distribution media and other process parameters to achieve complete wet-out of the fabric.

The distribution media for EPON 9504 was cut 12.7 mm (0.5 in.) short in the length direction and 0.75 in. (19 mm) short near the vacuum line, as shown in figure 2-7. The resin distribution line was placed on top of the distribution media, but the vacuum distribution line was placed below the top peel ply and next to the fabrics. Since the distribution media did not touch a vacuum line, the resin would not run through the vacuum line. It traveled to the edge of the distribution media in the width direction and then remained in the lay-up. There was no need to use a flow control device with this design. Resin was forced to remain in the lay-up because of the flow resistance created at the edges of the distribution media. The driving force created by the vacuum alone was sufficient for complete wet-out of the fabric. The impregnation in this case was very fast. It took only 10 minutes to impregnate a 22-in.-wide by 9.5-in.-long (56- by 24-cm) panel.

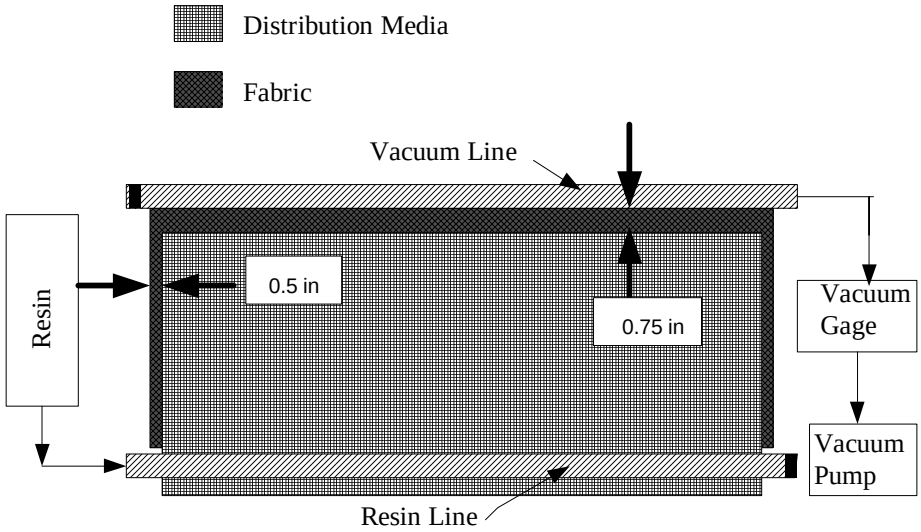

Figure 2-7. Vacuum-Assisted Resin Transfer Molding Using EPON 9504 Resin System

2.3.2.2 Processing Temperature and Gel Time.

A viscosity study for EPON 9504 was performed in a laboratory where the room temperature was 70ºF (21ºC). The viscosity changed from 310 to 395 cp in 100 minutes, and the temperature rose from 70ºF (21ºC) to 93ºF (34ºC). A graph of viscosity versus time and temperature is shown in figure 2-8. The viscosity led to the conclusion that VARTM processing of this resin is also possible at a room temperature of 70ºF (21ºC).

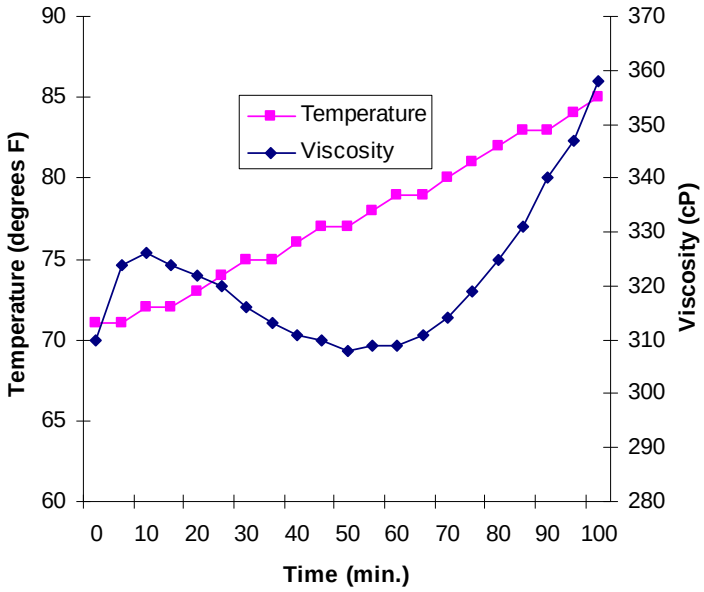

Figure 2-8. Graph of Viscosity vs Time and Temperature

The quality of composite panels, however, was not satisfactory when processing was performed at room temperature of 70ºF (21ºC). Random shiny spots (air pockets) were observed on the top surface of the cured composite panels as displayed in figure 2-9. All of the entrapped air and vapors (of volatile contents) in the mold were not removed by the vacuum alone. Some accumulated at the top surface of the composite. Premature opening of the mold could cause this problem, but this was not the case here.

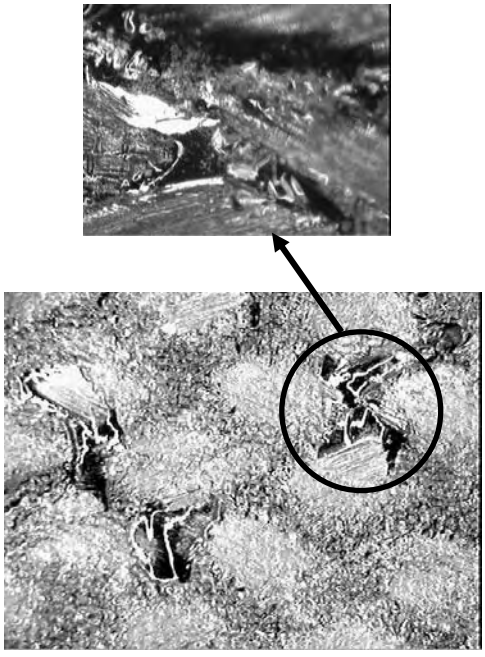

Figure 2-9. Surface Defects—Processing at 70ºF (21ºC)

Random air pockets at the surface are simply voids at the surface. A void is any physical and mechanical discontinuity occurring within a material or part and may be 2D (e.g., disbands, delaminations) or 3D (e.g., vacuum-, air-, or gas-filled pockets). Voids are incapable of transmitting structural stresses and create stress concentrations that lead to crack initiation. Both void and dry spots indicate incomplete wetting of the fabrics in the resin.

The important parameters responsible for complete wetting of the fabric by the resin are use of a flow control device, fiber/matrix adhesion (type of sizing component on the fiber), volatile content in the size and the resin, wetting and air release agent, and temperature of the resin (in turn viscosity) and the mold. An investigation was performed to determine the problem parameter/s. It should be noted that other parameters such as the permeability of the fabric, the fiber architecture of the fabric, and the fabric's crimp are fixed once a particular fabric is selected. The following sections describe the investigation efforts in chronological order.

2.3.2.2.1 Flow Control Device.

Flow control is very often useful to achieve complete fiber saturation and a void-free fill. Although a flow control device was not used, it was determined that the use of a peristaltic pump with an ON-OFF timer would not help solve the problem of random air pockets at the surface.

2.3.2.2.2 Fiber/Matrix Adhesion.

Fiber/matrix adhesion is not only critical in processing, but is also critical to the performance of composites. Fiber/matrix debonding is one important damage state in composites under loading. Fiber/matrix adhesion may affect the wetting of fiber with a matrix. A fiber/matrix interface is shown in figure 2-10. Adhesion is a complex phenomenon that depends on compatibility of the resin with the size of carbon fibers and braids used during braiding. The manufacturers of carbon fibers and braids confirmed that the size used was compatible with the EPON 9504 epoxy resin system.

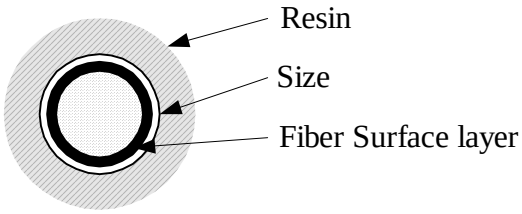

Figure 2-10. Fiber/Matrix Interface

2.3.2.2.3 Volatile Content.

Styrene is used as a cross-linking agent in vinyl ester resins. The typical percentage in vinyl esters is 35%. Styrene has a volatile organic content (VOC), and there are restrictions on its emission. Other volatiles such as water and alcohol are used in sizing or resin formulation. There is a possibility of evaporation of these volatiles at a very low vacuum. If vapors are not pushed out of the mold during processing, a tacky, air-inhibited composite surface may be created. The VOC was not a major issue in the processing of EPON 9504.

2.3.2.2.4 Wetting and Air Release Agent.

This problem was reported to the EPON 9504 manufacturer. The manufacturer's engineer suspected that the carbon fabrics might be aged. There is always a possibility of damage in the sizing of fibers if a fabric is improperly stored or old. The braid manufacturer confirmed that the supplied lot was not old. The manufacturer further suggested the use of an air release agent, BYK A530, or a wetting agent, BYK W390, to improve wetting. BYK Chemie, Inc., manufactures BYK A530 and BYK W390. The suggested percentage to be used was 0.5% by weight based on the total resin and curing agent. The manufacturer claimed that the very low percentage would not affect mechanical properties. An air release agent or a wetting agent reduces surface tension between the resin and the fabric, which improves wetting and spreading.

Fluorad Fluorosurfactant FC-4430, manufactured by 3M, Inc., was available in the laboratory. This surfactant could also work according to the EPON manufacturer. This surfactant is popular in many industrial and commercial applications, including paints, resins, adhesives, and inks. One panel was manufactured using FC-4430 with a concentration of 250 ppm. While the problem of random air pockets was resolved, the plies separated easily after the postcure of composite panels, as shown in figure 2-11. This demonstrated an adhesion failure between two plies, which is known as disbond.

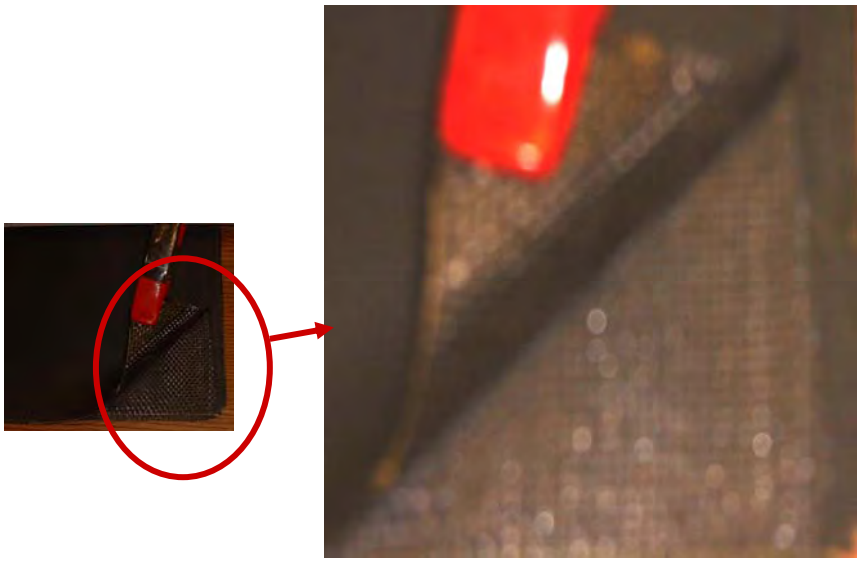

Figure 2-11. Separation of Plies (Disbond) After Using of Surfactant

The molecules of the surfactant are composed of a soluble group and an insoluble group. The insoluble end tends to push out of the liquid and the soluble end tends to be pulled into the liquid. The combined action lowers the surface energy of a resin allowing it to better wet and flow over a surface (3M Company, http://www.3m.com). It was concluded that the accumulation of an insoluble group at the interface of the two adjacent plies caused the separation. There was no further investigation of the surfactant, wetting agent, or air release agent because there was no strong database available to explain the effect of these agents on the performance of the composites.

2.3.2.2.5 Temperature of Resin and Mold.

During the experiments, the resin solidified at the bottom of the container in the laboratory environment at ~70ºF (21ºC). The top resin in the container may have been nonhomogeneous (i.e., with an incorrect proportion of ingredients); therefore, this resin was heated at 80ºF (27ºC) for a few hours in the oven to achieve a homogeneous resin. The resin was then used for impregnation at room temperature. The problem remained unresolved.

The cross-linking (reactivity) of the thermoset resins was governed by a curing agent and its temperature, as shown in figure 2-12.

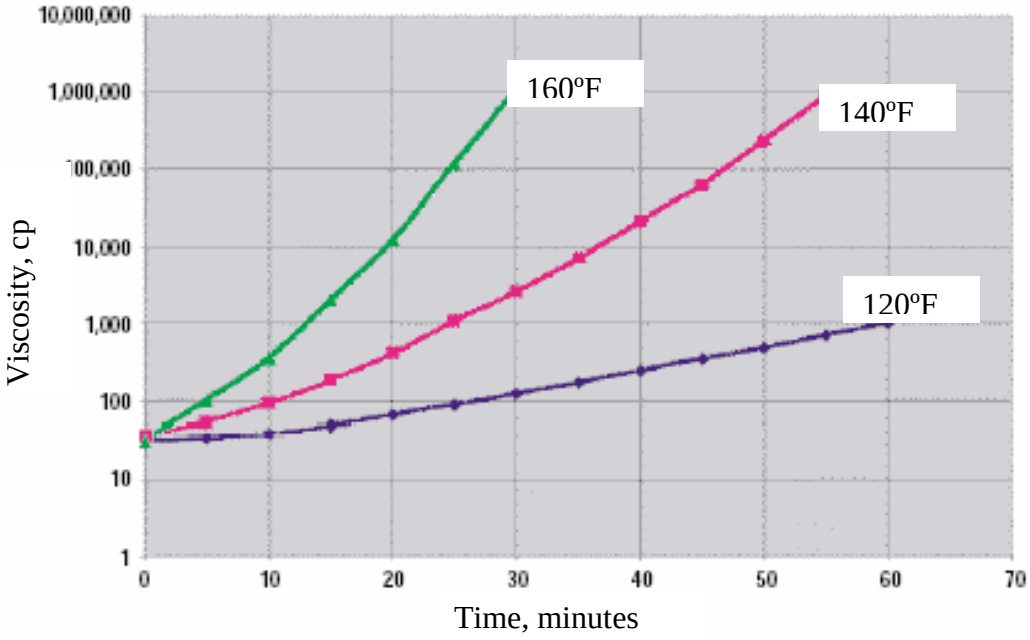

Figure 2-12. Viscosity of EPON Resin System at Various Temperatures
(Courtesy of Resolution Performance Products, Inc.)

In the next panel, both resin and mold were heated at 80ºF (27ºC) overnight (approximately 20 hours) in the oven and impregnation was then performed at a room temperature of 70ºF (21ºC). Random air pockets were still observed, but their quantity was reduced.

It was concluded that the sudden temperature drop from 80ºF (27ºC) to 70ºF (21ºC) could have aggravated the problem. Thus, for the next panel, both the resin and mold were heated at 80ºF (27ºC) and processing was performed at 80ºF (27ºC). The quantity of random air pockets was significantly reduced, as shown in figure 2-13. Therefore, efforts were continued in this direction.

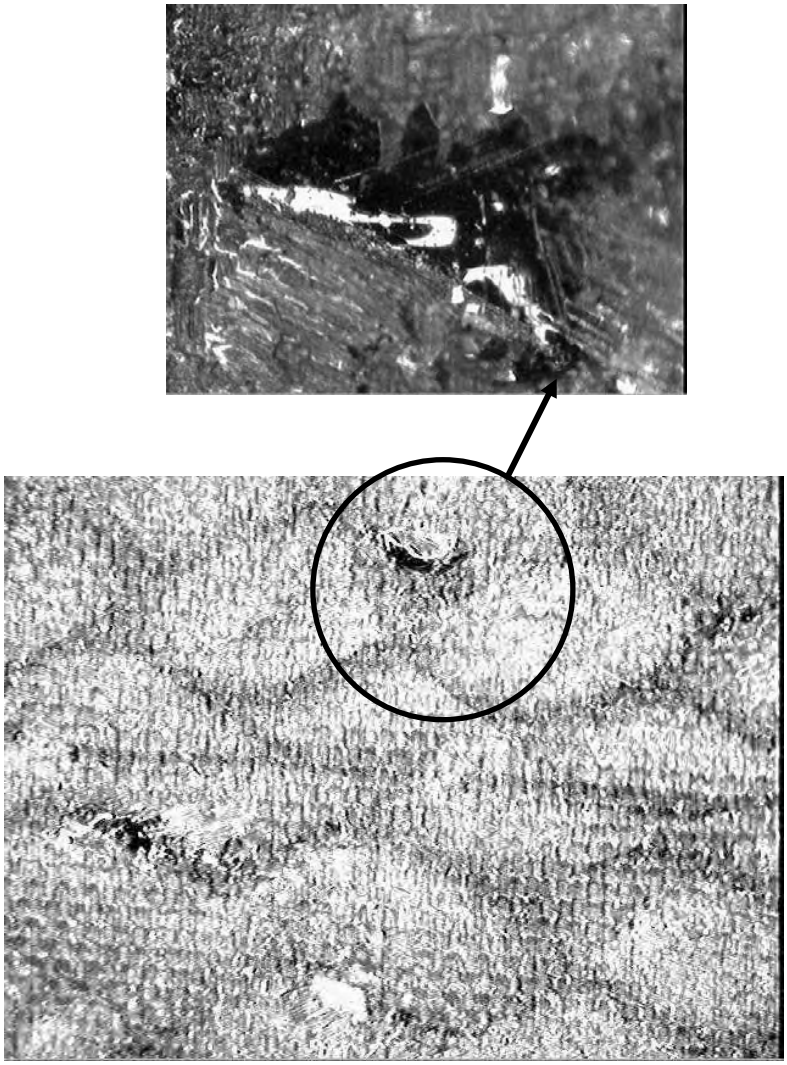

Figure 2-13. Surface Defects—Processing at 80ºF (27ºC)

The series of composite flat panels were fabricated to achieve better quality panels. Table 2-4 explains the various experimental combinations. Different process parameters were varied to observe their effects on the quality of the panel. The better quality panel was one that had a higher fiber volume fraction, uniform thickness, and almost a zero void content.

Table 2-4. Experimental Data for VARTM-Processed Panels Using EPON 9504 Resin

Serial No.	Parameter	Panel 1	Panel 2	Panel 3	Panel 4
1	Duration of heating mold and temperature	~20 hours/ 80ºF (27ºC)	~20 hours/ 120ºF (49ºC)	No	~8 hours/ 120ºF (49ºC)
2	Duration of heating resin and temperature	~20 hours/ 80ºF (27ºC)	~20 hours/ 120ºF (49ºC)	~20 hours/ 120ºF (49ºC)	~20 hours/ 120ºF (49ºC)
3	Duration of heating curing agent and temperature	4 hours/ 80ºF (27ºC)	4 hours/ 80ºF (27ºC)	1 hour/ 90ºF (32ºC)	1 hour/ 80ºF (27ºC)
4	Temperature at the time of mixing (resin/curing agent)	80ºF (27ºC)/ 80ºF (27ºC)	115ºF (46ºC)/ 80ºF (27ºC)	110ºF (43ºC)/ 90ºF (32ºC)	89ºF (32ºC)/ 77ºF(25ºC)
5	Temperature after mixing	------	110ºF (43ºC)	105ºF (41ºC)	84ºF (29ºC)
6	Degassing time/vacuum	15 min/ 10-15 torr	15 min/ 10-15 torr	No Degassing	*10 min/ 10-15 torr
7	Temperature after degassing	85ºF (29ºC)	118ºF (48ºC)	116ºF (47ºC)	93ºF (34ºC)
8	Number of times bubbles broken	1	3	-----	3
9	Double bagging	Yes	Yes	No	No
10	Bottom peel ply	Yes	No	No	No
11	Impregnation time	<10 min	<10 min	<15 min	<22 min
12	Green cure	~2 hours/ 80ºF (27ºC) followed by 8 hour ramp down	~2 hour/ 120ºF (49ºC) followed by 8 hour ramp down	16 hours/ Room temperature	~2 hour/120ºF (49ºC) followed by 8 hour ramp down
13	Postcure	200ºF (93ºC)/ 1 hour	200ºF (93ºC)/ 1 hour	200ºF (93ºC)/ 1 hour	200ºF (93ºC)/ 1 hour
14	Inclination of mold	Yes	Yes	No	Yes
15	Control on flow of resin	No	No	No	**Yes
16	Observations	-----	Exothermic[#]	Exothermic[#]	----
17	Thickness near resin line/vacuum line, inch (mm)	0.157 (3.98)/ 3.53 (0.139	0.164 (4.17)/ 0.172 (4.37)	0.170 (4.32)/ 0.152(3.86)	0.147 (3.73)/ 0.131 (3.33)
18	Overall fiber volume fraction (density method)	0.47	0.45	0.46	0.53
17	Problems	Random air pockets at top surface	OK	Random air pockets at top surface	Top surface tows not impregnated fully

Table 2-4. Experimental Data for VARTM-Processed Panels Using EPON 9504 Resin (Continued)

Serial No.	Parameter	Panel 5	Panel 6	Panel 7
1	Duration of heating mold and temperature	~20 hours/ 120ºF (49ºC)	~20 hours/ 120ºF (49ºC)	~20 hours/ 120ºF (49ºC)
2	Duration of heating resin and temperature	~20 hours/ 120ºF (49ºC)	~20 hours/ 120ºF (49ºC)	~20 hours/ 120ºF (49ºC)
3	Duration of heating curing agent and temperature	1 hour/ 80ºF (27ºC)	1 hour/ 80ºF (27ºC)	1 hour/ 80ºF (27ºC)
4	Temperature at the time of mixing (resin/curing agent)	104ºF (40ºC)/ 82ºF (28ºC)	103ºF (39ºC)/ 87ºF (31ºC)	114ºF (46ºC)/ 87ºF (31ºC)
5	Temperature after mixing	100ºF (38ºC)	100ºF (38ºC)	110ºF (43ºC)
6	Degassing time/vacuum	13 min/ 10-15 torr	10 min/ 10-15 torr	10 min/ 10-15 torr
7	Temperature after degassing	113ºF (45ºC)	110ºF (43ºC)	114ºF (46ºC)
8	Number of times bubbles broken	2	2	2
9	Double bagging	No	No	No
10	Bottom peel ply	Yes	Yes	Yes
11	Impregnation time	<10 min	<10 min	<10 min
12	Green cure	~2 hours/120ºF (49ºC) followed by 8-hour ramp down	~2 hours/120ºF (49ºC) followed by 8-hour ramp down	~2 hours/120ºF (49ºC) followed by 8-hour ramp down
13	Postcure	200ºF (93ºC)/ 1 hour	200ºF (93ºC)/ 1 hour	200ºF (93ºC)/ 1 hour
14	Inclination of mold	Yes	Yes	Yes
15	Control on flow of resin	No	No	No
16	Observations	-----	-----	Exothermic[#]
17	Thickness near resin line/vacuum line, inch (mm)	0.157 (3.98)/ 0.139 (3.53)	0.134 (3.40)/ 0.131 (3.33)	0.136 (3.45)/ 0.131 (3.33)
18	Overall fiber volume fraction (density method)	0.54	0.58	0.52
17	Problems	Random air pockets at bottom surface	OK	OK

Note: *Resin was degassed separately for 15 minutes and bubbles were broken three times.
**The resin line was partly clamped and then opened slowly.
[#]Exothermic reaction burned the resin flask when resin was in the flask for 15 minutes.
Panels 1-5 were manufactured using biaxial braid sleeves or tubes, and panels 6-7 were manufactured using biaxial braid slit sleeves.

The proper combination of process parameters was finally achieved. This combination consistently produced composite panels of good quality. The combination is explained as follows:

- The resin distribution media was cut 0.75 in. (19 mm) short from the vacuum line and 0.5 in. (12.7 mm) short along the width side. The vacuum distribution line was placed below the distribution media and the top peel ply next to the fabrics.

- The mold and the entire resin container were heated at 120ºF (49ºC) for approximately 20 hours overnight in the oven, as shown in figure 2-5.

- The curing agent EPI-CURE 9554 was heated at 80ºF (27ºC) for approximately 1 hour.

- Mixing was completed when the resin was between 110ºF (44ºC) and 120ºF (49ºC), and the curing agent was between 77ºF (25ºC) and 80ºF (27ºC).

- Mixed resin was carefully degassed for 8 to 10 minutes at approximately 5 to 10 torr.

- The impregnation was performed with the mold at 120ºF (49ºC).

- The composite panel was kept in the mold at 120ºF (49ºC) for 2 hours and then the oven was turned off. The composite panel remained at room temperature for 16 hours, which is commonly known as the green cure.

- The composite panels were postcured at 199ºF (93ºC) for 2 hours, as recommended by the manufacturer.

2.4 OVERALL FIBER VOLUME FRACTION.

It is very important to evaluate the overall fiber volume fraction (V_f^{Overall}) in the composite panels after manufacturing. Since the fibers are the main load carrying elements in the composites, their percentage has a direct effect on mechanical properties of the composites. Various methods are available to determine the overall fiber volume fraction in composite panels:

- Ignition Method (ASTM D 2584-68)
- Areal Weight Method (ASTM D 792-86)
- Density Method

2.4.1 Ignition Method.

The resin is burned off in a high-temperature oven. The ash is rinsed from the remaining fiber (using acetone or alcohol) and the fiber is dried and weighed. The volume of the fiber is calculated by dividing the mass of the fiber by the density of the fiber material. This method cannot be used with carbon fiber because carbon oxidizes at elevated temperatures.

2.4.2 Areal Weight Method.

The fiber volume fraction is determined from the areal weight of the reinforcing fabric and the volume of the composite using the following relationship.

$$V_f^{\text{Overall}} = \frac{(V)_{\text{Fiber}}}{(V)_{\text{Composite}}} = \frac{(n*W*A)/\rho_f}{A*t} = \frac{n*W}{t*\rho_f}$$

where

$(V)_{\text{Fiber}}$ = Volume of the fiber material in the specimen
$(V)_{\text{Composite}}$ = Volume of the composite specimen
n = Number of layers or plies in the composite specimen
W = Areal weight of the fabric
A = Cross-sectional area of the composite specimen
t = Thickness of the composite specimen
ρ_f = Mass density of fiber material

The areal weight changes in the case of braided fabric according to the braid angle. It is very difficult to maintain a constant braid angle in the VARTM process when braided tubes are used as fabric. It is also necessary to know the accurate relationship between areal weights and the braid angle. Further, this method may produce wrong answers due to errors in the braid angle measurement and the areal weight-braid angle relationship.

2.4.3 Density Method.

The fiber volume fraction is determined from the densities of the composite, assuming that voids are negligible or less than 1% (Daniel and Ishai, 1994). The density of braided composite, postcured resin, and carbon fibers are found by using the techniques explained by ASTM D 792-86. The expression for fiber volume fraction based on the density of the composite is:

$$V_f^{\text{Overall}} = \frac{\rho_c - \rho_m}{\rho_f - \rho_m}$$

where ρ_f, ρ_m, ρ_c = Densities of fiber, matrix, and composite.

This method is easy to implement and, therefore, was used to calculate the overall fiber volume fraction of the braided composites manufactured in this research. Typically, five 0.5- by 1-in. (12.7- by 25.4-mm) specimens or smaller were cut from each panel and their densities were evaluated. The densities of carbon fibers, cured DM 411-350 vinyl ester resin, and cured EPON 9504 epoxy resin was 1.79 g/cm^3, 1.13 g/cm^3, and 1.134 g/cm^3, respectively. The sample calculations pertaining to the carbon/epoxy braided composite panel (braid angle 45º) are presented in table 2-5. The overall fiber volume fraction was calculated using the above equation. It was observed that the average overall fiber volume fraction for this panel was 0.53.

In general, the composite panels manufactured by the VARTM process provide a fiber volume fraction of 0.5.

Table 2-5. Overall Fiber Volume Fraction for Braided Composites (Braid Angle 45° ±1°)

Specimen No.	Density of the Specimen (g/cm^3)	Overall Fiber Volume Fraction
1	1.488	0.54
2	1.462	0.50
3	1.485	0.54
4	1.476	0.52
5	1.468	0.52
	Average	0.53

The VARTM-processed composite panels exhibited almost 12% higher thickness near the vacuum line compared to the thickness near the resin line. The effects of thickness and fiber volume fraction on mechanical properties are discussed in the next section.

2.5 FIBER VOLUME FRACTION IN THE TOW.

The fiber volume fraction in the tow (V_f^{Tow}) is also an important characteristic in finite element modeling. Micrographs were used to observe the shape of the tow, and a software package (Image-Pro) was used to measure the tow area. Figure 2-14 shows the scanning electron microscope (SEM) micrograph of tows. The diameter of the carbon fiber was measured as 7 μm using the SEM micrograph shown in figure 2-15. The fiber volume fraction in tow varied from 0.66 to 0.72 in the braided composites. Therefore, an average value of 0.69 was used for the further calculations.

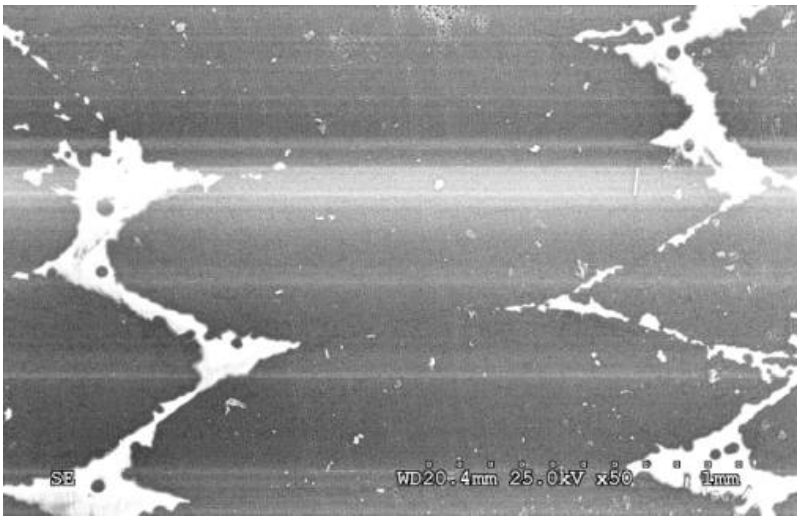

Figure 2-14. Micrographs of Braided Tows Using SEM

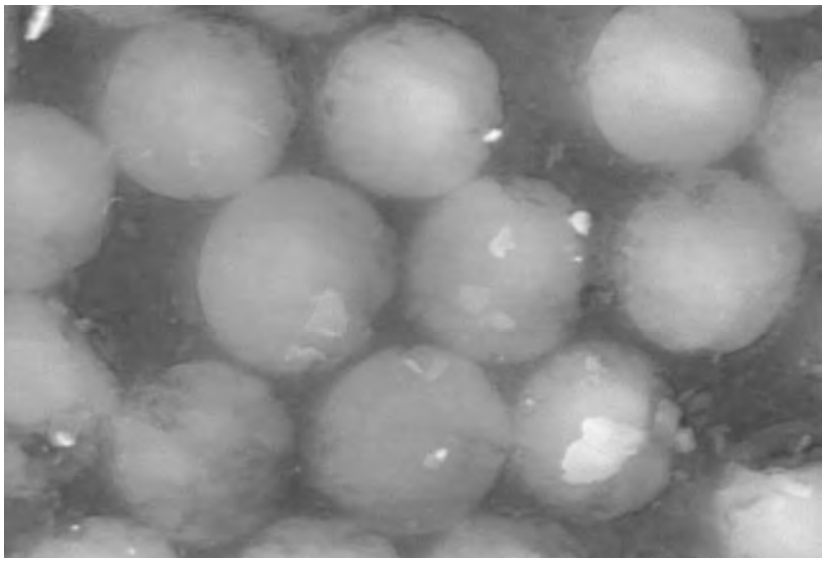

Figure 2-15. An SEM Micrograph of Fibers (Fiber diameter 7 μm)

The sample calculations for the tow fiber volume fraction are listed below.

- Average braid angle = 25º
- Average tow area = 0.7361 mm^2
- Area of fiber (ϕ = 7 μm) = $\pi/4 * (7*10^{-3})^2 = 3.848*10^{-5}$ mm^2
- Area of fiber at angle 25º = $3.848*10^{-5}/\cos(25º) = 4.246*10^{-5}$ mm^2
- Area of 12000 fibers (12K/tow) = 0.5095 mm^2
- Fiber volume in the tow fraction = 0.5095/0.7361 = 0.69

2.6 SUMMARY OF SECTION 2.

The following conclusions were drawn from the experimental study regarding VARTM processing in general and braided composites in particular:

1. When EPON 9504 resin was formulated at 120ºF (49ºC), its gel time reduced to approximately 25 minutes. This fact limited the size of the component and added further costs to the processing.

2. The use of a flow control device in the case of DM 411-350 and the heating of the entire mold for a prolonged period of 20 hours in the case of EPON 9504 increases the cost of processing.

3. The VARTM processed composite panels varied in thickness, which in turn caused fiber volume fraction variation. The thickness of the panels near the vacuum line was greater than that at the resin line. Thickness variation was due to the drop in pressure differential. Initially, the pressure differential was at a maximum level and later dropped as resin flowed in the mold.

4. It is sometimes claimed that the use of two vacuum bags (termed double bagging) improves fiber volume fraction. However, there was no effect on fiber volume fraction from the double bagging in this research. However, double bagging definitely helped to maintain a leak-proof bag.

5. The use of a bottom release fabric is actually optional. However, if it is not used, then the final bottom surface is shiny. This shiny surface needs to be roughened using sandpaper before tabbing. Even with a properly roughened surface, the tabs slipped in the grip in this study. This meant that the shear strength of the adhesive between the tab and the specimen became less than the applied load. Therefore, to avoid the problem of tab slipping, the use of top and bottom peel plies is strongly recommended.

6. Although VARTM is a simple process, as far as equipment is concerned, it is quite complicated and has many variables. Designing the proper VARTM process for a particular material combination is a challenge. Some of the important variables are listed below:

    a. Processing temperature and viscosity of resin
    b. Temperature of mold
    c. Fabric architecture (type of weave and size)
    d. Degassing
    e. Proper placement of resin distribution media
    f. Placement of resin and vacuum distribution lines
    g. Use of flow control device

7. It was recently reported by Bolick and Kelkar (2004) that EPON 9504 produces panels of good quality if processing is completed in a room where temperature is continuously maintained at 80ºF (27ºC). The fabric used in this study was a carbon plain-woven fabric with a 3 K tow size, manufactured by BGF Industries, Inc. It is interesting that the same fibers in braided fabric with a 12 K tow size have a wetting problem with the same resin. Therefore, it is concluded that the size of tow and fabric crimp may have an effect on wetting.

8. Further investigation regarding the use of an air release agent or wetting agent is highly recommended to successfully perform processing at a room temperature of 77ºF (21ºC).

The braided composite panels were cut into test coupons according to ASTM standards. Section 3 discusses the performance evaluation of the braided composites in static and tension-tension fatigue loading.

3. PERFORMANCE EVALUATION.

3.1 INTRODUCTION.

Section 2 discussed the low-cost VARTM manufacturing process for biaxial braided composites in detail. This section discusses the performance evaluation of the braided composites under static and tension-tension fatigue loading. The effect of the braid angle on mechanical properties and fatigue life was also studied. All the static and fatigue tests were performed according to the ASTM standards discussed below.

3.1.1 Static Tensile Tests.

Static tensile tests were performed according to ASTM D 3039/D 3039M, "Standard Test Method for Tensile Properties of Fiber Resin Composites." The in-plane tensile properties like ultimate tensile strength (UTS) or strain at UTS (S_u), longitudinal tensile modulus, and Poisson's ratio were evaluated using the ASTM D 3039/D 3039M standard. The axial extension was measured by an extensometer and transverse strain was measured by a strain gage. All static tensile tests were conducted in the displacement control mode with a cross lead rate of 0.05 in./min (1.27 mm/min).

3.1.2 Tension-Tension Fatigue Tests.

Tension-tension fatigue tests were performed according to ASTM D 3479/D 3479M, "Standard Test Method for Tension-Tension Fatigue of Polymer Matrix Composite Materials." This test method is limited to unnotched test specimens subjected to constant-amplitude uniaxial in-plane loading that is defined in terms of a test control parameter (defined by Procedure A and B of ASTM D 3479/D 3479M).

- Procedure A (Load Controlled)—A system in which the test control parameter is the load (stress) and the machine is controlled so that the test specimen is subjected to repetitive constant amplitude load cycles.

- Procedure B (Displacement Controlled)—A system in which the test control parameter is the strain in the loading direction and the machine is controlled so that the test specimen is subjected to repetitive constant-amplitude strain cycles.

All tension-tension fatigue tests were conducted according to Procedure A. Spectrum loading (variable amplitude) is also often used to simulate real-life loading conditions. In constant-amplitude load-controlled tests, stress is applied as a percentage of UTS. The stress was applied from 80% of UTS and reduced in steps of 10% until specimens survived 1 million cycles. Typically, the stress level at infinite life is referred to as the fatigue limit or endurance limit, but for most engineering purposes, infinite life is usually considered between 1 million and 10 million cycles. In this research, endurance limit refers to the stress level at 1 million cycles.

The other test parameters selected were sinusoidal waveform, 10-Hz frequency, and 0.1 stress ratio. Stress ratio (R) is defined as

$$R = \frac{\sigma_{min}}{\sigma_{max}} = \frac{P_{min}}{P_{max}}$$

where:

σ_{min} = Minimum stress and corresponding load is P_{min}
σ_{max} = Maximum stress and corresponding load is P_{max}

The test methodology in the present research is to define methodology to accelerate testing time. Accelerated testing consists of test methods that deliberately shorten (in a measured way) the life of the tested product or accelerate the degradation of the product's performance. Most accelerated testing is performed on materials or products to characterize their degradation mechanisms (e.g., fatigue, creep, cracking, wear, corrosion/oxidation, and weathering (Battat, http://amptiac.alionscience.com/pdf/2001MaterialEase16.pdf)). In accelerated fatigue testing, the frequency is limited to 5-10 Hz for polymer composite materials because of their viscoelastic nature. These materials may show dramatic change in fatigue life and different failure mechanisms at lower temperatures. The FAA recommended a frequency of 10 Hz and an R ratio of 0.1 was recommended by the FAA. Most of the primary structures of aircraft, such as the fuselage, experience tension-tension fatigue. The fuselage is pressurized with air when the plane reaches a high altitude and the pressure is released when the plane reaches the ground. When the fuselage is pressurized it stretches, and when pressure is released the fuselage contracts. Thus, it experiences tension-tension fatigue.

3.1.3 Specimen Geometry.

The geometry of the test specimens was identical for both tension and fatigue tests, as shown in figure 3-1. The length and width of the specimens were 10 in. (254 mm) and 1 in. (25.4 mm), respectively. The thickness varied between 0.14 in. (3.55 mm) and 0.16 in. (4 mm), depending upon the braid angle. All the specimens were tabbed to avoid failure in the grip.

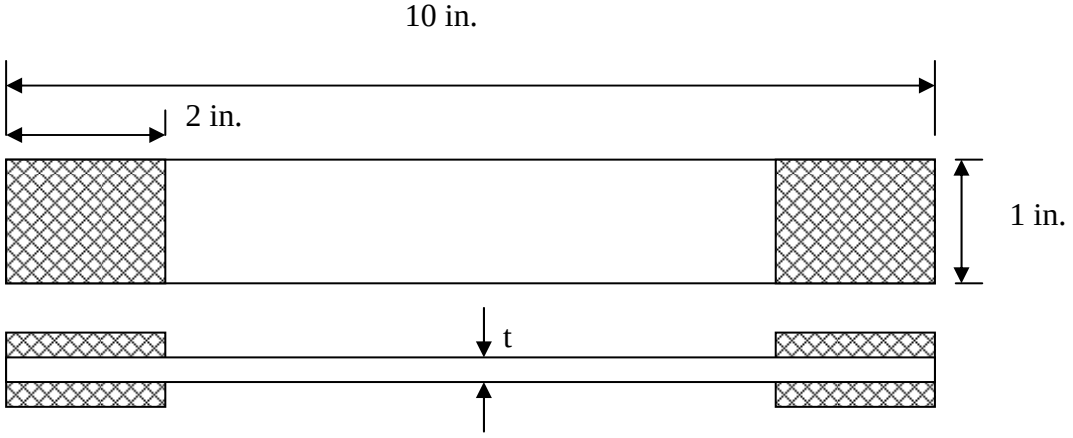

Figure 3-1. Tensile Test Specimen Geometry

The specimens that met the requirements of the ASTM D 3039/D 3039M and the ASTM D 3479/D 3479M standard were selected. The critical requirements of the specimens were a width tolerance of ±1% and a thickness tolerance of ±4%.

3.1.4 Dynamic/Fatigue Testing System.

All the tests were performed on a Dynamic/Fatigue Testing System, as shown in figure 3-2. The capacity of the load frame was 490 kN (110 kips), and the capacity of the load cell was 245 kN (50 kips). The accuracy of the load cell was ±8.9 N (2 lb). The hydraulic grips in which the specimen was clamped can apply a maximum pressure of 10 ksi (69 MPa) with a grip capacity of 300 kN (67.5 kips). The machine was capable of conducting static tensile, static compression, flexural or bending, and fatigue tests. It was controlled by the use of Max software developed by the INSTRON Corporation.

Figure 3-2. Dynamic/Fatigue Testing System

3.1.5 Test Matrix.

Table 3-1 presents the test matrix used for the experimental study. A sufficient number of specimens needed to be tested for statistical relevance. Since the manufacturing of composites, preparation of specimens (cutting and tabbing) and fatigue testing take a considerable amount of time and effort, only the minimum numbers of specimens necessary for statistical considerations were used.

Table 3-1. Test Matrix

Material System	Braid Angle	Tensile Test Specimens	Fatigue Test Specimens
Neat Resin EPON 9504	-	2	-
Carbon/Vinyl Ester	25	5	15
Carbon/Epoxy	25	5	15
Carbon/Epoxy	30	5	15
Carbon/Epoxy	45	5	15
Frequency Effect	30	--	5
Stiffness Degradation Study	25	--	5
Total		22	70

Once the biaxial braided composite panels were postcured, specimens were cut according to the plan shown in figure 3-3. The side view of this figure shows the thickness variation in the composite panels processed by VARTM. The issues related to thickness variations are discussed in subsequent sections. Ten tension/fatigue specimens and five overall fiber volume fraction specimens were typically cut from each panel.

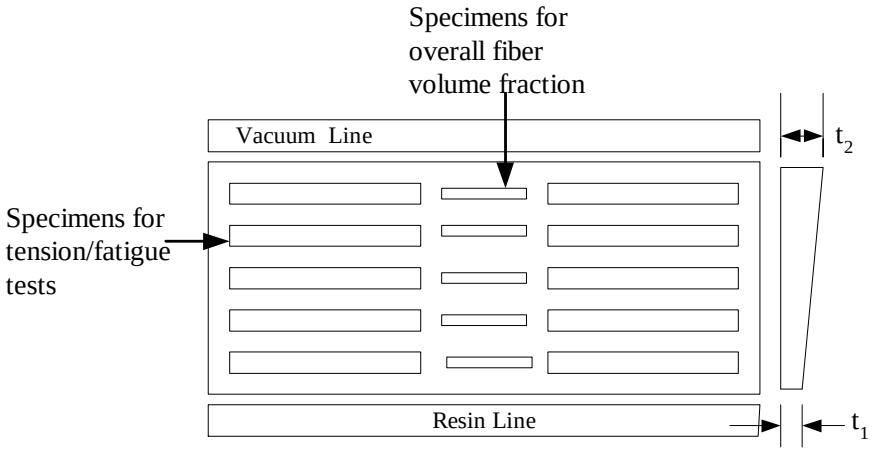

Figure 3-3. Plan of Test Specimens From Panel (Thickness varies from t_1 to t_2)

3.1.6 Tensile Test Results of Neat EPON 9504 Epoxy Resin.

The properties of DM 411-350 vinyl ester resin and EPON 9504 epoxy resin are presented in table 2-2. Previous research of the DM 411-350 vinyl ester resin data, found that tensile properties were readily available (Smith, 2001). The tensile properties of EPON 9504 epoxy resin were evaluated by static tension tests on neat resin coupons according to ASTM D 638. The resin was mixed with the curing agent in the recommended proportion and degassed. Then, it was poured into a 12-in.-wide by 12-in.-long (25.4- by 25.4-cm) steel mold and kept for almost 16 hours at a room temperature of 77ºF (25ºC) that is termed green cure. After the green cure, the panel was kept in the oven for postcure at 200ºF (93ºC) for 1 hour as recommended by the

manufacturer. After postcuring, the dog bone specimens were cut and tested according to ASTM D 638. This ASTM D 638 standard recommends selecting a test speed to produce rupture in 1/2 to 5 minutes. The selected speed of testing was 0.2 in./min (5 mm/min). The axial and lateral strains were measured using an extensometer and a strain gage, respectively. The geometry of the test specimens is shown in figure 3-4, and the stress-strain diagram is presented in figure 3-5. The average tensile strength, axial modulus, and Poisson's ratio were 9.42 ksi (64.94 MPa), 2.96 Msi (0.43 GPa), and 0.38, respectively.

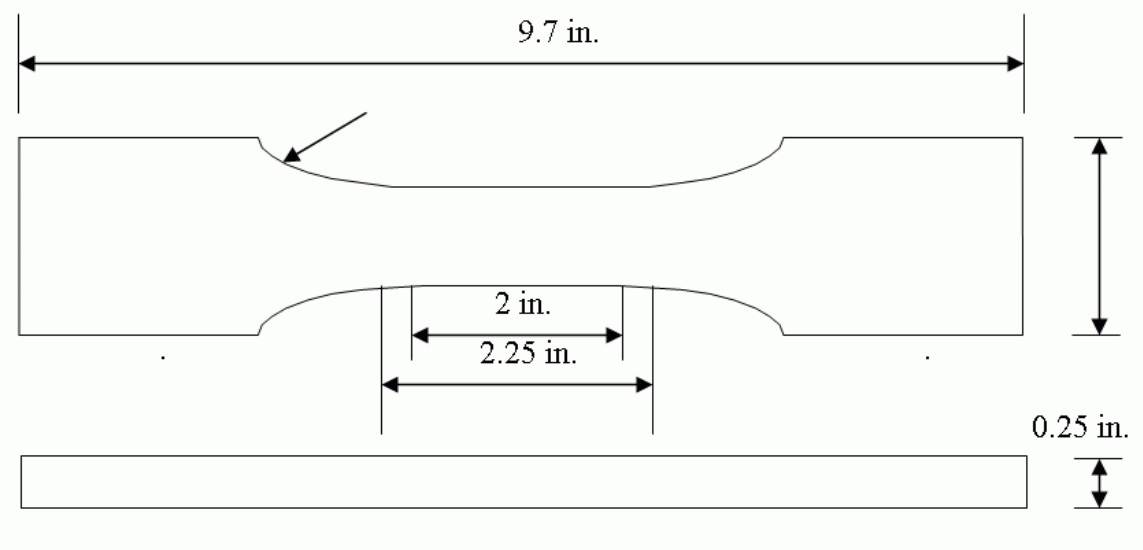

Figure 3-4. Specimen Geometry for Neat Resin Coupon (ASTM D 638)

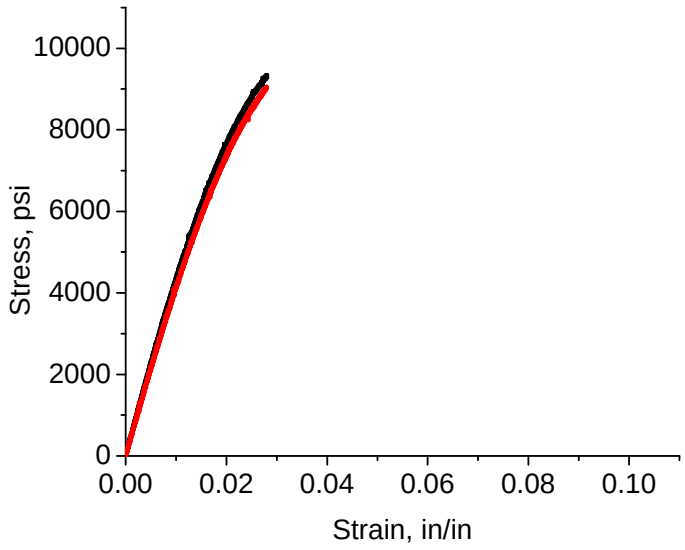

Figure 3-5. Stress-Strain Diagram of EPON 9504 Epoxy Neat Resin

3.2 TENSILE AND FATIGUE TEST RESULTS OF BRAIDED COMPOSITES MANUFACTURED USING BRAIDED TUBES.

In the first stage of the research, biaxial braided composite panels were manufactured using braided tubes and two different resin systems, DM 411-350 vinyl ester and EPOPN 9504 epoxy. Braided tubes were flattened and their width was maintained at 1.75 in. (44.5 mm) to ensure a braid angle of approximately 25°. Two braided tubes were stacked on top of each other to obtain four layers. The braid angle of all the specimens was measured on a micrograph using Image-Pro software, as shown in figure 1-3. It was found that the braid angle varied from 24° to 32°. This could be due to increased flattening of the braided tubes after application of the vacuum in VARTM. Specimens whose braid angle fell in the range of 25° ±2° were selected. All the selected specimens met the requirements of the ASTM standard of width and thickness tolerance as discussed in section 3.13.

3.2.1 Carbon/Vinyl Ester Braided Composites.

The overall fiber volume fraction in the carbon/vinyl ester braided composites panel was 0.52 ±0.04. Table 3-2 lists the results of tensile tests for five specimens. The "s" represents the sample standard deviation, and CV is the sample coefficient of variation in percentage terms. E_x was computed based on a linear regression fit to the stress-strain data over the 0.1% to 0.3% strain range. Experimental error was calculated using the student-t distribution at a confidence level of 95%.

Table 3-2. Tensile Test Results of Carbon/Vinyl Ester Braided Composites
(Braid Angle 25° ±2°)

Specimen	UTS		E_x		% ε_{ut}	ν_{xy}
	ksi	MPa	Msi	GPa		
1	99.11	683.31	10.35	71.33	1.11	1.22
2	88.84	612.52	9.94	68.52	0.98	1.17
3	92.62	638.59	9.24	63.71	1.16	1.16
4	106.40	733.52	10.18	70.18	1.24	1.11
5	100.70	694.22	10.48	72.25	1.04	1.02
Average	97.53	672.37	10.04	69.22	1.19	1.14
s	6.91	47.62	0.49	3.38	0.10	0.08
CV	7.08	7.08	4.88	4.88	8.15	6.66
Experimental Error	±8.58	±59.12	±0.61	±4.20	±0.13	±0.10

It was assumed that the properties in table 3-2 represented the entire panel. Fatigue tests were conducted to obtain the stress level at 1 million cycles. The test parameters were those explained in section 3.1.2. Three specimens were tested at each stress level. The fatigue test data are tabulated in table 3-3.

Table 3-3. Fatigue Test Results for Carbon/Vinyl Ester Braided Composite
(Braid Angle 25° ±2°)

% of UTS	1	2	3
85	146	1416	5560
75	1887	16590	570
65	3854	98830	2540
55	34451	13430	11607
45	1000000*	107340	39733
40	1000000*	1000000*	1000000*

* No failure, run-out

3.2.2 Carbon/Epoxy Braided Composites.

The overall fiber volume fraction in the carbon/epoxy braided composites panel was 0.51 ±0.05. Table 3-4 lists the tensile test results, and table 3-5 presents fatigue test data. The stress-strain diagram and the stress-fatigue life diagram (S/S_u-N) for both carbon/vinyl ester and carbon/epoxy composites are displayed in figures 3-6 and 3-7, respectively.

Table 3-4. Tensile Test Results of Carbon/Epoxy Braided Composites
(Braid Angle 25° ±2°)

Specimen	UTS		E_x		% ε_{ut}	ν_{xy}
	ksi	MPa	Msi	GPa		
1	94.78	653.41	7.44	51.29	1.86	1.46
2	98.78	681.00	7.93	54.67	1.99	1.44
3	96.55	665.62	7.85	54.12	1.96	1.46
4	85.8	591.50	7.00	48.25	1.68	1.40
5	102.8	708.70	9.12	73.52	1.35	1.47
Average	95.74	660.03	7.87	54.26	1.77	1.44
s	6.314	43.53	0.792	5.46	0.263	0.027
CV	6.60	6.60	10.06	10.06	14.85	1.88
Experimental Error	±7.84	±54.04	±0.98	±6.78	±0.33	±0.03

Table 3-5. Fatigue Test Results for Carbon/Epoxy Braided Composite
(Braid Angle 25° ±2°)

% of UTS	1	2	3
80	516	434	274
70	986	693	839
60	5575	2258	1225
50	4807	4372	3470
45	24135	1000000*	1000000*
40	1000000*	1000000*	1000000*

* No failure, run-out

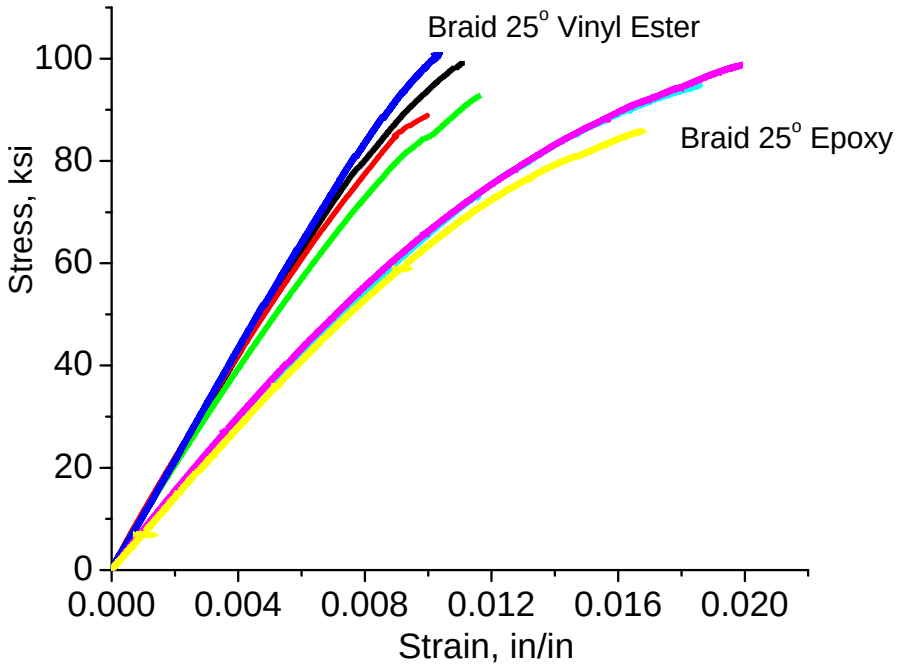

Figure 3-6. Stress-Strain Behavior of Braided Composites Using Flattened Braided Tubes
(Braided Angle 25° ±2°)

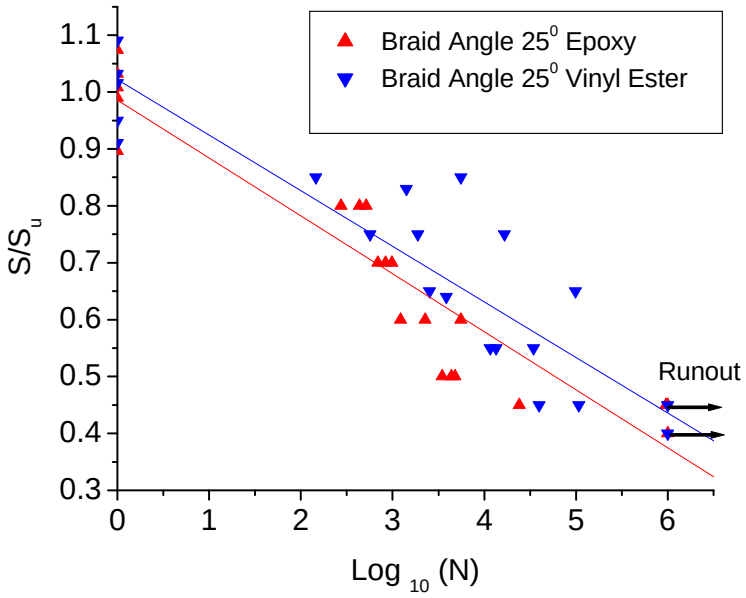

Figure 3-7. S-N Diagram for Braided Composites Using Flattened Braided Tubes Showing Large Scatter in the Fatigue Data (Braid Angle 25° ±2°)

3.2.3 Braided Tube Findings.

- It was found that the UTS for both the carbon/vinyl ester and the carbon/epoxy braided composites were almost identical at a braid angle of 25º. However, carbon/vinyl ester composites were stiffer than carbon/epoxy composites. Carbon/epoxy composites had excessive nonlinear behavior and a higher strain at UTS. Poisson's ratio was found to be greater than 1 for the braided composites because of their anisotropic nature.

- The CV values in tables 3-2 and 3-4 generally demonstrate that UTS and failure strain measurements exhibited less repeatability and reproducibility than stiffness parameters.

- The student-t distribution indicated an experimental error of ±8.58 ksi (±59.12 MPa) in the case of the carbon/vinyl ester composites and ±7.84 ksi (±54.04 MPa) for the carbon/epoxy composites. This was a very significant error and was mainly due to the heterogeneity of the material as opposed to the tensile test itself. Increasing the sample size and studying the repeatability of the manufacturing process and material behavior can reduce this error.

- Fatigue data of braided composites exhibited large scatter, especially for carbon/vinyl ester composites. The stress was applied as a percentage of UTS in load-controlled fatigue tests. Thus, the experimental error in UTS was the main cause of large scatter in the fatigue data.

- Since the failure strain of carbon/epoxy composites was greater than that of the carbon/vinyl ester braided composites, one might expect higher fracture toughness (damage tolerance) and better performance in fatigue and impact for these composites. However, the carbon/vinyl ester braided composites exhibited better fatigue performance at higher loads. Both composites survived 1 million cycles at a fatigue load of 40% of UTS.

Fibers are the major load carrying members in composites. Thus, the fiber volume fraction has a direct effect on mechanical properties including UTS. The literature review also indicates that braid angle variation drastically changes in-plane tensile properties including UTS. The next section discusses the effect of fiber volume fraction and braid angle variation on UTS.

3.3 EFFECT OF FIBER VOLUME FRACTION AND BRAID ANGLE VARIATIONS ON UTS.

The large scatter in the fatigue data was mainly due to the scatter of UTS. The UTS was directly affected by variations in fiber volume fraction and braid angle. The main causes of the effects were the limitation of the VARTM process and misalignment of braided tubes in the mold during processing.

3.3.1 Effect of Fiber Volume Fraction on UTS.

Even with the proper design and placement of distribution media and the proper placement of vacuum and resin lines, the thickness of VARTM processed composites varied from the resin line to the vacuum line. The thickness increased by 12% at the vacuum line compared to the thickness at the resin line. The thickness of the panel was a function of the instant of time when a particular location was impregnated with resin. Thickness variation was also due to the drop in pressure differential. When resin enters a mold, the pressure differential is at a maximum, and as resin flows forward in a mold, the pressure drops. Therefore, VARTM manufactured flat panels are thicker at the vacuum line. Thickness variations within a panel are one of the limitations of the VARTM process. The greater thickness at the vacuum line results in a local resin rich area. Thus, fiber volume fraction (V_f) varies from location to location. V_f is at a maximum near the resin line and at a minimum near the vacuum line.

According to simplified micromechanics equations (Chamis, 1984), the longitudinal tensile strength of unidirectional lamina is

$$S_{lt} \sim S_{ft} * V_f$$

where:

S_{1t} = Longitudinal tensile strength of unidirectional lamina,
S_{ft} = Tensile strength of fiber, and
V_f = Fiber volume fraction

The carbon/vinyl ester and carbon/epoxy braided composites manufactured by VARTM exhibited fiber volume fractions of 0.52 ±0.04 and 0.53 ±0.05, respectively. This variation in V_f

may alter UTS as much as ±9%. It should be noted that the above equation is not applicable to braided composites. This is because tows in the braided composites, unlike laminates, are mechanically interlocked and have undulations. The purpose of the above equation is to show the effect of V_f on UTS. Thickness variation (in turn V_f variation) in VARTM was inevitable and could not be controlled to less than ±6% in this research.

3.3.2 Effect of Braid Angle on UTS.

When braided tubes were used to manufacture braided composites in the VARTM process, the braid angle varied from 24º to 32º within the panel. The braid angle variation was caused by the misalignment of braided fabric. This misalignment could occur while stacking braided tubes one above the other, or it could occur at high vacuum (0.5 torr) during vacuum bagging. Almost all the in-plane properties were affected by the braid angle, including UTS. As the braid angle increased, UTS decreased exponentially, as shown in figure 3-8. When the braid angle increased from 25º to 30º, UTS dropped from 95.74 ksi (660.03 MPa) to 64.09 ksi (441.84 MPa). The 5º decline in the braid angle caused a decline of approximately 33% in the UTS. Braid angle must be controlled because it has a significant effect on UTS.

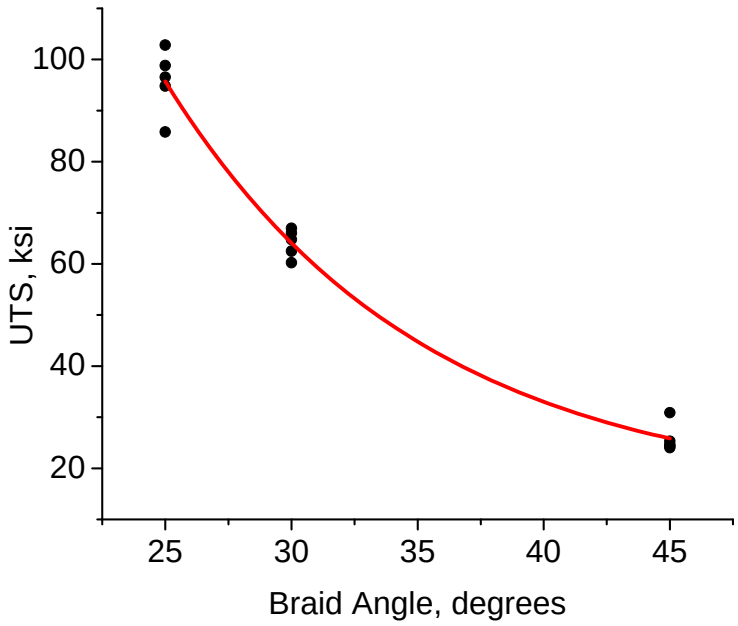

Figure 3-8. Ultimate Tensile Strength Decreasing Exponentially With an Increase in Braid Angle

Braid angle can be controlled if slit sleeves are used instead of braided tubes. As discussed in section 2, the slit sleeve is a special braid manufactured with a constant braid angle throughout the braided fabric. Braided tubes are manufactured at required braid angles and then slit to produce slit sleeves. The edges are fused with a small amount of EVA adhesive. The adhesive maintains a constant braid angle even during handling. Slit sleeves with fixed braid angles of 30º and 45º were used for further study. A change in the braid angle in braided tubes does not affect the fiber volume fraction of braided composites (appendix A).

3.4 TENSILE AND FATIGUE TEST RESULTS OF BRAIDED COMPOSITES MANUFACTURED USING SLIT SLEEVES.

In a later phase of the research, biaxial braided composite panels were manufactured using slit sleeves with 30° and 45° braid angles and EPOPN 9504 epoxy resin. Four slit sleeves were stacked to obtain four layers. Braid angle variation with the slit sleeves was ±2° within each panel. Specimens were selected whose braid angle fell at 30° ±1º and 45° ±1º. All the selected specimens met the requirements of ASTM standards for width and thickness tolerance, as discussed in section 3.1.3.

3.4.1 Carbon/Epoxy Braided Composites (Braid Angle 30° ±1º).

The overall fiber volume fraction was 0.53 ±0.05 for 30º slit sleeves. Table 3-6 shows the results of tensile tests, and table 3-7 presents fatigue test data.

Table 3-6. Tensile Test Results for Carbon/Epoxy Braided Composites (Braid Angle 30° ±1°)

Specimen	UTS		E_x		% ε_{ut}	ν_{xy}
	ksi	MPa	Msi	GPa		
1	66.97	461.74	6.02	41.51	2.42	1.33
2	64.74	447.69	5.74	39.57	2.61	1.29
3	62.48	430.73	5.07	34.95	2.48	1.31
4	66.03	455.21	5.36	36.95	2.60	1.42
5	60.23	415.23	5.39	37.16	2.19	1.33
Average	64.09	441.84	5.52	38.05	2.46	1.34
s	2.737	18.87	0.369	2.54	0.171	0.050
CV	4.27	4.27	6.67	6.67	6.95	0.04
Experimental Error	±3.40	±23.42	±0.46	±3.15	±0.22	0.06

Table 3-7. Fatigue Test Results for Carbon/Epoxy Braided Composite (Braid Angle 30° ±1°)

% of UTS	1	2	3
80	450	475	392
70	578	910	660
60	1880	1910	2240
50	6020	3688	4562
45	5333	12836	7770
40	1000000*	1000000*	1000000*

*No failure, run-out

3.4.2 Carbon/Epoxy Braided Composites (Braid Angle 45° ±1°).

The overall fiber volume fraction was 0.52 ±0.03 for 45º slit sleeves. Table 3-8 shows the tensile test results, and table 3-9 presents fatigue test data. The stress-strain diagram and the stress-fatigue life diagram (S/S_u–N) epoxy carbon/epoxy composites are shown in figures 3-9 and 3-10, respectively.

Table 3-8. Tensile Test Results for Carbon/Epoxy Braided Composites
(Braid Angle 45° ±1°)

Specimen	UTS		E_x		% ε_{ut}	ν_{xy}
	ksi	MPa	Msi	GPa		
1	25.31	174.48	2.15	14.82	2.16	0.70
2	24.32	167.68	2.03	13.99	2.08	0.68
3	24.62	169.73	2.07	14.27	1.98	0.69
4	24.03	165.66	2.63	18.13	2.06	0.69
5	30.9	213.03	2.67	18.41	2.03	0.71
Average	25.84	178.14	2.31	15.93	2.06	0.69
S	2.87	19.79	0.32	2.17	0.07	0.013
CV	11.11	11.11	13.62	13.62	3.40	1.88
Experimental Error	±3.56	±24.57	±0.40	±2.69	±0.09	±0.02

Table 3-9. Fatigue Test Results for Carbon/Epoxy Braided Composite
(Braid Angle 45° ±1°)

% of UTS	1	2	3
80	369	1533	967
70	3507	29475*	2339
60	8236	9031	139329*
50	1000000^{+}	1000000^{+}	1000000^{+}

* Not included in the graph
$^{+}$ No failure, run-out

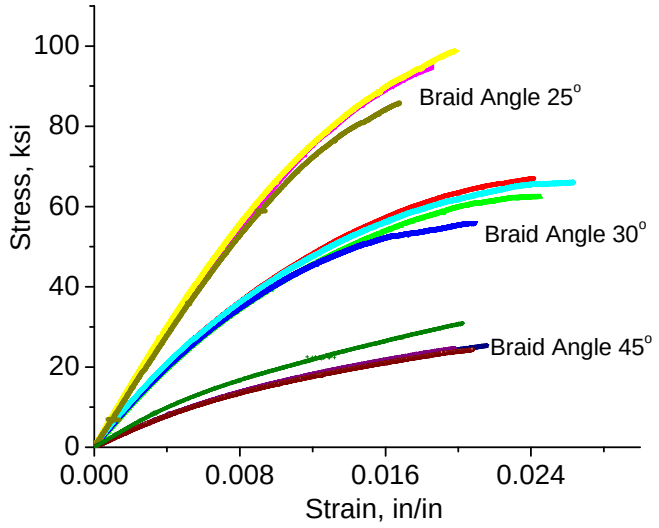

Figure 3-9. Stress-Strain Behavior of Carbon/Epoxy Braided Composites (Braid Angles 25° ±2°, 30° ±1°, and 45° ±1°)

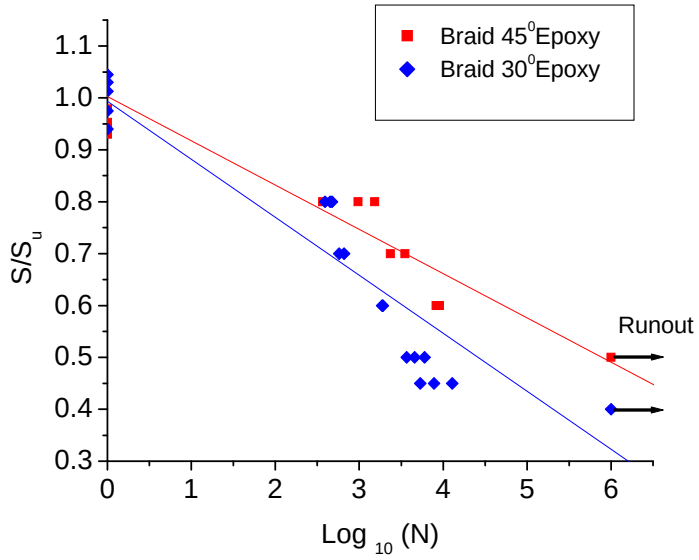

Figure 3-10. S-N Diagram for Braided Composites With Slit Sleeves Showing Less Scatter in the Fatigue Data (Braid Angles 30° ±1° and 45° ±1°)

3.4.3 Slit Braided Sleeve Findings.

Table 3-10 presents comparisons of the tensile properties for different material systems. The following are a few of the conclusions from the tensile test data:

- Experimental error in the UTS was reduced after the use of slit sleeves. The experimental error values were ±3.4 ksi (±23.42 MPa) and ±3.56 ksi (±24.57 MPa) for braided composites with braid angles of 30º and 45º, respectively.

- Fatigue data had less scatter with less error in the UTS. Thus, it can be concluded that the braid angle variation within a specimen changes the UTS among the specimens and created large scatter, especially in load-controlled fatigue tests. The use of slit sleeves is highly recommended for the fatigue study of braided composites to control braid angles within a specimen.

- Classical laminate theory is well developed and accepted for multidirectional laminates. The biaxial braided composites resemble angle ply laminates $[\pm\theta]_s$. Therefore, it is useful to compare the trend in E_x and ν_{xy} of biaxial braided composites with that of angle-ply laminates. Figure 3-11 shows Young's modulus, and figure 3-12 shows the Poisson's ratio of UD laminate and an angle ply laminate as a function of fiber orientation. As the angle increases, longitudinal modulus decreases and increasingly becomes a matrix-dominated property. Poisson's ratio increases with an angle up to 25º and then decreases. Poisson's ratio is greater than 1 with angles in the range of 15º to 35º. Similar behavior was observed in the case of braided composites. E_x was a fiber-dominated property and ν_{xy} was a matrix-dominated property. The higher Poisson's ratio of carbon/epoxy composites could be solely due to the higher Poisson's ratio of the epoxy itself. As the braid angle increased from 25º to 45º, E_x decreased, as shown in figure 3-13. The Poisson's ratio of the braided composites peaked at 25º and later decreased as the braid angle increased form 25º to 45º, similar to angle ply laminates as shown in figure 3-14. Poisson's ratio was greater than 1 at angle between 25º and 30º and less than 1 for 45º angles. When the braid angle increased from 25º to 45º, the percentage drop in the UTS, modulus, and Poisson's ratio was 75%, 70%, and 96%, respectively.

Table 3-10. Comparisons of Tensile Properties of Braided Composites With Different Material Systems and Braid Angles

Property	Carbon/ Vinyl ester	Carbon/Epoxy	Carbon/Epoxy	Carbon/Epoxy
Braid Angle	25° ±2° Braided Tubes	25° ±2° Braided Tubes	30° ±1° Slit Sleeves	45° ±1° Slit Sleeves
UTS, ksi (MPa)	97.53 (672.37)	95.74 (660.03)	64.09 (441.84)	24.84 (178.14)
ε_{ut}, %	1.19	1.77	2.46	2.06
E, Msi (GPa)	10.04 (69.22)	7.87 (54.26)	5.52 (38.05)	2.31 (15.93)
ν_{xy}	1.14	1.44	1.34	0.69
Fiber Volume Fraction*	0.52 ±0.04	0.51 ±0.05	0.53 ±0.05	0.52 ±0.03
Thickness*, in.	0.162 ±0.009	0.155 ±0.009	0.140 ±0.007	0.129 ±0.005

*These values vary among different panels and not within a single tensile test specimen.

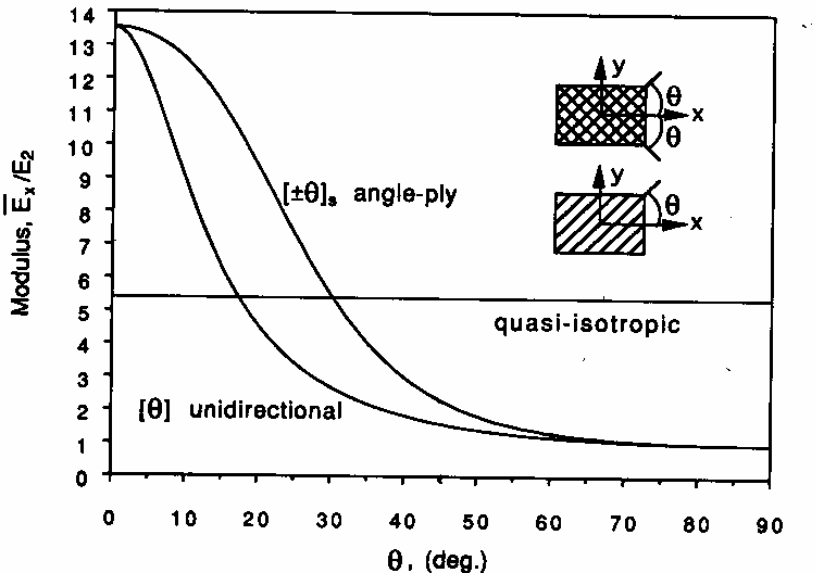

Figure 3-11. Modulus of Angle-Ply Laminates as a Function of Orientation Angle

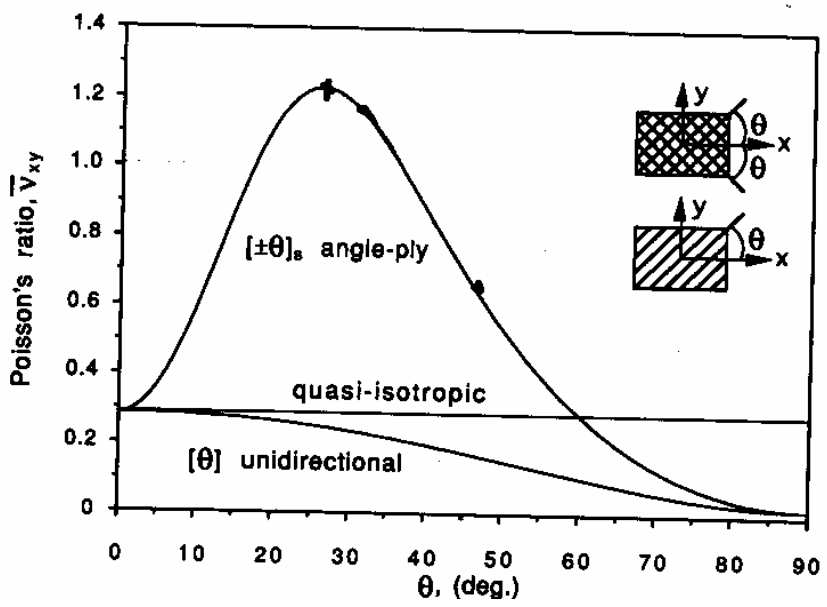

Figure 3-12. Poisson's Ratio of Angle-Ply Laminates as a Function of Orientation Angle (Daniel and Ishai, 1994)

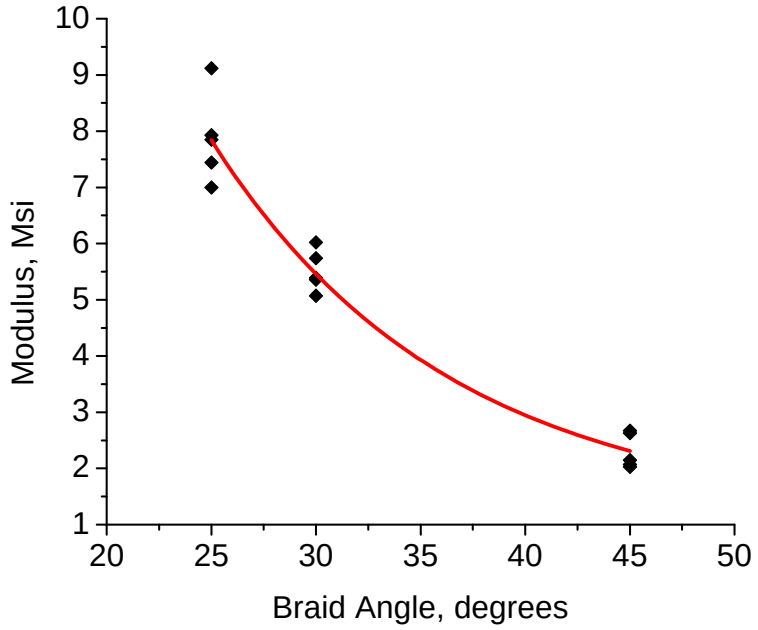

Figure 3-13. Modulus of Braided Composites as a Function of Braid Angle

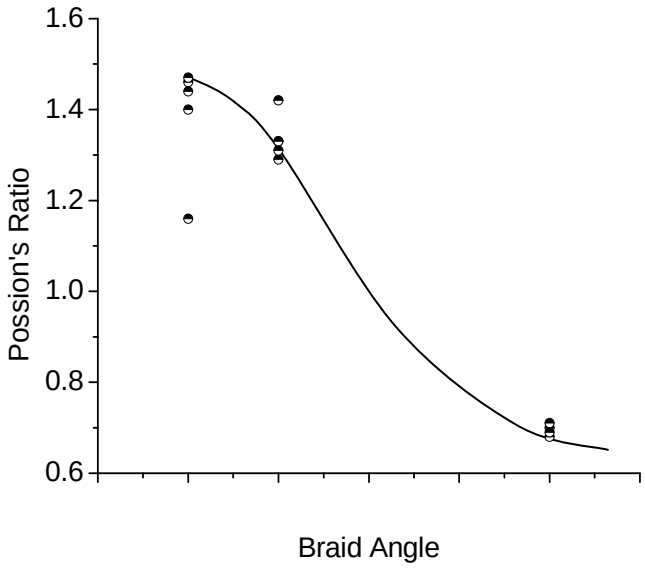

Figure 3-14. Poisson's Ratio of Braided Composites as a Function of Braid Angle

- For carbon/epoxy braided composites, the endurance limit at 1 million cycles was 40% of the UTS for braid angles of 25º and 30º, whereas it was 50% of the UTS for braid angles of 45º. The fatigue strength values for 25º, 30º, and 45º angles were 38.3 ksi (264 MPa), 25.6 ksi (176.5 MPa), and 12.9 ksi (88.94 MPa), respectively.

- Fiber volume fraction is mainly dependent on the manufacturing process. The composites manufactured with the VARTM process typically yield a fiber volume fraction of 0.5. Since slit sleeves were manufactured individually for 30º and 45º angles, their percentage cover (spacing between two tows) could differ. This could result in a small variation in the fiber volume fraction (appendix A).

- All braided composites manufactured in this research had four layers. As the braid angles increased, the thickness of the composite decreased. The thickness variation in braided composites is quite a complicated issue mainly due to braid angle variation within panels and the limitation of the VARTM process.

- UTS is sensitive to braid angle and fiber volume fraction. Statistically, UTS can be expressed as a function of braid angle and fiber volume fraction. This is explained in appendix B.

3.5 MODELING OF THE S-N DIAGRAM.

There are many models to represent the S-N diagram. The most popular is the simple linear model represented as a straight line on a semilog plot. The equation of the line is represented as

$$S = S_u\,(m \log N + d)$$

The lower the value of the slope (*m*) and the higher the value of the y-axis intercept (*d*), the higher the value of the fatigue strength. Figure 3-15 shows the linear fit of an S-N diagram for braided composites. Table 3-11 displays a comparison of UD laminates' and braided composites' S-N curves.

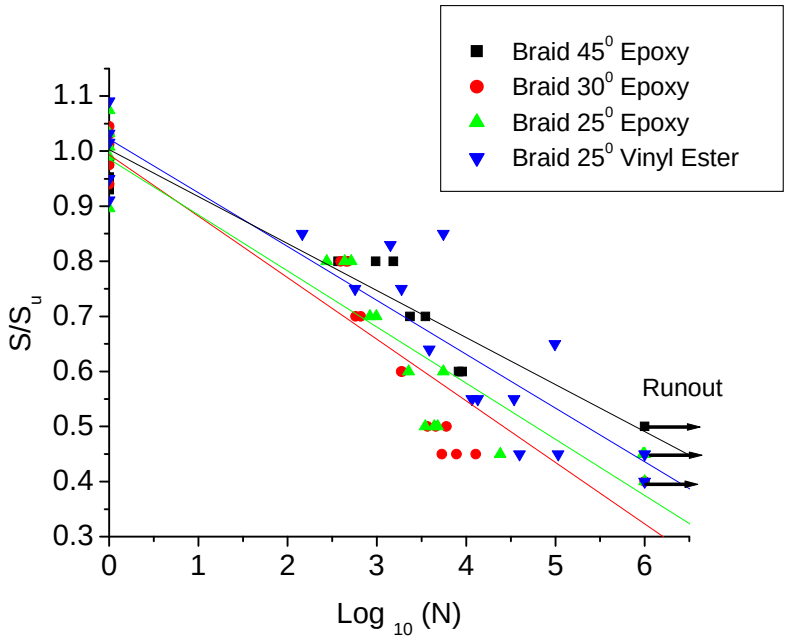

Figure 3-15. Linear Representation of S-N Diagram for Carbon/Vinyl Ester and Carbon/Epoxy Material System

Table 3-11. Comparison of UD Laminates' and Braided Composites' S-N Curve

Material	R	m	d
T300 carbon/ductile epoxy-UD (Amateau, 2003)	0.1	-0.0542	1.0420
T300 carbon/brittle epoxy-UD (Amateau, 2003)	0.1	-0.0873	1.2103
BASF G30-500 carbon/epoxy-3D Triaxial Braid (Carlos, 1994)	0.1	-0.0770	1.000
AS4/Vinyl Ester Biaxial Braid 25º	0.1	-0.0977	1.0221
AS4/Epoxy Biaxial Braid 25º	0.1	-0.1018	0.9861
AS4/Epoxy Biaxial Braid 30º	0.1	-0.1117	0.9935
AS4/Epoxy Biaxial Braid 45º	0.1	-0.08531	1.0028

Table 3-11 shows that UD laminates have superior endurance limits (at 1 million cycles) compared to those of the braided composites' material system. The linear model did not represent the fatigue of the braided composites. It either underpredicted or overpredicted the endurance limit. The trend of fatigue data can be best represented by a Sigmoidal (Boltzman) fit,

as shown in figure 3-16. The R-square values and the predicted fatigue strength at 1 million cycles are tabulated in table 3-12.

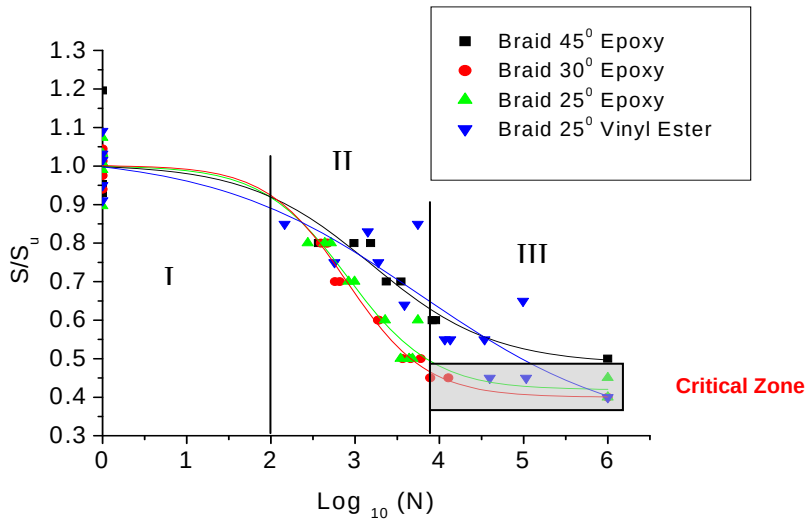

Figure 3-16. Sigmoidal (Boltzmann) Fit for Carbon/Epoxy Material System (Braid Angles 25° ±2°, 30° ±1°, and 45° ±1°)

Table 3-12. Comparison of Linear Model and Sigmoidal Model Results With Experimental Results

Material System Biaxial Braid (Braid Angle)	R^2 Value		Applied Stress for N $\geq 10^6$ (% of UTS)		
	Linear	Sigmoidal	Exp. (%)	Linear (%)	Sigmoidal (%)
AS4/Vinyl Ester (25º)	0.8603	0.8917	40	44	40
AS4/Epoxy Biaxial (25º)	0.9007	0.9659	40	37	42
AS4/Epoxy Biaxial (30º)	0.8913	0.9874	40	32	40
AS4/Epoxy Biaxial (45º)	0.8893	0.9057	50	49.1	49.7

Sigmoidal curves (S-shaped) are frequently used in biology to describe growth patterns. The growth in fatigue life with reduction in the applied fatigue load can be described using this curve (mirrored S-shape) for of braided composites. The equation for the Sigmoidal (Boltzmann) curve is given by

$$y = \frac{A_1 - A_2}{1 + e^{(x - x_o)/dx}} + A_2$$

where:

$$y = \frac{S}{S_u}$$

$$x = \log_{10}(N)$$

A_1, A_2, x_o, and dx are the parameters in the equation. The value of y varies from A_1 at the top to A_2 at the bottom. The dx describes the steepness of the curve and the larger values denote more shallow curves. The x_o indicates the value of x when y is halfway between A_1 and A_2. The values of these four parameters for all material systems are listed in table 3-13. The higher values of A_2 and dx indicate better fatigue life.

Table 3-13. Parameters in Sigmoidal (Boltzmann) Curve for Braided Composites for Different Material Systems and Braid Angles

Material System	A_1	A_2	x_o	dx
AS4/Vinyl Ester Biaxial Braid 25º	1.0304	0.30124	3.7700	1.2297
AS4/Epoxy Biaxial Braid 25º	1.0011	0.41909	2.916	0.50788
AS4/Epoxy Biaxial Braid 30º	1.0023	0.40005	2.8982	0.47307
AS4/Epoxy Biaxial Braid 45º	1.0046	0.48598	3.1882	0.72782

The S-N diagram exhibited three major stages when represented in this manner.

- Stage I: In this stage, fatigue life was almost constant and less than 100 cycles until the applied load was 80% of the UTS. This stage was termed low-cycle (high-stress) fatigue.

- Stage II: In this stage, when the applied load decreased from 80% to 50%, there was no considerable increase in fatigue life in the laminates. The number of cycles to failure typically increased to 7000, except for the carbon/epoxy braid (braid angle 45°±1º). The middle zone is very important in designing composite structures. This stage was termed midcycle fatigue.

  A linear model showed a large error in this region. For example, for the carbon/epoxy braid (braid angle 25° ±2°) at an applied load of 50% of the UTS, a linear model predicted a fatigue life of 59,573 cycles, whereas a Sigmoidal model predicted 6,952 cycles. Experimentally, the average fatigue cycles at this load varied from 3,470 to 4,807 cycles. Other examples are shown in table 3-14. Damage accumulation was very fast in the mid stage.

- Stage III: Failure cycles jumped from 7000 to 1 million in this stage when applied stress was decreased by only 10% from 50% to 40%. This indicated that major damage occurs between the applied loads of 40% and 50% of the UTS. This stage was termed high-cycle (low-stress) fatigue.

  For braided composites, the transition from Stage II to Stage III was very critical. The major damage occurred in this critical zone. If the component was subjected to overload for a small period of time in this zone, catastrophic failure could occur. A higher factor of safety had to be used. Even with this problem, braided composites are preferred because of their suitability for complex components and their low cost compared to woven composites.

  Even with its complexity, the Sigmoidal (Boltzmann) model is superior because it captures fatigue life in the critical zone and also in all fatigue stages.

Table 3-14. Fatigue Life Predicted by Linear and Sigmoidal Model at Different Fatigue Loads for Carbon/Epoxy Braided Composites

% of UTS	25º			30º			45º		
	Exp.	Linear	Sigmoidal	Exp.	Linear	Sigmoidal	Exp.	Linear	Sigmoidal
80	274-516	**68**	**391**	392-475	**54**	**377**	369-1533	**238**	**18**
70	693-986	**647**	**894**	578-910	**425**	**798**	2339-3507	**3543**	**2787**
60	1225-5575	**6205**	**2092**	1880-240	**3333**	**1695**	8236-9031	**56675**	**12883**
50	3470-4807	59573	6952	3688-020	26187	4592	1 M	783067	625437
45	24135-1 M	**184590**	**23940**	5333-2836	**73403**	**10840**	---	---	---

It is possible to predict fatigue strength at the endurance limit from a careful study of the stress-strain diagram of the static tension test. It is very interesting to note that stress-strain diagrams were linear up to 0.6%, 0.5%, and 0.4% strain for braided composites with braid angles of 25º, 30º, and 45º, respectively. The corresponding stresses for braided composites with braid angles of 25º, 30º, and 45º were approximately 40 ksi (275 MPa), 25 ksi (172 MPa), and 7.5 ksi (52 MPa) and were 42%, 39%, and 29% of the UTS, respectively. The stress and strain were directly proportional to each other in the linear zone. After this zone, the stress-strain curve became nonlinear. Nonlinearity indicates a continuous decline in the slope (or, instantaneous modulus). The increase in strain was much greater than the increase in stress. Thus, the inflection point where the stress-strain curve became nonlinear could be used to predict the range of fatigue strength at the endurance limit (infinite cycles). These predictions were not valid in the fatigue experiments in this research.

Researchers have used the kinks in stress-strain diagrams to predict fatigue strength at 1 million cycles. The basis for these predictions was the stress and strain. From the CV values in tables

3-2 and 3-4, it is clear that failure strain and UTS measurements have less repeatability and reproducibility (at least for carbon/vinyl ester composites), while the modulus provides the highest. Therefore, the more reliable models in the prediction of fatigue strength are the stiffness degradation (or modulus reduction) models. These models are explained in detail in section 4.

3.6 OTHER OBSERVATIONS.

This section elaborates the observations related to failure patterns of braided composites under tension-tension fatigue loading, viscoelastic behavior, and effect of frequency and temperature on fatigue life.

3.6.1 Failure Pattern.

Irrespective of the resin system and the braid angle, braided composites did not exhibit any noticeable matrix cracks either at the surface or at the edges until 90% of the fatigue life, when tested at 10-Hz frequency. Failure occurred very quickly in the last 10% of the fatigue life. Figures 3-17 and 3-18 show the failure patterns of braided composites in static and fatigue loadings for both the carbon/vinyl ester and the carbon/epoxy resin system. The failure in tensile loading was fiber dominated and as the applied fatigue load increased the fatigue failure resembled the tensile failure.

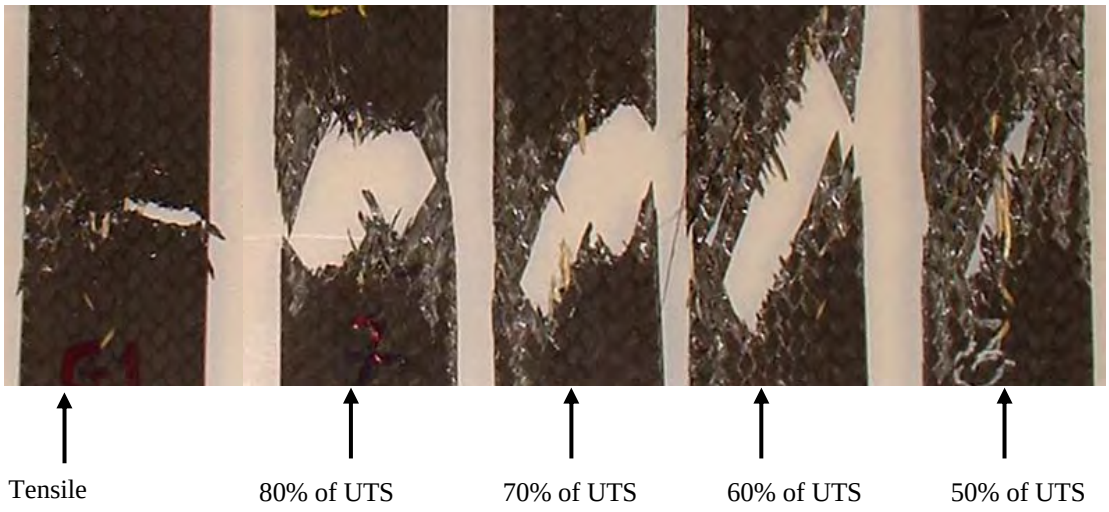

Figure 3-17. Failure Patterns of Static Tensile- and Fatigue-Loaded Carbon/Vinyl Ester Specimens (Braid Angle 25° ±2°)

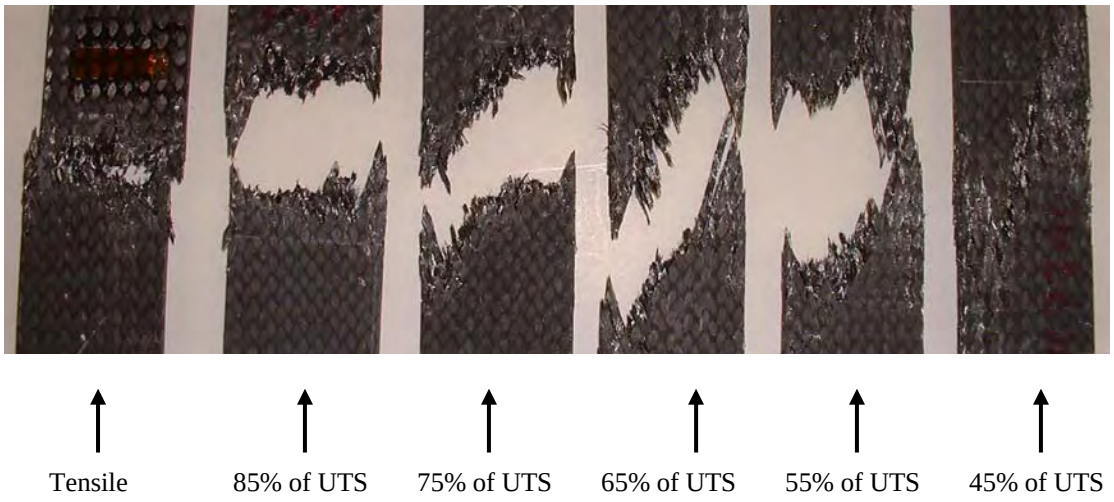

Figure 3-18. Failure Patterns of Static Tensile- and Fatigue-Loaded Carbon/Epoxy Specimens (Braid Angle 30° ±1°)

3.6.2 Viscoelastic Behavior of Braided Composites.

All materials deviate from Hooke's law of linear elasticity, (e.g., by exhibiting viscous-like as well as elastic characteristics). Viscoelastic materials are materials whose stress and strain depend on time. Some phenomena in viscoelastic materials are (Lakes, 1998):

- If the stress is held constant, the strain increases with time (creep).
- If the strain is held constant, the stress decreases with time (stress relaxation).
- The effective stiffness depends on the rate of application of the load.
- If cyclic loading is applied, hysteresis (a phase lag) occurs, leading to a dissipation of mechanical energy.
- Acoustic waves experience attenuation.
- Rebound of an object after an impact is less than 100%.
- Frictional resistance occurs during rolling.

The focus of this research was not directed toward the study of the viscoelastic behavior of braided composites. Limited tests were conducted on carbon/epoxy braided composites (braid angle 30° ±1°) to study the creep, stress relaxation, and frequency effect on fatigue life and the stiffness degradation of braided composites.

Figure 3-19 displays the creep of a carbon/epoxy braided composite (braid angle 30° ±1°). When a load of 2 kips was held constant, strain increased with time. It should be noted that there was only a 0.91% increase in the strain in 1020 seconds (17 minutes), which was not very significant. Figure 3-20 shows the stress relaxation of a carbon/epoxy braided composite (braid

angle 30° ±1º). When a displacement of 0.0338 in. was held constant, the load began to drop. The load dropped by 4.4% in 1110 seconds (18 minutes). Figure 3-21 shows the stiffness degradation of a carbon/epoxy braided composite (braid angle 30° ±1º) at two different frequencies, 5 and 10 Hz, at an applied stress of 60% of the UTS. The stiffness at 10 Hz declined from 4.62 Msi to 4.11 Msi (i.e., an 11% decrease), whereas at 5 Hz, stiffness declined from 4.89 Msi to 1.09 Msi (i.e., a 77% decrease). These declines occurred in the same amount of time, 138 seconds. Thus, the rate of loading (frequency) had a dominating effect on the damage rate. Figure 3-22 shows stress-strain curves for the 1st, 10th, 20th, and 30th cycles for carbon/epoxy braided composites (braid angle 25° ±2°) at a fatigue load of 50% of the UTS. There was no significant hystersis loss at this low stress level and in the early fatigue life. Figure 3-23 shows stress and strain versus time during a phase shift. As discussed earlier, viscoelastic materials such as carbon/epoxy braided composites exhibit hysteresis loss (a phase lag), which leads to a dissipation of mechanical energy in the form of heat. This fact was confirmed by measuring the surface temperature of the specimens at different frequencies.

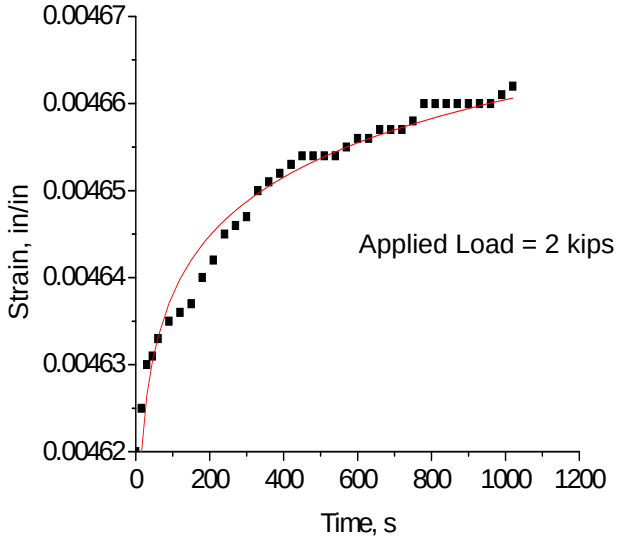

Figure 3-19. Creep of Carbon/Epoxy Braided Composite (Braid Angle 30° ±1°)

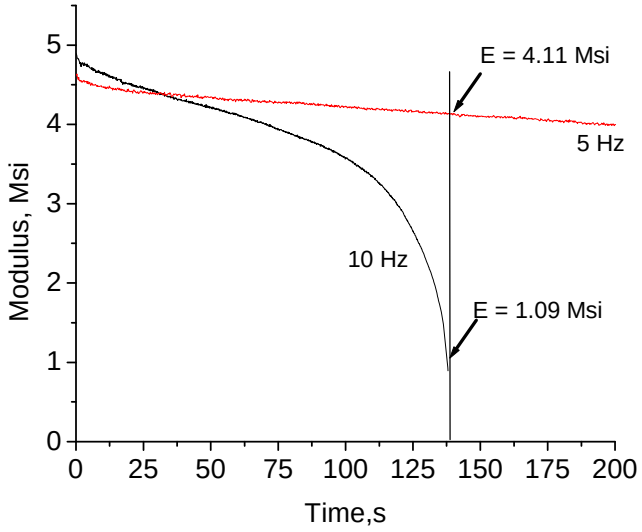

Figure 3-20. Stress Relaxation of Carbon/Epoxy Braided Composite (Braid Angle 30° ±1°)

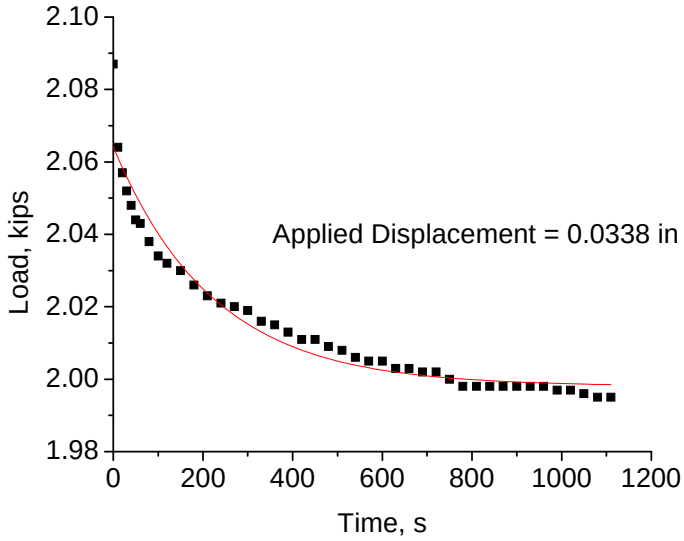

Figure 3-21. Stiffness Degradation of Carbon/Epoxy Braided Composites (Braid Angle 30° ±1°) at Different Frequencies (Applied Stress 60% of UTS)

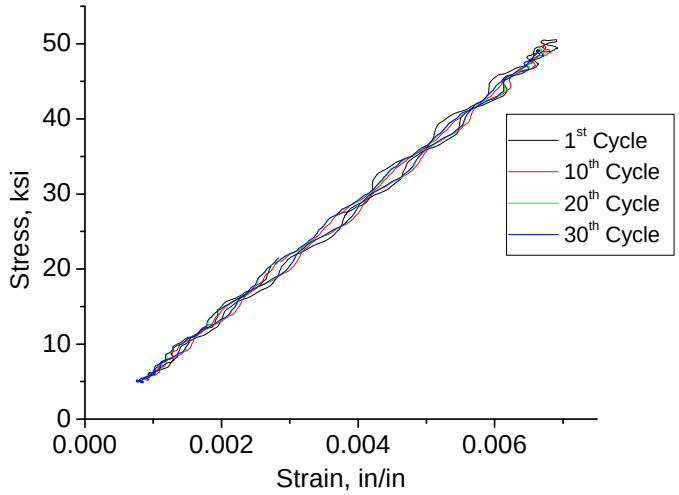

Figure 3-22. Hystersis Loops of Carbon/Epoxy Braided Composites (Braid Angle 25° ±2°) (Applied Stress 50% of UTS, 10-Hz Frequency, and R = 0.1)

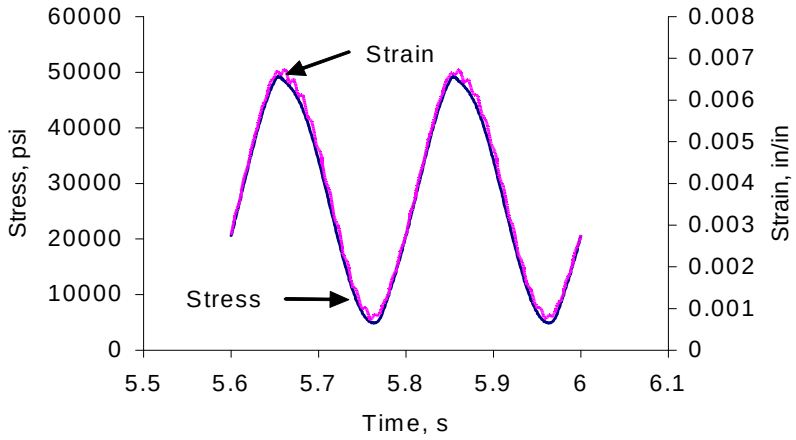

Figure 3-23. Stress and Strain vs Time With a Phase Shift Carbon/Epoxy Braided Composites (Braid Angle 30° ±1°) (Applied Stress 50% of UTS, 29th Cycle)

3.6.3 Frequency and Temperature Effect.

As discussed in detail in the literature review, frequency has a dominant effect on the fatigue life of polymer matrix composites. A limited number of tests were conducted to understand the effects of frequency. Tables 3-15 and 3-16 present the test results.

Table 3-15. Effect of Frequency on Fatigue Life of Carbon/Epoxy Braided Composites at Braid Angle 30° ±1° and Fatigue Load of 60% of UTS

Frequency (Hz)	Room Temperature (ºF)	Maximum Temperature on the Surface (ºF)	Maximum Temperature Rise (ºF)	Fatigue Life (cycles)
2	76	88.6	12.6	19,980
5	77.4	96.2	18.8	2,439
10	76	100.2	24.2	1,535

Table 3-16. Effect of Frequency on Fatigue Life of Carbon/Epoxy Braided Composites at Braid Angle 45° ±1° and Fatigue Load of 60% of UTS

Frequency (Hz)	Room Temperature (ºF)	Maximum Temperature on the Surface (ºF)	Maximum Temperature Rise (ºF)	Fatigue Life (cycles)
2	77	86	9	110,406
5	77	88.4	11.4	124,736
10	74.7	96	21.3	8,236

At 5 and 10 Hz, there was no noticeable damage, such as matrix cracking and delamination at the edges. But at 2 Hz, a small amount of matrix cracking and delamination was observed at the edges. The surface temperature of each braided composite specimen reached a maximum at all frequencies and then remained almost constant during the remainder of the test.

The effect of frequency on laminates is dependent on the lay-up. This was also true for braided composites. When the braid angles were 30º and 45º, the composite was matrix-dominated. For 30º braided composites, fatigue life was sensitive from 2 to 5 Hz, and was almost the same at 5 and 10 Hz. For 45º braided composites, fatigue life was almost the same at 2 and 5 Hz and was sensitive from 5 to 10 Hz. However, the fatigue life of 30º and 45º braided composites at 10-Hz frequency declined by almost 1/14 compared to fatigue life at 2 Hz.

As frequency increased, internal friction between tows increased, and generated heat caused a rise in temperature. There was almost a 24ºF (13.4ºC) temperature increase at 10 Hz, as shown in figure 3-24. The reduction in fatigue life could also have been due to an internal friction between tows and a rise in temperature from the internal friction. The maximum temperature at 10 Hz was 100.2ºF (38ºC) when a test was performed at 77ºF (25ºC). Therefore, a test was conducted at an elevated temperature of 101.5ºF (39ºC) at 5-Hz frequency for the 45º braided composite (matrix dominated lay-up) to determine the effect of temperature alone. Fatigue life was not reduced and doubled (214,839 cycles) in comparison to a similar test performed at 77ºF when the specimen survived 124,736 cycles.

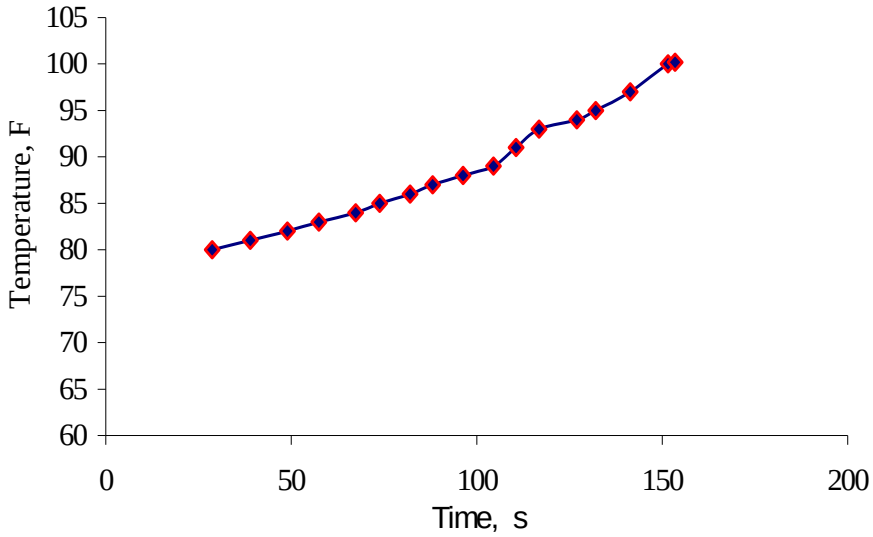

Figure 3-24. Rise in Temperature of Carbon/Epoxy Braided Composites (Braid Angle 30° ±1°) at 10-Hz Frequency Until Failure at Fatigue Load of 60% of UTS

More study is needed for a more reliable understanding of the frequency and temperature effects. The following observations about braided composites were made based on the limited numbers of tests.

- The creep, stress relaxation, hystersis (a phase lag), and frequency effect on stiffness degradation and fatigue life demonstrated that carbon/epoxy braided composites exhibit viscoelasticity.

- Internal friction generated heat within the specimen. This heat would not dissipate quickly to surrounding areas and created a temperature gradient. This temperature gradient was responsible for the reduction in fatigue life.

- The higher temperature of surrounding areas had no effect on fatigue life. In fact, it eliminated the temperature gradient and could have improved fatigue life.

- Figure 3-25 shows that the stiffness degradation mechanisms at 5- and 10-Hz frequencies were unchanged (Normalized E_n/E_1 and n/N). This is important in the issue of accelerated fatigue.

- The size of the tow in this study was 12 K (12,000 fibers/tow). The amount of heat generation from internal friction could be dependent on tow size.

- The tubular structure of braided composites has fiber continuity from end to end of the part. Flat specimens of braided composites were used in this study. It is essential to test the tubular specimens for fatigue before drawing any final conclusions about the fatigue life of braided composites.

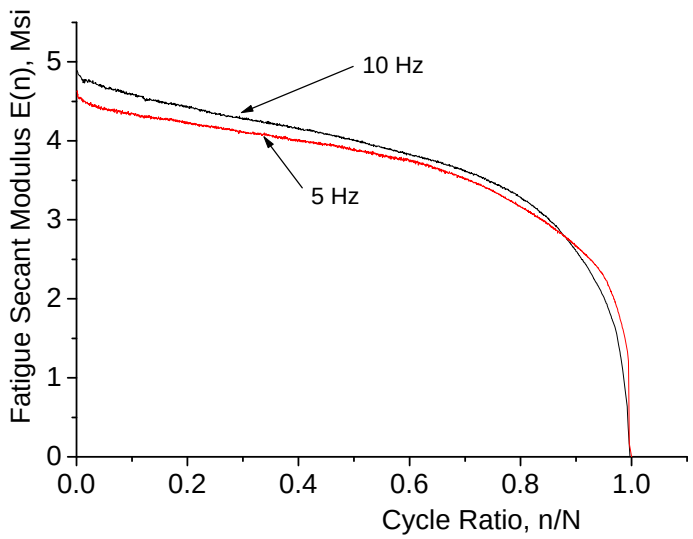

Figure 3-25. Stiffness Degradation of Braided Composites (Braid Angle 30° ±1°) at Different Frequencies at Fatigue Load of 60% of UTS

The VARTM process is prone to thickness variation. The change in thickness causes a change in fiber volume fraction. The change in fiber volume fraction changes the UTS of the specimen, and the change in UTS from specimen to specimen causes large scatter in the fatigue data. In the case of braided composites, the braid angle variation within a specimen causes a dramatic variation in the UTS. Thus, the fiber volume fraction and the braid angle are the two most important parameters to be monitored in the case of braided composites. A specific monitoring method for these parameters was developed and is explained in appendix B.

Stiffness degradation is always related to the damage in composites. Stiffness degradation curves can be effectively used to predict fatigue life, modulus at a particular cycle, and endurance limits. The next section discusses the efforts related to stiffness degradation modeling.

4. STIFFNESS DEGRADATION MODELING.

4.1 IMPORTANCE OF STIFFNESS DEGRADATION STUDY.

Aircraft components are subjected to a variety of loads termed environmental stress factors. The most important factors contributing to the reduction of component lifetime are mechanical loads (static and fatigue), moisture (hygrothermal effects), and temperature. Other factors include oxygen, ultraviolet radiation, and ozone. The net effects of these factors are physical aging, chemical aging, and damage (Gates, 2002).

The fatigue damage mechanism of composites is highly complex and may be in one or more forms such as fiber/debonding, matrix cracking, delaminations, and fiber breakage. Some of these damage mechanisms may interact simultaneously. Damage during fatigue is reflected in strength, stiffness, and fatigue life reduction. Different damage mechanisms, such as matrix cracking and delamination, reduce stored energy, which in turn reduces stiffness. There is always a correlation between damage and stiffness reduction. Thus, stiffness reduction is the only parameter that can be monitored to evaluate the useful life of a component. Stiffness reduction is often referred to as stiffness degradation or modulus reduction in the literature. All of these terms are used interchangeably in this research.

The evaluation of residual strength and fatigue life involves destructive testing, whereas stiffness can be measured using nondestructive techniques such as ultrasound. It is well-known that the wave speed of sound in a material is related to its stiffness. The presence of defects (e.g., voids, cracks, micro damages, etc.) changes the effective stiffness of a material. When a wave is propagated through a material, the change in stiffness is manifested as a change in the sound velocity. Furthermore, the defects act as wave scatterers. As a result, the defect population also manifests itself in an attenuation of the wave that passes through the material. Many researchers have used the changes in wave speed and attenuation due to damage as a nondestructive tool for stiffness measurement.

In the aircraft industry, many components are designed in such a way that the maximum strain does not exceed 3000 με (i.e., 0.3%). The typical life of the primary components of an aircraft (e.g., skins, wings, and fuselage) is 60,000 flying hours. The components experience 100,000 load cycles during their lifetime (Gates, 2002). Accelerated fatigue tests are conducted in the laboratory. These accelerated tests deliberately shorten the life of a specimen or accelerate degradation mechanisms (e.g., fatigue, creep, wear, etc.). Degradation is usually achieved by performing constant-amplitude fatigue tests at higher frequencies. However, frequency is limited to 10 Hz for polymer matrix composites because of their viscoelasticity.

4.2 REPRESENTATION OF TENSILE MODULUS AND STIFFNESS DEGRADATION CURVES.

There are different ways to define modulus in the literature, as shown in figure 4-1. E_O is the initial tangent modulus and is usually calculated according to ASTM D 3039. This is a very convenient way to define modulus if the stress-strain response is linear as in the case of the fiber-dominated lay-ups of laminates. As laminates become matrix-dominated, the stress-strain

response becomes nonlinear. In these materials, E_S is defined as a static secant modulus, which is the UTS divided by the corresponding strain

$$E_S = \frac{S_u}{\varepsilon_u}$$

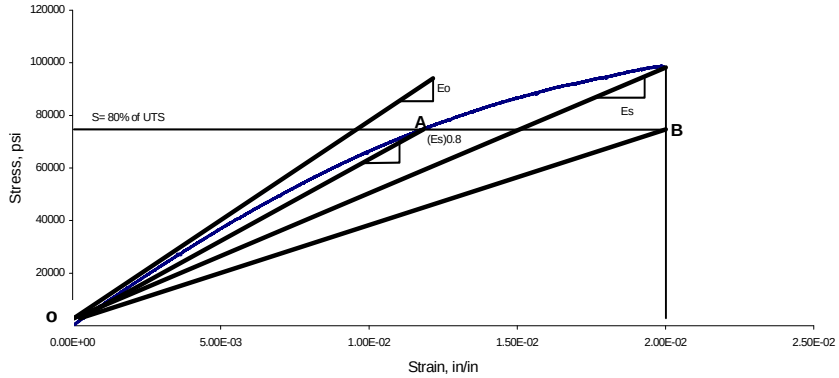

Figure 4-1. Representation of Tensile Modulus

In fatigue studies, a specimen is subjected to applied maximum stress (*S*) and is cycled for a set number of cycles (viz., 1000) before the fatigue test is completed. The specimen is then tested for tension. The load is applied until the stress reaches the applied fatigue stress (*S*) and the initial tangent modulus is then calculated (E_n). The specimen is cycled again for the next set of cycles and the procedure is repeated. Ten readings are typically taken at each applied stress (S). This is a very laborious method of evaluating modulus.

Fatigue secant modulus is a much more convenient way to define modulus. The axial strain is measured continuously during the fatigue test using an extensometer or a strain gage. The fatigue secant modulus $E(n)$ is defined at each cycle as applied fatigue stress (*S*) divided by the corresponding strain at the n^{th} cycle. Thus, $E(N)$ is fatigue secant modulus at failure cycle (N).

$$E(N) = \frac{S}{\varepsilon_{\text{fatigue}}}$$

A different concept of static secant modulus is introduced in this study. The secant modulus is defined at a particular stress level (e.g., 80% of S_u). Thus, $E_{S(0.8)}$ is 0.8 times S_u divided by the corresponding strain on the tensile stress-strain diagram.

$$(E_S)_{0.8} = \frac{(0.8 * S_u)}{(\varepsilon)_{\text{at } 0.8 * Su}}$$

This static secant modulus can be represented as the slope of line OA in figure 4-1. The static secant modulus is denoted as $(E_S)_{\frac{S}{Su}}$ in the present discussion. Typically, stiffness degradation

curves are presented as normalized curves. The numbers of fatigue cycles (n) are normalized with the number of failure cycles (N). Thus, the x axis is always represented as n/N. However, there are two ways to normalize the modulus. If the fatigue modulus is calculated by stopping the test after n cycles (i.e., E_n), E_n is normalized with an initial tangent modulus in the static tensile test (E_O). Thus, the y axis is represented as E_n/E_O. The fatigue secant modulus cannot be normalized with E_O. This is because the fatigue secant modulus at the first cycle $E(1)$ may be larger or smaller than E_O for nonlinear materials. It should be noted that for nonlinear materials, $E(1)$ usually differs depending on the applied stress (S). As applied stress (S) increases, $E(1)$ decreases. Therefore, the fatigue secant modulus $E(n)$ is normalized with the fatigue secant modulus at the first cycle, $E(1)$. Thus, the y axis is $E(n)/E(1)$. The following section explains how stiffness degradation curves can be used to predict the endurance limit (fatigue stress at 1 million cycles).

4.3 STIFFNESS DEGRADATION CURVES AS A TOOL TO PREDICT THE ENDURANCE LIMIT.

Figure 4-2 displays the stiffness degradation curve for the entire life at of carbon/vinyl ester braided composites (braid angle 25° ±2°) at an applied stress of 75% of the UTS. The number of cycles (n) were normalized with the number of cycles at failure (N), and the fatigue secant modulus $E(n)$ was normalized with the fatigue secant modulus at the first cycle $E(1)$. Thus, the x axis was n/N and the y axis was $E(n)/E(1)$. This curve exhibited a rapid reduction in the modulus in the first few cycles (Stage I). Later, there was a gradual, almost linear, modulus decay (Stage II), and the modulus decreased rapidly (Stage III) until the specimen failed (Kelkar and Tate, 2003c). This behavior for braided composites was different than that for woven composites, as shown in figure 1-11. In the case of woven composites, the maximum decrease in fatigue secant modulus until failure was 25% of the fatigue secant modulus at the first cycle. In braided composites, the decrease in modulus until failure could have been as high as 60% of the modulus in the first cycle.

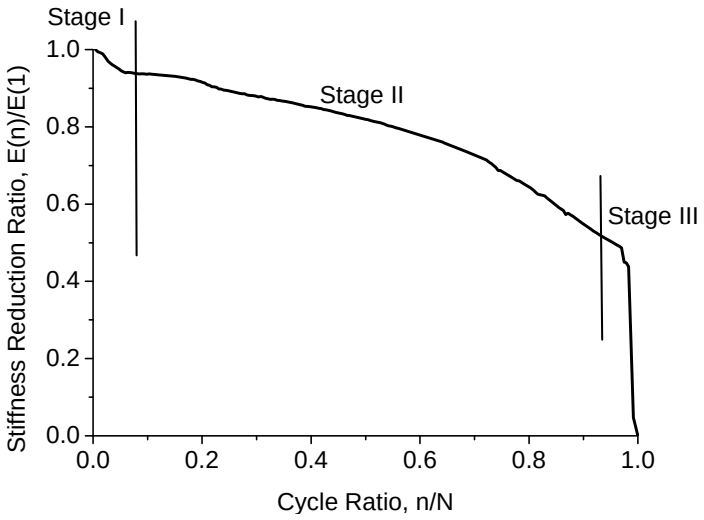

Figure 4-2. Stiffness Degradation Over Entire Fatigue Life for Carbon/Epoxy Braided Composites at 75% of UTS (Braid Angle 25° ±2°)

After careful observation of the stiffness degradation curve, it was determined that Stage I lasted only about 5% of the fatigue life. Thus, it was possible to predict the endurance limit by conducting fatigue tests for only approximately 5% of the fatigue life. For this study, constant-amplitude fatigue tests according to ASTM D 3479 were performed at a frequency of 1 Hz, with an R ratio of 0.1 and applied stress (S) ranging from 45% to 85% of the ultimate tensile strength. The material system used was carbon/vinyl ester (braid angle 25° ±2°). The load and strain data were collected for every cycle for the first 400 cycles.

The fatigue secant modulus $E(n)$ was calculated at every cycle. $E(n)$ was then normalized with $E(1)$. The curves representing normalized stiffness reduction $E(n)/E(1)$ versus the number of cycles (n) are presented in figure 4-3. The smoothened stiffness degradation curves are displayed in figure 4-4. All of the stiffness degradation curves indicate that the initial portion of the curve was linear. The linear segments of the stiffness degradation curves are presented in figure 4-5. The slope of each curve was computed. Figure 4-6 is a representation of the absolute values of the slopes versus the applied stress as a percentage of the UTS. The applied stress, where the slope of an initial region approached zero, represented the endurance limit of the material. From the graph in figure 4-6, it is evident that the endurance limit for the material system was 40% of the UTS, which is the same value obtained in the S-N studies (table 3-3). Thus, stiffness degradation studies in Stage I can be used to predict the endurance limit of a material.

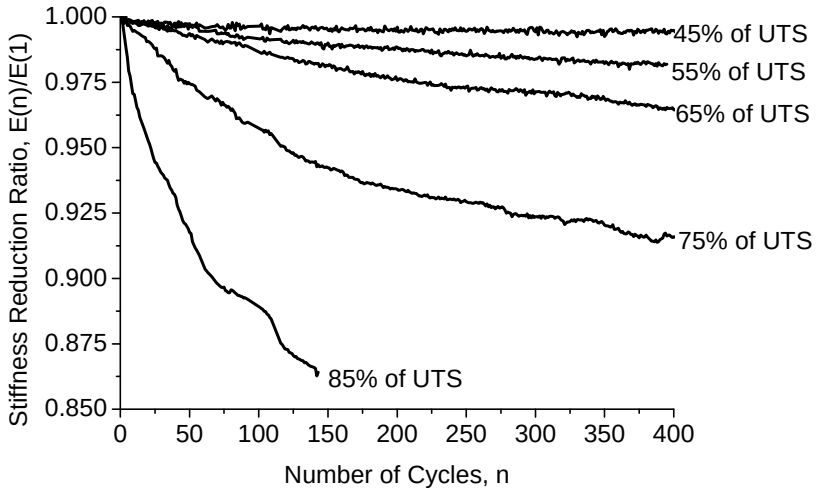

Figure 4-3. Stiffness Degradation Curves for First 400 Cycles

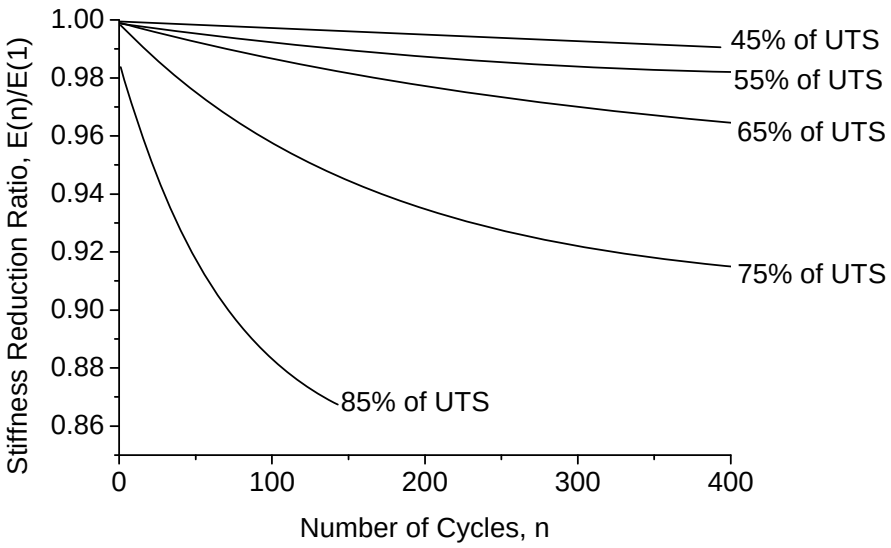

Figure 4-4. Smoothened Stiffness Degradation Curves for First 400 Cycles

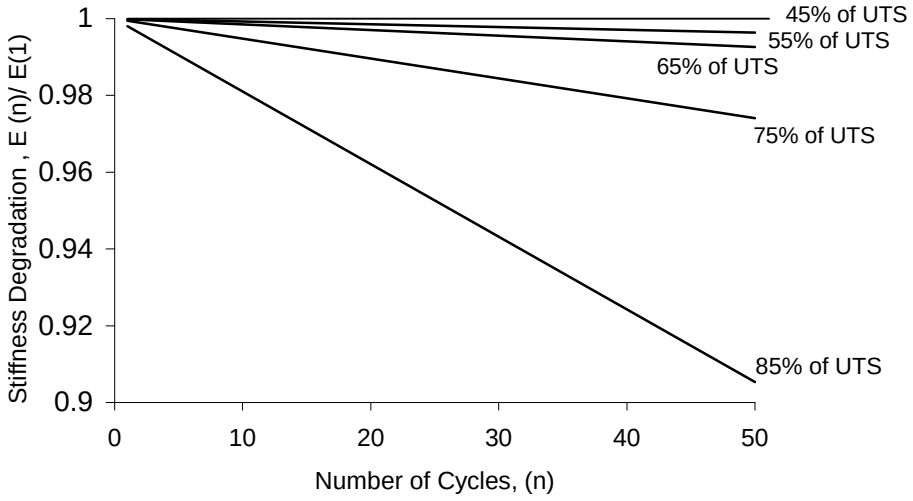

Figure 4-5. Linear Representation of First 50 Cycles of Stiffness Degradation Curves

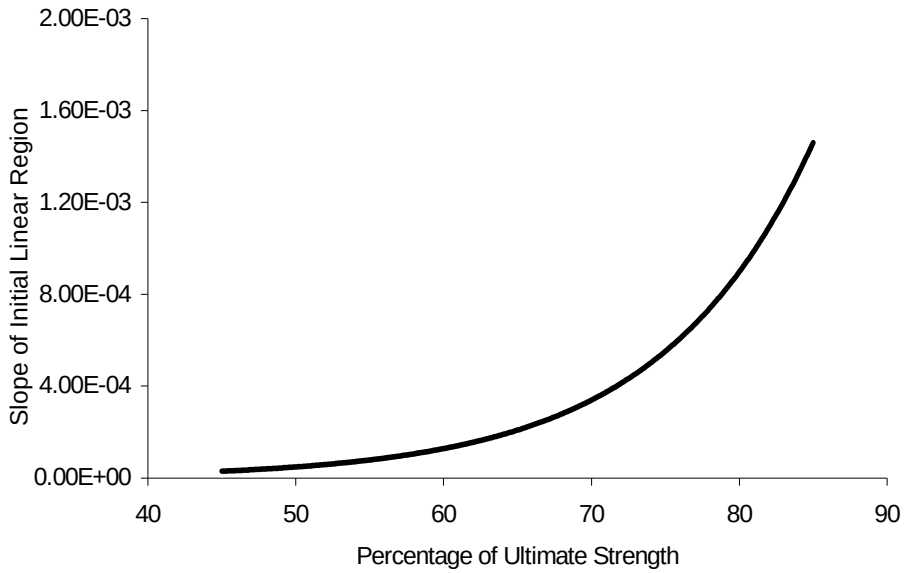

Figure 4-6. Slope of Initial Region of Stiffness Degradation Curve vs Applied Stress as Percentage of Ultimate Tensile Strength

4.4 STIFFNESS DEGRADATION MODEL TO PREDICT RESIDUAL STIFFNESS.

There are many models available to predict the residual stiffness in a fatigue study. The typical strategy is represented in the flow chart shown in figure 4-7. This is a stiffness degradation model developed by Whitworth (1998) for carbon/epoxy angle-ply $[\pm 35]_{2s}$ composite laminates subjected to tension-tension fatigue (R = 0.1) at a frequency of 10 Hz. The model is discussed here due to its similarity for braided composites and angle-ply laminates. In short, the fatigue secant modulus $E(n)$ is represented as a function of the number of fatigue cycles n and the fraction of the applied stress $\frac{S}{S_u}$. An appropriate failure criterion is then used to define unknown parameters in the equation of $E(n)$. For example, a failure criterion for linear materials is often defined as follows: "…failure occurs when the fatigue strain in the fatigue test reaches to ultimate strain at UTS in the static tensile test." (O'Brian and Reifsnider, 1981)

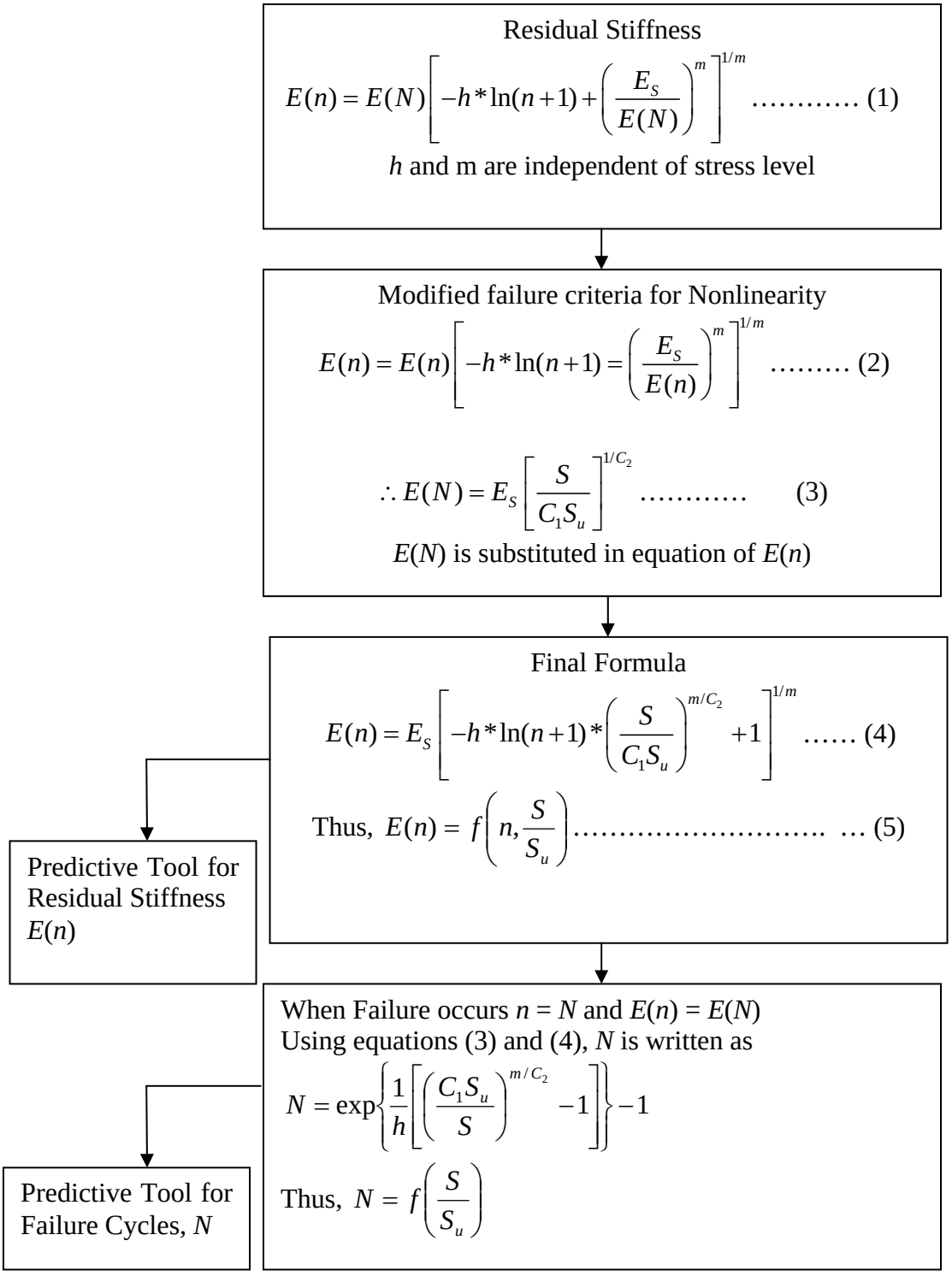

Figure 4-7. Flow Chart Representing General Strategy for Stiffness Degradation Modeling (Whitworth, 1998)

Thus, failure occurs when the fatigue secant modulus $E(N)$ reaches a value represented by the slope of line OB in figure 4-1. The value of $E(N)$ is calculated by using an appropriate criterion and substituting it back into the general equation of $E(n)$ to compute the failure cycle, N.

The general equation of the model developed by Whitworth (1998) is

$$E(n) = E(N)\left[-h * \ln(n+1) + \left(\frac{E_S}{E(N)}\right)^m\right]^{1/m}$$

The failure criterion for linear materials was modified to consider the effect of nonlinearity as

$$\frac{S}{S_u} = c_1\left(\frac{E(N)}{E_S}\right)^{C2}$$

$E(N)$ was calculated from this failure criterion and substituted into the general equation of $E(n)$ as

$$E(n) = E_s\left[-h * \ln(n+1) * \left(\frac{S}{C_1 S_u}\right)^{m/C_2} + 1\right]^{1/m}$$

Failure occurred when $E(n) = E(N)$. Thus, the number of cycles at failure, N could be computed as

$$N = \exp\left\{\frac{1}{h}\left[\left(\frac{C_1 S_u}{S}\right)^{m/C_2} - 1\right]\right\} - 1$$

This model and many other models do not use valuable information available from the S-N diagram and the nonlinear stress-strain curves obtained from static tensile tests. A different approach to stiffness degradation modeling was planned and is discussed below.

- First, the number of cycles at failure can be predicted accurately from a properly modeled S-N diagram. The S-N diagram has a natural failure criterion, which can be stated as, "failure occurs when the applied stress (S) reaches to the residual strength of the specimen." The best model of the S-N diagram for braided composites is the Sigmoidal (Boltzmann) curve. It was decided that the number of failure cycles N would be computed from the S-N diagram model and used in the stiffness degradation model.

- Second, the failure strain criteria used in different models relate fatigue strains at failure cycles with either E_S or E_O. However, E_S or E_O may not accurately represent nonlinearity in a stress-strain curve, and therefore, the static secant modulus at each stress level was defined and denoted as $(E_S)_{\frac{S}{Su}}$ as discussed earlier. Thus, nonlinearity could be captured

based on the stress level. There is a definite relationship between strain on the stress-strain curve at a stress level S and fatigue strain at failure cycle at the same stress level. The stress-strain curve for carbon/epoxy braided composites is nonlinear in nature. It was determined that fatigue strain at the failure cycle $(\varepsilon_{fatigue})_N$ followed a nonlinear relationship with respect to the applied stress. Thus, there was a simple linear relationship between the fatigue secant modulus $E(N)$ and $(E_S)_{\frac{S}{Su}}$. This linear relationship could be used as the failure criteria. The relationship could be easily modified to consider the effects of frequency and temperature.

- Finally, a stiffness degradation model was developed based upon failure cycle N from the S-N diagram and the fatigue secant modulus at the failure $E(N)$ of the failure criterion.

Constant-amplitude fatigue tests according to ASTM D 3479 were performed at a frequency of 10 Hz, with an R ratio of 0.1 on carbon/epoxy braided composites (braid angle 25° ±2º). The applied stress (S) levels were 80%, 70%, 60%, 50%, and 45% of UTS. The load and strain data were collected for every cycle for the entire fatigue life. The fatigue secant modulus was calculated at every cycle. Figure 4-8 displays stiffness degradation curves represented as the fatigue secant modulus $E(n)$ versus the number of cycles (n). It should be noted that the fatigue secant modulus at the 1st cycle and the N^{th} cycle decreased with an increase in the stress level. Figure 4-9 shows the normalized fatigue secant modulus $E(n)/E(N)$ versus the cycle ratio (n/N). Table 4-1 lists the values of $E(1)$ and $E(N)$ for carbon/epoxy braided composites (braid angle 25 ±2º). It should be noted that the rate of modulus decay that can be represented by the slope of the stiffness degradation curve is undefined at $\frac{n}{N} = 0$ and $\frac{n}{N} = 1$.

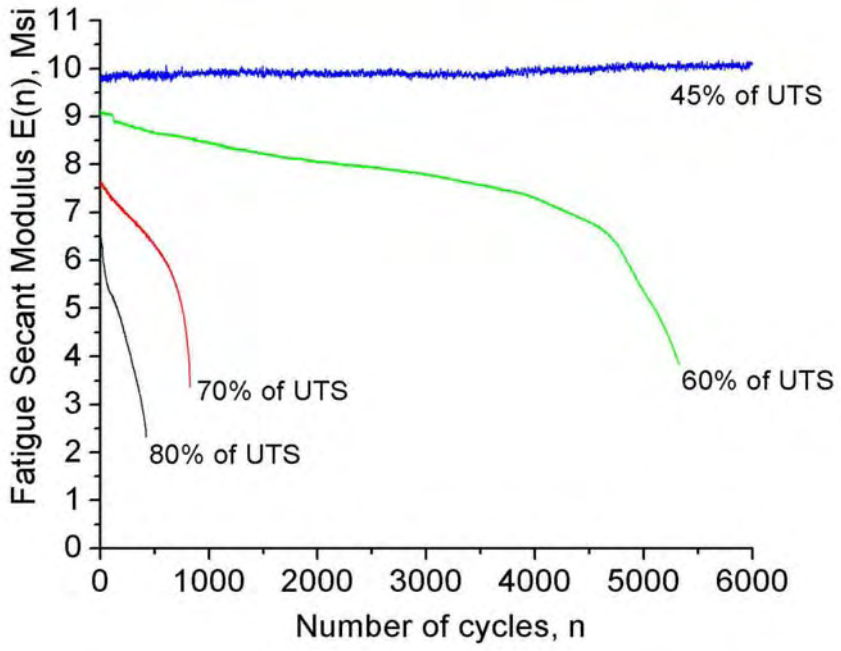

Figure 4-8. Fatigue Secant Modulus, $E(n)$ vs Number of Cycles, n

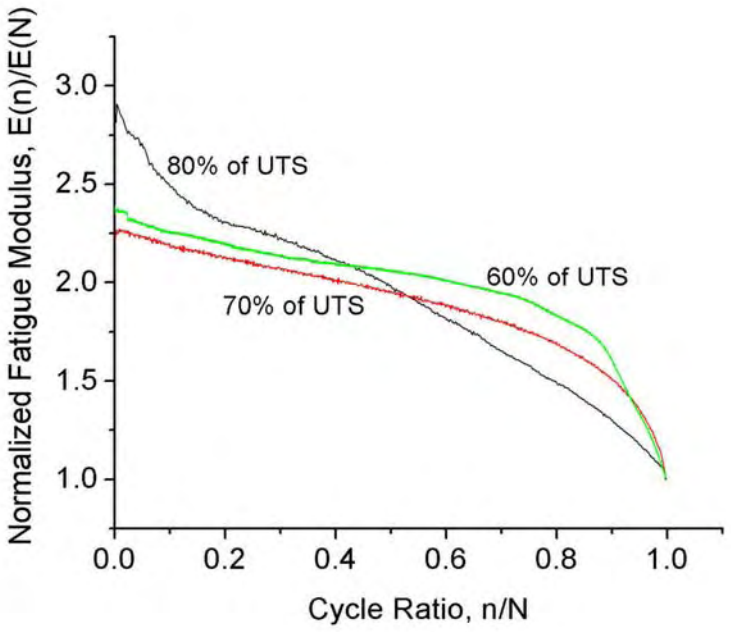

Figure 4-9. Normalized Fatigue Modulus $E(n)/E(N)$ vs Cycle Ratio (n/N)

Table 4-1. Fatigue Secant Modulus at 1st and N^{th} Cycle for Carbon/Epoxy Braided Composites (S_u = 95.74 ksi, E_o = 7.870 Msi, E_s = 5.409 Msi, and Braid Angle 25° ±2°)

Applied Stress as % of UTS	Failure Cycles N	$E(1)$		$E(N)$	
		Msi	GPa	Msi	GPa
45	935359	9.783	67.44	4.582	31.59
60	5325	9.140	63.01	3.831	26.41
70	824	7.470	51.50	3.366	23.21
80	424	6.541	45.10	2.325	16.03

Therefore, the rate of stiffness reduction was assumed to have the following relationship:

$$\frac{d(E^*)}{d(n^*)} = \frac{-a}{n^*.\ln(n^*)}$$

where

$$E^* = \frac{E(n)}{E(N)} \text{ and, } n^* = \frac{n}{N}$$

Integrating the above equation

$$E(n) = E(N) * \left\{-a * [\ln < \ln(n^*) >]\right\} + c \ \ldots\ldots\ldots\ldots\ldots\ldots \quad 0 < n^* < 1$$

and modifying the equation

$$E(n) = E(N) * \left\{ a * [\ln < -b * \ln(n^*) >] \right\} + c \quad \ldots\ldots\ldots\ldots\ldots\ldots \quad 0 < n^* < 1$$

This is a general equation for $E(n)$, and it is applicable for n^* values between 0 and 1. The purpose of this model was to track residual fatigue secant modulus $E(n)$. There was no need to compute $E(N)$ because it was already known from the failure criterion. However, this model could predict $E(n)$ at failure if $n^* = \dfrac{(N-1)}{N}$ was substituted into the equation.

In the above equation, the fatigue secant modulus at failure $E(N)$ was unknown. It could be found by using a suitable failure criterion. As discussed earlier, the secant modulus can be defined at a particular stress level as $(E_S)_{\frac{S}{Su}}$ and can be related to the fatigue secant modulus at failure, $E(N)$. Table 4-2 lists the values of the stress level and the corresponding strain values in the static tension test and the fatigue test. Figure 4-10 displays the linear relationship between $(E_S)_{\frac{S}{Su}}$ and $E(N)$. This linear relationship was used as the failure criteria and can be written as

$$E(N) = A * (E_S)_{\frac{S}{Su}} + B$$

Table 4-2. Static and Fatigue Secant Modulus for Carbon/Epoxy Braided Composites
(S_u = 95.74 ksi, E_o = 7.870 Msi, E_S = 5.409 Msi, and Braid Angle 25° ±2°)

Applied Stress as % of UTS	Static Tensile Strain at Stress Level $(\varepsilon_s)_{\frac{S}{Su}}$	Strain in Fatigue at Failure ε_f	Secant Modulus at Stress Level $(E_S)_{\frac{S}{Su}}$		Fatigue Secant Modulus at Failure $E(N)$	
			Msi	GPa	Msi	GPa
45	0.005963	0.009402	7.225	49.81	4.582	31.59
60	0.008342	0.014995	6.886	47.47	3.831	26.41
70	0.010131	0.01991	6.615	45.60	3.366	23.21
80	0.012248	0.032943	6.253	43.11	2.325	16.03

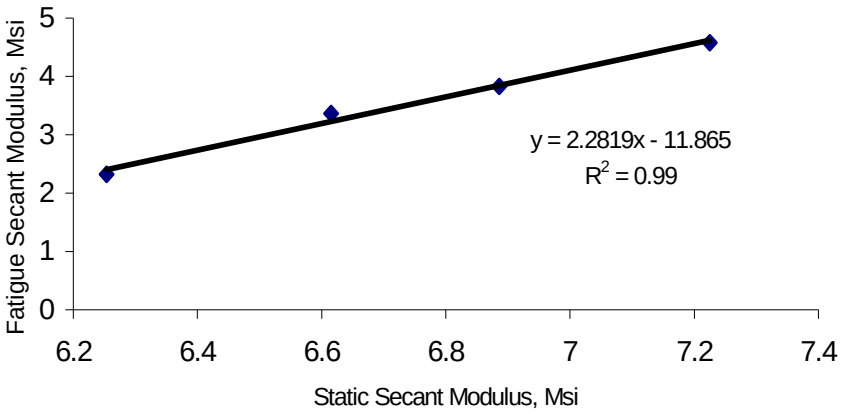

Figure 4-10. Linear Relationship Between Static and Fatigue Secant Modulus

For carbon/epoxy braided composites (braid angle 25° ±2°) under stated fatigue test parameters (10-Hz frequency, R ratio 0.1), the values of *A* and *B* were evaluated as 2.2819 and -11.865, respectively. The parameters a, b, and c from the equation were evaluated by using nonlinear regression analysis on the data from all the tests. These values were 0.2532, 0.06452, and 2.8228, respectively.

Figure 4-11 displays a comparison between the experimental and the theoretical curves of the residual fatigue secant modulus at a stress level of 70% of the UTS. At this stress level, the predicted fatigue life from the Sigmoidal model of the S-N diagram was 894 cycles, and the fatigue secant modulus *E*(*N*) from the failure criteria was 3.229 Msi (22.26 GPa). Thus, there was a very good agreement between the theoretical and the experimental stiffness degradation curves.

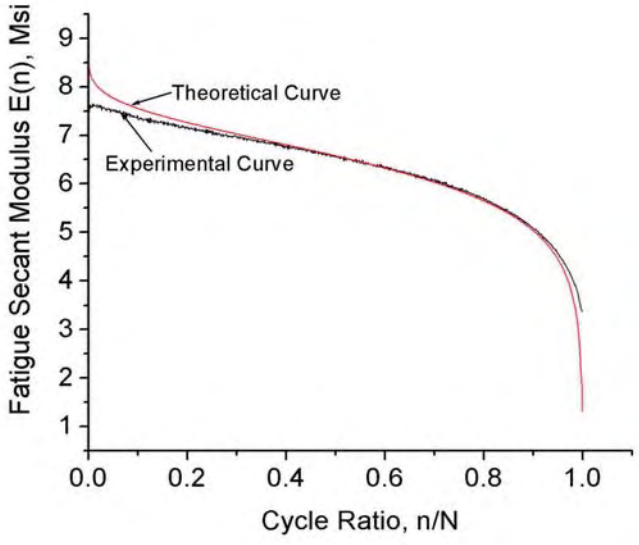

Figure 4-11. Comparison Between Experimental and Theoretical Stiffness Degradation Curves (Carbon/Epoxy Braided Composite, Braid Angle = 25° ±2°, Applied Stress = 70% of UTS)

If the stress level $\left(\frac{S}{S_u}\right)$ and the number of cycles (n) are known, then the residual fatigue secant modulus $E(n)$ can be very accurately predicted. The main advantage of the model is that it represents all three stages of a stiffness degradation curve. The parameters a, b, and c in the equations depend mainly on the stress level and the frequency. However, because of the limited availability of data, parameters a, b, and c were assumed to be independent of the stress level and the frequency. The model could be modified with more data.

Once the residual fatigue secant modulus is calculated, it can be compared with the modulus measured by nondestructive techniques. Thus, if measured stiffness is less than predicted stiffness, there is more damage than expected, or the component has experienced overload. In this case, the residual fatigue life would be less than (N-n). This stiffness degradation model could be used as a tool for tracking the residual modulus. Figure 4-12 explains the procedure for tracking the fatigue secant modulus with this model.

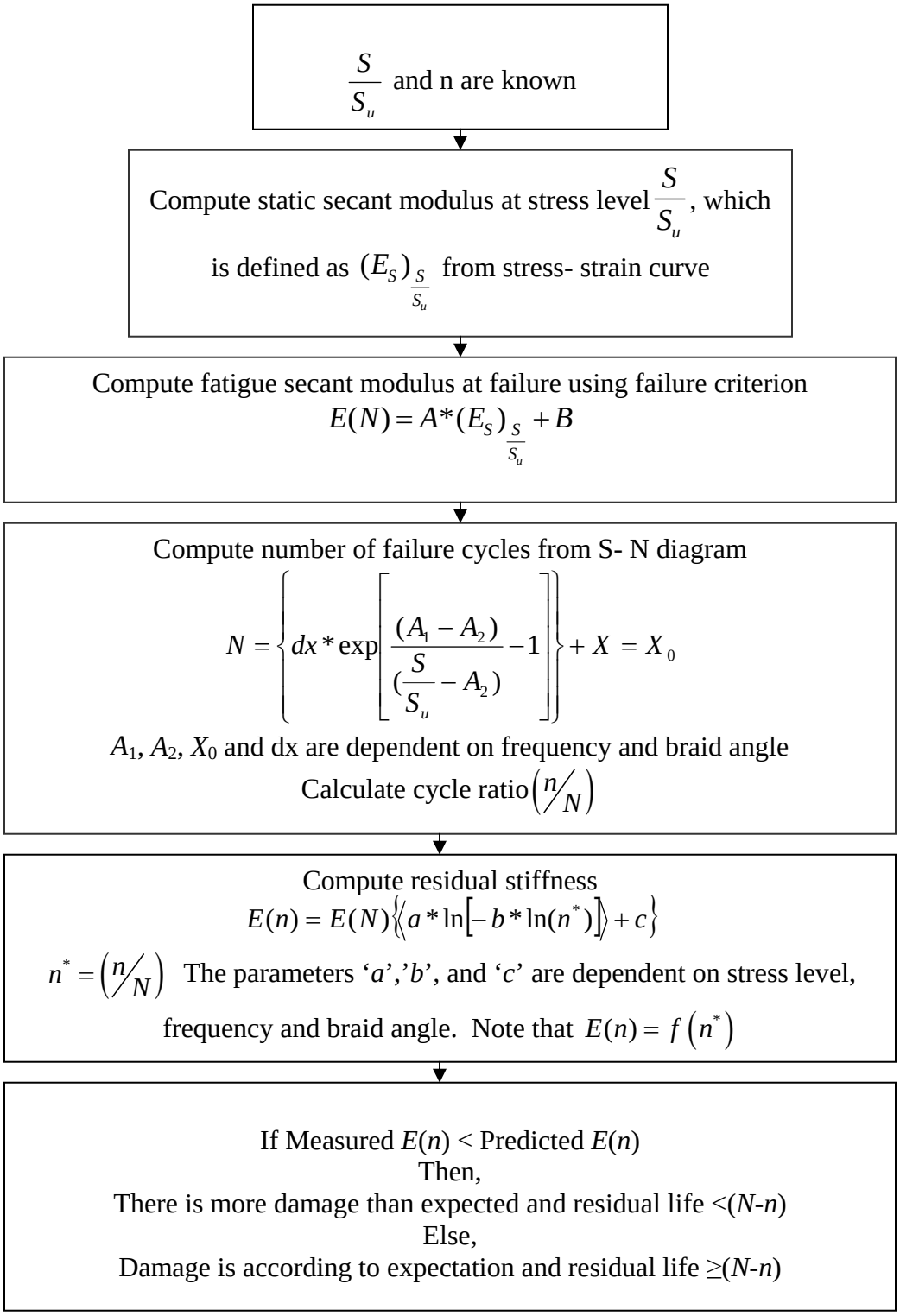

Figure 4-12. Tracking of Fatigue Secant Modulus

4.5 STIFFNESS DEGRADATION STUDY FINDINGS.

The stiffness degradation study findings are as follows:

- The stiffness degradation curve typically has three distinct stages. In the first stage, the modulus decreases rapidly. In the second stage, there is gradual modulus decay almost linearly, and in the third stage, the modulus decreases rapidly. In braided composites, the fatigue secant modulus loss can be as high as 60% of the fatigue secant modulus in the first cycle. In woven composites, the fatigue secant modulus decrease is 25% of the fatigue secant modulus in the first cycle.

- It is possible to predict the endurance limit (stress level at 1 million cycles) by testing specimens for only a few hundred cycles. The stress level at which the stiffness remains almost constant indicates the endurance limit.

- The developed stiffness degradation model agreed well with experimental results in all three stages of the stiffness degradation. The parameters a, b, and c from the equations could be modified to consider the effect of the stress level and the frequency.

- It should be noted that the proposed model predicts the fatigue secant modulus $E(n)$. However, most of the nondestructive techniques quantify the modulus that is best represented by the initial tangent modulus, E_O. Therefore, the fatigue secant modulus, E (n), needs to be related to the initial tangent modulus, E_O.

5. COMPUTATIONAL MICROMECHANICS.

5.1 INTRODUCTION.

In this section, the idealized geometry of 2x2 braids and different steps involved in the analysis of 2x2 braids will be discussed briefly. The finite element models used to obtain effective properties and stress distribution will be shown and the governing differential equations will be provided. A tape laminate configuration will also be discussed, which was used to compare the 3D finite element results for the braids with a simple laminate analysis.

5.2 IDEALIZED GEOMETRY OF THE 2X2 BRAID.

A 2x2 braid microstructure is formed by mutually intertwining two or more sets of tows (yarns) about each other (figure 5-1). There can be different types of braids. The braid that was studied here can be specified as a 2x2 biaxial ±θ braid. The numbers 2x2 mean that two +θ yarns pass over and under two -θ yarns and vice versa. Biaxial means that the yarns run in two directions (if there are yarns in the axial direction also, then the resulting structure is also called a triaxial braid), θ is the braid angle. Figure 5-1 shows an idealized braided mat with matrix pockets removed to show the geometry. As shown in the figure, the 2x2 biaxial braid structure has an interlaced tow structure characterized by any given tow passing over two opposing tows, then under two opposing tows, and repeating this pattern. A repeating unit cell can be defined in the structure, as labeled in figure 5-1.

Figure 5-1(b) shows a typical tow taken out of the braid microstructure of figure 5-1(a). In this figure, h is the mat thickness and λ is the wavelength of the wavy region. The WR is defined herein as h/λ. This tow has straight as well as undulated regions. Here the straight and undulated regions cannot be separated by planes parallel to yz plane except for the ±45° braid. This is due to the fact that the braid tows are not orthogonal to each other (except for the ±45º braid). Hence, different fibers in a single tow do not have the same phase angle. This means that the different fibers of the tow do not uniformly undulate and straighten at the same x coordinate. The phase of a fiber running at the edge of the tow is not the same as that of a fiber running in the middle of the tow. This phase shift is $= j = y * \tan(\theta)$, where θ is the braid angle. Since the tows are not orthogonal to each other, this causes the tow cross-section to vary in an unusual fashion. This is illustrated in figure 5-1(b), which shows the cross-sections at different points along the towpath. It should be noted that although the cross-sections are of different shapes, the cross-sectional area is constant. Hence, there is no concern about disappearing material or varying fiber volume fraction in the tow. The shape of the cross-section in the straight region of the tow is lenticular and can be described by simple sinusoidal function as

$$z = \frac{h}{4}\cos\left(\frac{2\pi y}{\lambda}\right)$$

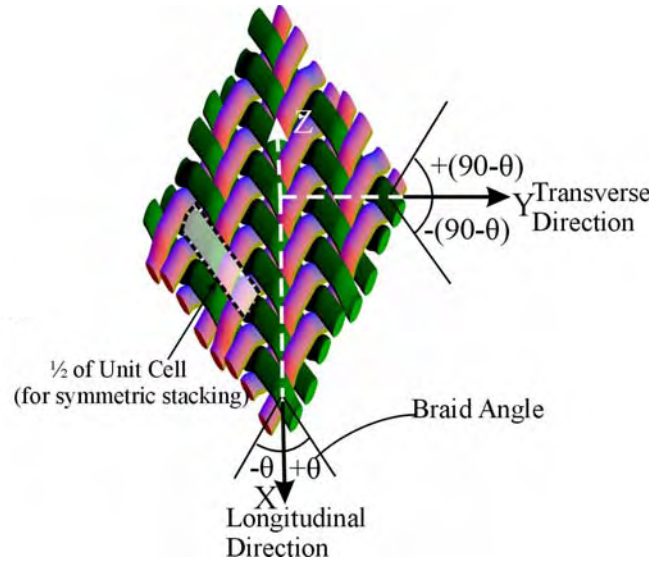

(a) Braid Angle and Coordinate System
(transparent region is half of the unit cell for symmetric stacking)

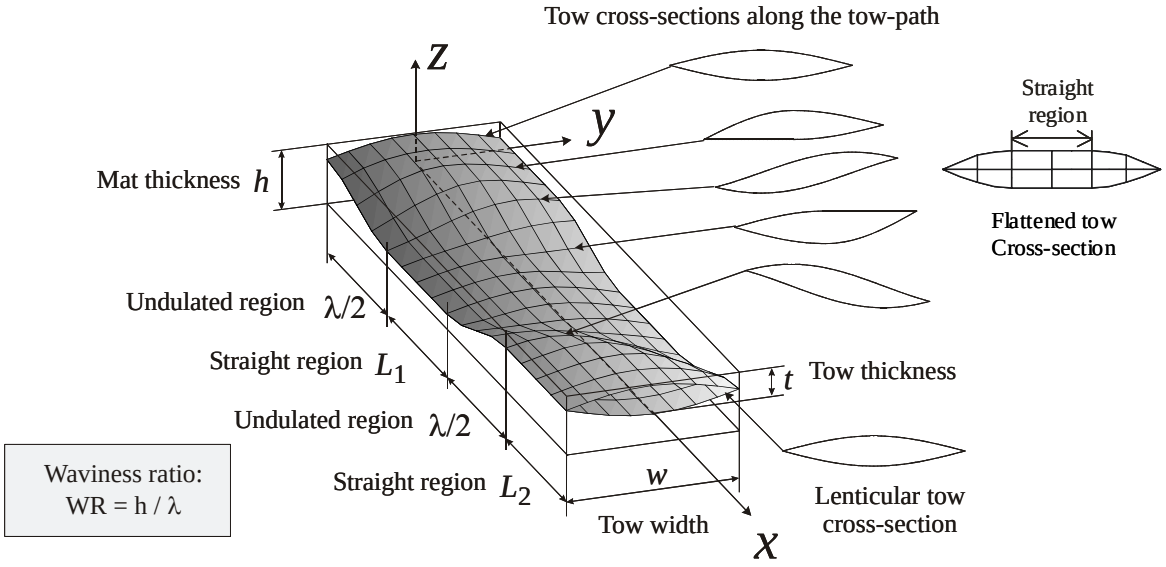

(b) Tow Path, Tow Cross Sections, and WR

Figure 5-1. Architecture of 2x2 Braid

A few parameters are used to describe the braid architecture: the braid angle, which is measured by ±θ and the tow WR, which is defined as h/λ. The overall fiber volume fraction V_f^{Overall} is used to specify the fiber volume fraction in the entire braid, while the tow fiber volume fraction V_f^{TOW} is used to specify the fiber volume fraction in the tows. The parameter that bridges V_f^{Overall} and V_f^{TOW} is the tow volume fraction V_{TOW} ($\geq 2/\pi$), which measures how much volume the tow occupies in the entire braid unit cell model. Note that $V_f^{\text{Overall}} = V_f^{\text{TOW}} V_{\text{TOW}}$. The tow volume fraction V_{TOW} is related to the tow cross-section shape. Specifically, when $V_{\text{TOW}} = 2/\pi$, there is no straight region in the boundary of the tow cross-section and the corresponding tow cross-

section shape is called lenticular. When $V_{TOW} > 2/\pi$, the corresponding tow cross-section shape is flattened. Given the overall fiber volume fraction and either the tow fraction or fiber volume fraction in the tow, the other can be calculated. For a lenticular cross-section, the model geometry requires the tow fraction to be equal to $2/\pi$. In these studies, the glass/epoxy material system had a lenticular cross-section (i.e., $V_T = 2/\pi$). The overall fiber volume fraction was 50%, so the fiber volume fraction in the tow was 78.5%. For the carbon/epoxy material system, both lenticular and flattened cross-sections were considered (for the same overall fiber volume fraction) to see the effect of tow cross-section shape on the effective properties. For the same overall fiber volume fraction, the lenticular tow has a larger fiber fraction than a flattened tow.

Finite element models were built for the unit cell defined in figure 5-1. Since the tow cross-section along the towpath is not uniform, direct finite element mesh generation for the model is difficult. A twill weave is shown in figure 5-2. Careful examination of the tow architecture of the 2x2 twill weave and 2x2 biaxial braid (see figures 5-1 and 5-2) reveals that a ±45° 2x2 biaxial braid is geometrically indistinguishable from a 2x2 twill rotated by 45°. Both configurations have orthogonal tows. Inspired by this fact, a mapping technique was developed to generate the finite element mesh for various 2x2 biaxial braids from the mesh for the twill weave, which had been developed in previous studies (Tang, 2001). The mapping transformation is defined in equation 5-1.

$$\begin{Bmatrix} x' \\ y' \end{Bmatrix} = \begin{bmatrix} \sin\theta & -\cos\theta \\ \cos\theta & \sin\theta \end{bmatrix} \begin{bmatrix} \sin 2\theta & 0 \\ -\cos 2\theta & 1 \end{bmatrix} \begin{Bmatrix} x \\ y \end{Bmatrix} \tag{5-1}$$

where (x, y) and (x', y') are the coordinates in the twill and braid models, respectively, and θ is the braid angle.

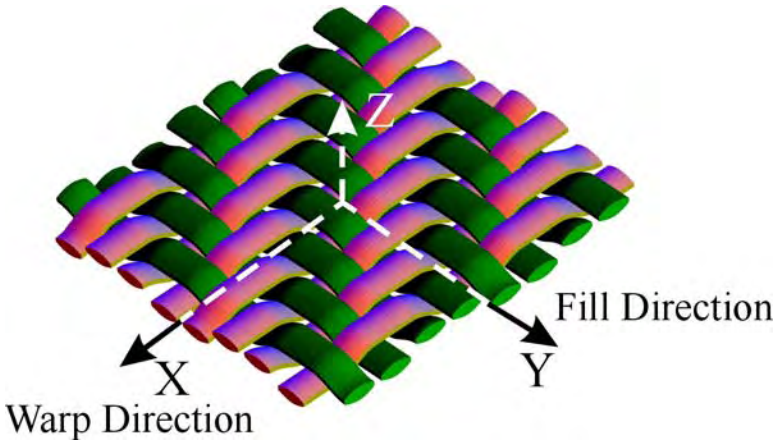

Figure 5-2. Twill Weave

5.3 ANALYSIS STEPS.

Different steps involved in the analysis are shown in figure 5-3, starting with the fiber and matrix and moving in a counter clockwise direction. It is assumed that the fibers are arranged in a hexagonal array in the matrix. The properties of tow are calculated using micromechanics. The

tows are interlaced with each other to get a mat and the mats are stacked on the top of each other in some kind of stacking sequence to get the required thickness. The mats impregnated with the matrix constitute the braid under investigations. A part of this braid microstructure can be analyzed to predict the behavior. This braid is finally used to make structural components like the one shown in the figure.

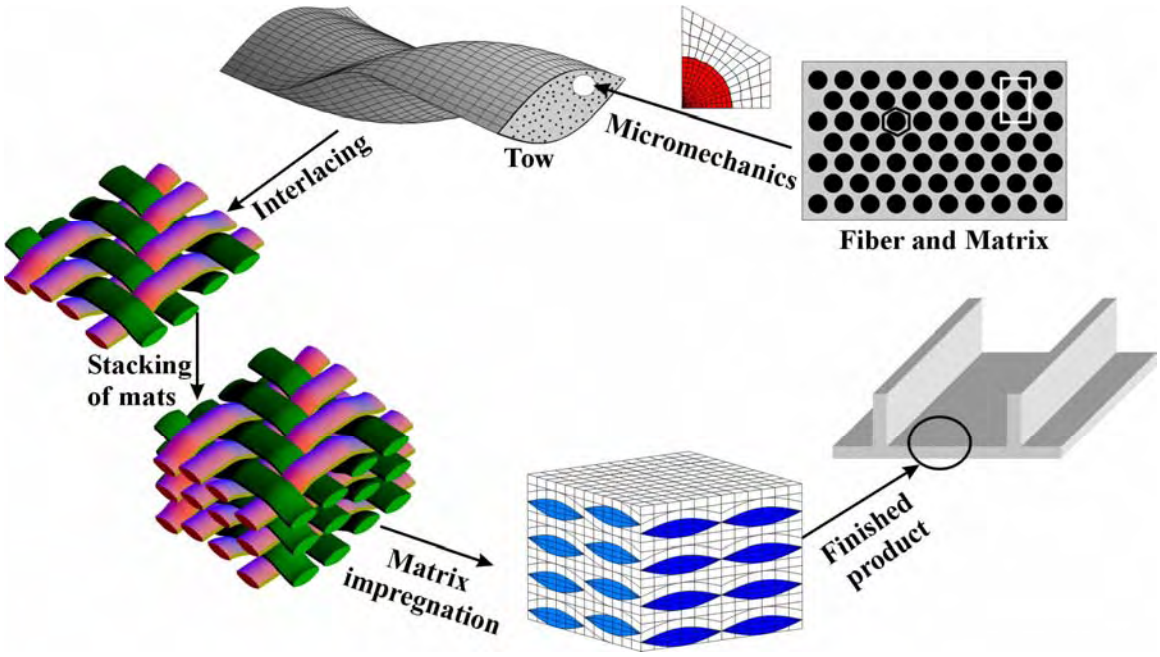

Figure 5-3. Analysis Steps

5.4 FINITE ELEMENT MODELS.

Figure 5-4 shows a micrograph (Whitcomb and Kelkar, 2002) of a dry braid mat. Clearly shown in the figure, there is a repeated pattern of interlacing. In micromechanics, this is referred to as periodicity. If the periodicity is exploited, finite element models can be developed for a single representative volume element that will behave as though it is surrounded by many other RVEs. The unit cell of a periodic microstructure is the smallest region that can produce the whole structure by spatially translating its copies without the use of rotation or reflection. One does not need to model the entire microstructure. A single unit cell can be modeled to reduce the analysis region. But in textile composites, modeling even a single unit cell can be very expensive because of the complex geometry involved. Fortunately, textile composites often exhibit symmetry inside a single unit cell. The analysis region can be further reduced from a single unit cell to a smaller subcell (for example, one-half or one-fourth of a unit cell, etc.) by exploiting symmetry operations like mirroring, rotation, or a combination of the two. Hence, the unit cell should be chosen such that it can offer some symmetry to reduce the analysis region. Here, the symmetries were exploited and the analysis region was reduced to one-fourth of the unit cell for the symmetric stacking and to one-half for the simple stacking (see figure 5-5) of the braided mats. The boundary conditions were derived using the technique described by Whitcomb, Chapman, and Tang, 2000 and Tang and Whitcomb, 2003a. Boundary conditions are imposed on the paired regions as labeled by the paired letters through multipoint constraints shown in

figure 5-6. For example, the displacements on the partial planes B and $\overline{B}$ are related through the multipoint constraints, which mean the displacements on one face are slaved (dependent) to the displacements on the other face. As clearly shown in the figure, the boundary conditions are a bit unusual and are not intuitively obvious. Tables 5-1 and 5-2 give the complete set of boundary conditions for the various load cases for one-fourth of the unit cell of a symmetrically stacked mat. In the tables, u_1, u_2, and u_3 are the displacements, and T_1, T_2, and T_3 are the tractions in X_1, X_2 and X_3 directions, respectively.

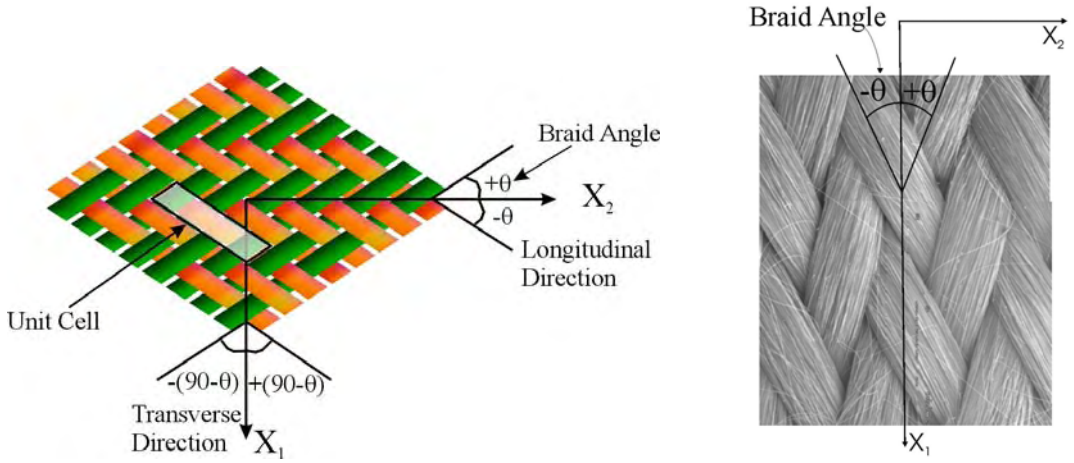

Figure 5-4. Schematics of Braids

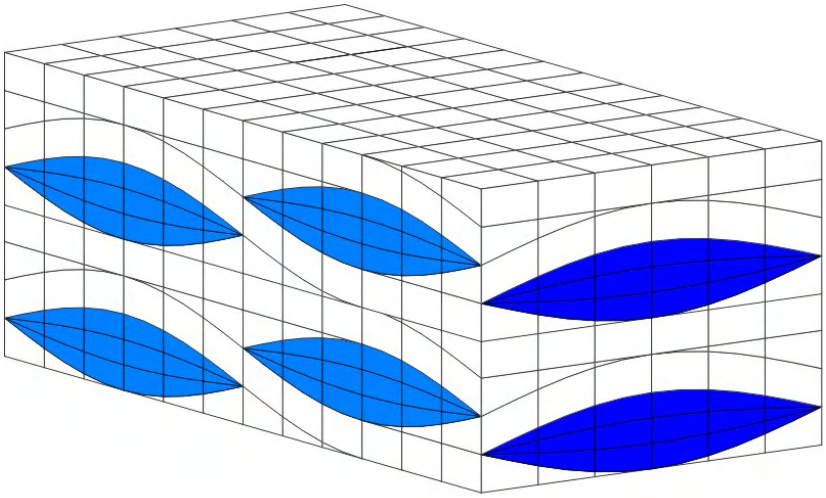

Simple stacking

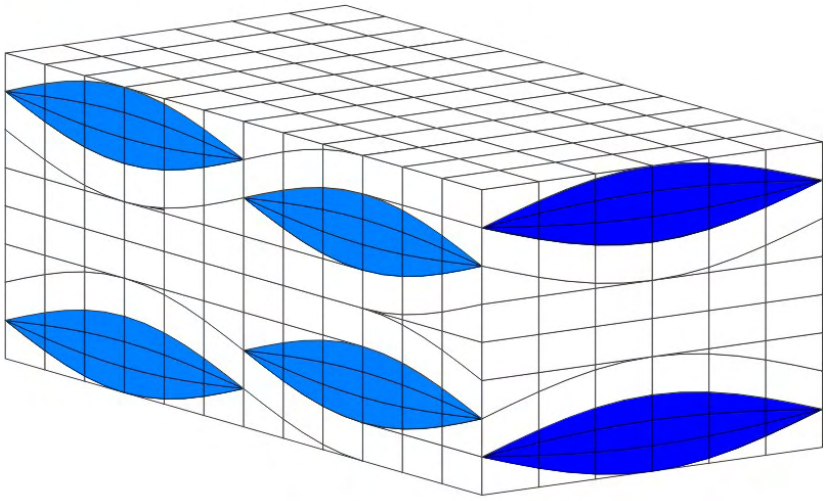

Symmetric stacking

Figure 5-5. Simple and Symmetric Stacking of Mats

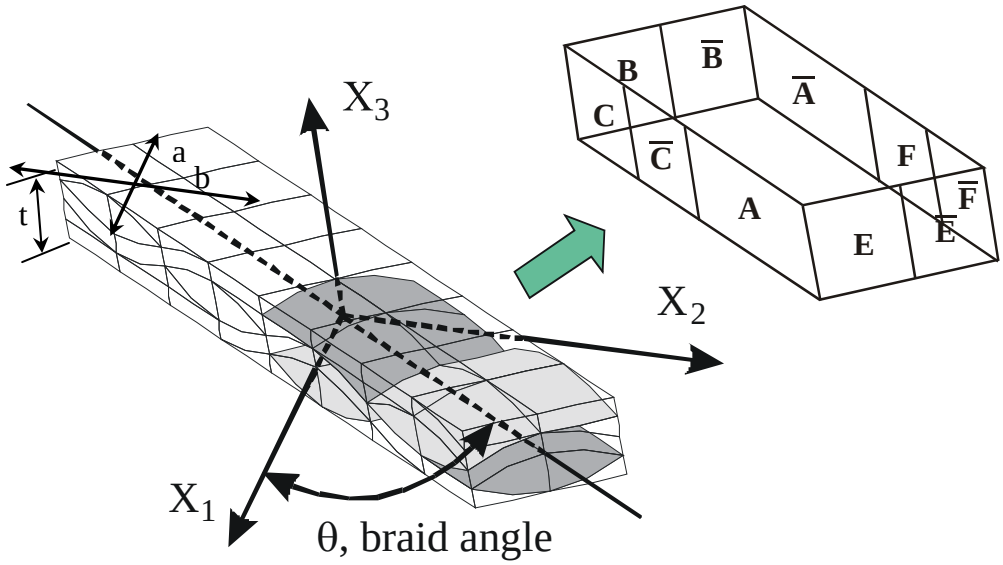

Figure 5-6. A Coarse Finite Element Mesh for Half of the Unit Cell
(The quarter unit cell model is the region in which the matrix pockets are shown transparent. Multipoint constraints are imposed on the paired regions (e.g., A and $\overline{A}$, B, and $\overline{B}$, etc.).)

Table 5-1. Multipoint Constraints for $\left\langle \frac{\partial u_1}{\partial X_1} \right\rangle$, $\left\langle \frac{\partial u_1}{\partial X_2} \right\rangle$, $\left\langle \frac{\partial u_2}{\partial X_2} \right\rangle$, or $\left\langle \frac{\partial u_3}{\partial X_3} \right\rangle$ Loading* $\left(where \left\langle \frac{\partial u_i}{\partial x_j} \right\rangle = \frac{1}{V} \int_V \frac{\partial u_i}{\partial x_j} dV \right)$

Figure	Faces (Figure 5-6)	Multipoint Constraint Relationships
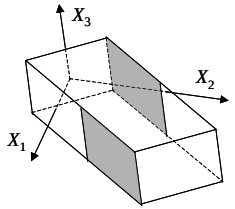	A and $\overline{\text{A}}$	$u_1\left(-\frac{1}{2}a+\frac{a\,X_2}{b}, X_2, X_3\right) = u_1\left(\frac{1}{2}a+\frac{a\,X_2}{b}, X_2, X_3\right) - \langle \frac{\partial}{\partial X_1} u_1 \rangle\ a$ $u_2\left(-\frac{1}{2}a+\frac{a\,X_2}{b}, X_2, X_3\right) = u_2\left(\frac{1}{2}a+\frac{a\,X_2}{b}, X_2, X_3\right) - \langle \frac{\partial}{\partial X_2} u_1 \rangle\ a$ $u_3\left(-\frac{1}{2}a+\frac{a\,X_2}{b}, X_2, X_3\right) = u_3\left(\frac{1}{2}a+\frac{a\,X_2}{b}, X_2, X_3\right)$
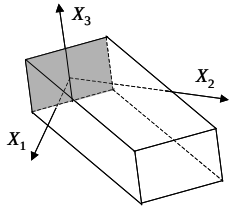	B and $\overline{\text{B}}$	$u_1\left(\frac{a\,X_2}{b}, -X_2, X_3\right) = -u_1\left(-\frac{a\,X_2}{b}, X_2, X_3\right)$ $u_2\left(\frac{a\,X_2}{b}, -X_2, X_3\right) = -u_2\left(-\frac{a\,X_2}{b}, X_2, X_3\right)$ $u_3\left(\frac{a\,X_2}{b}, -X_2, X_3\right) = u_3\left(-\frac{a\,X_2}{b}, X_2, X_3\right)$
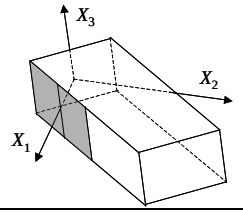	C and $\overline{\text{C}}$	$u_1\left(\frac{1}{4}a-\frac{a\,X_2}{b}, -X_2-\frac{1}{4}b, X_3\right) = -u_1\left(\frac{1}{2}a+\frac{a\,X_2}{b}, X_2, X_3\right) + \frac{3}{4}\langle \frac{\partial}{\partial X_1} u_1 \rangle\ a - \frac{1}{4}\langle \frac{\partial}{\partial X_2} u_1 \rangle\ b$ $u_2\left(\frac{1}{4}a-\frac{a\,X_2}{b}, -X_2-\frac{1}{4}b, X_3\right) = -u_2\left(\frac{1}{2}a+\frac{a\,X_2}{b}, X_2, X_3\right) + \frac{3}{4}\langle \frac{\partial}{\partial X_2} u_1 \rangle\ a - \frac{1}{4}\langle \frac{\partial}{\partial X_2} u_2 \rangle\ b$ $u_3\left(\frac{1}{4}a-\frac{a\,X_2}{b}, -X_2-\frac{1}{4}b, X_3\right) = u_3\left(\frac{1}{2}a+\frac{a\,X_2}{b}, X_2, X_3\right)$

*Only one of the $\left\langle \frac{\partial u_1}{\partial X_1} \right\rangle$, $\left\langle \frac{\partial u_1}{\partial X_2} \right\rangle$, $\left\langle \frac{\partial u_2}{\partial X_2} \right\rangle$, or $\left\langle \frac{\partial u_3}{\partial X_3} \right\rangle$ is specified for a particular analysis.

The geometric parameters a, b, and t are shown in figure 5-4.
The others are unknowns that are solved as part of the solution.

Table 5-1. Multipoint Constraints for $\left\langle \frac{\partial u_1}{\partial X_1} \right\rangle$, $\left\langle \frac{\partial u_1}{\partial X_2} \right\rangle$, $\left\langle \frac{\partial u_2}{\partial X_2} \right\rangle$, or $\left\langle \frac{\partial u_3}{\partial X_3} \right\rangle$ Loading* $\left(where \left\langle \frac{\partial u_i}{\partial x_j} \right\rangle = \frac{1}{V} \int_V \frac{\partial u_i}{\partial x_j} dV \right)$ (Continued)

Figure	Faces (Figure 5-6)	Multipoint Constraint Relationships
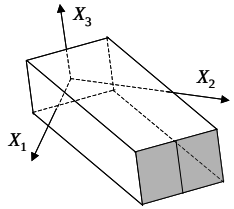	E and $\bar{E}$	$u_1\left(\frac{a X_2}{b}, -X_2 + 2b, X_3\right) = -u_1\left(2a - \frac{a X_2}{b}, X_2, X_3\right) + 2 \langle \frac{\partial}{\partial X_1} u_1 \rangle a + 2 \langle \frac{\partial}{\partial X_2} u_1 \rangle b$ $u_2\left(\frac{a X_2}{b}, -X_2 + 2b, X_3\right) = -u_2\left(2a - \frac{a X_2}{b}, X_2, X_3\right) + 2 \langle \frac{\partial}{\partial X_2} u_1 \rangle a + 2 \langle \frac{\partial}{\partial X_2} u_2 \rangle b$ $u_3\left(\frac{a X_2}{b}, -X_2 + 2b, X_3\right) = u_3\left(2a - \frac{a X_2}{b}, X_2, X_3\right)$
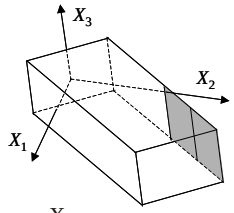	F and $\bar{F}$	$u_1\left(\frac{3}{2}a - \frac{a X_2}{b}, -X_2 + 2b, X_3\right) = -u_1\left(-\frac{1}{2}a + \frac{a X_2}{b}, X_2, X_3\right) + \langle \frac{\partial}{\partial X_1} u_1 \rangle a + 2 \langle \frac{\partial}{\partial X_2} u_1 \rangle b$ $u_2\left(\frac{3}{2}a - \frac{a X_2}{b}, -X_2 + 2b, X_3\right) = -u_2\left(-\frac{1}{2}a + \frac{a X_2}{b}, X_2, X_3\right) + \langle \frac{\partial}{\partial X_2} u_1 \rangle a + 2 \langle \frac{\partial}{\partial X_2} u_2 \rangle b$ $u_3\left(\frac{3}{2}a - \frac{a X_2}{b}, -X_2 + 2b, X_3\right) = u_3\left(-\frac{1}{2}a + \frac{a X_2}{b}, X_2, X_3\right)$
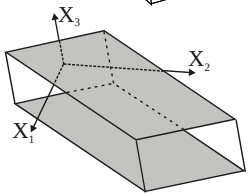	Top and Bottom (Simple Stacking)	$u_1\left(X_1, X_2, \frac{1}{2}t\right) = u_1\left(X_1, X_2, -\frac{1}{2}t\right)$ $u_2\left(X_1, X_2, \frac{1}{2}t\right) = u_2\left(X_1, X_2, -\frac{1}{2}t\right)$ $u_3\left(X_1, X_2, \frac{1}{2}t\right) = u_3\left(X_1, X_2, -\frac{1}{2}t\right) + \langle \frac{\partial}{\partial X_3} u_3 \rangle t$
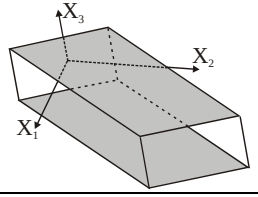	Top and Bottom (Symmetric Stacking)	$T_1\left(X_1, X_2, \frac{1}{2}t\right) = 0$ $T_2\left(X_1, X_2, \frac{1}{2}t\right) = 0$ $u_3\left(X_1, X_2, \frac{1}{2}t\right) = \frac{1}{2} \langle \frac{\partial}{\partial X_3} u_3 \rangle t$

*Only one of the $\left\langle \frac{\partial u_1}{\partial X_1} \right\rangle$, $\left\langle \frac{\partial u_1}{\partial X_2} \right\rangle$, $\left\langle \frac{\partial u_2}{\partial X_2} \right\rangle$, or $\left\langle \frac{\partial u_3}{\partial X_3} \right\rangle$ is specified for a particular analysis.

The geometric parameters a, b, and t are shown in figure 5-4.
The others are unknowns that are solved as part of the solution.

Table 5-2. Multipoint Constraints for $\left\langle \frac{\partial u_1}{\partial X_3} \right\rangle$ or $\left\langle \frac{\partial u_2}{\partial X_3} \right\rangle$ Loading* $\left(where \left\langle \frac{\partial u_i}{\partial x_j} \right\rangle = \frac{1}{V} \int_V \frac{\partial u_i}{\partial x_j} dV \right)$

Figure	Faces (Figure 5-6)	Multipoint Constraint Relationships
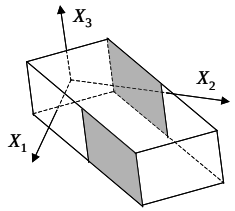	A and $\overline{\text{A}}$	$u_1\left(-\frac{1}{2}a+\frac{a\,X_2}{b}, X_2, X_3\right) = u_1\left(\frac{1}{2}a+\frac{a\,X_2}{b}, X_2, X_3\right)$ $u_2\left(-\frac{1}{2}a+\frac{a\,X_2}{b}, X_2, X_3\right) = u_2\left(\frac{1}{2}a+\frac{a\,X_2}{b}, X_2, X_3\right)$ $u_3\left(-\frac{1}{2}a+\frac{a\,X_2}{b}, X_2, X_3\right) = u_3\left(\frac{1}{2}a+\frac{a\,X_2}{b}, X_2, X_3\right) - \langle \frac{\partial}{\partial X_3} u_1 \rangle \; a$
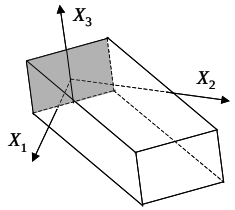	B and $\overline{\text{B}}$	$u_1\left(\frac{a\,X_2}{b}, -X_2, X_3\right) = u_1\left(-\frac{a\,X_2}{b}, X_2, X_3\right)$ $u_2\left(\frac{a\,X_2}{b}, -X_2, X_3\right) = u_2\left(-\frac{a\,X_2}{b}, X_2, X_3\right)$ $u_3\left(\frac{a\,X_2}{b}, -X_2, X_3\right) = -u_3\left(-\frac{a\,X_2}{b}, X_2, X_3\right)$
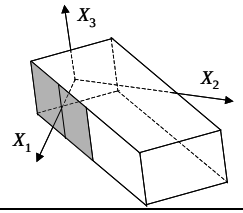	C and $\overline{\text{C}}$	$u_1\left(\frac{1}{4}a-\frac{a\,X_2}{b}, -X_2-\frac{1}{4}b, X_3\right) = u_1\left(\frac{1}{2}a+\frac{a\,X_2}{b}, X_2, X_3\right)$ $u_2\left(\frac{1}{4}a-\frac{a\,X_2}{b}, -X_2-\frac{1}{4}b, X_3\right) = u_2\left(\frac{1}{2}a+\frac{a\,X_2}{b}, X_2, X_3\right)$ $u_3\left(\frac{1}{4}a-\frac{a\,X_2}{b}, -X_2-\frac{1}{4}b, X_3\right) = -u_3\left(\frac{1}{2}a+\frac{a\,X_2}{b}, X_2, X_3\right) + \frac{3}{4}\langle \frac{\partial}{\partial X_3} u_1 \rangle \; a - \frac{1}{4}\langle \frac{\partial}{\partial X_3} u_2 \rangle \; b$

*Only one of the $\left\langle \frac{\partial u_1}{\partial X_3} \right\rangle$ or $\left\langle \frac{\partial u_2}{\partial X_3} \right\rangle$ is specified for a particular analysis.

The geometric parameters a, b, and t are shown in figure 5-4.
The others are unknowns that are solved as part of the solution.

Table 5-2. Multipoint Constraints for $\left\langle \frac{\partial u_1}{\partial X_3} \right\rangle$ or $\left\langle \frac{\partial u_2}{\partial X_3} \right\rangle$ Loading* $\left(where \left\langle \frac{\partial u_i}{\partial x_j} \right\rangle = \frac{1}{V} \int_V \frac{\partial u_i}{\partial x_j} dV \right)$ (Continued)

Figure	Faces (Figure 5-6)	Multipoint Constraint Relationships
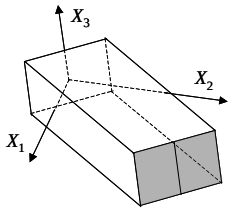	E and $\overline{\text{E}}$	$u_1\left(\frac{a\,X_2}{b}, -X_2 + 2\,b, X_3\right) = u_1\left(2\,a - \frac{a\,X_2}{b}, X_2, X_3\right)$ $u_2\left(\frac{a\,X_2}{b}, -X_2 + 2\,b, X_3\right) = u_2\left(2\,a - \frac{a\,X_2}{b}, X_2, X_3\right)$ $u_3\left(\frac{a\,X_2}{b}, -X_2 + 2\,b, X_3\right) = -u_3\left(2\,a - \frac{a\,X_2}{b}, X_2, X_3\right) + 2\,\langle\,\frac{\partial}{\partial X_3} u_1\,\rangle\;a + 2\,\langle\,\frac{\partial}{\partial X_3} u_2\,\rangle\;b$
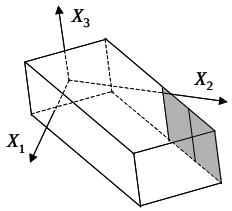	F and $\overline{\text{F}}$	$u_1\left(\frac{3}{2}a - \frac{a\,X_2}{b}, -X_2 + 2\,b, X_3\right) = u_1\left(-\frac{1}{2}a + \frac{a\,X_2}{b}, X_2, X_3\right)$ $u_2\left(\frac{3}{2}a - \frac{a\,X_2}{b}, -X_2 + 2\,b, X_3\right) = u_2\left(-\frac{1}{2}a + \frac{a\,X_2}{b}, X_2, X_3\right)$ $u_3\left(\frac{3}{2}a - \frac{a\,X_2}{b}, -X_2 + 2\,b, X_3\right) = -u_3\left(-\frac{1}{2}a + \frac{a\,X_2}{b}, X_2, X_3\right) + \langle\,\frac{\partial}{\partial X_3} u_1\,\rangle\;a + 2\,\langle\,\frac{\partial}{\partial X_3} u_2\,\rangle\;b$
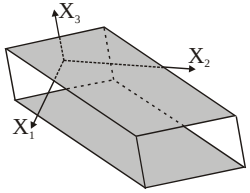	Top and Bottom (Simple Stacking)	$u_1\left(X_1, X_2, \frac{1}{2}t\right) = u_1\left(X_1, X_2, -\frac{1}{2}t\right) + \langle\,\frac{\partial}{\partial X_3} u_1\,\rangle\;t$ $u_2\left(X_1, X_2, \frac{1}{2}t\right) = u_2\left(X_1, X_2, -\frac{1}{2}t\right) + \langle\,\frac{\partial}{\partial X_3} u_2\,\rangle\;t$ $u_3\left(X_1, X_2, \frac{1}{2}t\right) = u_3\left(X_1, X_2, -\frac{1}{2}t\right)$
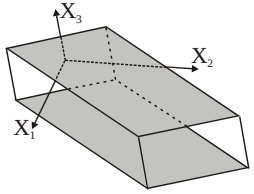	Top and Bottom (Symmetric Stacking)	$u_1\left(X_1, X_2, \frac{1}{2}t\right) = \frac{1}{2}\,\langle\,\frac{\partial}{\partial X_3} u_1\,\rangle\;t$ $u_2\left(X_1, X_2, \frac{1}{2}t\right) = \frac{1}{2}\,\langle\,\frac{\partial}{\partial X_3} u_2\,\rangle\;t$ $T_3\left(X_1, X_2, \frac{1}{2}t\right) = 0$

*Only one of the $\left\langle \frac{\partial u_1}{\partial X_3} \right\rangle$ or $\left\langle \frac{\partial u_2}{\partial X_3} \right\rangle$ is specified for a particular analysis.

The geometric parameters a, b, and t are shown in figure 5-4.
The Others are unknowns that are solved as part of the solution.

Finite element models (figure 5-7) were developed for the unit cell shown in figure 5-4. As discussed in section 5.2, the cross-sections of the braid tow are not uniform, so direct finite element mesh generation was difficult and a mapping technique was used to get finite element models of 2x2 braids from twill weave models, which were produced in earlier studies by a building-block technique (Tang, 2001). This resulted in a substantial time savings.

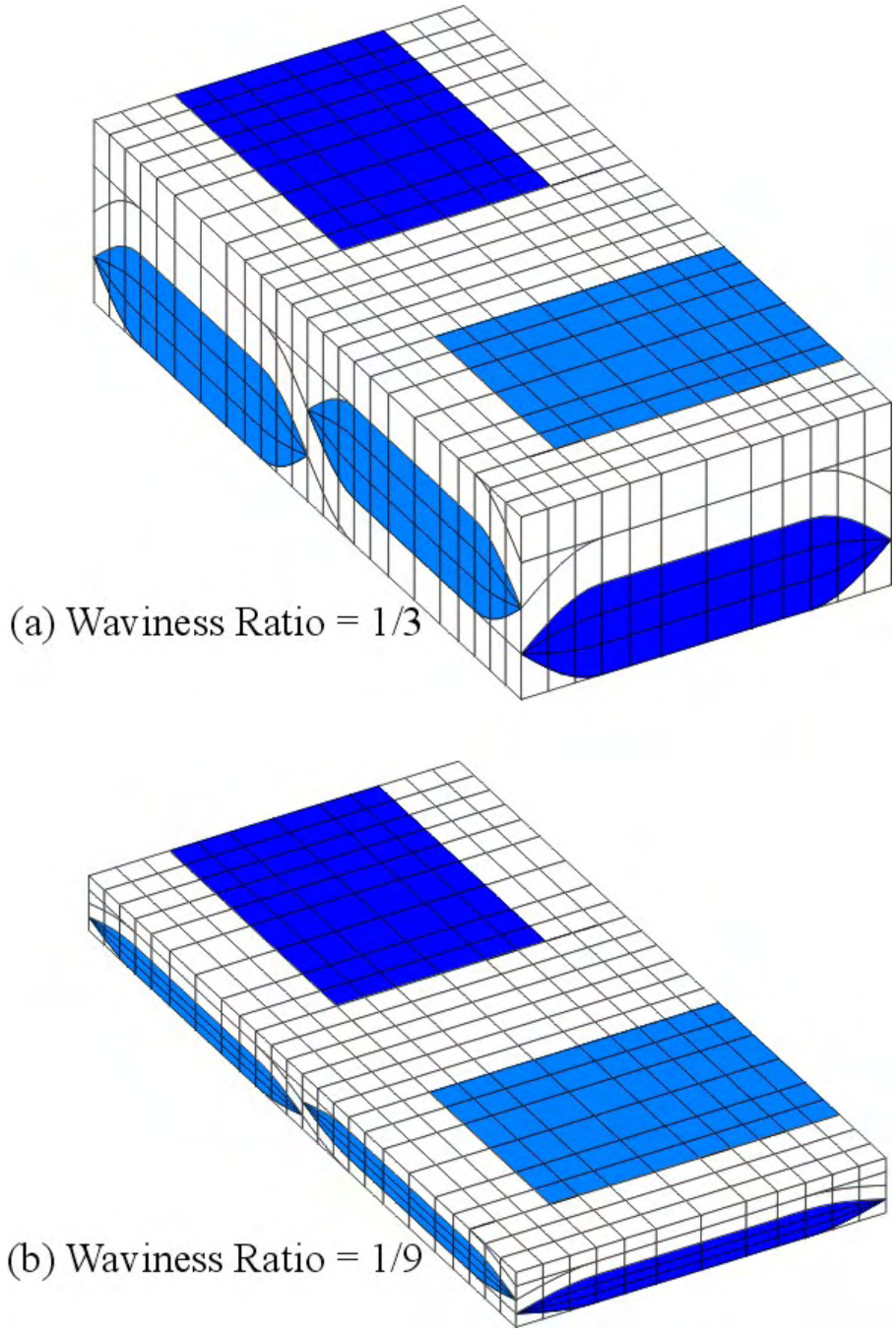

Figure 5-7. Typical Finite Element Models for Flattened Cross-Sections

Depending upon the requirement, any number of mats can be stacked on the top of each other. Figure 5-5 shows the simple and symmetric stacking of mats. The analysis region can be reduced to one-half for the simple stacking and to one-fourth for the symmetric stacking. The results produced by full unit cell and a part of the unit cell were compared with each other to validate the methodology, and it was seen that the results matched for the two cases.

Figure 5-7 shows two unit cells for ±70° braid. One has very large WR (1/3) and the other has small WR (1/9).

As discussed in section 5.2, depending on the tow volume fraction in a model, the tow cross-section will either be lenticular or flattened. For example, for the material systems used in the parametric studies (will follow in the next section), one material system had flattened cross-section and the other had lenticular. The finite element models with flattened tow cross-section are shown in figure 5-7 and ones with lenticular cross-section are shown in figure 5-8.

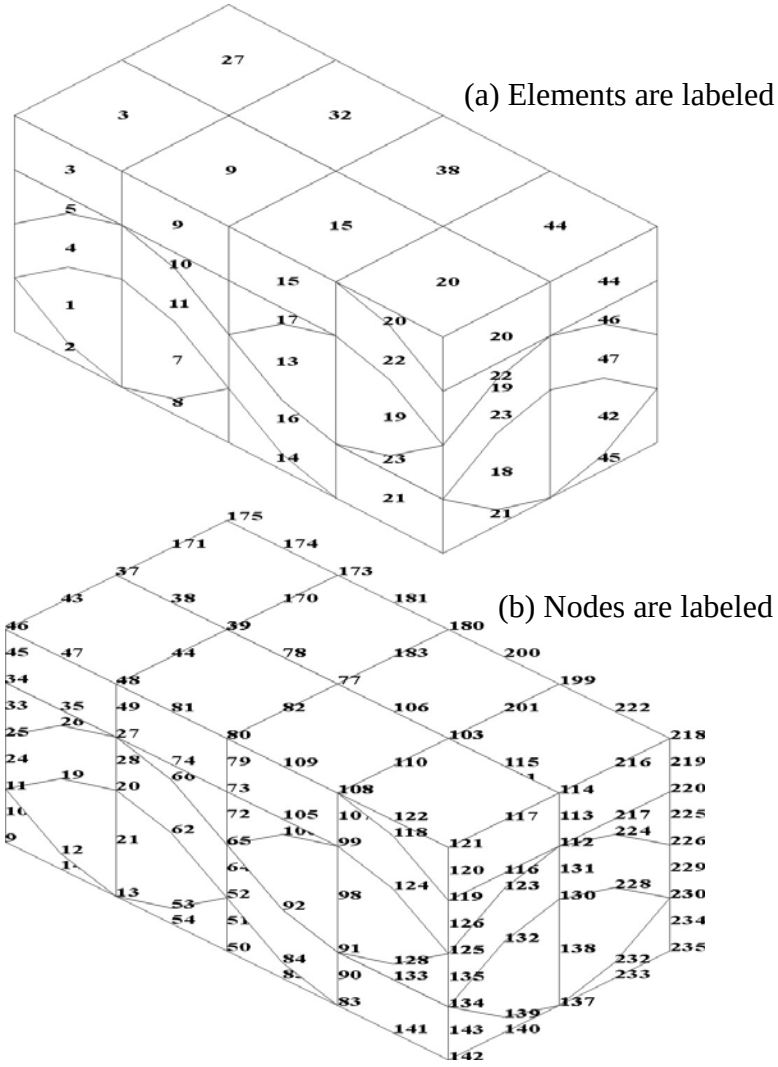

Figure 5-8. Finite Element Model for Lenticular Cross-Section With Nodes and Elements Labeled

For every combination of WR (braid angle and volume fraction), a different finite element model must be generated. For these studies, approximately 450 cases were run for the two material systems. A typical mesh used for obtaining effective properties contained 2,304 hexahedral 20-node brick elements and 10,060 nodes for models with flattened cross-section and 720 elements and 3130 nodes for models with lenticular cross-section. A 20-node brick element is also shown in figure 5-9. One coarse finite element model with 48 elements and 238 nodes is shown in figure 5-8.

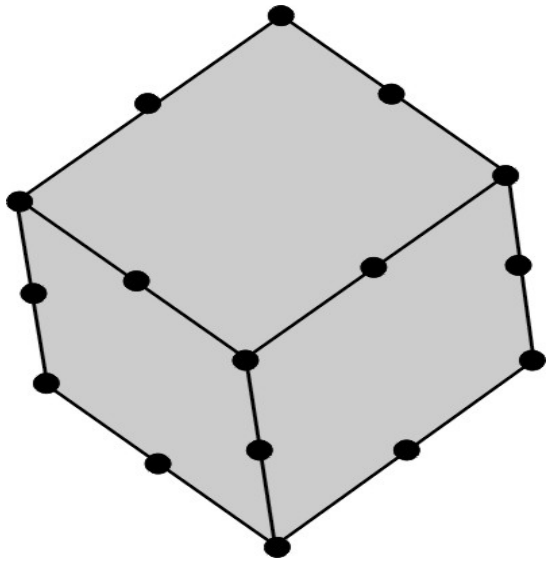

Figure 5-9. A 20-Node Brick Element

All the parametric studies for calculating the effective properties were done using an inexpensive personal computer (PC). For models with flattened cross-sections, the mesh generation time and equation solving time were considerably higher than for models with lenticular cross-sections. Equation solving time using a 400-MHz PC were approximately five to six times more than that using 2.4-GHz PC. Typical runtimes are shown in table 5-3.

Table 5-3. Runtimes on a Personal Computer for One Case

Computer Model	Pentium II 400 MHz CPU		Pentium IV 2.4 GHz CPU	
Tow Cross-Section	Lenticular	Flattened	Lenticular	Flattened
Mesh Generation Time	21 sec	01 min, 06 sec	07 sec	14 sec
Equation Solving Time	02 min, 45 sec	11 min, 31 sec	28 sec	01 min, 56 sec

5.5 GOVERNING DIFFERENTIAL EQUATIONS.

The governing differential equations are reviewed in this section (Reddy and Miravete, 1995). The equations of motion and deformation of a solid body can be classified into following four categories:

1. Kinematics (strain-displacement relations)

2. Compatibility equations
3. Kinetics (conservation of linear and angular momentum)
4. Constitutive equations (stress-strain relations)

An overview of the above equations is presented below.

5.5.1 Kinematics.

Kinematics involves the study of the geometric changes or deformations in the body without considering the forces acting on it. Let ε, the strain tensor in Voight's notation, be given by

$$\varepsilon = \left\{ \varepsilon_{xx}, \varepsilon_{yy}, \varepsilon_{zz}, \varepsilon_{xy}, \varepsilon_{yz}, \varepsilon_{zx} \right\}$$

Let u denote the displacement vector and the coordinates X = (X_1, X_2, X_3) denote the material coordinates of the body. The coordinate system X is fixed on the given body in the undeformed configuration and its position x at any time is referred to as the material coordinate X as

$$x = x\ (X_1, X_2, X_3)$$

If one assumes the strains and rotations are infinitesimal, the strain-displacement relations can be given by

$$\varepsilon_{ij} = \frac{1}{2}\left(\frac{\partial u_i}{\partial x_j} + \frac{\partial u_j}{\partial x_i} \right) \tag{5-2}$$

For infinitesimal deformations, components of the infinitesimal strain satisfy $\left|\varepsilon_{ij}\right| << 1$. The use of the infinitesimal strain tensor to characterize the infinitesimal deformation of the body is in fact linearization, which means that if $\varepsilon^{(1)}$ is the strain corresponding to displacement field $u^{(1)}$ and $\varepsilon^{(2)}$ is the strain corresponding to displacement field $u^{(2)}$, then $\varepsilon^{(1)}+ \varepsilon^{(2)}$ is the strain corresponding to displacement field $u^{(1)}+u^{(2)}$.

5.5.2 Compatibility Equations.

If a displacement field is given, the Cartesian components of the strain tensor are uniquely obtained by the strain-displacement relations of equation 5-2. But if a strain field is given for which a corresponding displacement field *u* is not given, one seeks to find the solution for the displacement field. To do that, one has to solve the strain-displacement relations for *u*. That involves six independent equations and only three unknown components of *u*. Hence, a single valued solution for *u* might not exist. But if an allowable displacement field does exist, then the corresponding strain field is said to be compatible. The following is an example of the compatibility equations, which ensure that a single-valued displacement field exists.

$$\frac{\partial^2 \varepsilon_{kn}}{\partial x_l \partial x_m} + \frac{\partial^2 \varepsilon_{lm}}{\partial x_k \partial x_n} - \frac{\partial^2 \varepsilon_{km}}{\partial x_l \partial x_n} - \frac{\partial^2 \varepsilon_{ln}}{\partial x_k \partial x_m} = 0 \tag{5-3}$$

This set of compatibility equations contains 81 individual equations, out of which only 6 are linearly independent. The compatibility equations are not needed in the finite element analysis because the governing equations were written in terms of displacements.

5.5.3 Kinetics.

Forces acting on a body can be classified into internal and external forces. Kinetics is the study of static or dynamic equilibrium of forces acting on a body. If one considers a given mass with density ρ, on which some forces are acting, then from the balance of linear momentum, the equations of equilibrium can be written as

$$\begin{aligned}
\frac{\partial \sigma_{xx}}{\partial x} + \frac{\partial \sigma_{xy}}{\partial y} + \frac{\partial \sigma_{xz}}{\partial z} + \rho b_x &= \rho a_x \\
\frac{\partial \sigma_{yx}}{\partial x} + \frac{\partial \sigma_{yy}}{\partial y} + \frac{\partial \sigma_{yz}}{\partial z} + \rho b_y &= \rho a_y \\
\frac{\partial \sigma_{zx}}{\partial x} + \frac{\partial \sigma_{zy}}{\partial y} + \frac{\partial \sigma_{zz}}{\partial z} + \rho b_z &= \rho a_z
\end{aligned} \tag{5-4}$$

where $\sigma = \left\{\sigma_{xx}, \sigma_{yy}, \sigma_{zz}, \sigma_{xy}, \sigma_{yz}, \sigma_{zx}\right\}$ denotes the Voight's stress tensor, *b* is the body force, and *a* is the acceleration of the body. If there are no body forces and no acceleration, then the terms containing body force *b* and acceleration *a* vanish. In the absence of any body moments, the conservation of angular momentum leads to symmetry of the stress-tensor.

5.5.4 Constitutive Equations.

The kinematics, mechanical principles are applicable to any material body irrespective of its constitution. The constitutive equations characterize the individual material response of a body. They relate the dependent variable introduced in the kinetic equations to those in the kinematic relations. Constitutive equations give a relationship between stresses and strains. In general, the stress-strain relation for infinitesimal deformation of an elastic material is nonlinear, as stress does not have to be linearly proportional to strain. But if components of stress are assumed to be in linear proportion to components of stress, then the constitutive equations can be written in the following general form.

$$\sigma_i = C_{ij}\varepsilon_j$$

where C_{ij} is the stiffness matrix, which is symmetric and has at most 21 independent stiffness coefficients. The inverse of stiffness matrix is the compliance matrix (S_{ij}) and is given as:

$$\varepsilon_i = S_{ij}\sigma_j$$

$$\text{where } S_{ij} = \begin{bmatrix} \frac{1}{E_{11}} & \frac{-\upsilon_{12}}{E_{11}} & \frac{-\upsilon_{13}}{E_{11}} & \frac{\eta_{14}}{E_{11}} & \frac{\eta_{15}}{E_{11}} & \frac{\eta_{16}}{E_{11}} \\ \frac{-\upsilon_{21}}{E_{22}} & \frac{1}{E_{22}} & \frac{-\upsilon_{23}}{E_{22}} & \frac{\eta_{24}}{E_{22}} & \frac{\eta_{25}}{E_{22}} & \frac{\eta_{26}}{E_{22}} \\ \frac{-\upsilon_{31}}{E_{33}} & \frac{-\upsilon_{32}}{E_{33}} & \frac{1}{E_{33}} & \frac{\eta_{34}}{E_{33}} & \frac{\eta_{35}}{E_{33}} & \frac{\eta_{36}}{E_{33}} \\ \frac{\eta_{41}}{G_{12}} & \frac{\eta_{42}}{G_{12}} & \frac{\eta_{43}}{G_{12}} & \frac{1}{G_{12}} & \frac{\eta_{45}}{G_{12}} & \frac{\eta_{46}}{G_{12}} \\ \frac{\eta_{51}}{G_{23}} & \frac{\eta_{52}}{G_{23}} & \frac{\eta_{53}}{G_{23}} & \frac{\eta_{54}}{G_{23}} & \frac{1}{G_{23}} & \frac{\eta_{56}}{G_{23}} \\ \frac{\eta_{61}}{G_{31}} & \frac{\eta_{62}}{G_{31}} & \frac{\eta_{63}}{G_{31}} & \frac{\eta_{64}}{G_{31}} & \frac{\eta_{65}}{G_{31}} & \frac{1}{G_{31}} \end{bmatrix} \quad (5\text{-}5)$$

Here, E_{11}, E_{22} , E_{33} denote the Young's moduli in the 1, 2, and 3 material directions, respectively, G_{12} is the in-plane shear modulus, and G_{23} and G_{13} are out-of-plane shear moduli. The Poisson's ratio ν_{ij} is defined as the negative of the ratio of transverse strain in the j^{th} direction to the axial strain in the i^{th} direction when stressed uniaxially in the i^{th} direction. The shear coupling coefficient η_{ij} is the ratio of strain in the j^{th} direction to the strain in the i^{th} direction when stressed uniaxially in the i^{th} direction. The compliance matrix shown in equation 5-5 is fully populated. When the analysis is done, it will be shown that some of the engineering constants are zero for 2x2 braids and the material is orthotropic ($\eta_{ij} = 0$) with only 9 independent constants.

5.6 MATERIAL SYSTEMS.

Two material systems were used for the parametric studies. One consists of S2 glass fibers and SC-15 epoxy resin. The other consists of AS4 carbon and 411-350 epoxy (vinyl ester or derakane momentum) resin. The fibers are assumed to be arranged in a hexagonal array (figure 5-10) in the matrix in the tow. The tow properties were found using 3D finite element micromechanics analysis using an in-house finite element code alpha. One-fourth of the unit cell was used to calculate the tow properties and is shown in figure 5-11. The material properties of the fiber, matrix, and the tow are given in table 5-4 for both material systems. For carbon/epoxy material system, the properties of the tow are given both for lenticular and flattened cross-sections as the fiber volume fraction in them is different.

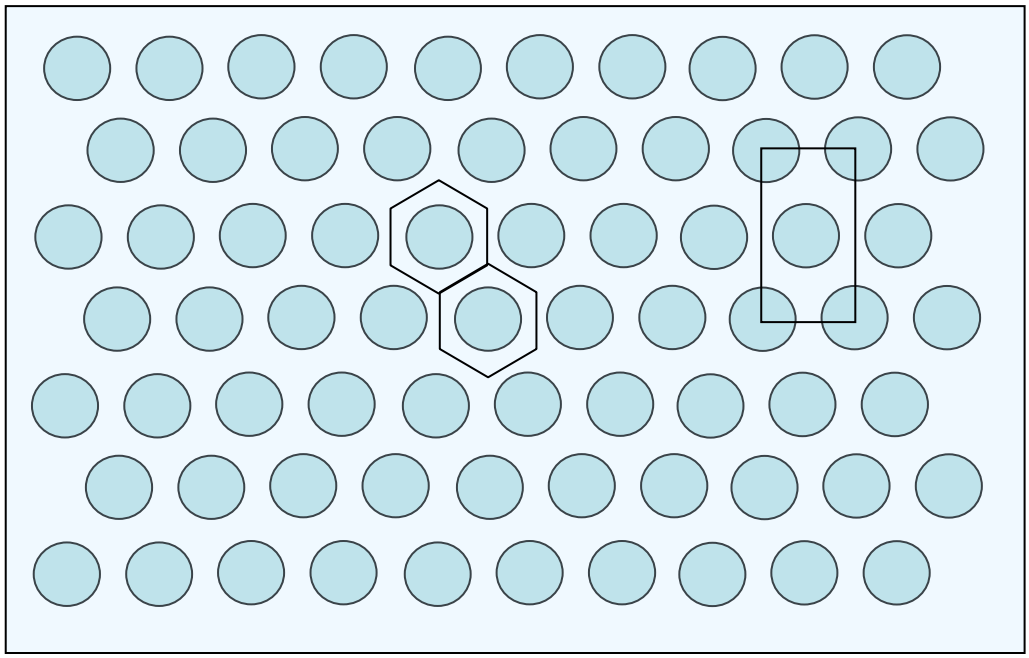

Figure 5-10. Distribution of Fibers Inside the Tow

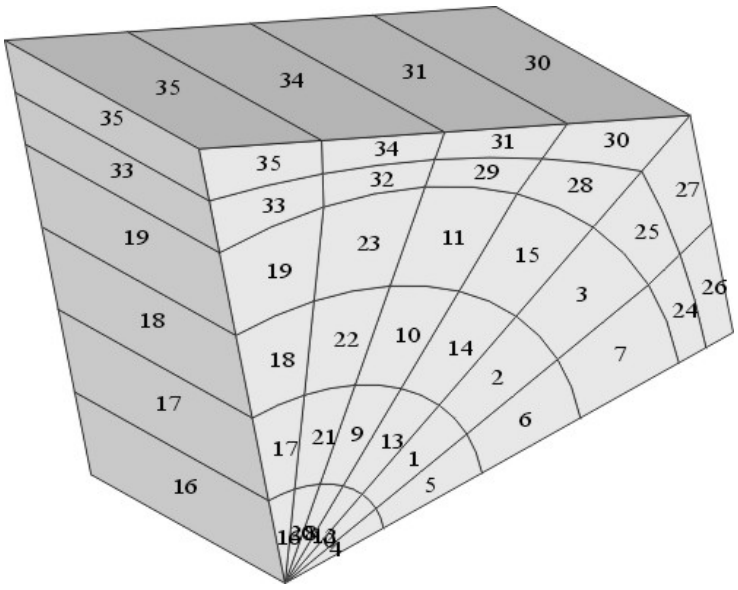

Figure 5-11. Finite Element Mesh for Calculating Tow Properties

Table 5-4. Material Properties for Fiber, Matrix, and Tow

Property*	Glass/Epoxy Material System			Carbon/Epoxy Material System			
	Fiber	Resin	Tow[a]	Fiber	Resin	Tow[b] Flattened x Section	Tow[c] Lenticular x Section
E_{11}	96.53	2.82	76.42	228	3.1	157.95	204.36
E_{22}	96.53	2.82	20.18	16.54	3.1	9.027	13.4
E_{33}	96.53	2.82	20.18	16.54	3.1	9.027	13.4
ν_{12}	0.23	0.395	0.2654	0.2	0.35	0.2412	0.2122
ν_{23}	0.23	0.395	0.3352	0.25	0.35	0.3749	0.2974
ν_{13}	0.23	0.395	0.2654	0.2	0.35	0.2412	0.2122
G_{12}	39.23	1.01	7.4	24.82	1.15	5.12	14.62
G_{23}	39.23	1.01	4.03	6.89	1.15	3.34	5.33
G_{13}	39.23	1.01	7.4	24.82	1.15	5.12	14.62

[a]Fiber volume fraction in tow = 0.7854
[b]Fiber volume fraction in tow = 0.69
[c]Fiber volume fraction in tow = 0.895
*All moduli in GPa

5.7 TAPE LAMINATE APPROXIMATION.

The predictions of the effective properties of the 2x2 braids using finite element analysis were compared with the predictions of a tape laminate. In the braid, tows run at an angle of $+\theta$ and $-\theta$, and mats are symmetrically stacked. Hence, one-half the laminate configuration essentially consists of two unidirectional laminas (with properties of the tow) in $+\theta$ and $-\theta$ directions and a third layer as matrix to account for matrix pockets in the braid, as shown in figure 5-12. The thickness of each layer was specified such that the laminate and the braid had the same volume fraction of resin and tows in the model. The reason for doing this laminate analysis is threefold: (1) It will compare the performance of 2x2 braids with equivalent laminated materials. (2) It would be helpful in investigating whether the effective properties of the braids can be predicted using simple analysis like laminate theory (laminate theory codes are easily accessible and well understood by designers). (3) The properties predicted by 3D finite element analysis of braids were normalized by the laminate predictions to see the exclusive effect of interlacing. The effective properties for the equivalent laminate were obtained using a 3D finite element model with periodic boundary conditions. It should be noted that it is usually more convenient to use classical laminated plate theory for the in-plane properties or the full 3D homogenization formulas, given in several references (Sun and Li, 1988; Whitcomb and Noh, 2000), if out-of-plane properties are needed.

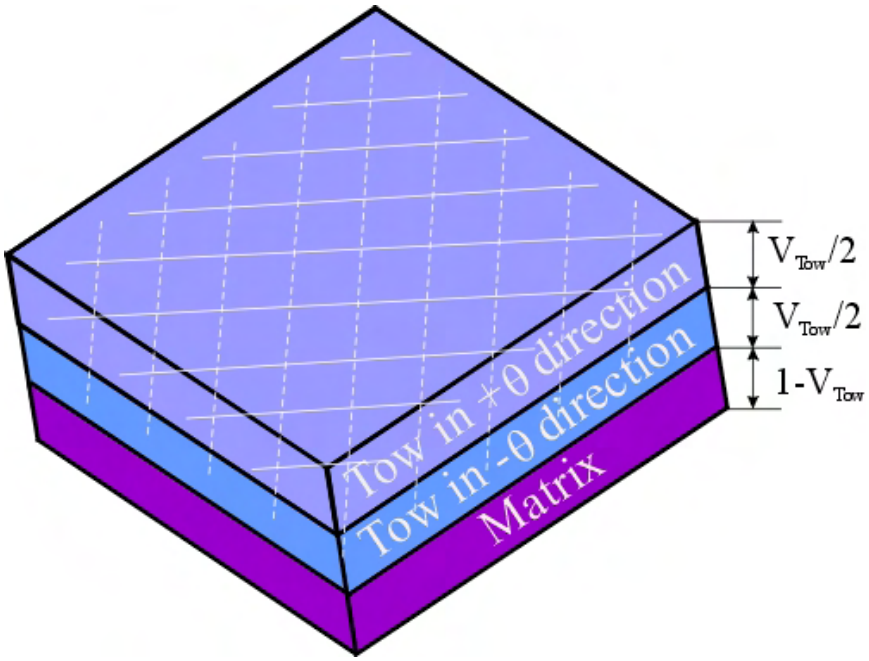

Figure 5-12. An Equivalent Laminate Configuration

6. PARAMETRIC STUDIES: EFFECT OF VARIOUS PARAMETERS ON EFFECTIVE ENGINEERING PROPERTIES.

6.1 INTRODUCTION.

Obtaining effective mechanical properties is the first order of concern in any structural analysis. This section presents an investigation of the effect of various parameters like braid angle, WR, material properties, and cross-section shape on the effective engineering properties of the 2x2 braids. Extensive parametric studies were conducted to determine the behavior of the 2x2 braids. The studies were conducted for two material systems: glass fiber/epoxy (S2/SC-15) matrix and carbon fiber/epoxy (AS4/411-350) matrix. The properties were compared with those for an equivalent laminated material with angle plies and a resin layer. The results of parametric studies will be discussed in detail.

The predictions of the moduli and the Poisson's ratio were also compared with the experimental data (Kelkar, et al., 2003a) for the carbon/epoxy material system.

6.2 RESULTS OF PARAMETRIC STUDIES.

To characterize the mechanical behavior of braided composites, the effective engineering properties were calculated for a wide range of braid angle and WR for glass/epoxy and carbon/epoxy material systems. For carbon/epoxy material system, the effect of tow cross-section shape on effective properties was also determined. Then the predictions of the finite element analyses were compared with the predictions of a simple 3D laminate analysis. All the elements of the 6x6 compliance matrix were calculated and it was observed that all the shear coupling coefficients were almost zero, which predicted the material to be effectively orthotropic. The braid patterns along the longitudinal and transverse directions differ, which caused the complementary properties to differ along these directions. The difference in complementary properties due to unbalance in material architecture was investigated. The results of parametric studies are presented here. Finally, the predictions are compared with the experimental results.

6.3 EFFECT OF VARIOUS PARAMETERS ON EFFECTIVE PROPERTIES.

Figure 6-1 shows the variation of E_{11} with braid angle and WR for the carbon/epoxy material. The dots in the figure are finite element data. The data were fitted to obtain the surface plot. The outlined curve shows the values for the reference laminate. The figure shows that most of the effect of braid angle on the E_{11} can be predicted using laminate theory. This is the case for other effective properties. Hence, to reveal the exclusive effects of the braid architecture and to filter out the braid angle effect by the laminate theory, the results were normalized by the respective reference laminate values.

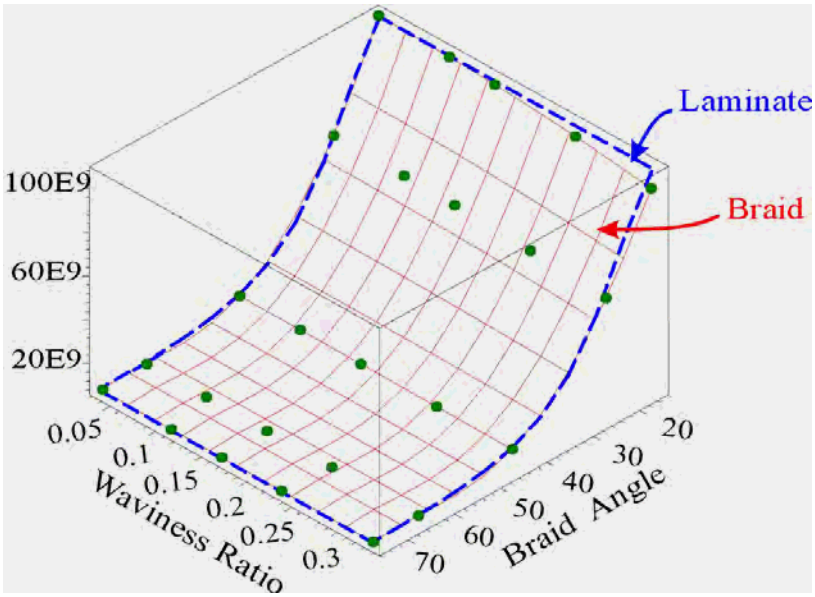

Figure 6-1. Effective Longitudinal Modulus E_{11} as a Function of Braid Angle and Waviness Ratio for Carbon/Epoxy Material (Discrete points are the data from the finite element analysis.)

Figures 6-2 and 6-3 show the normalized effective engineering properties as a function of braid angle and WR for glass/epoxy and carbon/epoxy, respectively. Figure 6-3a shows the properties of the carbon/epoxy material system with flattened tow cross-section, and figure 6-3b shows those calculated with lenticular cross-section. For carbon/epoxy material system effect of tow cross-section on effective properties was also determined. The range for the waviness change is from 0.03 (very flat) to 0.33 (very wavy) for both materials. The range for the braid angle is 20º~70º for glass/epoxy and 15º~75º for carbon/epoxy. Figure 6-2 shows that for the glass/epoxy material system, E_{11}, E_{22}, E_{33}, and G_{12} decrease while G_{23}, G_{13}, ν_{23}, and ν_{13} increase with an increase in WR for all braid angles. The ν_{12} does not change much with WR for all braid angles. Figures 6-3a and 6-3b show that for the carbon/epoxy material system, the in-plane moduli (E_{11}, E_{22}, and G_{12}) decrease while the out-of-plane shear moduli G_{23} and G_{13} increase with an increase in WR. The out-of-plane extensional modulus E_{33}, remains almost constant and is greater than the corresponding laminate values for all braid angles and WR. The change in the υ_{12} is small but not uniform for different braid angles. For some braid angles, υ_{12} decreases with WR, and for others, it first increases and then decreases. As far as ν_{23} and ν_{13} are concerned, the normalized values do not change much with WR as long as corresponding reference values are not very small (i.e., close to zero). But, it should be noted that there are cases in which the reference laminate value for the out-of-plane Poisson's ratio is extremely small in magnitude at certain braid angles. For example, the value of ν_{23} for reference laminate of carbon/epoxy material system corresponding to ±65.25° braid was 0.0023. As a result, a small deviation will result in an extremely large normalized value. Hence, some range of braid angle for carbon/epoxy material with lenticular cross-section was excluded in the results presented for ν_{23} and ν_{13}.

Further, it can be noted from figures 6-2 and 6-3 that even for very low WR, the values do not converge to the values predicted by the laminate model. This is due to the fact that, although the laminate model can account for the braid angle effect, it cannot account for the effect of material distribution.

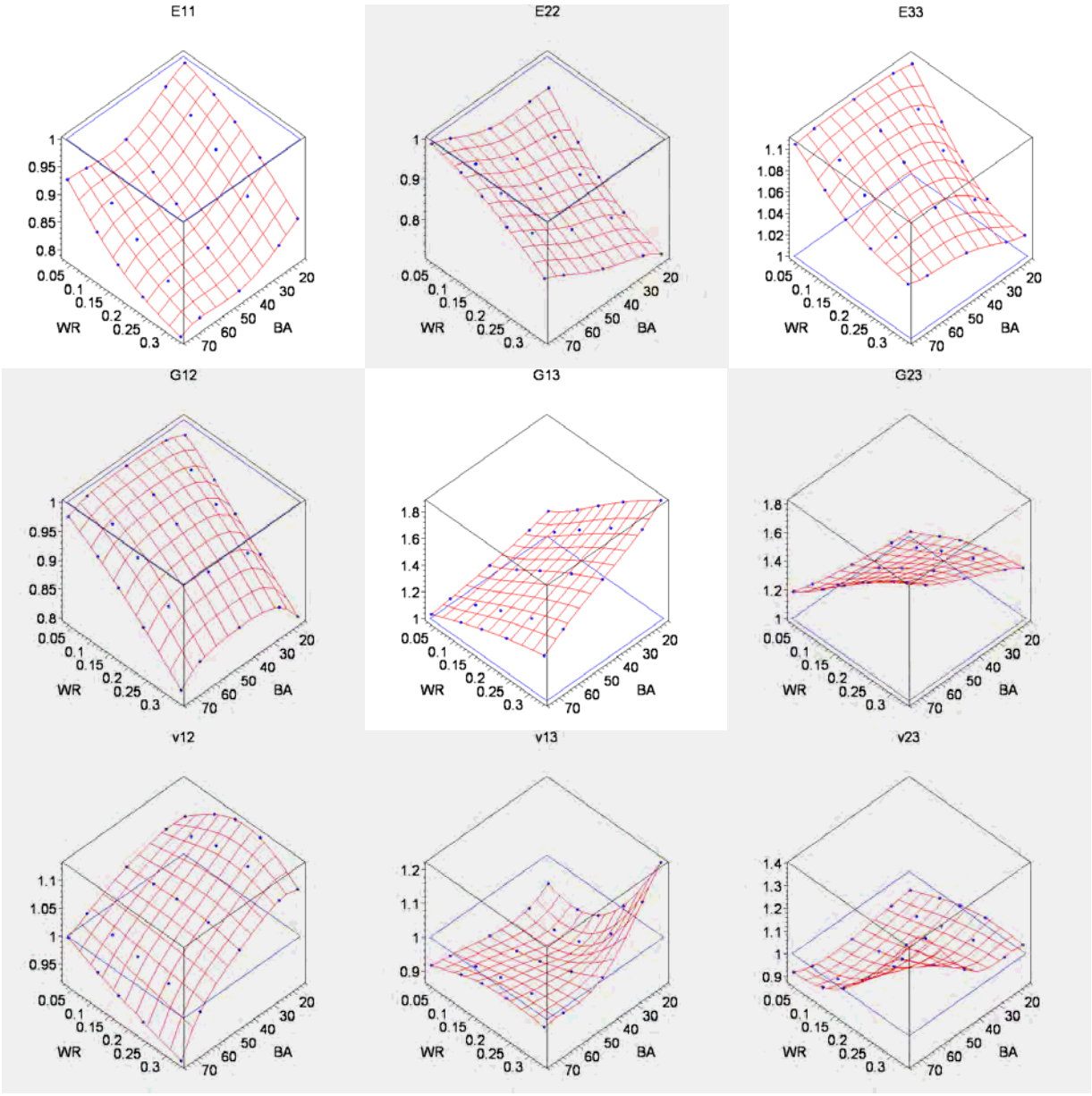

Figure 6-2. Normalized Effective Engineering Properties as a Function of Braid Angle and Waviness Ratio for Glass/Epoxy Material System With Lenticular Cross-Section (The properties are normalized by the laminate values.)

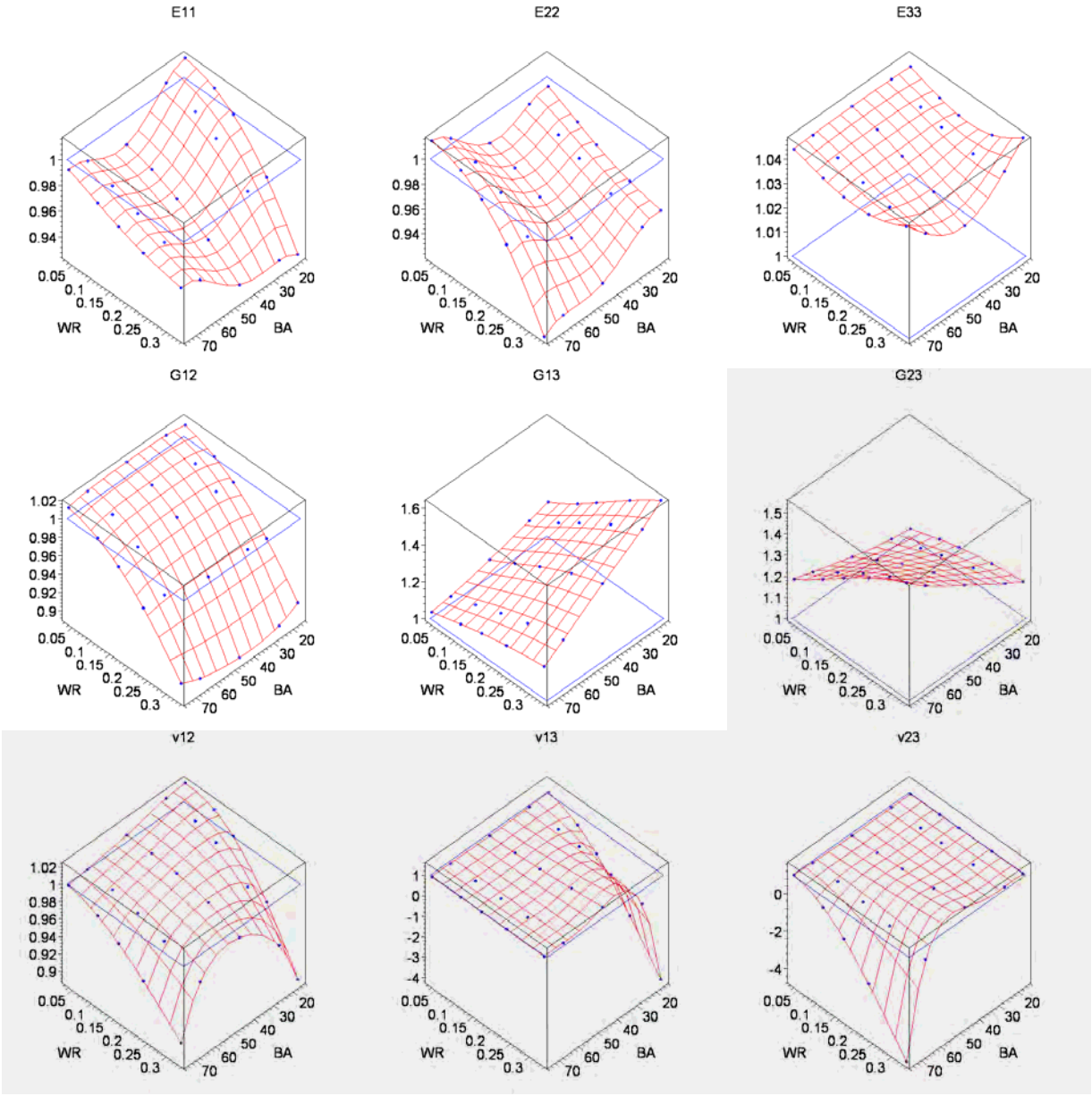

Figure 6-3a. Normalized Effective Engineering Properties as a Function of Braid Angle and Waviness Ratio for Carbon/Epoxy Material System for Tow With Flattened Cross-Section (The properties are normalized by the laminate values.)

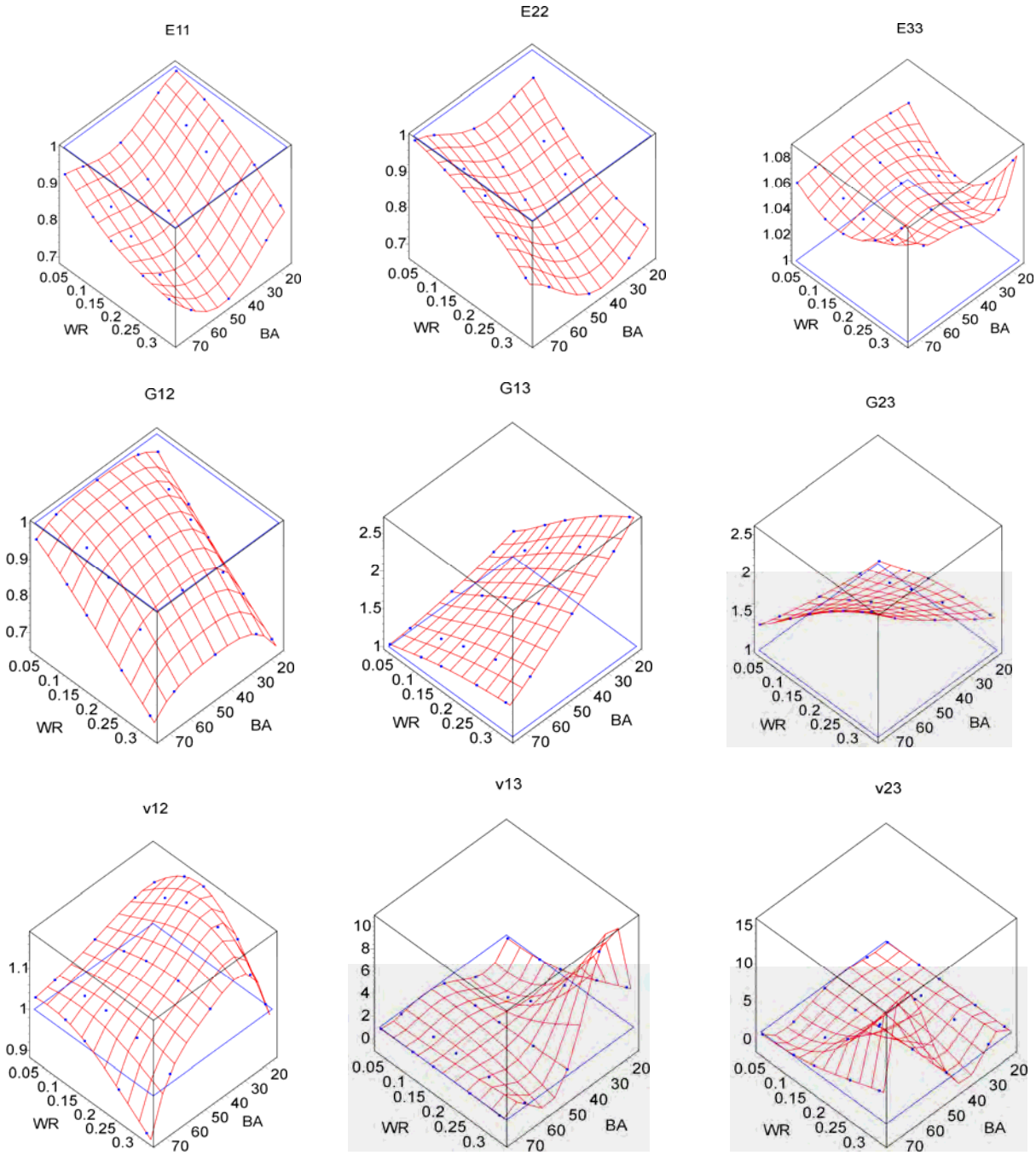

Figure 6-3b. Normalized Effective Engineering Properties as a Function of Braid Angle and Waviness Ratio for Tow With Lenticular Cross-Section
(The properties are normalized by the laminate values.)

6.4 DEVIATION OF THE PROPERTIES FROM REFERENCE LAMINATE VALUES.

The deviation of the properties from the reference laminate values is measured by $(E^{extreme}-1)*100\%$, where $E^{extreme}$ is either E^{min} or E^{max}, which are the normalized minimum and maximum property values for the range in which the parameters vary. Therefore, E^{min} and E^{max} correspond to the lower and upper deviations from laminate theory, respectively. The deviation of properties from laminate theory is plotted in figures 6-4 through 6-6. The closer the extremity of the band to zero, the smaller is the deviation from laminate theory.

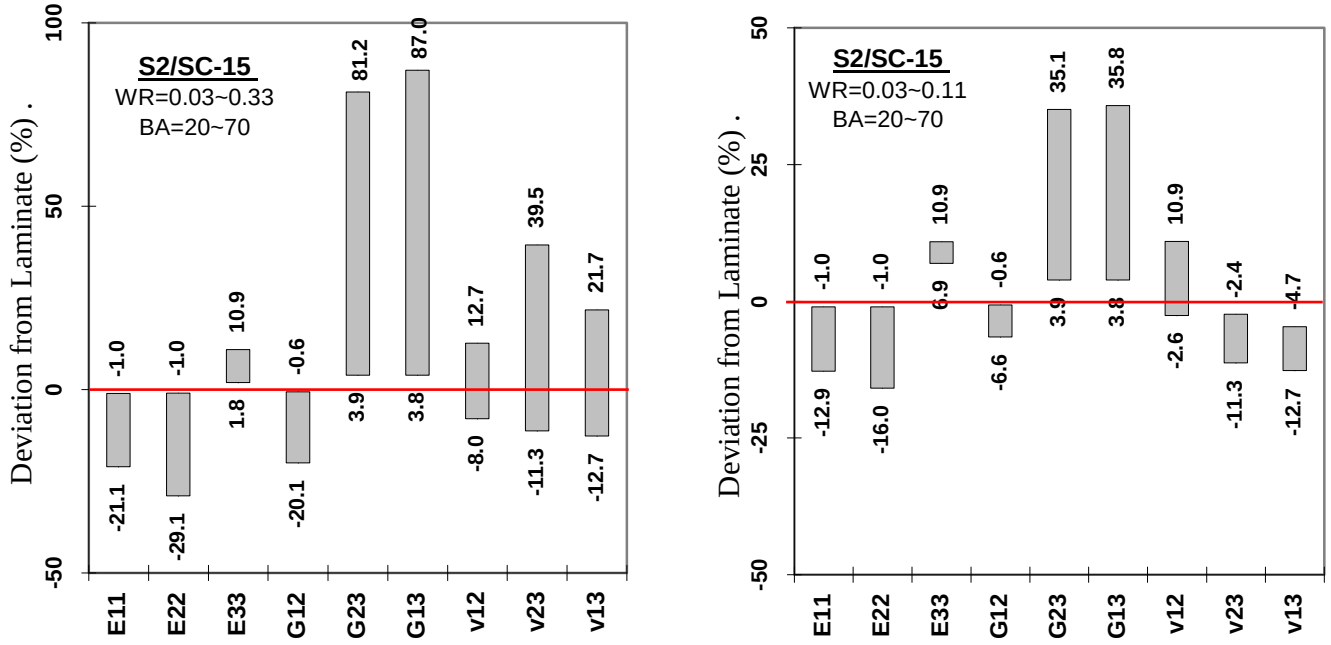

(a) For full range of WR

(b) For realistic range of WR

Figure 6-4. Deviation of 3D Finite Element Results From the Laminate Results for Glass/Epoxy Material System With Lenticular Cross-Section

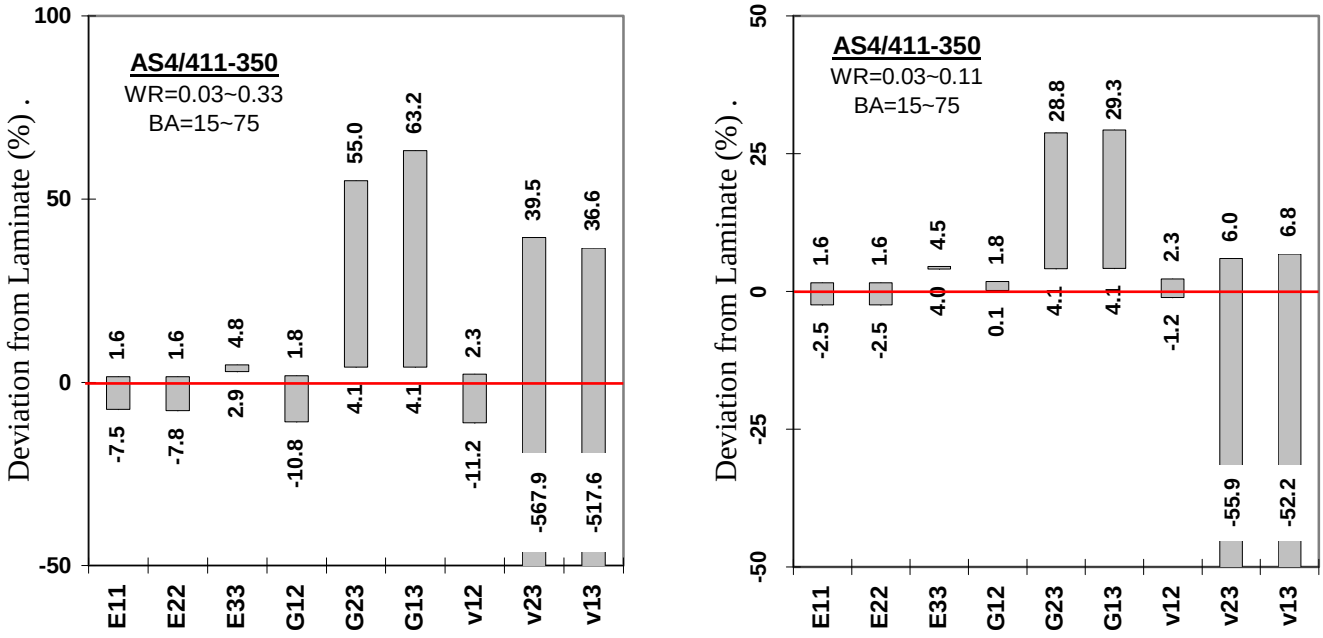

(a) For full range of WR

(b) For realistic range of WR

Figure 6-5. Deviation of 3D Finite Element Results From the Laminate Results for Carbon/Epoxy Material System With Lenticular Cross-Section

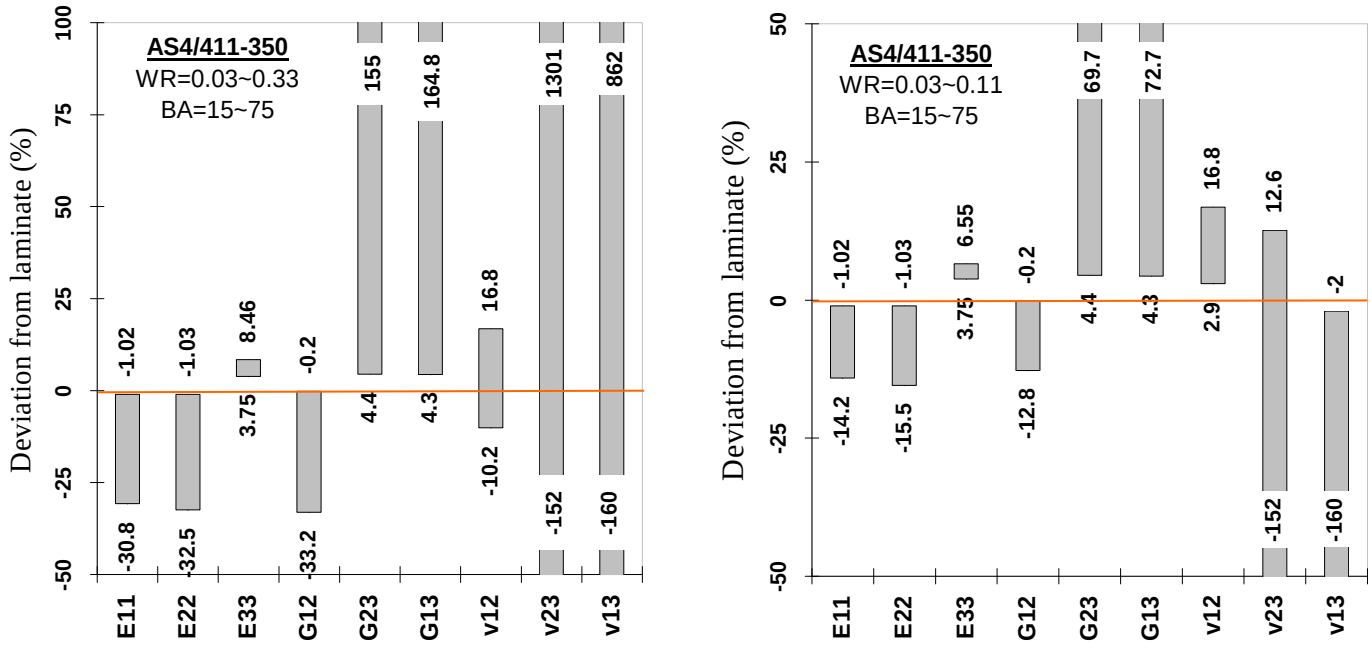

(a) For full range of WR

(b) For realistic range of WR

Figure 6-6. Deviation of 3D Finite Element Results From the Laminate Results for Carbon/Epoxy Material System With Lenticular Cross-Section

For the full range of WR studied (0.03-0.33), the deviation of the finite element results from the laminate results for the effective properties is shown in figures 6-4(a), 6-5(a), and 6-6(a) for both the material systems. In general, the out-of-plane properties have higher deviation than in-plane properties. Maximum deviation is observed for out-of-plane shear moduli for both the material systems (ignoring the high deviation of out-of-plane Poisson's ratios for the reason mentioned earlier). The maximum deviation is 87% for the glass/epoxy and around 165% for carbon/epoxy material system and is for G_{13}. The largest deviation (absolute value) for in-plane properties is 33.2% for the carbon/epoxy and 29.1% for the glass/epoxy. In general, the glass/epoxy material system has a larger deviation for almost all the properties (excluding ν_{23} and ν_{13} for the reasons already mentioned) than for carbon/epoxy material system with flattened cross-section, but has a smaller deviation than one with lenticular cross-section. Figures 6-5(a) and 6-5(b) show that carbon/epoxy with lenticular cross-section has considerably more deviation than that with flattened cross-section for all the properties. Hence, it is more difficult to predict the response of a braid using simple laminate approximation for material system with lenticular tows that ones with flattened tows even if the model contains the same overall fiber volume fraction.

Since out-of-plane modulus E_{33} has a small deviation from the laminate value, it can be predicted easily using 3D laminate analysis. For the two material systems used in this study, the E_{33} is larger than the laminate value, as shown in figures 6-2 and 6-3. In general, the E_{33} can be more than, equal to, or less than the laminate value, depending on the material system used. For example, for the material system used by Paumelle, et al., 1990, the E_{33} is smaller than the laminate value (the results for that material system are not shown here).

In figures 6-4(b), 6-5(b), and 6-6(b), the deviation is shown for the reduced WR range (0.03~0.11). As the WR range is reduced, the deviation band also shrinks. For carbon/epoxy with flattened cross-section, the in-plane properties (E_{11}, E_{22}, G_{12}, and ν_{12}) can be predicted quite accurately with a maximum error of 2.5%. But for both the glass/epoxy and carbon/epoxy material systems with lenticular cross-sections, the in-plane properties have larger deviation from the laminate predictions. The deviation can be as large as 16%, which suggests that simple laminate model may not be a good choice for approximation. So it can be concluded that the use of laminate theory to approximate the properties of the braids is contingent upon the material system and tow cross-section shape. For the transverse shear properties (G_{13} and G_{23}), the deviation is more than 29% for both material systems, which suggests the necessity for a more accurate simple analytical model than 3D laminate theory.

6.5 COMPLEMENTARY BRAIDS.

If the braid angle is $\pm\theta$, then its complementary braid angle is defined here to be $\pm(90-\theta)$. Furthermore, the property pairs (E_{11}, E_{22}), (υ_{23}, υ_{13}), and (G_{23}, G_{13}) are defined to be complementary of each other if the first property in any pair belongs to $\pm\theta$ braid and the second belongs to $\pm(90-\theta)$ braid. The complementary properties are equal for an ordinary tape laminate. But this is not the case for braids. This effect, which is not intuitively obvious, is due to the difference in material architecture that exists in braids. This difference in material architecture is called unbalance herein. This aspect of 2x2 braids was explored to see if there was an advantage in selecting one braid over its complementary braid.

To illustrate the idea, figure 6-7 shows the axial moduli of a 2x2, -45° braid along four different directions. It was observed that the value of $E_{11}^{'}$ and $E_{22}^{'}$ is exactly the same (= 26.8 GPa) (Tang, 2001), as shown in figure 6-7. This is due to the fact that material architecture is identical along $X_1^{'}$ and $X_2^{'}$ axes. One might expect the same for a 2x2, ±45° braid also. But, in the case of 2x2 braid, there exists a difference of approximately 3% in the values of E_{11} and E_{22}, as shown in figure 6-7 (E_{11} = 12.7 GPa and E_{22} = 12.3 GPa). This is because the interlace pattern is different along lines marked by aa′ and bb′. Along aa′, each +θ braid tow passes over -θ braid tow, but along bb′, one +θ tow passes over and then under a -θ tow making the interlace pattern different along these two lines.

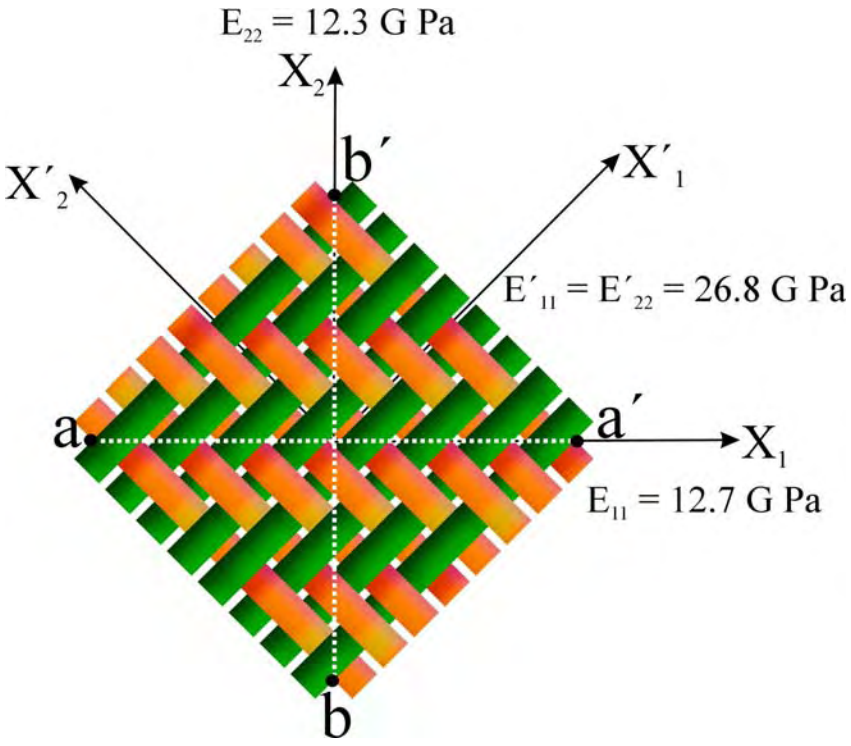

Figure 6-7. Difference in Properties of Complementary Braids

It was observed that the maximum difference in modulus is ~11% for the full range of WR (0.03-0.3). For the realistic range of WR (0.03-0.11), the difference between complementary moduli is negligibly small. The moduli have the largest differences (<4%), which is very small for both the material systems. Hence, detailed results are skipped here.

6.6 COMPARISON OF PREDICTIONS WITH EXPERIMENTAL DATA.

A comparison was made with some of the preliminary experimental results for the carbon/vinyl ester epoxy and carbon/EPON epoxy material systems used by Kelkar, et al., 2003. Experimental results for carbon/vinyl ester are listed in tables 6-1 and 6-2 and carbon/EPON are listed in table 6-3. The modulus and Poisson's ratio available for comparison are E_{11} and ν_{12}, respectively.

Table 6-1. Experimental Results for Carbon/Vinyl Ester

Specimen	1	2	3
Area, mm^2 (in^2)	129.03 (0.20)	123.95 (0.191)	128.06 (0.197)
Failure load, KN (Kips)	88.25 (19.84)	75.55 (16.99)	81.78 (18.39)
Ultimate tensile strength, MPa (Ksi)	683.31 (99.11)	612.52 (88.84)	638.59 (92.62)
% Elongation at failure	1.108	0.997	1.160
Modulus, GPa (Msi)	71.33 (10.35)	68.52 (9.94)	63.71 (9.24)
Poisson's ratio	1.22	1.17	1.16
Braid angle	24.52	25.05	25.95

Kips = Kilo instructions per second

Table 6-2. Comparison With Experimental Results for Carbon/Vinyl Ester, BA 25° ±1°

All Moduli in GPa	Finite Element Model Prediction		Experiment		
	Flattened	Lenticular	Specimen 1	Specimen 2	Specimen 3
E_{11}	64.67	77.6	71.33	68.52	63.71
E_{22}	8.69	12.96	-	-	-
E_{33}	8.26	8.52	-	-	-
G_{12}	21.82	23.6	-	-	-
G_{23}	2.75	2.51	-	-	-
G_{13}	3.55	3.4	-	-	-
ν_{12}	1.532	1.06	1.22	1.17	1.16
ν_{23}	0.313	0.30	-	-	-
ν_{13}	-0.226	-.02	-	-	-

Table 6-3. Comparison With Experimental Results for Carbon/EPON

	Experimental	FEM	Experimental	FEM	Experimental	FEM
Fiber volume fraction	$0.51^{\pm 0.05}$	0.51	$0.53^{\pm 0.05}$	0.51	$0.52^{\pm 0.03}$	0.51
Braid angle	25° ±2° Braided Tubes	25º	30° ±1° Slit Sleeves	30º	45° ±1° Slit Sleeves	45º
Average E_{11}, Msi	54.23	57.03	38.04	40.31	15.92	13.59
Average ν_{12}	1.44	1.53	1.34	1.469	0.69	0.797

FEM = Finite element model

The finite element results are also listed in table 6-2 along with experimental values for comparison for carbon/vinyl ester material system. The braid angle of each specimen varies within ±1° of 25°. The average of measured braid angles was used for the finite element results. The finite element results are given for both flattened as well as lenticular cross-section. The table shows that the experimental values of E_{11} and υ_{12} fall within the range of predicted results. If one can determine the shape of cross-section in the actual material, finite element results might be able to make a good prediction. Comparison for carbon/EPON is shown in table 6-3. Three braid angles were used for experiments: ±25°, ±30°, and ±45°. For this material system, experimental values of E_{11} and υ_{12} fall within the range of predicted results.

6.7 SUMMARY OF EFFECTIVE PROPERTY RESULTS.

The effective properties of the 2x2 braids were obtained using 3D finite element analysis. The analysis showed that the material was essentially orthotropic. It was observed that in the range of WR 0.03 to 0.11, which is more representative of most structural 2D braids, the in-plane properties of carbon/epoxy material system with flattened cross-section can be predicted very well by using a simple laminate model. However, for the glass/epoxy and carbon/epoxy with lenticular cross-section, the laminate analysis can produce as large as 16% error for the in-plane properties of the 2x2 biaxial braids. The most sensitive effective properties were found to be the transverse properties (G_{13}, G_{23}, υ_{13}, and υ_{23}). This suggests that the simple laminate theory cannot be used to get reasonable approximation for the transverse properties of the braid. It was observed that the G_{13} and G_{23} can be as much as 72% greater than the laminate value, which means a considerable increase in transverse shear modulus can be achieved using the 2x2 biaxial braid, as compared to the equivalent angle-ply tape laminate. This can be significant for structural applications in which higher G_{13} and G_{23} are desirable.

To predict the properties of braids using simple laminate analysis, it is important to know the cross-section shape of the braid under investigation, as the response of a braid with flattened cross-section can be predicted more confidently and with less error than that with a lenticular cross-section. For the same overall fiber volume fraction for carbon/epoxy material system, the lenticular cross-section was stiffer than a flattened cross-section.

The properties of complementary braids differ from each other due to unbalance in material architecture that exists in braids. It was seen that for realistic range of WR (0.03-0.11) and braid angle of 15°-75°, the different between complementary moduli was less than 4%, which is not very significant.

7. PROGRESSIVE FAILURE ANALYSIS.

7.1 INTRODUCTION.

Periodic analysis is generally used in the modeling of textile composites, which are usually idealized to possess perfectly uniform periodic microstructures. However, the as-manufactured textile composites generally do not have perfectly uniform microstructures due to variations in tow geometric properties such as waviness, cross-section shape, and fiber volume fractions. Therefore, their behavior cannot be fully characterized by conducting periodic analysis on a single unit cell model. This section focuses on the effect of variation in braid parameters on the progressive failure behavior of a 2x2 braided composite laminate subjected to uniaxial loading. A multiscale analysis approach (Ghosh, et al., 2001; Rudd and Broughton, 2000; and Oden, et al., 1999) was used. The laminate consists of stacked 2x2 braid mats. Each mat is made of interlaced tows and matrix pockets, and the tow contains fibers and matrix. A bottom-up multiscale finite element modeling approach was employed that sequentially considered the fiber/matrix scale, the tow architecture scale, and the laminate scale. The emphasis was placed on examining the difference between the responses from the periodic analysis and the responses from a model that considers the variation in braid parameters throughout the model. The details of the analysis approach, the multiscale finite element models, and the numerical results are described and the analysis results are presented and discussed.

7.2 DESCRIPTION OF MULTISCALE ANALYSIS.

The multiscale analysis method and approach used in this study is a sequential coupling method, which individually considers three scales: fiber/matrix scale, tow architecture scale, and laminate scale. Figure 7-1 illustrates these scales.

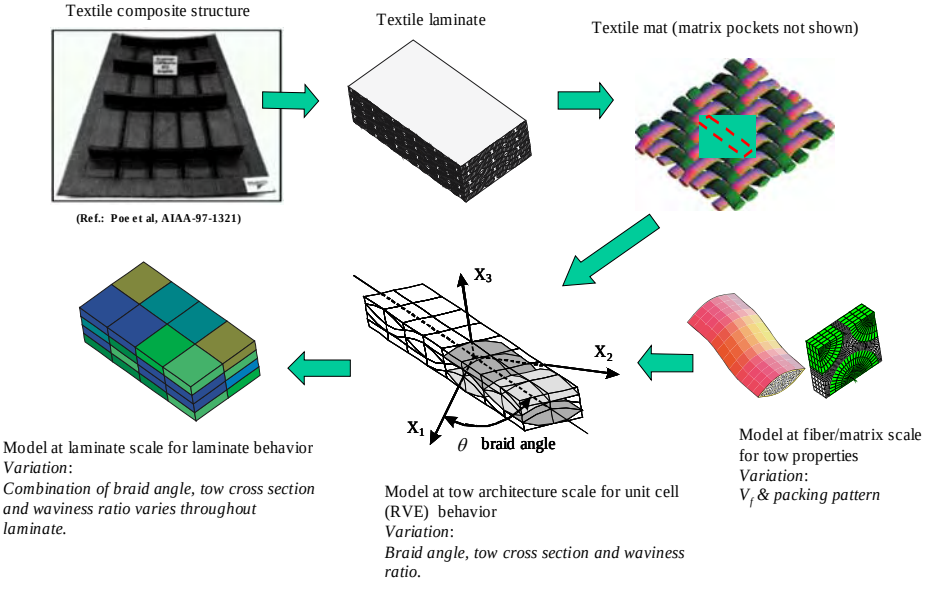

Figure 7-1. Overview of Multiscale Modeling of Textile Composites

The model for the fiber/matrix scale contains fibers and matrix. The fiber packing pattern and its volume fraction can vary from model to model. In this study, only a hexagonal arrangement of fibers was considered. The input requirements for properties at this scale are the moduli and strengths for the fibers and pure matrix. Finite element models were built to obtain the effective moduli of the fiber/matrix unit cell for a given fiber volume fraction, while the strength data of the fiber/matrix unit cell are calculated using the Chamis simplified formulas (Chamis, 1984). The results were used for the tows that were treated as a homogeneous transversely isotropic material and were used in the unit cell models at the tow architecture scale.

The model at the tow architecture scale contains tows and matrix pockets. The construction of the model depends on many geometric parameters required to define a specific textile, such as waviness ratio, tow volume fraction, tow interlacing pattern, and tow braid angle. For the 2x2 braid considered in this research, a series of unit cell models were built to study the effect of variation in the tow volume fraction, tow waviness, and braid angle. Periodic boundary conditions were imposed. The properties of matrix pockets are the same as those used at the fiber/matrix scale, while the properties of tows are the results coming from the analyses at the previous scale, the fiber/matrix scale. Progressive failure analysis was conducted for each unit cell model under uniaxial load condition. The progressive failure responses were then used in the analysis at a larger scale, the laminate scale. To facilitate such utilization, the predicted response was replaced by the equivalent nonlinear behavior of the unit cell model. In this way, there was no failure information being passed onto the next modeling scale except this equivalent nonlinear behavior, thus removing the need for a coupling between two scales. This was accomplished as follows: At each loading step, the full set of effective properties of the unit cell models were calculated based on the current damage state of the model. Six loading cases needed to be considered to obtain the full set of 3D properties. This set of 3D properties was then stored with the corresponding the applied strain. The collection of these results formed a database and was used for the calculation of overall response at the laminate scale. It was assumed that failure at a material point in the laminate model was governed by the axial stress only. This results in a great simplification, which is probably justified, since the laminate is subjected to uniaxial load only.

The analysis model at the laminate scale contained four 2x2 braid mats, stacked together with the same orientation. Symmetry conditions were imposed on the lower surface and periodic conditions on the upper surface. Hence, the model represented the behavior of an infinitely thick laminate with a repeating eight mat group. To account for the variation in the braid parameters, each finite element in the model was treated as a homogeneous orthotropic material whose effective properties were determined from the previous modeling scale, the tow architecture scale, for a specific combination of braid angle, tow volume fraction, and WR. The progressive failure analysis proceeded such that at each loading step, the stiffness properties at each gauss point of the element were updated using the predicted strain state from the laminate model and the effective properties generated at the previous modeling scale.

7.3 TYPICAL FINITE ELEMENT MODELS.

The following describes the finite element models built for all three scales: fiber/matrix, tow architecture, and laminate scales.

7.3.1 Fiber/Matrix Model.

As described in section 5, at the fiber/matrix scale, a hexagonal fiber arrangement was assumed and a finite element model was built for a quarter of the full unit cell after exploiting the symmetries (figure 5-11). Depending on the load conditions, different multipoint constraints were imposed to the model. The fiber/matrix finite element model was used for the computation of the effective moduli of material.

7.3.2 Tow Architecture Model.

The tow architecture models are similar to those shown in section 5-4. To study the effect of variation in braid parameters on the predicted progressive failure behavior, a collection of finite element meshes were built for various combinations of braid angle and tow volume fraction (V_{TOW}) while maintaining the overall fiber volume fraction ($V_f^{Overall}$ = 57%) constant. The complete list of the models is given in table 7-1. The model (B13) with braid angel BA = 28° and V_{TOW} = 74.33% was chosen as the reference unit cell model. Figure 7-2 shows the finite element mesh for the reference unit cell model, which contains 480 hexahedral 20-node brick elements and 2158 nodes.

Table 7-1. Parameters for Defining Various Unit Cell Models

Model	$V_f^{Overall}$ (%)	V_{TOW} (%)	Braid Angle	Waviness Ratio
B01	57	63.76	24	0.167
B02	57	68.99	24	0.195
B03	57	74.33	24	0.236
B04	57	79.66	24	0.298
B05	57	85	24	0.404
B06	57	63.66	26	0.177
B07	57	68.99	26	0.207
B08	57	74.33	26	0.250
B09	57	79.66	26	0.316
B10	57	85	26	0.428
B11	57	63.66	28	0.200
B12	57	68.99	28	0.218
B13	57	74.33	28	0.273
B14	57	79.66	28	0.345
B15	57	85	28	0.451
B16	57	63.66	30	0.194
B17	57	68.99	30	0.236
B18	57	74.33	30	0.275
B19	57	79.66	30	0.347

Table 7-1. Parameters for Defining Various Unit Cell Models (Continued)

Model	V_f^{Overall} (%)	V_{TOW} (%)	Braid Angle	Waviness Ratio
B20	57	85	30	0.507
B21	57	63.66	32	0.202
B22	57	68.99	32	0.236
B23	57	74.33	32	0.286
B24	57	79.66	32	0.360
B25	57	85	32	0.489

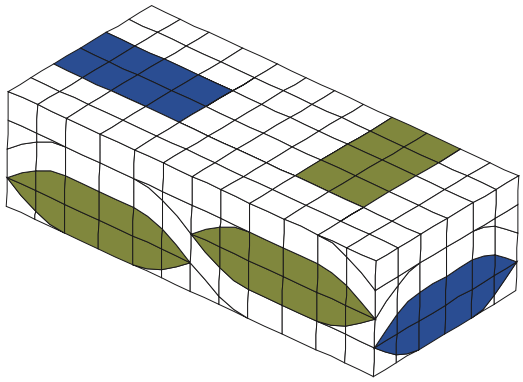

Figure 7-2. Finite Element Mesh for Reference Unit Cell Model

It should be noted that the variation in tow waviness was not explicitly considered due to the findings from a previous study (Tang, et al., 2003). In that study, it was found that the in-plane effective moduli were not very sensitive to the change of WR. Initial modeling results of this study also showed little sensitivity of progressive failure behavior under in-plane axial loading to small changes of tow waviness.

7.3.3 Laminate Model.

In this study, the finite element model was constructed as shown in figure 7-3. There were four layers of braid mat along the thickness direction. The size of each element is comparable to the size of the unit cell model at tow architecture scale. Each element is associated with one of the unit cell models at the tow architecture scale to simulate the variation in braid angle and tow volume fraction. Thus, the effective properties (nonlinear as described in the next few sections) obtained at the tow architecture scale will be used for one element in the laminate model.

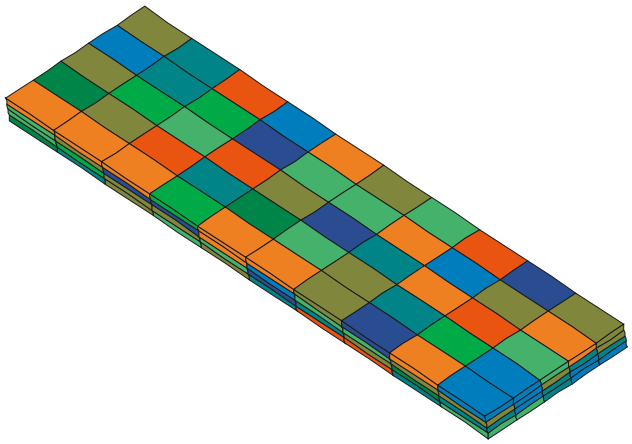

Figure 7-3. Finite Element Model at the Laminate Scale

7.4 MATERIAL PROPERTIES FOR FAILURE ANALYSIS.

The material system used was carbon fiber/epoxy (AS4/411-350). Elastic behavior was assumed for both the fibers and matrix. The basic input requirements are the engineering moduli, and strength data for the fibers and matrix are listed below.

- Resin: 411-350 vinyl ester (Isotropic)
  $E_{11} = E_{22} = E_{33} = 3.1$ GPa, $\nu_{12} = \nu_{23} = \nu_{13} = 0.35$, and $G_{12} = G_{13} = G_{23} = 1.15$ GPa
  $X_{11} = X_{22} = X_{33} = 79$ MPa and $X_{12} = X_{13} = X_{23} = 72$ MPa

- Fiber: AS4 (Transversely isotropic)
  $E_{11} = 227.53$ GPa, $E_{22} = E_{33} = 16.55$ GPa, $\nu_{12} = \nu_{13} = 0.2$, $\nu_{23} = 0.25$,
  $G_{12} = G_{13} =$ 24.82 Gpa, $G_{23} = 6.89$ GPa, and $X_{11} = 4156$ MPa

The effective moduli of tow were determined using finite element model of a hexagonal array of fibers. Although the failure model implemented into the code considered difference of tensile and compressive strength data, this particular study assumed identical tension and compressive strength.

7.5 FAILURE CRITERIA, DEGRADATION MODEL.

To focus on the objective of this study, i.e., to understand the effect of variation in braid parameters on the predicted progressive failure behavior of a braided composite laminate, no elaborate failure study was conducted to identify the best failure criterion and properties degradation model. Instead, all the progressive failure analyses conducted in this study used a selected failure criterion and a degradation model. The material response was assumed to be linear elastic until damage was predicted. The response after damage occurred was also assumed to be linear elastic, but with degraded moduli. The maximum stress failure criterion was used to predict damage. When a particular stress component exceeds its respective strength, the damage mode caused by that stress component has occurred. The corresponding modified compliance matrix $\bar{S}$ in terms of the original compliance matrix S is then given by

$$\overline{S_{ij}} = \begin{cases} a_i S_{ii}, & i = j, \quad \text{no sum on } i \\ S_{ij}, & i \neq j \end{cases} \tag{7-1}$$

where a_i are the degradation factors that are based on a modified version of Blackketter's model (Blackketter, 1993 and Chapman and Whitcomb, 2000) and are listed in table 7-2 (Chapman and Whitcomb, 2000). Specifically, the degradation factors are chosen based on micromechanics analysis of nonwoven laminates containing discretely modeled transverse matrix cracks (Srirengan and Whitcomb, 1998).

Table 7-2. Degradation Factors for All Damage Modes

Degradation Factors	Mode of Damage in Fiber Tows						Mode of Damage in Matrix					
	σ_{11}	σ_{22}	σ_{33}	σ_{12}	σ_{23}	σ_{13}	σ_{11}	σ_{22}	σ_{33}	σ_{12}	σ_{23}	σ_{13}
a_1	100	1	1	1	1	1	8	1	1	8	1	8
a_2	8	8	1	8	8	1	1	8	1	8	8	1
a_3	8	1	8	1	8	8	1	1	8	1	8	8
a_4	8/3	8/3	1	8/3	8/3	1	8/3	8/3	1	8	1	1
a_5	8/3	8/3	8/3	1	8/3	1	1	8/3	8/3	1	8	1
a_6	8/3	1	8/3	1	8/3	8/3	8/3	1	8/3	1	1	8

The assumed fiber direction is x_1

When the finite element method is used for the progressive failure analysis, the damage is predicted at each quadrature point in the material coordinate system. Thus, for an element at a certain point in the loading history, some quadrature points may or may not contain damage, which is collectively taken into account in the element stiffness matrix calculation by degrading the properties at each quadrature point in terms of the degree of predicted damage.

7.6 PROGRESSIVE FAILURE ANALYSIS FINDINGS.

There were multiple sets of results that were associated with each scale considered in the multiscale analysis carried out in this study. Some were intermediate results, which transfer data from a smaller scale to a larger scale, while others were from the entire multiscale analysis. In the following, the results from each modeling scale will be presented and discussed.

7.6.1 Fiber/Matrix Scale.

At fiber/matrix scale, the results from the analysis were the effective moduli and strengths of the fiber/matrix unit cell model. The effective moduli were obtained from the fiber/matrix finite element model. Four loading cases, $<\sigma_{11}>$, $<\sigma_{22}>$, $<\sigma_{12}>$, and $<\sigma_{23}>$, were considered to get the full 3D effective properties for a transversely isotropic material.

Figure 7-4 shows some of the effective properties of the fiber/matrix unit cell as a function of fiber volume fraction. The axial engineering properties E_{11} and ν_{12}, which vary linearly with the

fiber volume fraction and can be calculated using simple rule of mixture formulas, are not shown.

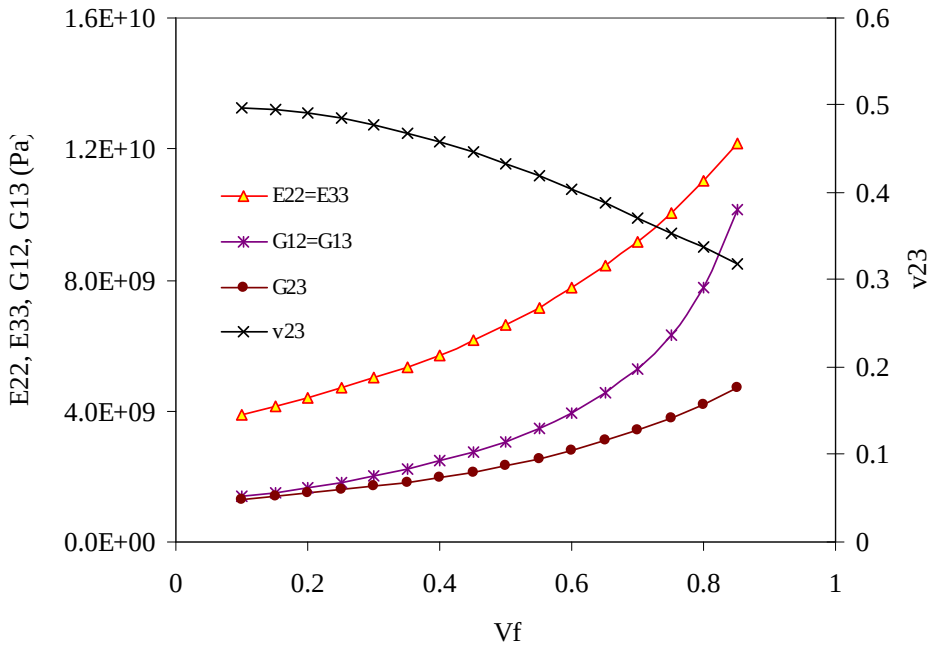

Figure 7-4. Effective Properties of the Fiber/Matrix Scale as a Function of Fiber Volume Fraction (The E_{11}, ν_{12}, and ν_{13} can be easily calculated using simple mixture rule.)

These results are used as the input properties for the tows contained in the unit cell model for the tow architecture scale. Since at the tow architecture scale, the tow volume fraction varies from model to model, the tow properties used are also different from model to model.

7.6.2 Tow Architecture Scale.

At tow architecture scale, the unit cell model is built for the given braid angle and tow volume fraction (V_{TOW}) while maintaining the overall fiber volume fraction ($V_f^{Overall}$) constant. The reference unit cell model was built using BA = 28°, V_{TOW} = 74.33%, and V_f^{TOW} = 76.69%. As mentioned earlier, the input required from the previous smaller scale, fiber/matrix scale, was the tow properties (effective moduli and strengths) for the tows contained at this scale. Therefore, for the reference model, the tow properties were calculated at the previous scale using $V_f = V_f^{TOW}$ = 76.69%.

Progressive failure analyses were conducted for all unit cell models with parameters listed in table 7-1. The load condition was the axial tensile loading <σ11>. As indicated in the description of adopted multiscale analysis approach, no coupling between the current scale and the next scale, the laminate scale, was considered. Consequently, the behavior of the unit cell model for the current scale must be fully characterized before going to the analysis for laminate scale. The precomputed progressive failure behavior at the tow architecture scale was then recast in the form of equivalent nonlinear behavior. That is, all effective properties of the unit

cell model were expressed as function of the damage states predicted at each applied loading step.

Figure 7-5 shows the progressive failure behavior for the reference unit cell model. It is observed that the predicted response curve has some saw-teeth. This is typical for the failure analysis of unit cell models of elastic material, especially when the unit cell has a large material volume with a high stress. This results in a relatively large volume of material failing at about the same time. Also shown are effective moduli calculated by considering the damage states predicted at each loading step. Six loading cases were considered to obtain the full set of 3D effective properties for the unit cell. It is clear that as the applied load increases, damage initiates and then accumulates, as indicated by the decreasing effective moduli. To understand how damage state causes moduli drop, figure 7-6 shows the damage state in the braided tows ($\pm\theta$) predicted at the given applied strain levels.

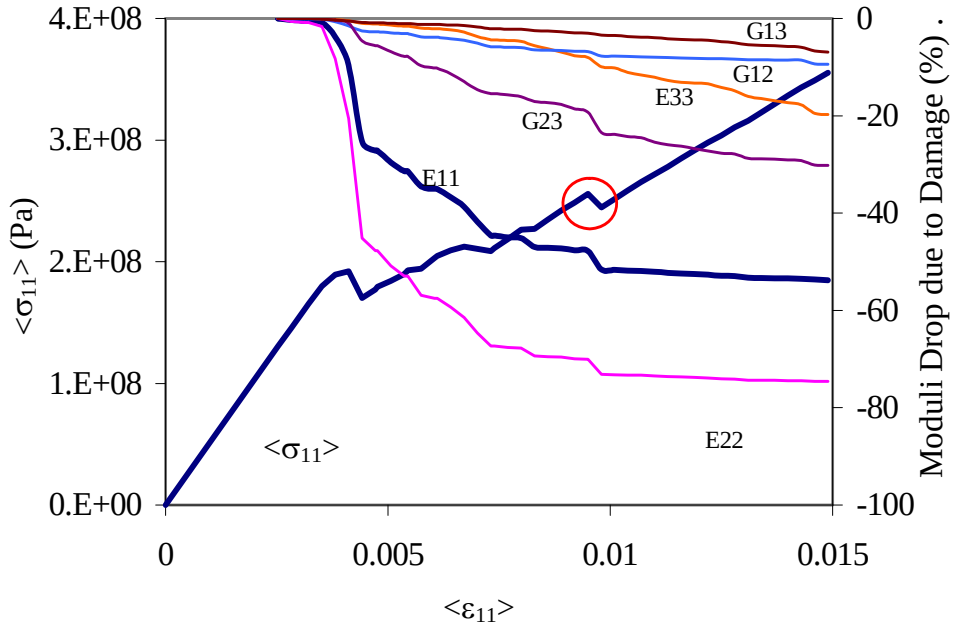

Figure 7-5. Progressive Failure Response and Effective Properties as Function of Damage State for the Reference Model

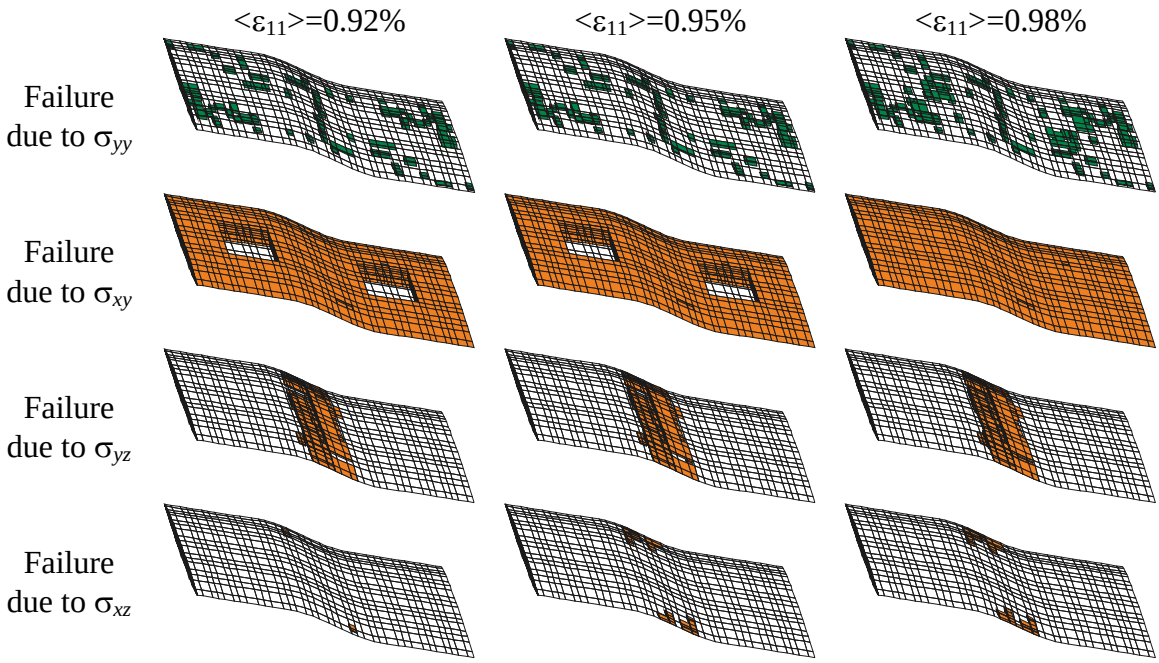

Figure 7-6. Failure States at Given Loading Levels for Reference Model

The progressive failure responses of models with different variation in braid angle and tow volume fraction (see table 7-1) are compared in figure 7-7. Figure 7-7(a) shows the effect of variation in tow volume fraction on the predicted behavior for a braid angle of 28°. It was found that even when the models have the same braid angle (BA = 28°) and overall fiber volume fraction (V_f^{Overall} = 57%), the variation in tow volume fraction (V_{TOW} = 74.33 ±n·5.33%, n = 1, 2) considerably affects the progressive failure responses. Since the variation in the tow cross-section shape (thus the tow volume fraction) is not unusual in the manufactured textile structures, it is beneficial to understand its effect on the progressive failure behavior of the material.

The effect of variation in braid angle (BA = 28 ±n·2°, n = 1, 2) is shown in figure 7-7(b). Obviously, the variation in braid angle has a significant effect on the progressive failure predictions, even with a variation as small as ±2°, which is not uncommon in realistic textile structures.

Combined effect of variation in both braid angle (BA = 28 ±n·2°, n = 1, 2) and tow volume fraction (V_{TOW} = 74.33 ±n·5.33%, n = 1, 2) on the predicted behavior is shown in figure 7-7(c). Significantly different predictions can be obtained from the periodic analysis of the unit cell model when slightly varying braid angle and tow volume fraction from a desired braid configuration. Understanding the effect of deviation from the desired nominal braid parameters is significant.

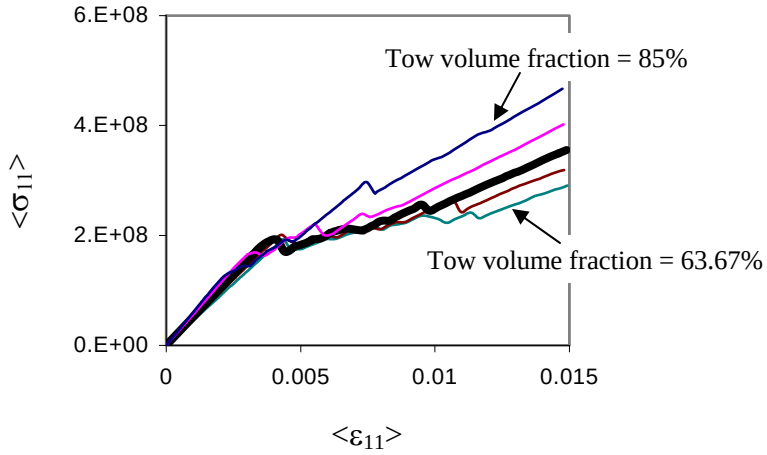

(a) Effect of variation in tow volume fraction

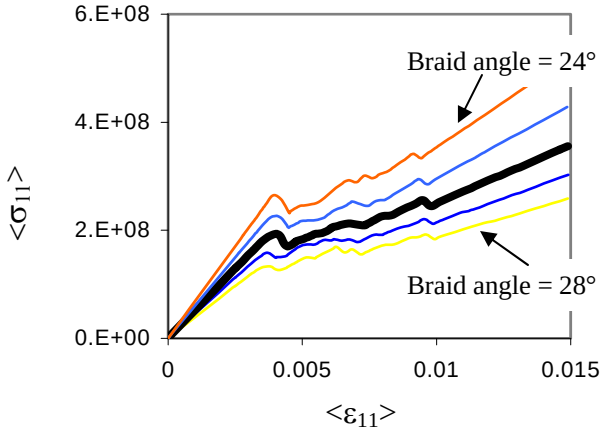

(b) Effect of variation in braid angle

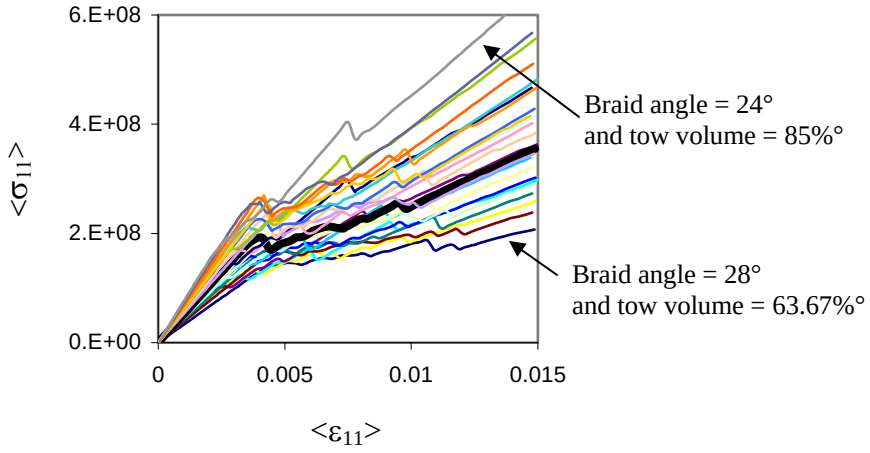

(c) Combined effect of variations in braid angle and tow volume fraction

Figure 7-7. Comparison of Progressive Failure Responses for Various Unit Cell Models

7.6.3 Laminate Scale.

The effect of deviation from the desired nominal braid parameters on the progressive failure behavior of a braid laminate was investigated at the laminate scale. The laminate has a desired braid configuration, which is the same as the reference model for the tow architecture scale, with BA = 28°, V_{TOW} = 74.33%, and $V_f^{Overall}$ = 57%. The deviation of braid angle and V_{TOW} from the nominal values was considered in the laminate model by including behavior of tow architecture unit cell model with deviated braid parameters.

Six laminate models were built. The L11 model considered smaller deviations of tow volume fraction (V_{TOW} = 74.33 ±5.33%), and the L12 a larger deviation (V_{TOW} = 74.33 ±n·5.33%, n = 1, 2). The effect of deviation of braid angle was consider in model L21 (BA = 28° ±2°) and L22 (BA = 28 ±n·2°, n = 1, 2). The combined effect of deviation of braid angle and tow volume fraction were addressed using model L31 (BA = 28°° ±2°, V_{TOW} = 74.33 ±5.33%) and L32 (BA = 28 ±n·2°, V_{TOW} = 74.33 ±n·5.33%, n = 1, 2).

Each element in the finite element laminate model was randomly associated with a unit cell model from the previous scale, which had the required braid parameters. For example, in the L11 model, the unit cell models used are B12, B13, and B14 (see table 7-1). The equivalent nonlinear behavior of these unit cell models, predicted by progressive failure analysis at the tow architecture scale, was then used in the progressive analysis of the laminate model.

Figure 7-8 shows the predicted behavior of laminate models. Despite the different variations in the braid parameters, all laminate models provided response close to that from the periodic analysis of the reference unit cell model. Moreover, the saw-teeth exhibited in the response of the reference unit cell model had been smoothed out. It was found that even a smaller deviation of braid parameters, e.g., ±2° variation in braid angle, could basically eliminate the saw-teeth. This is because when the laminate is not uniform, uniform failure can hardly occur on the entire laminate level. This probably explains why the saw-teeth is seldom seen in actual experimental tests of textile specimens, since highly uniform material microstructure is extremely difficult, if not impossible, to manufacture.

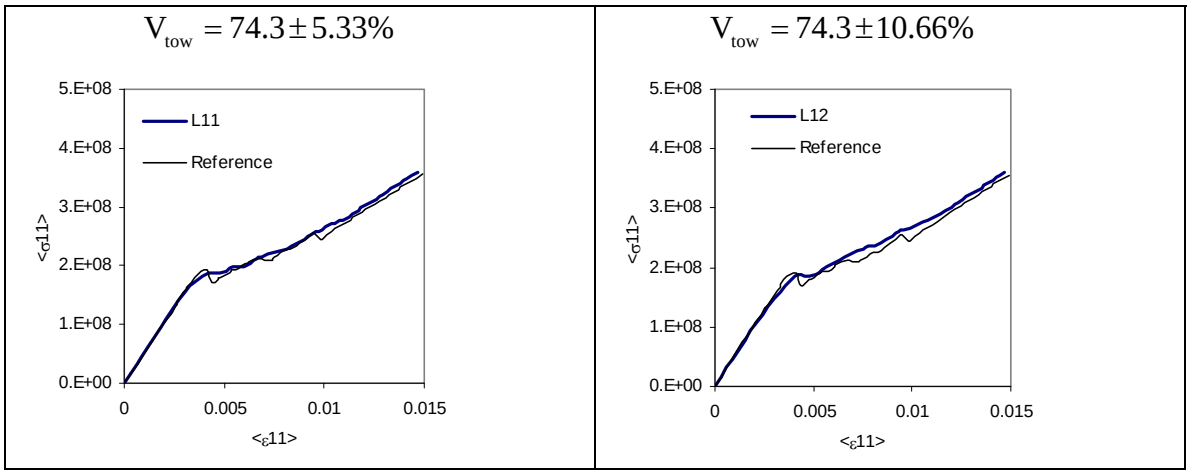

(a) Effect of deviation in to volume fraction

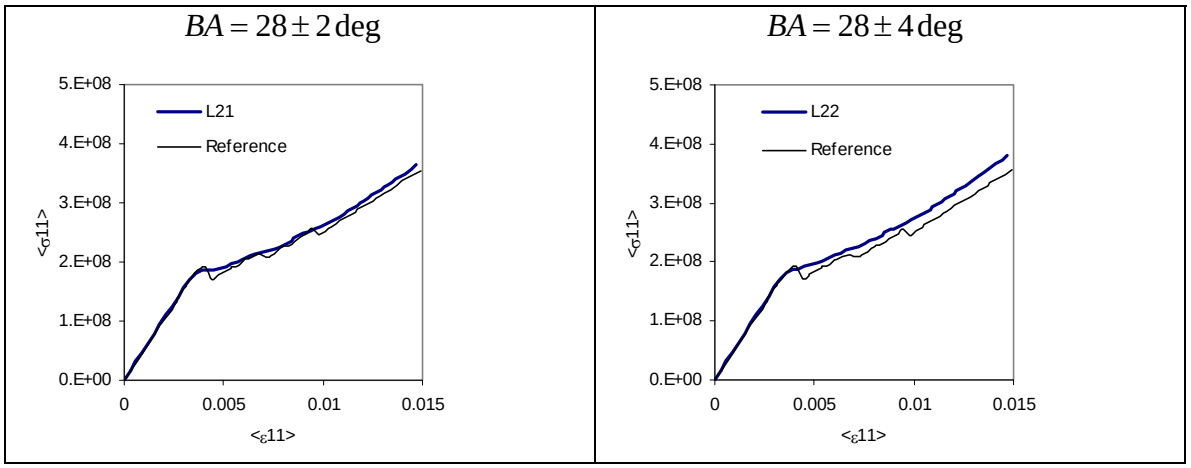

(b) Effect of deviation in braid angle

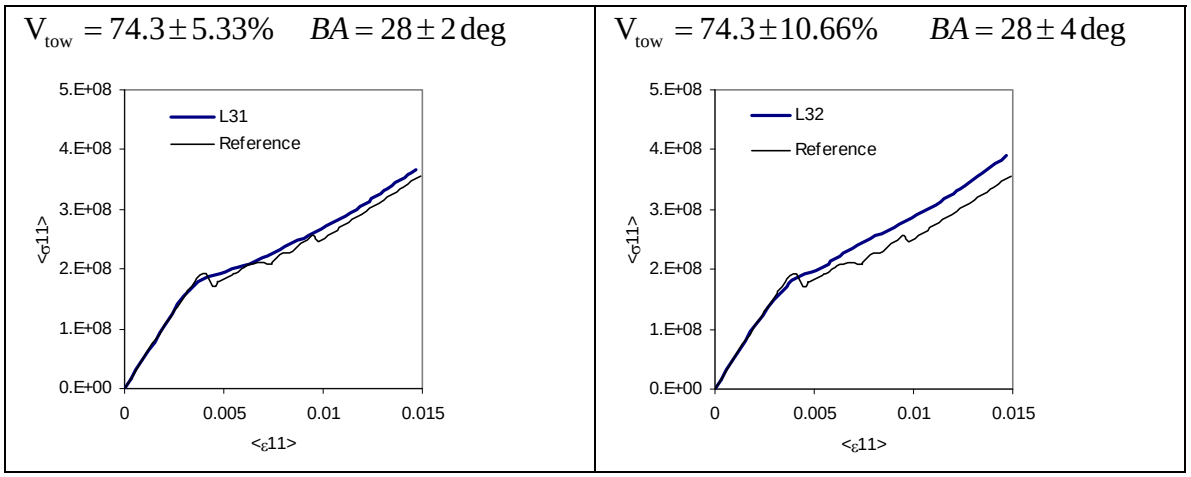

(c) Effect of deviation in both tow volume fraction and braid angle

Figure 7-8. Reponses of Braid Laminate Containing Variation in Tow Geometric Properties

7.7 SUMMARY.

Textile composite are traditionally idealized to have periodic tow architecture so that periodic analysis can be conducted. However, the as-manufactured textile composite does not have perfectly uniform periodic tow architecture. Therefore, understanding the behavioral differences between the material with uniform microstructure and distorted microstructure is significant.

A multiscale analysis approach was adopted to study the progressive failure behavior of a 2x2 braid composite laminate. Three scales, fiber/matrix, tow architecture and laminate, were sequentially considered and modeled. The basic input requirements are the material properties of fiber and matrix, and nominal tow geometric properties such as braid angle and tow volume fraction. The output from the analysis at a smaller scale is generally used as the input for the analysis at a larger scale. Progressive failure analysis was conducted at the tow architecture scale. The nonlinear (due to progressive failure) responses at this scale were then passed to the next scale, the laminate scale, so that the progressive failure analysis at the laminate scale could approximated by nonlinear analysis for a laminate containing a collection of different nonlinear material points.

For the elastic material system and damage model used in this study, it was shown that the progressive failure response from periodic analysis of the reference model (with nominal tow architecture parameters) exhibits saw-teeth in the response curves. These saw-teeth are due to a relatively large amount of material failing almost simultaneously. Once the variation in braid angle and tow volume fraction was considered at the laminate scale, these saw-teeth were smoothed out. This could explain why the saw-teeth are seldom seen in actual tests of textile specimens, since highly uniform material microstructure is extremely difficult, if not impossible, to manufacture.

The adopted process is actually a multilevel homogenization process. Several fundamental assumptions were made to focus on gaining insight from the analysis. First, weak coupling between the scales was assumed such that each scale can be treated individually and sequentially. This assumption can be voided by increasing the model size and computation time. Second, both matrix and fiber are treated elastic. In most cases, polymer or metal matrix exhibits significant nonlinear behavior (e.g., due to plasticity). This can be considered by using more elaborate material constitutive relationships in the model, such as in Tang, et al., 2001. Third, the effectiveness of the failure criterion and property degradation model needs to be validated for the textile architecture and material system under consideration.

8. STRESS DISTRIBUTIONS.

8.1 INTRODUCTION.

The stress distribution in braided composites is complex even for simple uniaxial loading. The interlacing of the tows creates a complex load path that results in full 3D stress distributions. The location and magnitude of peak stresses depend on the particular stress component and vary with various braid architecture parameters such as braid angle and degree of waviness. Finite element analyses for different braids were performed and it was seen that the peak stresses in the tow mainly occur at the undulating region and along the edges of the tow. Stress distribution in braids was compared with those in equivalent laminates.

Various techniques were used to process the stress distribution data. Stress contours give some surface information about stress distributions. Of course, much of the information is not seen in the contour plots. Stress volume distribution plots were used to characterize the extent of high stress regions. It was shown that even for simple uniaxial loading, the stress state in braids is fully 3D. The location and magnitude of peak stresses in the tow was shown.

A considerable volume of the tow (10%-45% for the considered range of parameters) had stresses larger than an equivalent lamina. The severity of stresses in a braid compared to those in an equivalent lamina depends upon braid geometric parameters. Braid angle changes the stress distribution in the tow considerably. However, most of that effect is due to the orientation of the tows in the $+\theta$ and $-\theta$ directions and can be eliminated by matching the loading on the tow of different braids. The severity of peak stresses seems to be increasing linearly with an increase in WR.

8.2 CONFIGURATIONS ANALYZED.

The effect of various parameters on the stress distributions in a symmetrically stacked braid was studied. Uniaxial loading was applied along the longitudinal direction. The overall fiber volume fraction in the model was assumed to be 50%. The range of braid angle considered in the stress studies was ±15° to ±65°. Very low (1/20, 1/9), moderate (1/6) and very high (1/3) WRs were considered.

The material system used consists of AS4 carbon fibers and EPON epoxy resin. The resin is isotropic with E = 2.96 GPa and υ = 0.38. The fiber is transversely isotropic with the following properties: E_{11} = 227.53 GPa, $E_{22} = E_{33}$ = 16.55 GPa, $G_{12} = G_{13}$ = 24.82 GPa, G_{23} = 6.89 GPa, $\upsilon_{12} = \upsilon_{13}$ = 0.2, and υ_{23} = 0.25, where the one direction is along the longitudinal axis of the fiber. The symbols E, G, and υ refer to extensional modulus, shear modulus, and Poisson's ratio respectively. The fibers were assumed to be arranged in a hexagonal array in the tow, and the properties of the tow were calculated using finite element based micromechanics. The fiber fraction in the tow was assumed to be 0.69. The properties of the tow were determined to be E_{11} = 157.9 GPa, $E_{22} = E_{33}$ = 9.088 GPa, $G_{12} = G_{13}$ = 4.839 GPa, G_{23} = 3.276 GPa, $\upsilon_{12} = \upsilon_{13}$ = 0.251, υ_{23} = 0.4117.

8.3 STRESS DISTRIBUTION IN BRAIDS.

Figure 8-1 shows the locations of peak stresses in the tow when unit uniaxial load ($<\sigma_{xx}> = 1$) along the longitudinal direction is applied to a ±25° braid with WR of 1/3. Even for simple loading like this, a 3D stress state exists in the tow and any stress component could be critical, depending upon the allowables. Figure 8-1 shows the contours for all the six stress components with their respective ranges. The value of each stress component for an equivalent lamina is also given. For a lamina, only in-plane stresses are nonzero and the value of each stress component lies within the braid stress range. The out-of-plane stress values are zero because there are no free edge effects. Moreover, the in-plane stresses in the lamina of a tape laminate are constant, but the value of each stress component varies significantly in the braid tow.

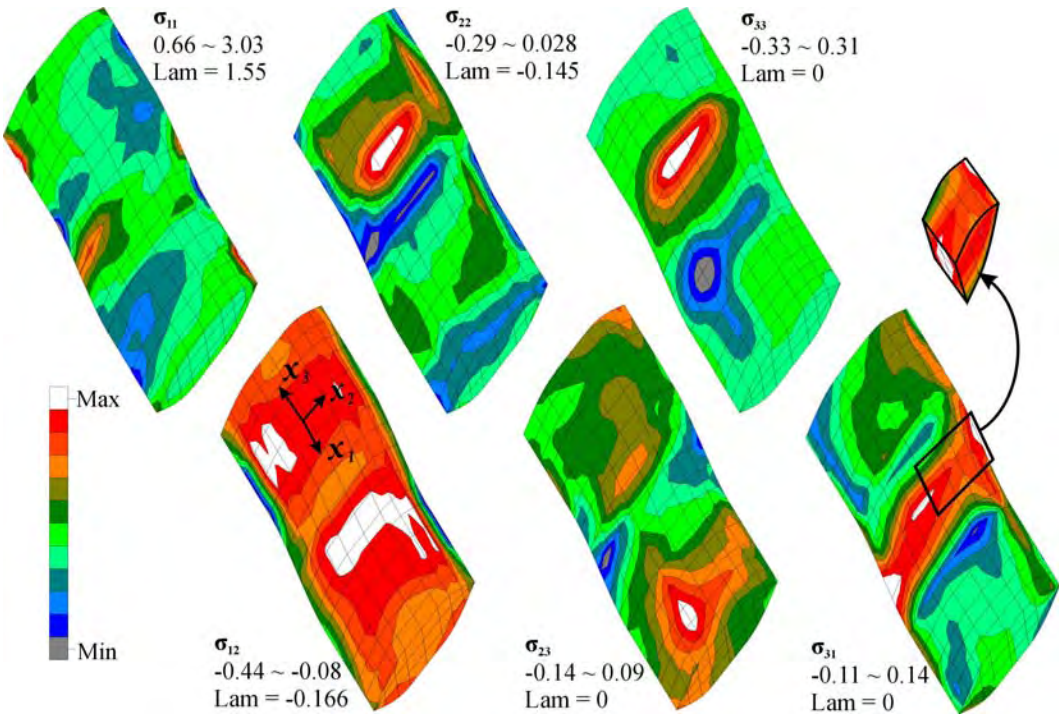

Figure 8-1. Three-Dimensional Stress State in Tow for ±25° Braid With WR = 1/3 ($<\sigma_{xx}> = 1$)

Three-dimensional stress distributions exist for ±45° and ±65° braid tows (not shown in figure 8-1) also, but there are certain similarities and differences in the stress distributions as one changes the braid angle. The σ_{11} stress peaks in the tow are tensile for all the braid angles. In contrast, the peaks for σ_{22} are compressive for ±25° and tensile for ±45° and ±65°, which is consistent with equivalent laminates. Peaks for σ_{12} lie on the edge of the tow. The σ_{13} is the only component whose peaks extend through the thickness of the tow, as shown in figure 8-1. For the rest of the stress components, the peaks are only on the surface of the tow. For all the braid configurations, there were significant tensile and compressive σ_{33} concentrations. However, for a ±65° braid, tensile peaks were much larger than the compressive peaks. Figure 8-2 shows the effect of braid angle on the σ_{33} stress distribution. Braids with different braid angles were stressed at the same stress level ($<\sigma_{xx}> = 1$). It is clear that stress distribution differs considerably with braid angle. With increase in braid angle to ±65°, the peak stresses change

from tension to compression in nature in the center portion of the tow. Also, the location of peak stresses changes from center portion of the tow to the edge of the tow. Magnitudes of tensile peaks also change from 0.22 to 0.367 for a ±15° and ±65° braid, respectively. The ±65° braid tow has a smaller tensile area, which is near its edges, but a larger tensile value than the others. In summary, the location and magnitude of peak stresses vary considerably with braid angle.

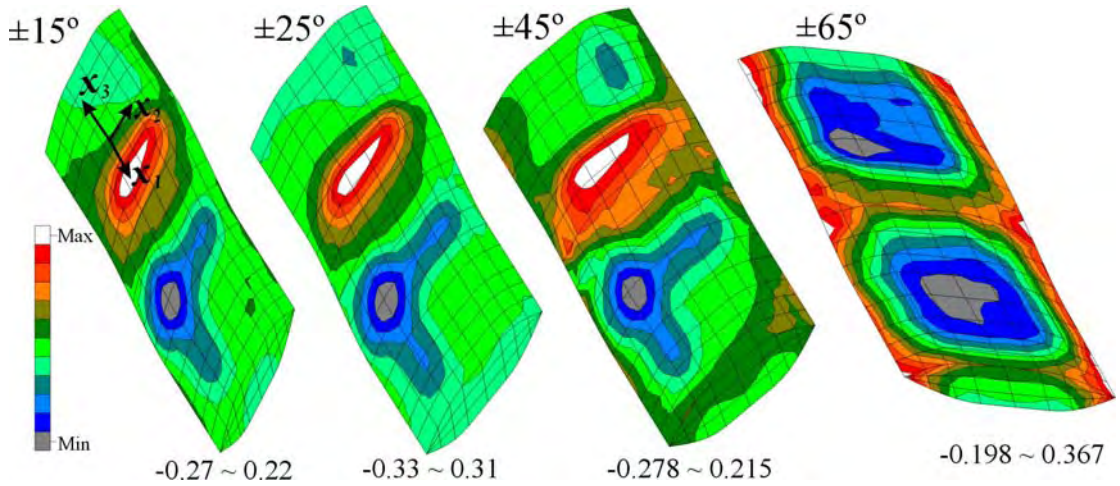

Figure 8-2. Effect of Braid Angle on σ_{33} Stress Concentration
(Uniaxial loading ($<\sigma_{xx}>$ = 1), WR = 1/3)

8.4 VOLUME DISTRIBUTION CURVE.

Stress contour plots shown in figures 8-1 and 8-2 give stress information only on the surface of the tow. To get internal information, one has to cut the tow and show more plots. The percentage of the tow having peak stress can be small enough not to be noticeable in the stress contours. Also, it is possible that peak stresses are hidden in the interior of the tow. One needs to determine what percentage of the tow exceeds a certain stress level. A volume distribution plot quantifies the percentage volume of the material that is stressed more than a particular value. Figure 8-3 shows a typical volume distribution plot of σ_{33} in the $+\theta$ tow of a ±30° braid with WR = 1/3 when uniaxial load is applied. The σ_{33} in an equivalent lamina is also plotted. For the lamina, σ_{33} is zero. The σ_{33} in the braid is normalized by the applied stress. The figure shows that 18% of the volume of the tow has a tensile σ_{33}. Point A, which is in the tensile region, indicates that 10% of the volume has a σ_{33} that is larger than 0.037 times the applied stress. Point B, which is in the compressive region, indicates that 24% of the volume has a compressive stress larger than 0.1 times the magnitude of the applied stress. The information provided by a volume distribution plot can be used in several ways. For example, the percentage of the tow having larger stress than that in an equivalent lamina can be found; the percentage of the tow having tensile or compressive stress can be found; the percentage of the tow having stress larger than a particular value can be found. Also, questions like, what percentage of the tow has a larger σ_{33} than 0.25 times the applied stress can be answered.

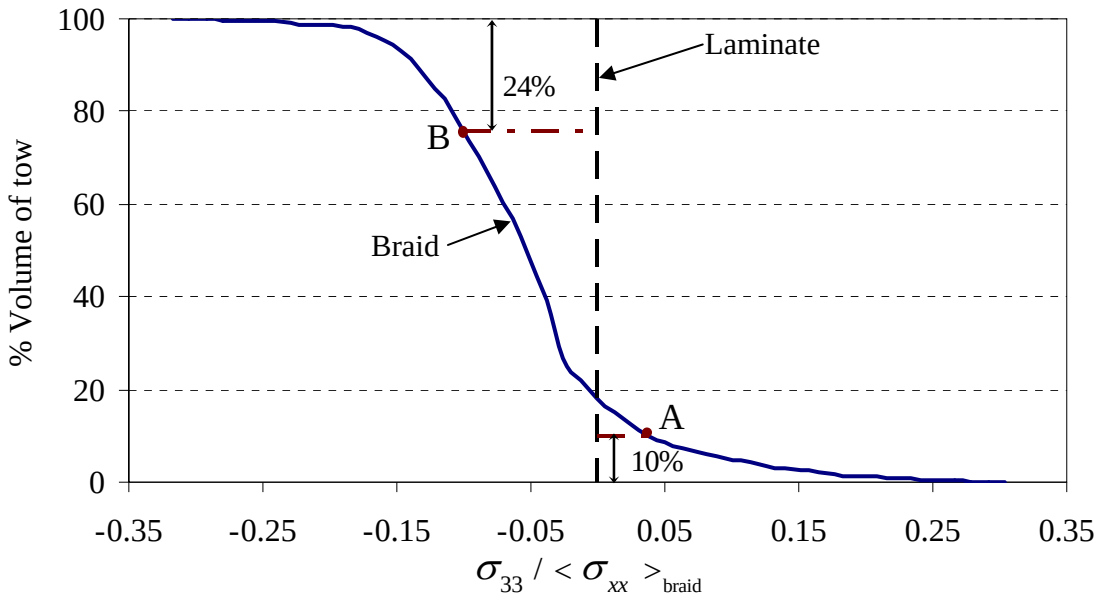

Figure 8-3. σ_{33} Volume Distribution in ±30° Braid Tow With WR = 1/3 When $<\sigma_{xx}> = 1$ was Applied

8.5 COMPARISON OF STRESS DISTRIBUTION IN BRAIDS WITH EQUIVALENT LAMINATES.

Tape laminates and braids have their own advantages and disadvantages in terms of ease and cost of manufacturing, engineering properties, and ease of analysis. Analysis of tape laminates is easily understood by designers and engineers, but tapes have the disadvantage of hand lay-up and high manufacturing cost. In contrast, analysis of braids is complicated, but they have an edge in terms of manufacturing cost. Here, the severity of stresses in braids compared to those in equivalent tape laminates is discussed. Figure 8-4 shows the volume distribution of in-plane normal stresses in the +θ tow of ±45° braid when unit uniaxial load along the longitudinal direction was applied ($<\sigma_{xx}> = 1$). In both the plots, the volume distribution curves correspond to five WRs: 1/3, 1/4, 1/6, 1/9, and 1/20. The vertical straight line corresponds to the constant stress value in the +θ lamina of an equivalent tape laminate. The stresses shown in figure 8-4 are normalized with the corresponding absolute +θ lamina values. That is, the plots show $\sigma_{11\_tow}/|\sigma_{11\_lamina}|$ and $\sigma_{22\_tow} / |\sigma_{22\_lamina}|$. There are several differences between the stress distribution in a braid tow and a lamina. Figure 8-1 showed that braid tows have a wide variation in in-plane stresses. In contrast, in-plane stresses in a lamina are constant. The volume of the tow that exceeds the value of stresses in a tape lamina gives the severity of stresses in a tow as compared to those in lamina. Figure 8-4(a) shows the volume distribution of σ_{11} for a ±45° braid tow for several WRs. The figure shows that 19% of the tow (marked by arrow A) has larger σ_{11} than an equivalent lamina for WR = 1/3 and the severity is maximum for this WR. When the WR is reduced to 1/20, the severity reduces to 11.5% (marked by arrow B). The σ_{11} severity is smallest for the smallest WR (1/20) in the considered range of WR (1/20-1/3). Figure 8-4(b) shows the volume distribution of σ_{22}. The figure shows that 31% of the tow (marked by arrow A) has larger σ_{22} than an equivalent lamina for WR = 1/3. When the WR is reduced to 1/20, the severity reduces to 19% (marked by arrow B). For all other WRs considered, the

severity lies in between the highest WR (1/3) and lowest WR (1/20) for both the in-plane stresses shown in figure 8-4.

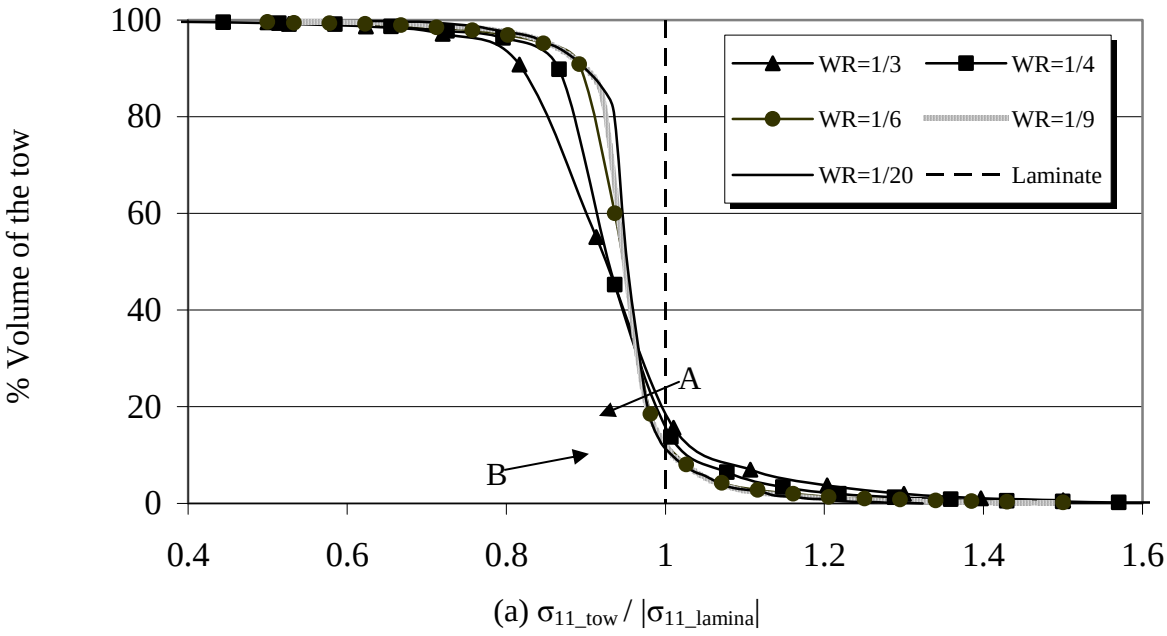

(a) $\sigma_{11\_tow} / |\sigma_{11\_lamina}|$

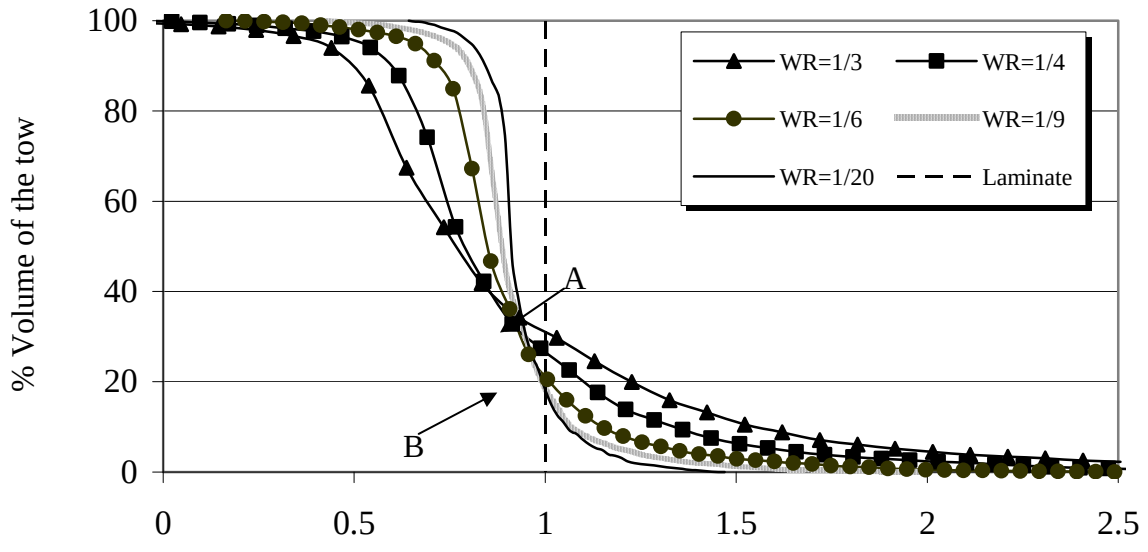

(b) $\sigma_{22\_tow} / |\sigma_{22\_lamina}|$

Figure 8-4. Comparison of Stress Volume Distribution in a ±45° Braid With That in an Equivalent Tape Laminate
(Normalized stress ($\sigma_{tow}/|\sigma_{lamina}|$) in the tow vs percentage volume of the tow exceeding a particular value is plotted.)

Figure 8-4 shows the stress distribution for ±45° braid only. The severity of stresses in ±25° and ±65° braids was also investigated. The results are tabulated in table 8-1, which show the severity of stresses for the considered range of BA (±25°-±65°) and WR (1/20-1/3).

Table 8-1. Severity of Stresses in Braid Compared to an Equivalent Tape Laminate

Range of BA = ±25°-±65°, Range of WR = 1/20-1/3												
	% volume of tow having more severe stress than those in an equivalent lamina											
	WR =1/3			WR =1/6			WR =1/9			WR =1/20		
BA	±25°	±45°	±65°	±25°	±45°	±65°	±25°	±45°	±65°	±25°	±45°	±65°
σ_{11}	40	18.5	24.6	19.5	12.3	27.5	16	12.1	28.8	15	11.2	30
σ_{22}	45	31	27.3	38.5	21	31	36	18.5	30	36	18.2	29.5
σ_{12}	24.5	33	9.5	24.5	33	26.5	27.5	33.7	29.5	28	34	30

The severity decreases with a decrease in WR for ±25° and ±45° braids for both the in-plane normal stresses. For ±65° braid, the severity increases with a decrease in WR for σ_{11} and remains almost constant for σ_{22}. For σ_{12}, the severity increases with a decrease in WR for all the braid angles. Overall, in this range of parameters, maximum volume of the tow that could have more stresses than an equivalent lamina is 40% for σ_{11}, 45% for σ_{22}, and 34% for σ_{12}.

8.6 EFFECT OF MATCHING THE LOADING ON STRESS DISTRIBUTION = EFFECT OF BRAID ANGLE AND INTERLACING.

Figure 8-5 shows the effect of braid angle on the σ_{22} and σ_{13} stress volume distribution. The WR = 1/3 and a unit volume averaged stress of $<\sigma_{xx}>$ was applied. Also shown are the values of equivalent tape laminates corresponding to each braid. The dotted lines show the constant lamina stress values. There is wide variation in the stresses in the tow of all the braids. Figure 8-5(a) shows that as the braid angle changes, the σ_{22} stress distribution changes considerably. The ±15° braid tow has compressive stresses in >95% of its volume, whereas ±45° and ±65° braid tows have only tensile stresses in their entire volume. The peak values of σ_{22} for ±15°, ±45°, and ±65° tows are -0.14, 0.4, and 1.5, respectively. Figure 8-5(b) shows the variation for σ_{13}. The laminate value is zero for all equivalent laminates in this case, but braids have wide variation. The wide variation in σ_{22} is mostly due to orientation effect and is expected based on the behavior of an equivalent laminate. The orientation affects the volume distribution for other stress components also. Hence, a technique was used to eliminate the effect of orientation. A volume averaged stress $<\sigma_{xx}> = 1$ was applied on ±45° braid. The +45° braid tow experienced certain amount of loading because of this. That is, the tow was subjected to the following volume averaged stresses: $<\sigma_{11}> = 1.203$, $<\sigma_{22}> = 0.087$, $<\sigma_{33}> = -0.0026$, $<\sigma_{12}> = -0.593$, $<\sigma_{23}>=0$, and $<\sigma_{13}>=0$, where the 1 direction is along the axis of the braid tow. The same amount of loading was applied on a +25° braid tow. This was made possible by applying multiaxial loading on the ±25° braid model. The same thing was done for other braid angles. The stress volume distribution in the different braids was compared. The stress volume distribution after matching the loading on tows of different braids is shown in figure 8-6. It is interesting to see that now the stress volume distribution curves lie very close to each other compared to when the loading on tow was not matched (figure 8-5). The σ_{22} ranges from tensile to compressive for all the braids, as shown in figure 8-6(a). The peak values of all the braids are

also very close to each other for all the braids. Similarly, volume distribution curves came closer for σ_{13} stress also, as shown in figure 8-6(b). The orientation effect could be eliminated similarly for other stress components as well. The difference that still remains is attributed to the fact that the tows are interlaced and the tow shape of different braids is different due to phase shift in the undulation. This phase shift is shown in figure 8-7. In this figure, x, y, and z are the local coordinates. Different fibers across the width of the tow start to undulate at a different x distance, which means that they have a different phase angle. The phase shift is given by $\Phi = y*\tan(2\theta°-90°)$, where θ is the braid angle. Due to this, different fibers of the tow do not undulate and straighten at the same x coordinate. One fiber may have started undulating and another may not have yet started to undulate. The overall effect of this phase shift is different material architecture for different braids, which results in different stress distribution even if the loading on the tow of different braids was matched.

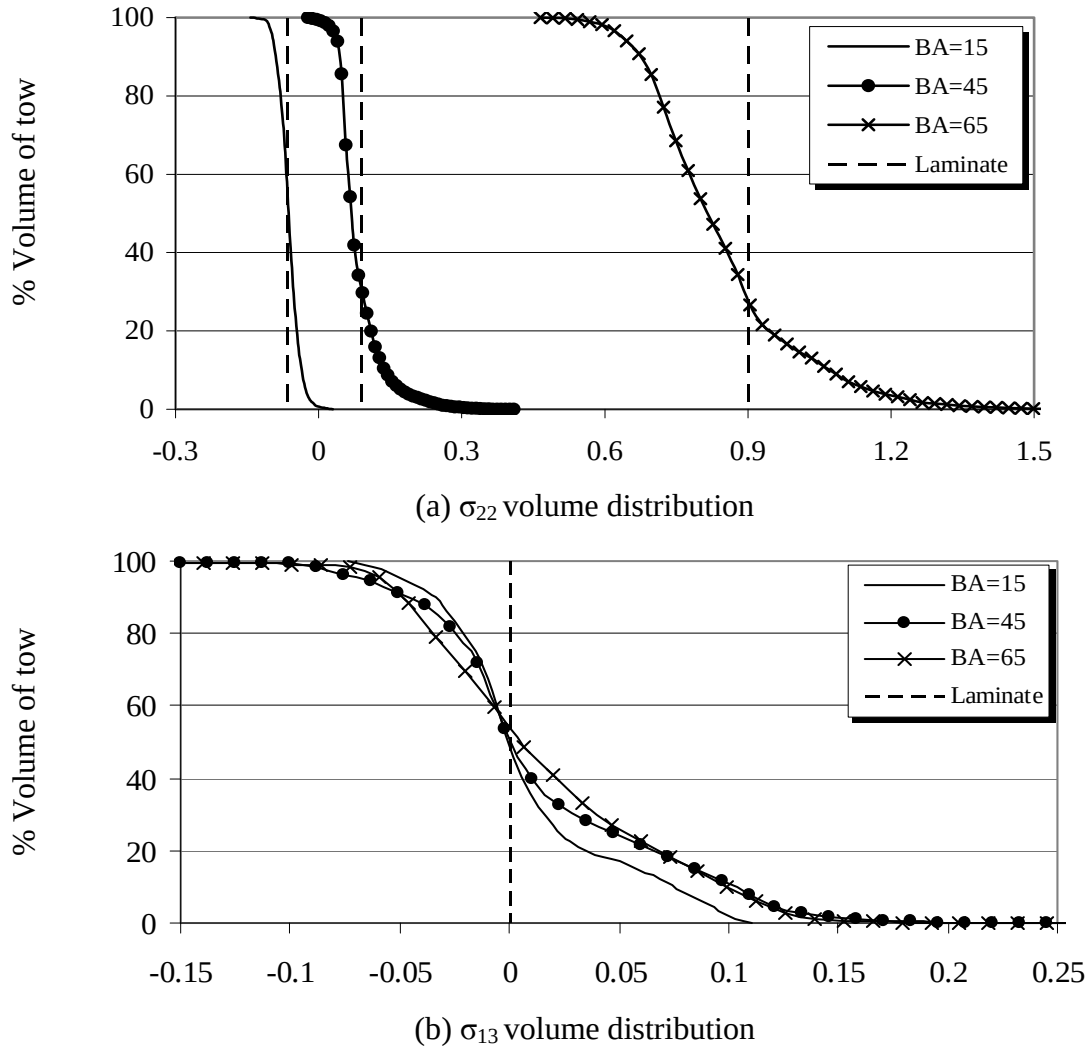

Figure 8-5. Effect of Braid Angle on σ_{22} and σ_{13} Volume Distribution ($<\sigma_{xx}> = 1$, WR = 1/3)

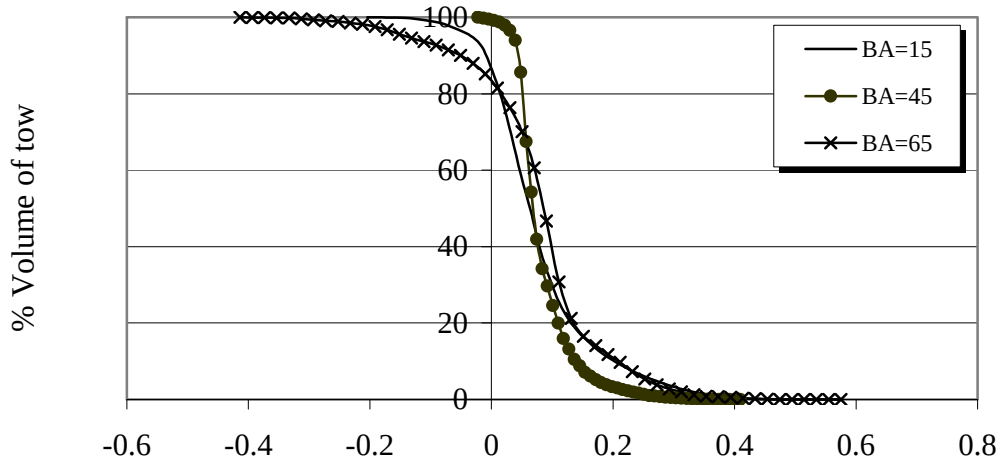

(a) σ_{22} volume distribution

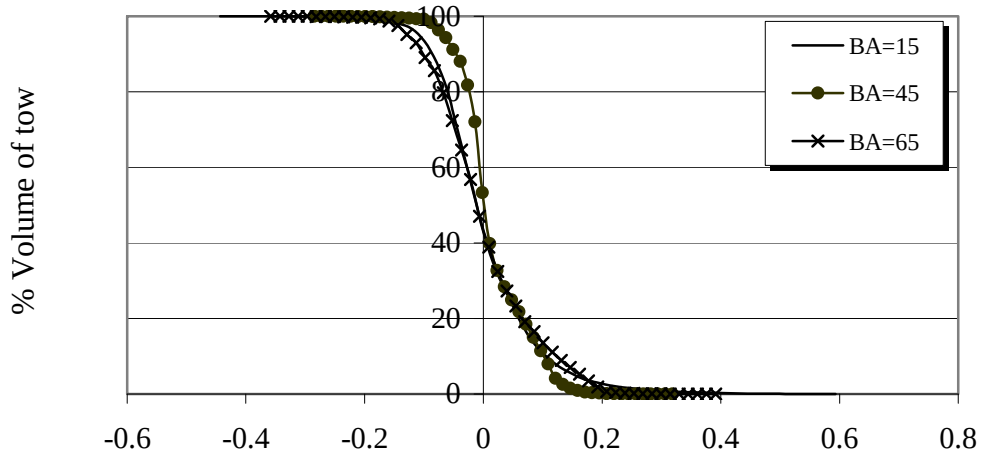

(b) σ_{13} volume distribution

Figure 8-6. Effect of Braid Angle on σ_{22} and σ_{13} Volume Distribution When $\langle\sigma_{ij}\rangle$ in the Tow are Matched (WR = 1/3)

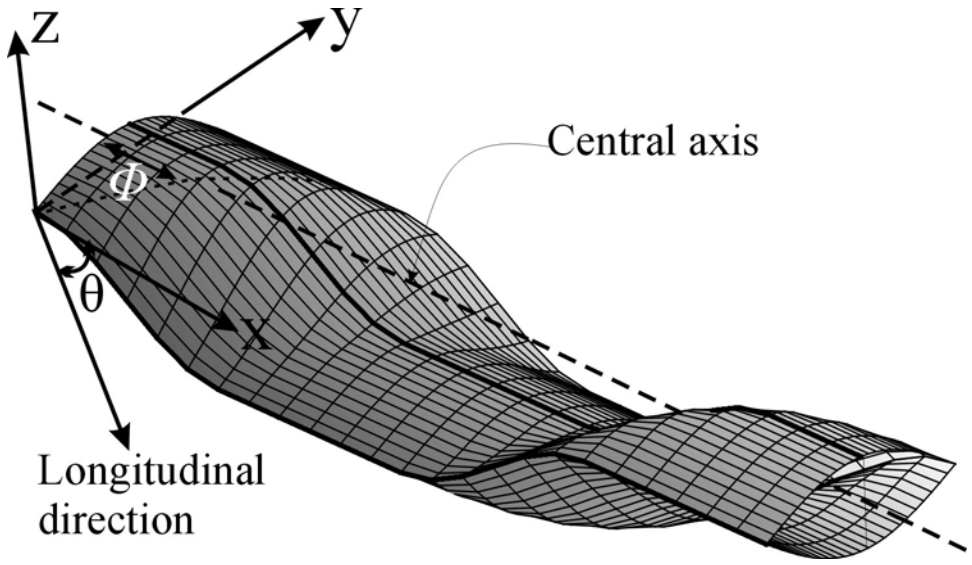

Figure 8-7. Phase Shift

8.7 EFFECT OF WAVINESS RATIO.

Figure 8-8 shows the effect of WR on the stress volume distribution for a ±45° braid. A unit uniaxial load ($<\sigma_{xx}> = 1$) was applied. Three different WRs (1/3, 1/6, and 1/9) were used. The figure shows the stress volume distribution for all the stress components. It is clear that for all the stress components, with an increase in WR, the volume distribution curve tends to broaden in the horizontal direction. Therefore, the severity of the peaks increases with an increase in waviness ratio for all the stress components. The effect of waviness ratio is more pronounced for out-of-plane stresses (σ_{33}, σ_{23}, and σ_{13}) than for in-plane stresses (σ_{11}, σ_{22}, and σ_{12}).

Figure 8-9 summarizes the effect of WR on the stress peaks. The figure shows the variation of normalized stress peak values with WR for all the six stress components. The peak values correspond to a particular percentage of the tow volume. For example, in figure 8-9(a), 5% of the tow volume had more severe stresses than the value plotted for all the stress components. Similarly, in figure 8-9(b), 2% of the tow volume was chosen to find the value of peak stresses. The σ_{ij} (where $i, j = 1, 2, 3$) peak values were normalized with the peak values corresponding to a WR of 1/9. The results are for a ±45° braid under unit uniaxial load ($<\sigma_{xx}> = 1$). It is clear that the peaks increase linearly with an increase in waviness ratio (except for σ_{12} for which there is little variation). Again, is clear that the effect of WR is more pronounced for out-of-plane stresses compared to in-plane stresses. Out-of-plane normal stress is most severely affected.

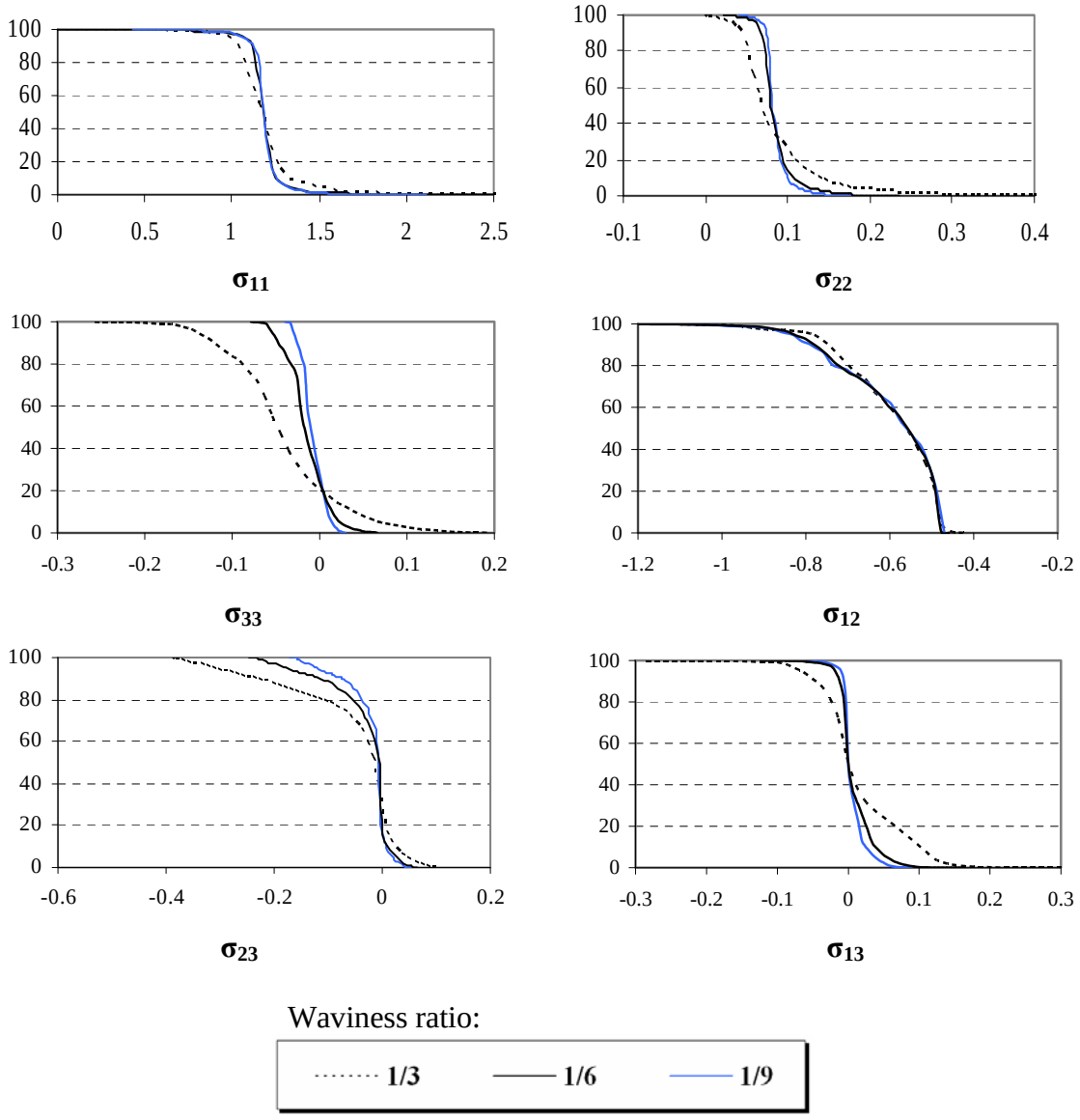

Figure 8-8. Effect of Waviness Ratio on Stress Volume Distribution, BA = ±45°
(For all the cases, stress component is plotted along the horizontal, and % volume of the tow is plotted along the vertical. Applied stress is $\langle\sigma_{xx}\rangle = 1$.)

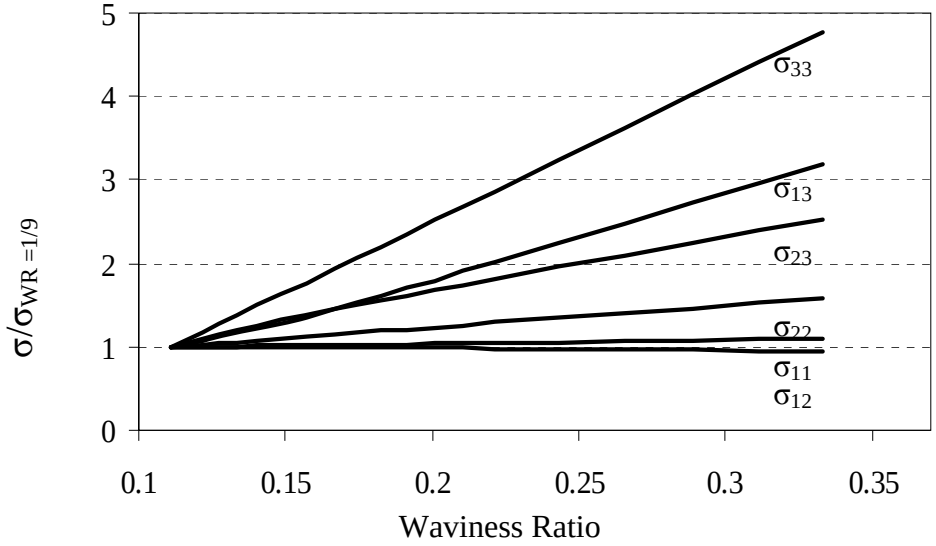

(a) Peak stresses correspond to 5% of the tow volume

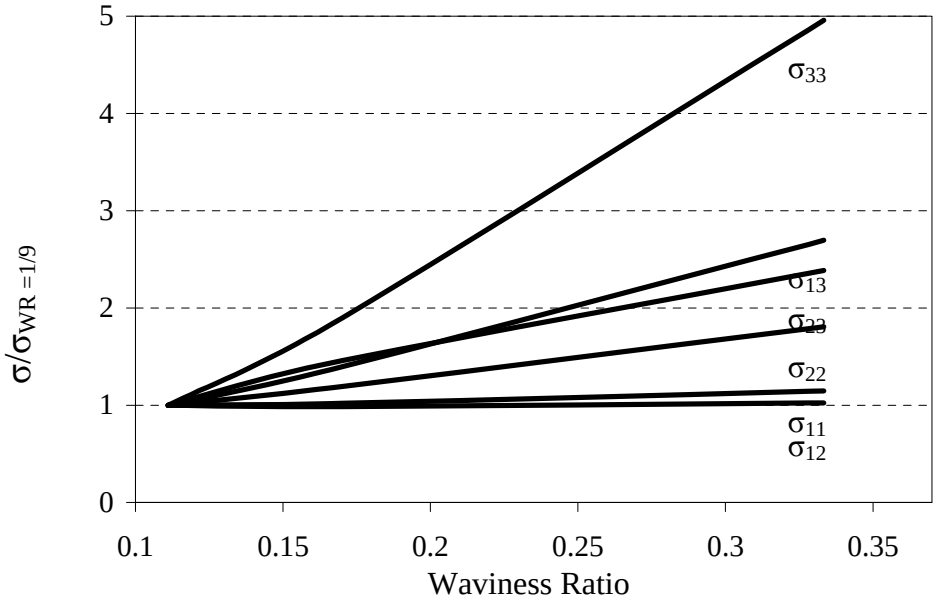

(b) Peak stresses correspond to 2% of the tow volume

Figure 8-9. Variation of Peaks With Waviness Ratio ±45° Braid Under $\langle\sigma_{xx}\rangle = 1$

8.8 SUMMARY.

The tow stress state in 2x2 braids was investigated. The effect of various parameters on the stress state was investigated. The following observations were made:

- A complex 3D stress state, which is fully 3D, exists in the tow even for simple uniaxial loading.

- In the considered range of parameters (WR = 1/3-1/20, BA = ±25°-±65°), a considerable volume of the tow has more stresses than an equivalent lamina.

- The wide variation in stress volume distribution with braid angle is due to simple orientation effects and can be eliminated by matching the loading on the tow. Some difference that still remains can be attributed to the phase shift and interlacing effect.

- The severity of the peaks increases linearly with an increase in WR for all stress components (except for σ_{12} for which there is little variation).

9. CONCLUSIONS.

Low-cost, vacuum-assisted resin transfer molding (VARTM) was successfully implemented to manufacture 2x2 biaxial braided composites using two different resin systems with carbon braids (i.e., DM 411-350 vinyl ester and EPON 9504 epoxy resin). The DM 411-350 vinyl ester resin system was previously studied by Smith in 2001, and the same process parameters of VARTM were used in the present study. The following are the conclusions concerning braided composites manufactured by using carbon braids and the EPON 9504 epoxy resin system:

- Good quality panels can be obtained if the processing is performed at an elevated temperature of 49ºC (120ºF). Both the mold and resin need to be heated to 49ºC (120ºF).
- The complete wet-out of the fabric was achieved by placing the resin distribution media and the vacuum line in a specific way.
- A flow control device like the peristaltic pump was not required for this resin system. This is in contrast to its requirement for the DM 411-350 vinyl ester resin system.
- Double bagging may prevent leakages in the vacuum bag, but it may not improve overall fiber volume fraction.
- A small amount of surfactant in the resin may cause the delamination of plies.
- The braided composite panels exhibited variation in thickness between the vacuum line and the resin line.
- The experimental study indicated that the overall fiber volume fraction is independent of the braid angle. The composites manufactured by VARTM yielded a 50% fiber volume.

The performance of 2x2 biaxial braided composites was studied in detail for two different resin systems (i.e., DM 411-350 vinyl ester and EPON 9504 epoxy resin) under static tension and tension-tension fatigue loading (R = 0.1). The effect of the braid angle on the fundamental mechanical properties and fatigue life was studied. The following are the conclusions of the performance evaluation:

- The fundamental mechanical properties (i.e., Young's modulus, Poisson's ratio, and ultimate tensile strength) for both carbon/vinyl ester and carbon/epoxy material systems were very close at a braid angle of 25º.
- The axial modulus, Poisson's ratio, and ultimate tensile strength decreased as the braid angle increased from 25º to 45º.
- The braid angle variation within a specimen was controlled to ±1º by using slit sleeves. A large variation in braid angle within a specimen caused large scatter in the ultimate tensile strength and the fatigue life.

- Based on a limited number of fatigue tests, the endurance limit of the braided composites was 40% to 50% of the ultimate tensile strength for the braid angles between 25º and 45º for carbon/epoxy and carbon/vinyl ester material systems. At higher stress levels, carbon/vinyl ester material systems showed better fatigue life.

- The S-N diagram of braided composites for various braid angles can be approximated using the Sigmoidal (Boltzmann) function.

- Stiffness degradation curves exhibit a typical three-stage pattern. However, stiffness degradation was more rapid in braided composites than in woven composites. The decrease in fatigue secant modulus at failure can be as high as 60% of the fatigue secant modulus in the first cycle. Thus, the damage accumulation rate was much higher for braided composites.

- The stress level near the endurance limit is very critical. Fatigue life dropped from 1 million cycles to 5000 cycles when stress levels increased from 40% to 50% for braid angles of 25º and 30º. In the same manner, fatigue life dropped from 1 million to 50,000 cycles when the stress level increased from 50% to 60% for a braid angle of 45º.

- The failure of braided composites always occurred suddenly in the last 10% of the fatigue life without any visible matrix cracking or delamination of plies.

An analytical model was developed from stiffness degradation curves to predict the residual fatigue secant modulus. The following are the conclusions concerning the modeling effort of 2x2 biaxial braided composites:

- The first stage of stiffness degradation curves, which displays a rapid decrease in the stiffness, exists for approximately the first 5% of the fatigue life. Therefore, the endurance limit of braided composites can be evaluated by performing fatigue tests for only 5% of the fatigue life. The stress level at which the stiffness remains almost constant indicates the endurance limit.

- A unique analytical model was developed based on stiffness degradation curves to predict the residual fatigue secant modulus. This model is in good agreement for all three stages of the stiffness degradation.

A computational micromechanics strategy was developed to model 2x2 braids. Solid models were also created to understand the material architecture of 2x2 braids. The following are the conclusions related to computational modeling of 2x2 braids.

- The tow x section along the length of the tow of 2x2 braids varies unusually.

- Since the tow cross-section along the tow path is not uniform, direct finite element mesh generation for the model is difficult. A mapping technique was developed to generate the finite element mesh for various 2x2 biaxial braids from the mesh for the twill weave, which had been developed in previous studies. This resulted in substantial time savings.

- The boundary conditions are complex and are in terms of many multipoint constraint relations. By exploiting symmetry operations like mirroring, rotation or a combination of the two, the analysis region was reduced to half (for simple stacking) or one-fourth (for symmetric stacking) of the unit cell.

The effect of various parameters like braid angle, waviness ratio (WR), material properties, and cross-section shape on the effective engineering properties of the 2x2 braids was investigated. The effective properties of braids were also compared with those of equivalent laminates. The following conclusions can be drawn from these parametric studies:

- In-plane properties of carbon/epoxy material system with flattened cross-section can be predicted very well by using a simple laminate model. However, for the glass/epoxy and carbon/epoxy with lenticular cross-section, the laminate analysis can produce as large as 16% error for the in-plane properties of the 2x2 biaxial braids.

- The most sensitive effective properties were found to be the transverse properties (G_{13}, G_{23}, υ_{13}, and υ_{23}). This suggests that the simple laminate theory cannot be used to get reasonable approximation for the transverse properties of the braid.

- The G_{13} and G_{23} can be as much as 72% greater than the laminate value, which means a considerable increase in transverse shear modulus can be achieved using the 2x2 biaxial braid compared to the equivalent angle-ply tape laminate. This can be significant for structural applications in which higher G_{13} and G_{23} are desirable.

- To predict the properties of braids using simple laminate analysis, it is important to know the cross-section shape of the braid under investigation as the response of a braid with flattened cross-section can be predicted more confidently and with less error than that with a lenticular cross-section.

- In-plane modulus of braids is less than those of equivalent tapes.

- Moduli predictions fall within the range of experiments.

The stress distribution in a braid tow was analyzed. The effect of various braid architecture parameters, such as braid angle and degree of waviness, on the location and magnitude of peak stresses was studied. Stress distribution in braids was compared with those in equivalent laminates. The conclusions are summarized below.

- A complex three-dimensional (3D) stress state, which is fully 3D, exists in the tow even for simple uniaxial loading.

- In the considered range of parameters (WR = 1/3-1/20 and braid angle (BA) = ±25°-±65°), a considerable volume (40% for σ_{11}, 45% for σ_{22}, and 34% for σ_{12}) of the tow has larger in-plane stresses than an equivalent lamina.

- The wide variation in stress volume distribution with braid angle is due to simple orientation effects and can be eliminated by matching the loading on the tow. Some difference that still remains can be attributed to the phase shift and interlacing effect.

- The severity of the peaks increases linearly with an increase in WR for all stress components (except for σ_{12}, for which there is little variation).

The effect of variation in braid parameters on the progressive failure behavior of a 2x2 braided composite laminate was studied. A bottom-up multiscale finite element modeling approach was employed that sequentially considered the fiber/matrix scale, the tow architecture scale, and the laminate scale. The following are the conclusions from progressive failure analysis of 2x2 braids with microstructural heterogeneity.

- The progressive failure response from periodic analysis of the reference model (with nominal tow architecture parameters) exhibits saw-teeth in the response curves. These saw-teeth are due to a relatively large amount of material failing almost simultaneously. Once the variation in braid angle and tow volume fraction was considered at the laminate scale, these saw-teeth are smoothed out. This could explain why the saw-teeth are seldom seen in actual tests of textile specimens, since highly uniform material microstructure is extremely difficult, if not impossible, to manufacture.

10. BIBLIOGRAPHY.

3M Company, http://www.3m.com

A&P Technology Inc. 2000, "Frequently Asked Questions,"
available at http://www.braider.com, accessed in June 2002.

Abdallah, M.G., Senior Staff Scientist, Hexcel Corporation-Composites/Carbon Fibers private communication via email, 2002.

Amateau, M.F., Professor of Engineering Science and Mechanics, The Pennsylvania State University, Course material for "Engineering Composite Materials EMCH471," http://www4.esm.psu.edu/academics/courses/emch471/Notes/Chapter18.PDF.

ASTM D 638, "Standard Test Method for Tensile Properties of Plastics," ASTM Standards and Literature References for Composite Materials, Philadelphia, Pennsylvania.

ASTM D 3039, "Standard Test Method for Tensile Properties of Fiber Resin Composites," ASTM Standards and Literature References for Composite Materials, Philadelphia, Pennsylvania.

ASTM D 3479, "Standard Test Method for Tension-Tension Fatigue of Polymer Matrix Composite Materials," ASTM Standards and Literature References for Composite Materials, Philadelphia, Pennsylvania.

Battat, http://amptiac.alionscience.com/pdf/2001MaterialEase16.pdf

Beck, W., 1993, "Designing the RTM Process and Product," *SME Technical Paper (Series)*, EM 1993, Publication by SME, pp. 1-13.

Beckwith, S.W. and Hyland, C.R., 1998, "Resin Transfer Molding: A Decade of Technology Advances," *SAMPE Journal*, V 34, pp. 7-19.

Blackketter, D.M., Walrath, D.E., and Hansen, A.C., 1993, "Modeling Damage in a Plain Weave Fabric-Reinforced Composite Material," *Journal of Composites Technology & Research*, 15(2): 136-142.

Bolick, R. and Kelkar A.D., North Carolina A&T State University, Greensboro, NC 27411, private communication via email, 2004.

Burr, S.T. and Morris, D.H., 1995, "Two-Dimensionally Braided Composites Subjected to Static and Fatigue Loading," Virginia Polytechnic Institute and State University, *Mechanics of Textile Composites Conference*, pp. 33-53 (SEE N96-25071 09-24).

Byun, J.H., 2000, "The Analytical Characterization of 2-D Braided Textile Composites," *Composites Science and Technology*, Vol. 60, pp. 705-716.

Carlos, K.G., 1994, “Fatigue Behavior of 3-D Triaxially Braided Composites,” Thesis (M.S.), North Carolina A&T State University.

Chamis, C.C., 1984, “Simplified Composite Micromechanics Equations for Strength, Fracture Toughness, Impact Resistance and Environmental Effects,” Report NASA TM-83696.

Chapman, C.D. and Whitcomb, J.D., 2000, “Thermally Induced Damage Initiation and Growth in Plain and Satin Weave Carbon-Carbon Composites,” *Mechanics of Composite Materials and Structures*, Vol. 7(2), pp. 177-194.

Chen, J., McBride, T.M., and Sanchez, S.B., 1998, “Sensitivity of Mechanical Properties to Braid Misalignment in Triaxial Braid Composite Panels,” *Journal of Composites Technology & Research*, Vol. 20(1), pp. 13-17.

Clemente, R., Castejon, L., and Miravete, A., 1998, “Energy Absorption of 2D Triaxial Braided Composite Structures,” *International SAMPE Technical Conference*, San Antonio, Texas, USA, Vol. 30, pp. 420-431.

Daniel, I.M. and Ishai, O., 1994, “Engineering Mechanics of Composite Materials,” Oxford University Press.

Deaton, J.W., Kullerd, S.M., Madan, R.C., and Chen, V.L., 1992, “Test and Analysis Results for Composite Transport Fuselage and Wing Structures,” *Second NASA Advanced Composites Technology Conference*, pp. 169-193.

Degrieck, J. and Paepegem W.V., 2001, “Fatigue Damage Modelling of Fibre-Reinforced Composite Materials: Review,” *Applied Mechanics Reviews*, Vol. 54(4), pp. 279-300.

Falzon, P.J. and Herszberg, I., February 1998, “Mechanical Performance of 2-D Braided Carbon/Epoxy Composites,” *Composites Science and Technology*, Vol. 58(2), pp. 253-265.

Fawaz, Z. and Ellyin, F., 1994, “Fatigue Failure Model for Fibre-Reinforced Materials Under General Loadings Conditions,” *Journal of Composites Materials*, Vol. 28(15), pp. 1432-1451.

Fujii, T. and Amijima, S., 1993, “Microscopic Fatigue Processes in a Plain-Weave Glass-Fiber Composite,” *Composites Science and Technology*, Vol. 49, pp. 327-333.

Gates, T.M., 2002, Unclassified Presentation, Mechanics and Durability Branch, NASA Langley Research Center.

Ghosh, S., Lee, K., and Raghavan, P., 2001, “A Multi-Level Computational Model for Multi-Scale Damage Analysis in Composite and Porous Materials,” *International Journal of Solids and Structures*, Vol. 38, pp. 2335-2385.

Heider, D., Hofmann, C., and Gillespie, J.W., Jr., 2000, "Automation and Control of Large-Scale Composite Parts by VARTM Processing," *International SAMPE Symposium and Exhibition (Proceedings)*, Long Beach, California, USA, V 45(2), pp. 1567-1575.

Hess, J.P., 1990, "Fabrication of Braided Composite Structures by Resin Transfer Molding," *National SAMPE Technical Conference*, V 22.

Houston, D.Q. and Chernenkoff, 1992, "RA Environmental Effects on the Fatigue Behavior of a Braided 'E' Glass Composite Resin System Advanced Composites: Design," *Materials and Processing Technologies*, Chicago, Illinois, USA, 2-5 November. 1992 ASM International (USA), pp. 343-353.

Hwang, W. and Han, K.S., 1986a, "Cumulative Damage Models and Multi-Stress Fatigue Life Prediction," *Journal of Composite Materials*, V 20, pp. 125-153.

Hwang, W. and Han, K.S., 1986b, "Fatigue of Composites-Fatigue Modulus Concept and Life Prediction," *Journal of Composite Materials*, V 20, pp. 154-165.

Juska, T.D. and Puckett, P.M., 1997, "Matrix Resins and Fiber/Matrix Adhesion," *Chapter 3, Composites Engineering Handbook, Marcel Dekker, Inc.*, New York, pp. 101-157.

Kelkar, A.D. and Tate, J.S., 2003a, "Fatigue Behavior of VARTM Manufactured Biaxial Braided Composites," *ASME 2003 International Mechanical Engineering Congress and RD & D Exposition*, Washington, DC, USA.

Kelkar, A.D. and Tate, J.S., 2003b, "Effect of Fatigue Loading on the Stiffness Degradation of VARTM Manufactured Biaxial Braided Composites," *9th International Conference on the Mechanical Behavior of Materials (ICM9), PALEXPO Congress Center*, Geneva, Switzerland.

Kelkar, A.D., Tate, J.S., Whitcomb, J., and Tang, X., 2003c, "Performance Evaluation and Modeling of Braided Composites," *44th AIAA/ASME/ASCE/AHS Structures, Structural Dynamics, and Materials Conference*, Norfolk, Virginia, USA.

Kelkar, A.D. and Tate, J.S., 2002, "Low Cost Manufacturing of Textile Composites Using Vacuum Assisted Resin Transfer Molding," *The 20th All India Manufacturing Technology, Design and Research Conference*, AIMTDR, Ranchi, India, pp. 712-716.

Kelkar, A.D., Chaphalkar, P., and Sankar, J., 1999, "Fatigue Behavior of Resin Infusion and Resin Transfer Molding S2-Glass Twill-Woven Composites," *40th AIAA/ASME/ASCE/AHS/ASC Structures, Structural Dynamics, and Materials Conference and Exhibit*, St. Louis, Missouri, 12-15 April 1999, AIAA-99-1438.

Kobayashi, H., Nakama, N., Maekawa, Z., Hamada, H., Fujita, A., and Uozumi, T., 1992, "Fabrication and Mechanical Properties of Braided Composite Truss Joint," *International SAMPE Symposium and Exhibition*, Vol. 37, pp. 1089-1103.

Kumar S. and Wang, Y., 1997, "Fibers, Fabrics, and Fillers," *Chapter 2, Composites Engineering Handbook*, Marcel Dekker, Inc., New York, pp. 83-87.

Lakes, R.S., 1998, *Viscoelastic Solids*, CRC Press, First Edition 1998, pp. 1-2.

Lee, C.W., Rice, B.P., Buczek, M., and Mason, D., 1997, "Resin Transfer Process Monitoring and Control," *SAMPE Journal 34*, 1998 SAMPE, pp. 48-55.

Lee, L.J., Fu, K.E., and Yang, J.N., 1996, "Prediction of Fatigue Damage and Life for Composite Laminates Under Service Loading Spectra," *Composites Science Technology*, V 56, pp. 635-648.

Loos, A.C., Sayre J., McGrane, R., and Grimsley B., 2001, "VARTM Process Model Development," *Proceedings of 46th International SAMPE Symposium*, pp. 1049-1060.

Maurice, F.A., 2000, Professor of Engineering Science and Mechanics, The Pennsylvania State University, Course material for "Engineering Composite Materials EMCH471," http://www4.esm.psu.edu/academics/courses/emch471/Notes/Chapter18.

Minguet, P.J.A., 1995, "Comparison of Graphite/Epoxy Tape Laminates and 2-D Braided Composites Mechanical Properties," *AIAA/ASME/ASCE/AHS Structures, Structural Dynamics & Materials Conference - Collection of Technical Papers*, New Orleans, Louisiana, USA, Vol. 1, pp. 17-26.

Munjal, A.K. and Maloney, P.F., 1990, "Braiding for Improving Performance and Reducing Manufacturing Costs of Composite Structures for Aerospace Applications," *National SAMPE Technical Conference*, Boston, Massachusetts, USA, Vol. 22, pp. 1231-1242.

Munjal, A.K., Spencer, D.F., Rahnenfuehrer, E.W., Pickett, B.E., and Maloney, P.F., 1990, "Design and Fabrication of High Quality Graphite/Epoxy Braided Composite Tubes for Space," *National SAMPE Symposium and Exhibition (Proceedings)*, Vol. 35, pp. 2.

Naik, N.K., 1994, *Woven Fabric Composite*, Technomic Publishing Co., Inc.

Naik, R.A. and Masters, J.E., 1995, "Analysis of the Effects of Fiber Architecture Parameters on the Strength Properties of 2D Triaxial Braided Composites," *American Society of Mechanical Engineers, Aerospace Division (Publication)* AD, San Francisco, California, USA, Vol. 50, pp. 145-173.

Nguyen, L.B., Juska, T., and Mayes, J.S., 1997, "Evaluation of Low Cost Manufacturing Technologies for Large Scale Composite Ship Structures," *Collection of Technical Papers - AIAA/ASME/ASCE/AHS/ASC Structures, Structural Dynamics & Materials Conference*, Vol. 2, pp. 992-1001.

O'Brien, R.K. and Reifsnider, K.L., 1981, "Fatigue Damage Evaluation Through Stiffness Measurements in Boron-Epoxy Laminates," *Journal of Composite Materials*, Vol. 15, pp. 55-70.

Oden, J.T., K. Vemaganti, and N. Moës, 1999, "Hierarchical Modeling of Heterogeneous Solids," *Computer Methods in Applied Mechanics and Engineering*, Vol. 172, pp. 3-25.

Paumelle, P., Hassim, A., and Léné, F., 1990, "Composites With Woven Reinforcements: Calculation and Parametric Analysis of the Properties of Homogeneous Squivalent," *La Recherche Aérospatiale*, Vol. 1, pp. 1-12.

Pike, T., McArthur, M., and Schade, D., 1997, "Vacuum Assisted Resin Transfer Molding of A Layered Structural Laminate for Application on Ground Combat Vehicles," *International SAMPE Technical Conference*, Seattle, Washington, USA, Vol. 28, pp. 374-380.

Portanova, M.A. and Deaton, J.W., 1995, "Impact and Fatigue Resistance of a [±30°/0°] 3-D Braided Carbon Epoxy Composite," *ASTM Special Technical Publication*, 1230.

Reddy, J.N. and Miravete, A., 1995, *Practical Analysis of Composite Laminates*, ISBN #0-8493-9401-5, CRC Press Inc, Florida.

Reifsnider, K.L., 1990, "Damage and Damage Mechanics of Composite Materials," *Elsevier*, New York, pp. 11-77.

Rigas, E.J., Walsh, S.M., and Spurgeon, W.A., 2001, "Development of a Novel Processing Technique for Vacuum Assisted Resin Transfer Molding (VARTM)," *International SAMPE Symposium and Exhibition 2001 a Materials and Processes*, Long Beach, California, pp. 1086-1094.

Rudd, R.E. and Broughton, J.Q., 2000, "Concurrent Coupling of Length Scales in Solid State Systems," *Physica Status Solidi* (b), Vol. 217, pp. 251-291.

Seemann, W.H., 1994, U.S. Patent 5, 316,462.

Seemann, W.H., 1990, U.S. Patent 4, 902,215.

Seobroto, H.B. and Ko, F.K., 1989, "Composite Perform Fabrication by 2-D Braiding," *5th Anuual ASM/ESD Advanced Composite Conference*, Dearborn, Michigan, pp. 307-316.

Shivkumar, K.N., Sundareshan, M.J., and Avva, V.S., 1999, "Structural Integrity of Discontinuous Stiffened Integrally Braided and Woven Composite Panels," FAA report DOT/FAA/AR-99/24, March 1999.

Smith, S., 2001, "Vacuum Assisted Resin Transfer Molding of Sandwich Structures: Material Processing, Evaluation, Fracture Testing and Analysis," Ph.D. thesis, North Carolina A&T State University.

Srirengan, K. and Whitcomb, J.D., 1998, "Finite Element Based Degradation Model for Composites With Transverse Matrix Cracks," *Journal of Thermoplastic Composites*, Vol. 11(3), pp. 113-123.

Strong A.B., 1989, "Fundamentals of Composite Manufacturing: Materials, Methods, and Applications," *Society of Manufacturing Engineers*, pp. 134-136.

Summerscales, J., 1998, *Microstructural Characterisation of Fibre-Reinforced Composites*, ISBN # 0-8493-3882-4, CRC Press, Woodhead Publishing, Ltd., Cambridge, England.

Sun, C.T. and Li, S.J., 1988, "3-Dimensional Effective Elastic-Constants for Thick Laminates," *Journal of Composite Materials*, Vol. 22(7), pp. 629-639.

Swain, D., 2000, "Advanced Manufacturing Techniques Utilizing Carbon Fiber Braid and RTM," *International SAMPE Symposium and Exhibition*, Raytheon Aircraft Company, Inc., Long Beach, California.

Swain, D. and Abbott, R., 2000, "Advanced Manufacturing Techniques Utilizing Carbon Fiber Braid and RTM," *International SAMPE Symposium and Exhibition (Proceedings)*, Long Beach, California, USA, Vol. 45(1), pp. 277-289.

Swanson, S.R. and Smith, L.V., 1996, "Comparison of the Biaxial Strength Properties of Braided and Laminated Carbon Fiber Composites," *Composites Part B: Engineering*, Vol. 27(1), pp. 71-77.

Tang, X. and Whitcomb, J.D., 2003a, "General Techniques for Exploiting Periodicity and Symmetries in Micromechanics Analysis of Textile Composites," *Journal of Composite Materials*, Vol. 37, No. 13, pp. 1167-1189.

Tang, X., Whitcomb, J.D., Goyal, D., and Kelkar, A.D., 2003b, "Effect of Braid Angle and Waviness Ratio on Effective Moduli of 2x2 Biaxial Braided Composites," *44th AIAA/ASME/ASCE/AHS Structures, Structural Dynamics, and Materials Conference*, April 7-10, 2003, Norfolk, Virginia, AIAA-2003-1877.

Tang, X., Whitcomb, J.D., Kelkar, A.D., and Tate, J.S., 2003c, "Progressive Failure Analysis of 2x2 Braided Composites Exhibiting Multiscale Heterogeneity," *18th ASC Technical Conference*, Gainesville, Florida, USA.

Tang, X., 2001, "Micromechanics of 2D Woven Composites," Ph.D. Dissertation, Department of Aerospace Engineering, Texas A&M University, College Station, Texas.

Tate, J.S., Kelkar, A.D., and Rice, J., 2003, "Feasibility Study of VARTM Manufacturing of Carbon Biaxial Braided Composites Using EPON 9504 Epoxy Resin System," *JISSE-8, 8th International SAMPE Symposium & Exhibition*, Tokyo.

TPI Composites, Inc., http://www.tpicomp.com/technology.

Whitcomb, J.D. and Kelkar, A.D., 2002, "Modeling and Performance Evaluation of Braided Composites," FAA annual report of Grant No. DTFA03-01-C00033.

Whitcomb, J.D., Chapman, C.D., and Tang, X., 2000, "Derivation of Boundary Conditions for Micromechanics Analyses of Plain and Satin Weave Composites," *Journal of Composite Materials*, Vol. 34(9), pp. 724-747.

Whitcomb, J. and Noh, J., 2000, "Concise Derivation of Formulas for 3D Sublaminate Homogenization," *Journal of Composite Materials*, Vol. 34(6), pp. 522-535.

Whitcomb, J.D. and Tang, X., 1999, "Effect of Tow Architecture on Stresses in Woven Composites," *40th AIAA/ASME/ASCE/AHS/ASC Structures, Structural Dynamics and Materials Conference*.

Whitworth, H.A., 1998, "A Stiffness Degradation Model for Composite Laminates Under Fatigue Loading," *Composite Structure*, Vol. 40(2), pp. 95-101.

Whitworth, H.A., 1990, "Cumulative Damage in Composites," *Journal of Engineering Materials and Techology*, Vol. 112, pp. 358-361.

Whitworth, H.A., 1987, "Modeling Stiffness Reduction of Graphite Epoxy Composite Laminates," *Journal of Composite Materials*, Vol. 21, pp. 362-372.

Yang, J.N., Lee, L.J., and Sheu, D.Y., 1992, "Modulus Reduction and Fatigue Damage of Matrix Dominated Composite Laminates," *Composite Structure*, Vol. 21, pp. 91-100.

Yang, J.N., Jones, D.L., Yang, S.H., and Meskini, A., 1990, "A Stiffness Degradation Model for Graphite/Epoxy Laminates," *Journal Composite Materials*, Vol. 24, pp. 753-769.

APPENDIX A—BRAID ANGLE CHANGE (IN THE CASE OF BRAIDED TUBES) DOES NOT CHANGE FIBER VOLUME FRACTION

The braid angle of a braided tube can be varied by pulling or compressing the braided tube axially. There is a misconception that a change in the braid angle changes the fiber volume fraction. This is not true because as the braid angle changes, it changes thickness as well. This can be proven by using the following relation for fiber volume fraction based on the areal weight method as discussed in section 2.4.2.

$$V_f = \frac{(n * W * A) / \rho_f}{A * t} = \left(\frac{n}{\rho_f}\right) * \left(\frac{W}{t}\right)$$

Usually, braided tubes are specified at braid angles of 45º. When braided tubes are used in configurations other than 45º, the areal weight (*W*) and ply thickness (*t*) change as a function of the braid angle. This is because braid tube diameter reduces and braid tows come closer to each other when a braid tube is pulled axially. This increases areal weight and ply thickness. Exactly the reverse happens when braid tube is compressed axially. The percentage variation in areal weight and the thickness of a composite with respect to braid angle is predictable and is usually provided by the braid manufacturer. The percentage change in the areal weight (*W*) and the ply thickness (*t*) is typically the same. Table A-1 lists the percentage variation in the areal weight and ply thickness with respect to the braid angle documented by A&P Technology, Inc., the supplier of braided fabric in the present research (Head, 1998). This variation is represented in figure A-1. Thus, in the above equation, ratio $\left(\frac{W}{t}\right)$ remains constant for any braid angle. For a particular lay-up of a braided composite, the number of layers (*n*) and the density of the fiber material (ρ_f) are also constant. The ratio $\left(\frac{n}{\rho_f}\right)$ remains constant. Thus, while braid angle variation of a braid tube causes a variation in thickness, it does not cause variation in the fiber volume fraction.

Table A-1. Percentage Reduction in Areal Weight and Ply Thickness

Braid Angle	Percent Variation in the Areal Weight and Ply Thickness
45	0
40	1
35	6
30	15
25	30
20	55
15	100

(Courtesy of A&P Technology, Inc.)

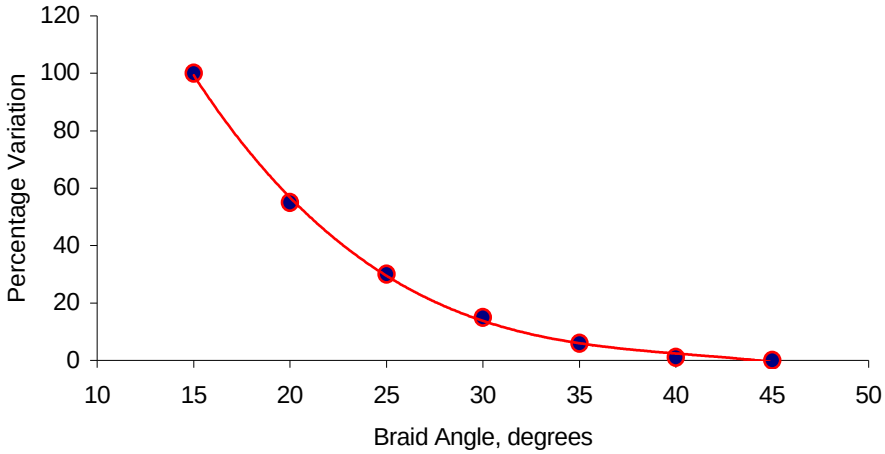

Figure A-1. Percentage Reduction in Areal Weight and Ply Thickness

This may not be true in the case of slit sleeves. Slit sleeves are manufactured individually for a certain braid angle and may have a different architecture for spacing between two tows. The spacing between tows (commonly termed cover factor by manufacturers) may increase or decrease fiber volume fraction by only a small amount. Fiber volume fraction is mainly dependent on the manufacturing process. Vacuum-assisted resin transfer molding typically results in a fiber volume fraction between 0.45 and 0.55.

BIBLIOGRAPHY.

Head, A., 1998, "New Braid Design Spreadsheet Calculates Fiber Architecture and Aerial Weight Simplifying the Design of Braid Reinforced Composites," *International SAMPE Symposium and Exhibition (Proceedings)*, Anaheim, California, USA, Vol. 43(2), pp. 1269-1274.

APPENDIX B—RECOMMENDED METHOD FOR FATIGUE TESTS

Resin transfer molding and vacuum-assisted resin transfer molding processes produce composites with thickness variations. When thickness changes, fiber volume fraction changes as well. Woven composites exhibit fiber misalignment, and braided composites exhibit braid angle variation. Thus, there is a considerable amount of heterogeneity within a specimen and also among different specimens. Most in-plane mechanical properties are dependent on fiber volume fraction and fiber orientation.

The average mechanical properties of tensile test specimens are commonly assumed as the properties of both an entire panel and a large number of panels. In load-controlled fatigue tests, stress is applied as a percentage of the average ultimate tensile strength (UTS). This may not be a correct approach because the UTS of different specimens may differ. Fatigue tests, with current practices, produce a large scatter in fatigue data.

Researchers have reported that the thickness variation in glass/epoxy composite laminates was induced by processing affects, static tensile strength, and tensile modulus. However, its influence on fatigue life is negligible (Hahn and Kim, 1976). It is actually, much more appropriate to relate static tensile strength to fiber volume fraction rather than to thickness.

Carlos (1994) reported that a braid angle variation of ±5º in three-dimensional triaxial braided composites caused a very large scatter in fatigue data (e.g., at a fatigue load of 80% of the UTS, failure cycles varied from 20 to 9000 cycles). Carlos emphasized the necessity of detailed study to determine the effect of braid angle on fatigue life.

A different approach for load-controlled fatigue tests of woven and braided composites is proposed based on this research. Measurement of the fiber volume fraction and fiber orientation, or braid angle, on each specimen before tabbing is recommended. The fiber volume fraction can be measured very easily by the density method. Fiber orientation, or braid angle, can be measured on micrographs using special software such as Image-Pro. A minimum of 15 specimens should be tested in tension tests.

UTS as a function of fiber volume fraction and fiber orientation, or braid angle, should now be evaluated using statistical analysis. The equation may be in the form

$$UTS = \beta_0 + (\beta_1 * \theta) + (\beta_2 * V_f) + (\beta_3 * \theta * V_f)$$

where

θ = Fiber misplacement angle in woven composites or braid angle in braided composites
V_f = Fiber volume percentage
β_0, β_1, β_2, and β_3 = Parameters in statistical analysis

Once this relation is established, it should be used in load controlled fatigue tests. Fiber volume fraction and fiber orientation of each fatigue test specimen should be measured before tabbing. Using the above relation, the UTS of each individual specimen should be computed. Stress

should be applied as a percentage of the computed UTS. Figure B-1 displays the flow chart of the recommended procedure.

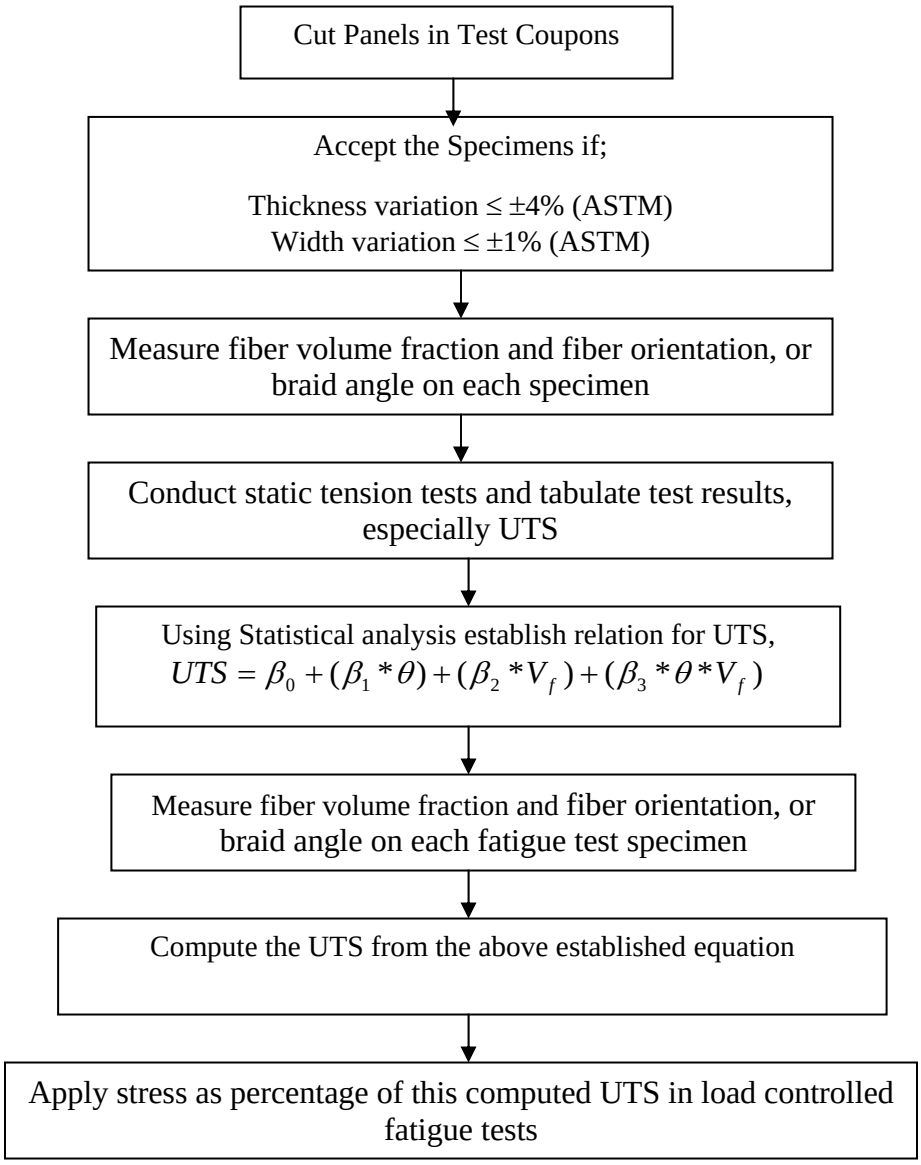

Figure B-1. Recommended Flow Chart for Load Controlled Fatigue Tests of Woven and Braided Composites

Table B-1 presents the tensile test results of 15 specimens of carbon/epoxy braided composites. The fiber volume fraction was not measured for each specimen before testing, but it was measured by the density method on a small rectangular piece cut from a failed specimen. The braid angle was measured on micrographs using Image-Pro software. A linear regression analysis was performed using SAS software to establish the relation for UTS as a function of braid angle and fiber volume fraction. The statistical parameters β_0, β_1, β_2, and β_3 were evaluated as 7.62, 5.24989, 3.331879, and -0.1707, respectively.

Table B-1. Effect of Braid Angle and Fiber Volume Fraction on UTS for Carbon/Epoxy Braided Composites

Specimen Number	Braid Angle	Fiber Volume Fraction	UTS
1*	0.0	0.00	7.62
2	26.2	0.49	85.80
3	25.1	0.46	94.78
4	25.0	0.51	96.55
5	24.9	0.47	98.78
6	23.8	0.54	102.80
7	30.8	0.51	60.23
8	30.1	0.52	62.48
9	30.0	0.54	64.74
10	29.6	0.56	66.03
11	29.4	0.54	66.97
12	45.9	0.49	24.03
13	45.6	0.51	24.32
14	45.3	0.50	24.62
15	45.5	0.51	25.31
16	44.0	0.53	30.90

*This row refers to the average UTS of neat epoxy resin coupons.

BIBLIOGRAPHY.

Carlos, K.G., 1994, “Fatigue Behavior of 3-D Triaxially Braided Composites,” Thesis (M.S.), North Carolina A&T State University.

Hahn, H.T. and Kim, R.Y., 1976, “Fatigue Behavior of Composite Laminate,” *Journal of Composite Materials,* Vol. 10, pp.176-180.

APPENDIX C—BRAIDED TUBES AND SLIT SLEEVES DATA SHEET

The properties of braided tubes and slit sleeves are shown in the table below.

	Slit Sleeve			Braid Tubes T56L200X
	A	B	C	
Width	2.356	1.666	1.395	
Diameter	0.750	0.530	0.444	2.000
Angle	45.0	30.00	25	45.0
Raw yd/lb	620	620	620	620
Carrier	36	36	36	96
Ends per carrier	1	1	1	1
Fiber density lb/cu in.	0.064	0.064	0.064	0.064
Part Fiber Volume	50.0%	50.0%	50.0%	50%
Outputs				
One layer thickness	0.0303	0.0349	0.0398	0.0303
Percent coverage	75.7%	82.8%		75.7%
Qz/sq yd	20.1	23.2	26.4	20.1
ft/lb	36.53	44.74	46.92	13.70
ppi: picks per inch	7.6	6.2	5.9	7.6

(Courtesy of A&P Technology, Inc.)